CT investigations of Australian Devonian fossil fishes, and the application of 3D segmentation and modelling in vertebrate morphology

YUZHI HU

October 2021

A thesis submitted for the degree of Doctor of Philosophy of
The Australian National University

Declaration

This thesis contains no material which has been accepted for the award of any other degree or diploma in any university. To the best of the author's knowledge, it contains no material previously published or written by another person, except where due reference is made in the text.

Yuzhi HU

October 2021

Preface

This thesis consists of four connected papers that present research I undertook for this doctoral program (Papers 1-4). A brief Context Statement frames the papers at the beginning, which explains the relationships between the papers and place this thesis in a broader virtual paleontological setting (e.g. Yin & Lu, 2019). A Synthesis summarises the importance of this project, applications of newly designed and developed methodologies and future study directions. Four papers have been published. The papers were written to stand alone, and for this reason, there is some unavoidable repetition between them, for example, study materials, background information and the description of study areas.

During my PhD, I also introduced the three-dimensional reconstruction workflow for fossils using an open-source software *Drishti*. I introduced new tools and methods to scientific colleagues and students to improve the efficiency and accuracy of 3D segmentation and visualisation of volumetric data.

Contributions made to work in this thesis are presented in the Statement of authorship section of each chapter. Consolidated thesis references are provided at the end.

- Paper 1: Hu, Y., Young, G.C., Lu, J., 2019. The Upper Devonian tetrapodomorph *Gogonasus andrewsae* from Western Australia: Reconstruction of the shoulder girdle and opercular series using X-ray Micro-Computed Tomography. *Palaeoworld* 28, 535–542. https://doi.org/10.1016/j.palwor.2019.07.008

- Paper 2: Hu, Y., Lu, J., Young, G.C., 2017. New findings in a 400 million-year-old Devonian placoderm shed light on jaw structure and function in basal gnathostomes. *Sci. Rep.* 7. https://doi.org/10.1038/s41598-017-07674-y

- Paper 3: Hu, Y., Young, G.C., Burrow, C., Zhu, Y.A., Lu, J., 2019. High resolution XCT scanning reveals complex morphology of gnathal elements in an Early Devonian arthrodire. *Palaeoworld* 28, 525–534. https://doi.org/10.1016/j.palwor.2018.12.003

- Paper 4: Hu, Y., Limaye, A., Lu, J., 2020. Three-dimensional segmentation of computed tomography data using *Drishti Paint*: new tools and developments. *R. Soc. Open Sci.* 7, 201033. https://doi.org/10.1098/rsos.201033

Acknowledgements

I am enormously grateful to my primary supervisor Gavin Young, chair supervisor Tim Senden and two associate supervisors John Long and Steve Eggins, for their continuous support and guidance.

My most clear acknowledgement goes to my primary supervisor Gavin Young. Gavin, who has driven my interest in broad aspects of Early Vertebrate Palaeontology, especially in Placoderm fishes and has freely offered more of his time and support than should ever be expected of any supervisor. The many discussions, the subtle guidance and steering, but also the free pursuit of my research directions despite regularly unproductive ends; these will be the most enduring memories for me. The completion of my Ph.D. would not have been possible without his tireless efforts and patience.

I would like to express my particular appreciation and respect to Tim Senden for his invaluable guidance and support. Tim encouraged me to think more openly and be more creative in the directions I am heading towards. He provided much help so that I can study full-time, go to international and domestic conferences, visit other labs and universities to grow my own network and initiate new ideas as well as future collaboration opportunities. I have benefited greatly from that. I could not have made it without his guidance and encouragements.

I am grateful to my associate supervisor, Steve Eggins who helped me re-shaped my research focus at the beginning of this Ph.D. and have continuously encouraged and challenged my intellectual curiosity. I extend my heartfelt thanks to my external supervisor, John Long (Flinders University), for serving on my Supervisory Panel and offering encouragement, patient guidance and detailed feedback. I will be always grateful for his generous support throughout my candidature.

Jing Lu (IVPP, Beijing, China), as an advisor and a mentor, took a genuine interest in my work, guided me during the tough times and helped me to remember that there is a reason for doing something so difficult. Jing directed me through most of my projects, hosted me in her own research groups, also worked together with Ajay Limaye and myself to create innovative methods. Her involvement, support and encouragement cannot be overstated.

Substantial recognition should also go to the advice and guidance offered by Carole Burrow (Queensland Museum) and You-an Zhu (IVPP, Beijing, China). Especially, for their help towards different revision stages of my papers. I would also like to thank Kate Trinajstic (Curtin

University) for her valuable advice and guidance towards my research topics and for helping me made this thesis much more well-structured.

My sincere thanks go to all my co-authors, Ajay Limaye (NCI, ANU), Benedict King (Max Planck Institute for Evolutionary Anthropology, Germany), Zhu Min (IVPP, Beijing, China) are particularly mentioned.

I would like to thank Alice Clement, Brian Choo and other colleagues in Flinders University as well as Matthew Mccurry and Patrick Smith at the Australian Museum for their continuous support.

I would like to thank my colleagues at Research School of Physics, who provided valuable program/ project level support and contributions. Adrian Sheppard, Mike Turner, Levi Beeching, Ben Young, Rob Middleton, Lydia Knuefing, Andrew Kingston, Bob Dunstone, Mohammad Saadatfar, Jin Tao, Roger Buckley, Dige Wang, Naiying Wang, Bijun Wang, Patrick Kluth, Lan Fu, Elena Ostrovskaya, Liudmila Mangos, Karen Nulty, Sue Wigley, Nikki Azzopardi and many others.

I would also like to thank Josie Smith at Centre for Advanced Microscopy ANU for sharing her interesting stories with me and for her continuous encouragement. I thank Candida Spence (Information Literacy Program, ANU) for providing useful Word Webinars on ANU thesis formatting.

I would also like to thank my partner Shouheng Li for helping me distinguish between the priorities and also for his support, understanding and encouragement. I thank my parents for their unconditional support and encouragement. There were many challenges, and unexpected situations in the first two years. From early 2020, the COVID-19 restrictions added further challenges to complete this thesis. Luckily, the support and understanding I had from all the above people made this Ph.D. possible.

This research was supported by an Australian Government Research Training Program (RTP) Scholarship and ANU Postgraduate Research Scholarship.

Abstract

This thesis by compilation covers four publications, which together demonstrate and apply computed tomography (CT) data, three-dimensional (3D) segmentation, and 3D printing, for the non-destructive high-resolution detection of internal structure in early vertebrate fossils.

Paper 1 (published 2019) studied the tetrapodomorph fish, *Gogonasus*, a three dimensionally well-preserved acid etched sarcopterygian from the Upper Devonian Gogo Formation of Western Australia. 3D modelling and printing were used for a reconstruction of its shoulder girdle and opercular series. A close fit of the opercular series against the upper bones of the shoulder girdle required a more horizontally aligned anocleithrum, supracleithrum and post-temporal than in previous reconstructions. Subopercular bone 2 partly covers the clavicle, and the ascending process of the clavicle, and the ventral process of the anocleithrum, do not fit closely inside the cleithrum, suggesting they may have functioned for ligamentous attachment. A rugose area on the anocleithral process has a similar relative position to muscle ligament attachments in the shoulder girdle of various living actinopterygians. The manipulation of 3D models demonstrates testing of morphological fit for extremely fragile acid-etched bones. It is suggested that previous reconstructions of extinct vertebrates that were based on 2D graphical reconstructions can be rigorously tested using these new technologies.

The second paper (published 2017) dealt with an articulated Devonian arthrodire placoderm. High-resolution computed tomography, 3D segmentation, and enlarged 3D models of a buchanosteid arthrodire, demonstrated a double ethmoid and a palatobasal connection for the palatoquadrate, but no otic connection. The dermal bone attachment for the quadrate is different to other placoderms. A separately ossified cartilage behind the mandibular joint is comparable to the interhyal of osteichthyans. Two articular facets on the braincase associated with the hyomandibular nerve foramen supported a possible epihyal element and a separate opercular cartilage. Reassembling and manipulating 3D printouts demonstrates the limits of jaw kinetics. Previously unrecognized similarities in jaw structure between arthrodires and osteichthyans, will clarify the sequence of character acquisition in the evolution of basal gnathostome groups. New details on the hyoid arch will help to reformulate characters that are key in the heated debate of placoderm monophyly or paraphyly.

Paper 3 (published 2019) describes the detailed morphology of the three gnathal elements of the same specimen as on the previous paper, giving insights into the morphology and organization of the dentition in arthrodires. Arthrodire placoderms, as a possible sister group of Chinese maxillate placoderms plus crown gnathostomes, provide important information

regarding early evolution of jaws and teeth. In displaying numerous denticle rows, the gnathal element morphology is very different from the much-reduced denticulation of higher brachythoracid arthrodires. Ossification centres are anterolateral on the anterior supragnathal (attached to the braincase), anteromesial on the posterior supragnathal (attached to the palatoquadrate), and in the central part of the biting portion of the infragnathal (attached to the Meckel's cartilage). The infragnathal shows no evidence of two ossification centres, as has been interpreted for more advanced arthrodires. The new evidence gives insights into the primitive arthrodire condition for comparison with the dermal jaw bones of Chinese 'maxillate' placoderms that have been homologised with the premaxilla, maxilla, and dentary of osteichthyans.

Paper 4 (published 2020) summarizes the relationship between different modules of *Drishti*, an open-source volume exploration, rendering and three-dimensional segmentation software program that was used in the previous three published papers. A new version (*Drishti* v2.7) is presented, with a new tool for thresholding volume data (i.e. gradient thresholding). A protocol is introduced for performing three-dimensional segmentation using the new 3D Freeform Painter tool. In *Drishti Paint*, these new tools and workflow enable more accurate and precise digital reconstruction, 3D modelling and three-dimensional printing/modelling results. Scan data from the buchanosteid arthrodire (Papers 2 and 3) was used as a case study, but published procedure is widely applicable in biological, medical and industrial research.

Table of Contents

List of Tables

List of Figures

Chapter 1 Context Statement

1.1 Introduction

Fossils represent tangible evidence for the history of life on Earth. Their scientific interpretation demonstrates the fact that life had evolved. However, many fossils are incomplete, and fossilization often involved deformation, damage, and distortion. Many fossils are preserved mainly in flattened (2D), for example when they have been compressed/compacted in sedimentary rocks like shales. To sort out evolutionary developmental questions or hypotheses of relationship, morphological features of fossils should preferably be studied in three dimensions (3D), to enable comparison with anatomy and morphology of living animals. Additionally, most fossils need to be extracted from rock matrix to study their internal morphology in detail, but soft tissue can be lost when performing acid preparation, and structures may be prepared away during mechanical preparation. Those damages are generally irreversible.

This thesis deals with fossil vertebrates, specifically two groups of fossil fishes (Placodermi, Osteichthyes) from the Devonian Period (~420-360 million years ago). In most fossils only the skeleton is preserved, and evidence of soft tissues is extremely rare. Examples of soft tissue preservation in Devonian fishes include lungs, heart and blood vessels in specimens from Miguasha, Canada (e.g. Janvier & Arsenault, 2009; Janvier et al., 2006; 2007) and phosphatised muscle and nerve tissues from Gogo, Western Australia (e.g. Trinajstic et al., 2007; 2013). The two groups dealt with here (Placodermi, Osteichthyes) have a bony skeleton, hence called ‘armoured fishes’ and ‘bony fishes’ respectively (e.g. Long, 2011). In contrast, the chondrichthyans (sharks and rays) have a cartilaginous skeleton. These are not considered further in this section. The bony vertebrate skeleton comprises numerous separate elements. Most vertebrate fossils are preserved as isolated bones, but this thesis is mainly concerned with two articulated specimens that are preserved uncrushed in calcareous nodules or concretions. The rock matrix is calcium carbonate, but the vertebrate skeleton is made of calcium phosphate, so the calcium carbonate can be removed using acetic or formic acid, leaving the bones in perfect condition. Acid-prepared fossils are extremely fragile and can be damaged just by handling. To study the internal morphological or histological features of fossils, the question of how to get the internally preserved information out without damaging the specimens is now being addressed with the latest techniques of high-resolution computed tomography (CT), and segmentation and 3D reconstruction of digital data, as used in this thesis.

The many tools and methods that have been developed and used by paleontologists over centuries to extract information from fossils were summarized by Janvier (1996, chapter 2). Serial sectioning, traditionally used in embryology, was adapted for palaeontology (Sollas 1901; 1904) and applied to the study of the enigmatic Devonian fish *Palaeospondylus* (Sollas & Sollas, 1904). E.A. Stensiö developed the Sollas technique by serial grinding of complete fish skulls, from which wax plate models were built to demonstrate skull and braincase anatomy (e.g. Stensiö 1927, 1963; Jarvik, 1980; Chang, 1982). Although this method completely destroyed very complete and well-preserved fossils, it gave details on internal anatomy that no other method would allow (Janvier, 1996), until the advent of acid preparation techniques for extracting preserved bone from calcareous rock matrix. Using acetic or formic acid to prepare away limestone matrix was first developed on fossil fish specimens from Burrinjuck, NSW (Young, 2011) by Toombs (1948; also, Toombs & Rixon 1959; Rixon, 1976), and then was extensively used on the Gogo fish fauna from Western Australia (Janvier, 1996).

The aim of my research was to investigate whether three-dimensional (3D) segmentation and modelling can advance palaeontology by extracting detailed information from computed tomography (CT) data of scanned fossil specimens, and then manipulating 3D models for improved reconstructions and functional analysis. This thesis by compilation covers four publications (Papers 1-4), which together demonstrate and apply CT data, 3D segmentation, and 3D printing, for the non-destructive high-resolution detection of internal structure in early vertebrate fossils. The research question initially addressed was whether 3D printouts of separate bones from a unique and very fragile acid-etched fossil fish (*Gogonasus* from Gogo, WA) could be manipulated and fitted back together to give a more accurate reconstruction of the skeleton, and provide insights for functional analysis of an extinct fossil fish (Paper 1). The same approach was then applied to a more complex functional problem, the jaw structure in an early arthrodiran placoderm (Paper 2). This research also investigated competing hypotheses about the structure of jaws and cheek in basal placoderms, for comparison with the ‘maxillate’ placoderms of China (Zhu et al., 2013; 2016), which share various jaw features with osteichthyans. Another controversial issue has been the structure of the denticles on the gnathal elements of placoderms, and whether they are comparable to or homologous with true teeth of osteichthyans (e.g. Rücklin & Donoghue, 2015; Burrow, Hu & Young, 2016). This was investigated in Paper 3. New developments of 3D segmentation techniques for computed tomography data were presented in Paper 4.

The two major Devonian fossil fish groups investigated for this thesis are the Osteichthyes and the Placodermi. Osteichthyans are jawed fishes with fully ossified external and internal skeletons. The two major osteichthyan subdivisions are the Sarcopterygii (lobe-finned fishes),

and the Actinopterygii (ray-finned fishes). The Actinopterygii are the most diverse vertebrate group living today, with up to 30,000 species (e.g. Nelson, 2006). The Sarcopterygii have fins with central fleshy lobes, which contain an internal skeleton of robust bones. The three living sarcopterygian sub-groups are the coelacanths and lungfishes (fish groups of very low modern diversity), and the highly diverse tetrapods or land vertebrates. In the Devonian, however, the sarcopterygians were the most diverse group of osteichthyan fishes. The Tetrapodomorpha is the major group of sarcopterygians, consisting of all the land vertebrates (tetrapods or four-limbed vertebrates) and their fossil relatives (i.e. fish-like forms that are more closely related to living tetrapods than to living lungfish). *Gogonasus andrewsae*, investigated in Paper 1, is the only published tetrapodomorph fish from the famous Gogo fossil fish assemblage of the Kimberley region in Western Australia.

The name 'placoderm' is derived from the Greek *plakos* (plate) and *derma* (skin), referring to the interlocking bony plates enclosing the anterior part of the body of typical placoderms. With their robust dermal skeleton, placoderms have an excellent fossil record, and they are the most diverse fossil vertebrates of the Devonian Period (Young, 2010). Placoderm fossils are found in Devonian rocks all over the world, and the earliest known placoderms come from the Early Silurian (e.g. purposed antiarch, *shimenolepis graniferans* Wang 1991, from the lower Silurian Xiushan Formation of Hunan, China), giving the group a total span from approximately 435 to 360 million years ago (Janvier, 2007). Placoderms by the Early Devonian were already diverse in both marine and freshwater environments, in the role of both predators and prey.

Formerly, the class Placodermi was considered an extinct side branch from the main trajectory of the evolution of jawed vertebrates (Denison,1978; Janvier,1996; Goujet & Young, 2004; Young, 2010). Especially, various characters of the placoderm jaws and dental structures were regarded as peculiarities (e.g. Ørvig, 1980). This viewpoint dramatically changed with documentation of the remarkable Xiaoxiang Fauna from the Silurian of China, which produced the 'maxillate' placoderms *Entelognathus* and *Qilinyu* (Zhu et al., 2013; 2016). These have typical features of the placoderm dermal skeleton, in combination with marginal jaw bones previously considered unique to the bony fishes (Osteichthyes). This evidence has seriously challenged assumptions of monophyly for the class Placodermi, and also its various subgroups.

Nine major placoderm subgroups were traditionally recognised as orders (Denison 1978; Young 2010): Arthrodira; Antiarchi; Phyllolepida; Ptyctodontida; Rhenanida; Acanthothoraci; Petalichthyida; Pseudopetalichthyida; Stensiöellida. Arthrodira is the most diverse subgroup, and often the stereotypical representative of all placoderms, comprising some 55% of about

330 named placoderm genera (Young, 2010). Arthrodira radiated during the Middle and Late Devonian, particularly in the marine environment, and underwent major evolutionary changes in jaw structure (see Young, 2010, fig 2). However, whether this assembly is a monophyletic group or not is still debated (Brazeau, 2009; Zhu et al., 2013; Dupret et al., 2014; Brazeau & Friedman, 2015; Qiao et al., 2016; Zhu et al., 2016; King et al., 2017; King & Rücklin, 2020). Zhu et al. (2013; 2016) proposed arthrodires plus ptyctodontids as the sister group of 'maxillate' placoderms plus crown gnathostomes. Alternative phylogenies have arthrodires as the sister group to crown gnathostomes (Davis et al., 2012; Giles et al., 2013), in a polytomy with rhenanids (Giles et al., 2015), or outside *Brindabellaspis* plus antiarchs as sister groups to 'maxillate' placoderms plus crown gnathostomes in a strict consensus tree (Zhu et al., 2021).

These competing hypotheses generated much renewed interest in the evolution of jaws and teeth in placoderms, in particular to distinguish characters representing the primitive gnathostome condition from those that are autapomorphies of placoderms (e.g. Rücklin & Donoghue, 2015; Burrow et al., 2016; Donoghue & Rücklin, 2016; Smith et al., 2017; Vaškaninová et al., 2020). However, jaw structure in basal members of the Arthrodira has remained poorly understood. The key specimen dealt with in Papers 2 and 3 is one of the best 3D preserved articulated acid-etched Early Devonian arthrodires, with gnathal elements in association and only very slightly dislocated from the complete skull, braincase and jaw cartilages, the latter preserved by complete perichondral ossification. In contrast, the braincase and jaw cartilages are mostly cartilaginous in Middle and Late Devonian arthrodires that have been the subject of most previous investigations of placoderm jaw evolution.

1.2 Material

Table 1 lists all the fossil fish specimens covered in Papers 1-4, and also other CT scanned specimens on which I have done significant segmentation and visualisation work for comparative morphology purposes during the course of this thesis.

All specimens described in this thesis come from two localities: the Gogo Formation in the Canning Basin of northern Western Australia (e.g. Long & Trinajstic, 2010; 2018), and the Murrumbidgee Group limestones of Burrinjuck, New South Wales (e.g. Young, 2011). Amongst numerous fossil fish localities in Australia (Young et al., 2010; Burrow et al., 2010; Young & Lu, 2020), these are the most famous and best studied sites for producing three-dimensionally preserved articulated fossil fishes that can be extracted by acid preparation.

The Gogo Formation is an inter-reef limestone deposit of Late Devonian age on the southern region of the Lennard Shelf (Playford, 1980; Long & Trinajstic, 2018). The Gogo fish fauna comprises almost 50 species of fishes described so far, including placoderms, actinopterygians, dipnoans, acanthodians, and single-taxon representatives of chondrichthyan, onychodontiform, actinistian, and osteolepiform fishes (Long & Trinajstic, 2010). *Gogonasus* (the osteolepiform) is one of the best-known Devonian lobe-finned fishes, providing crucial morphological data in understanding early stages of the fish-tetrapod transition (Long et al., 2006). The four described specimens are: ANU 21885 (the holotype) described by Long (1985); ANU 49259 and WAM 86.9.661 (Long et al., 1997); and NMV P221807 (Long et al., 2006; Holland & Long, 2009; Holland, 2013; 2014). Paper 1 used CT data to investigate the left shoulder girdle and opercular series of NMV P221807. Arthrodiran placoderms are the most diverse component of the Gogo fish fauna (e.g. *Holonema*, *Latocamurus*, *Mcnamaraspis*, *Eastmanosteus, Kimberleyichthys*; Long & Trinajstic 2010; 2018). *Eastmanosteus* cheek bones are illustrated in Paper 2, and gnathal elements of *Kimberleyichthys* were used for comparative study in Paper 3.

The Murrumbidgee Group limestones at Burrinjuck, the largest exposure of Early Devonian limestones in southern New South Wales, were deposited in an ancient coral reef environment. With a vertebrate faunal list of some 62 genera and 70 species, the Burrinjuck fossil fish assemblage is the most diverse fossil fish fauna known from the Devonian, and also the oldest coral reef fish assemblage from the fossil record (Young, 2011). The Burrinjuck limestones have produced only a few articulated placoderm specimens; most are isolated bones or skulls found in lumps of limestone, but many examples of skulls have complete braincase perichondral ossification. Unlike Gogo, nodules are very rare, and only a very few have articulated fish. One of these is ANU V244, first described by Young et al. (2001) as one of the best 3D preserved articulated acid-etched Early Devonian arthrodires known. The specimen is assigned unequivocally to the buchanosteid arthrodires, which are basal brachythoracids that display many primitive arthrodire characteristics. Research on the jaw structure and function of ANU V244 was published in 2017 (Paper 2), and detailed study of its gnathal elements was presented in Paper 3.

1.3 Methods

All scanning for this thesis was done on instruments developed and built at the CT Lab, Department of Applied Mathematics, Research School of Physics, Australian National University. All CT data were reconstructed using an in-house software called Mango (https://physics.anu.edu.au/appmaths/capabilities/mango.php). Mango can perform three-

dimensional tomographic reconstruction on CPU or GPU clusters. The CPU-only code is limited to analytic methods: Feldkamp–Davis–Kress (FDK) filtered back-projection (FBP) for a circular X-ray source trajectory and Katsevich FBP for helical/double-helical X-ray source trajectories (Varslot et al., 2011). The GPU code can also perform multi-grid iterative reconstruction (Myers et al., 2016) for a space-filling X-ray source trajectory (Kingston et al., 2018a). The reconstruction code has software for automatic geometric alignment capabilities (Kingston et al., 2011), X-ray source movement correction (Myers et al., 2011) and component or rigid-body sample movement correction (Latham et al., 2018).

Gogonasus andrewsae NMV P221807 (Paper 1) was scanned used an 80kV/140μA reflection-style X-ray source and 1 mm thick silicon dioxide filter. All components were imaged through 360 degrees rotation. All reconstructions were based on 1440 radiographic projections formed on a 1024 × 1024 48-bit pixels Perkin Elmer Flat Panel camera. The left clavicle was scanned (9 July 2012) with a resolution of 63 microns (at 286 mm from the source, and the detector 457 mm from the source). The left cleithrum was scanned (6 August 2012) with a resolution of 80 microns (at 485 mm from the source, and the detector 607 mm from the source). The left anocleithrum, supracleithrum and post-temporal bone were scanned separately (12 July 2012) with a resolution of 63 microns (at 286 mm from the source, and the detector 457 mm from the source). The opercular series was scanned (with associated cheek elements) in one scan (21 June 2012) with a resolution of 84 microns (at 510 mm from the source, and the detector 607 mm from the source).

Buchanosteid arthrodire ANU V244 (Papers 2&3) was scanned in 2011 and rescanned in 2015. In 2011, the whole specimen scan used an instrument with an 80kV/110 μA reflection-style X-ray source and 2 mm thick silicon dioxide filter. The specimen was placed 72 mm from the source, and the detector positioned 350 mm from the source. The specimen was imaged through 360 degrees rotation. Reconstruction was based on 2880 radiographic projections formed on a 2048 × 2048 Perkin Elmer Flat Panel camera. A 2015 rescan used a new double-helix HeliScan CT Scanner with higher resolution and a new algorithm to process and reconstruct CT data. 1.2 mm aluminium and 0.35 mm stainless steel filters were used, with specimen distance 85 mm from the source, and detector position 396 mm from the source, and probed separately with a polychromatic X-ray beam (Bremsstrahlung radiation). Accelerating voltage of the electron beam generating the Bremsstrahlung radiation was 110kV with a current of 100μA. A series of X ray transmission radiographs, collectively called the projection data, were acquired by the detector as the specimen was rotated through 360 degrees double-helically over a period of 18 hours. Reconstruction was based on 2520

radiographic projections formed on a 2048 × 1538 Varian Flat Panel camera. The three dermal gnathal elements (anterior and posterior supragnathals of the upper jaw, infragnathal of the lower jaw) of ANU V244 were illustrated in Paper 2 based on the segmented gnathal elements from the 2011 CT scan.

The left infragnathal and right anterior supragnathal of this specimen were removed from the articulated specimen for description in the original study of Young et al. (2001). They were scanned in 2015 with a higher resolution (1.45 and 1.79 microns respectively), to provide further information on external morphology and growth sequence (Paper 3). Both were scanned with the double helix HeliScan CT Scanner at ANU CT Lab. Scanning details are as follows. Right anterior supragnathal: 2 mm aluminium filter, specimen distance 3.95 mm from the source, detector position 309.5 mm from the source; probed separately with a polychromatic X-ray beam (Bremsstrahlung radiation), accelerating voltage of the electron beam 100kV with a current of 76 μA. The specimen was rotated through 360 degrees double-helically over a period of 22 hours. Reconstruction was based on 3600 radiographic projections formed on a 3040 × 3040 Varian Flat Panel camera. The final resolution reached 1.79 microns. Anterior end of left infragnathal: 1.5 mm aluminium filter, specimen distance 3.2 mm from the source, detector position 309.5 mm from the source, and probed separately with a polychromatic X-ray beam. Accelerating voltage of the electron beam generating Bremsstrahlung radiation 100kV with a current of 65 μA; specimen rotated through 360 degrees double-helically over a period of 19 hours; reconstruction based on 3600 radiographic projections formed on a 3040 × 3040 Varian Flat Panel camera with a final resolution of 1.45 microns.

All segmentation and rendering for this thesis (Papers 1-4) were carried out using the software program *Drishti*, an open-source volume exploration tool (Limaye, 2012). Segmentations were performed using 8-bits resolution volumetric data for Papers 1-3 and 16-bits full resolution in Paper 4 using an updated version (*Drishti* V2.7).

The segmented components (Papers 1-2) were saved as 3D surface models in .stl format (Stanford Triangle Format) for 3D printing using ZPrinter 650 (more details on ZPrinter 650, refer to Appendix B). Eight *Gogonasus* components were printed at three times natural size and buchanosteid arthrodire components were printed at six times natural size. Those 3D printouts (Papers 1&2) were manipulated into assumed life positions and fixed with dental wax using various morphological criteria as illustrated in the paper itself and the summary statements below.

Paper 3 used the volume data of the segmented posterior supragnathal from Paper 2 and the rendered volume data from the 2015 CT data of the right anterior supragnathal and anterior end of the left infragnathal to study external morphology of three gnathal plates in ANU V244.

Paper 4 cropped the 2015 ANU V244 whole specimen scan to focus on the region contains the suborbital and post-suborbital plates and used this cropped volume as a case-study to demonstrate the new developments and updates of the Drishti program. *Drishti* is updated with an ability to read 16-bits resolution volumetric data when perform segmenting tasks in *Drishti Paint* only by then. A general protocol to segment the three-dimensional volumetric data using *Drishti Paint* v. 2.7 is also developed, as introduced in Paper 4. These methods are the most recent developments of various other related techniques that have been applied to investigation of fossils, of which I now give a brief historical summary.

Various methods were already in use in the twentieth century to investigate the internal morphology of fossils, such as scanning electron microscopy to study fossil histology (e.g. first use, Gross, 1968); light transmission microscope to help investigate thin sections; using magnetic resonance imaging (e.g. Schultze & Cloutier, 1991) and finally high-resolution computed tomographic scanning (e.g. Rowe et al., 1992). However, even in the early 2000s CT scanning was not a widely known nor used tool in our field.

Since the initial attempts of using X-rays to investigate fossil materials in the nineteenth century (Cunningham et al., 2014), X-ray microtomography as a non-destructive and high-resolution investigation tool has become increasingly used in the last two decades (e.g. Sutton, 2008; Sutton et al., 2012; 2016) , coupled with increased contrast of the tomogram; reduction of signal-to-noise ratio in reconstruction of CT data and resolving of other known artefacts, such as beam hardening thus improving of the resolution and voxel size of the scan dramatically through the last decade (e.g. Kingston et al., 2018), which further enable this non-destructive investigation method as a prefect tool for examining the external and internal morphology, even histology of fragile or unique fossil specimens (e.g. Brazeau et al., 2020; Cloutier et al., 2020; Clement et al., 2018; Long et al., 2014).

Along with the more frequent use of the CT, other similar non-destructive tools are also known in the field, such as X-ray synchrotron microtomography (e.g. Tafforeau et al., 2006; Chen et al., 2016; 2017; 2020), computed laminography (CL) and augmented laminography (e.g. Zuber et al., 2017), neutron radiography and tomography (e.g. Mays et al., 2018), and energy dispersive X-ray spectrometry to work out the chemical composition of anatomical structures (e.g. Chevrinais et al., 2015). However, X-ray synchrotron microtomography facilities require

much more space than CT facilities and are currently restricted by the locations of these facilities. CL is great for specimens with relatively equally distributed spatial dimensions but does not work well for flat fossils. Neutron radiation is hindered by reliance on nuclear reactor facilities, which are also difficult to access due to logistical issues. However, neutron radiation may be able to penetrate denser materials than X-ray radiation; thus it can be used together with CT if access to such a facility is available.

In the past few decades, image analysis and visualization software programs, and other 3D tools (e.g. 3D printing) have been introduced (e.g. Cunningham et al., 2014; Lautenschlager, 2016; Sutton et al., 2017; Johnson et al., 2019). 3D segmentation and modelling are used for both volumetric and surface mesh data. In summary, the past 10 years or so has seen much increased use of computed tomography in palaeontology, and a range of necessary tools have emerged; e.g. scientific visualization that utilises computer graphics, image processing, 3D segmentation and modelling, and other techniques to create graphical and visual representations of the results from computations and simulations, all of which are being continuously adapted, upgraded and improved.

Table 1.1 CT scanned specimens investigated during the course of this thesis.

Species information & Specimen number	**Location**	**Date of scan**	**Voxel size (um)**	**Papers cited**
'buchanosteid' sp. V244 (skull, braincase, eye capsules, etc.)	Burrinjuck, NSW	Sep 2011 & Jun 2015	41.14 /41.64	Young et al., 2001; Young 2008, 2010; Hu et al.,2017,2019
'buchanosteid' sp. V244 (right ASG)	Burrinjuck, NSW	Apr 2015	1.79	Young et al., 2001; Hu et al., 2017, 2019
'buchanosteid' sp. V244 (anterior part left IG)	Burrinjuck, NSW	Jun 2015	1.45	Young et al., 2001; Hu et al., 2017, 2019
arthrodire sp. V 79 (SO+PSO)	Burrinjuck, NSW	Jun 2016	23.75	King, Hu & Long, 2018a
Bothriolepis sp. indet. V1039	Gogo, WA	Nov 2017	21.72	NA
Brindabellaspis ANU 49493 (partial skull and braincase)	Burrinjuck, NSW	Aug 2017	30.42	Zhu, Giles, Young & Hu et al., 2020
Brindabellaspis AM F81911 (partial skull and braincase)	Burrinjuck, NSW	Aug 2018	35.33	Zhu, Giles, Young & Hu et al., 2020
Eastmanosteus V1045 (IG)	Gogo, WA	Oct 2018	10.96	Dennis-Bryan 1987 (fig. 18E-G)
Kimberleyichthys ANU 35687 (IG)	Gogo, WA	Nov 2018	19.84	Dennis-Bryan & Miles 1983 (fig. 8)
Cavanosteus V78(IG) / ANU 17789 (IG)	Burrinjuck, NSW	Nov 2018	8.22/ 11.93	Young 2004 (fig.2A-C; fig.3A, B, E, F)
Nawagiaspis V1635 (IG)	Broken River, QLD	Nov 2018	3.25	Young 1990 (fig.9c-d)
arthrodire sp. V3119 (IG)	Burrinjuck, NSW	Nov 2018	5.13	NA
Palaeospondylus QMF 52826	Cravens Peak beds, QLD	Nov 2017/ Mar 2019	10.96 / 5.42	Burrow, Hu et al., 2021 (in prep)
Palaeospondylus MJN 1188	Scotland	Nov 2017	5.29	Burrow, Hu et al., 2021 (in prep)

Chapter 2 Paper 1: Hu, Y.-Z., Young, G.C., Lu, J. 2019 The Upper Devonian tetrapodomorph *Gogonasus andrewsae* from Western Australia: Reconstruction of the shoulder girdle and opercular series using X-ray Micro-Computed Tomography. *Palaeoworld*. 28:4, 535-542

[for pdf see Appendix A]

2.1 Statement of Contribution

G.Y. and J.L. designed the study. Y.H. performed all digital segmentations, scientific visualizations, 3D printing; undertook the anatomical interpretation and comparative analysis; produced illustrations; Y.H. and J.L. prepared figures; Y.H. drafted the manuscript; all authors revised the manuscript.

2.2 Summary Statement

This paper records my research on the first 3D printed Devonian lobe-finned fish from the Gogo Formation, WA.

2.3 Key Results

1. Opercular series

The opercular series as reconstructed using 3D printouts generally agree with the reconstruction of Long et al. (1997). However, manipulation of 3D printouts indicates some differences in detail. The subopercular bone 2 has a broader triangular overlap on its dorsal margin. Fitting these together gives a larger notch posteriorly. The anterodorsal corner of both subopercular bones also project slightly forward (Hu et al., 2019, fig. 2D). With the entire opercular unit evenly curved in posterior view (Hu et al., 2019, fig.2E), the second subopercular curves under the fish so that the subopercular bone 2 is only slightly visible in lateral view (Fig. 2.1B).

2. Shoulder girdle series

Drishti images of the anocleithrum show a slightly curved elongate bone with a strong unornamented anocleithral process, and distinct overlap areas for the cleithrum posteriorly, and supracleithrum anteriorly. However, manipulating 3D printouts showed the anocleithrum fitted more horizontally compared to the reconstruction of Holland (2013). His reconstruction evidently followed Jarvik (1944; 1980) for *Eusthenopteron* (Fig. 2.2C). However, a

Eusthenopteron specimen in which the operculum was prepared away to show the shoulder girdle underneath (Jarvik, 1944, fig. 5A-B) indicates a more horizontal orientation for the anocleithrum (Fig. 2.2B), as indicated by 3D printouts of *Gogonasus* (Fig. 2.2A).

The left clavicle of NMV P221807 is preserved as a separate element, but Holland (2013) figured only the right clavicle, which is preserved attached to the cleithrum. It is unsure that the figured right clavicle by Holland is complete, as the separated left clavicle, which was CT scanned and 3D printed, is larger (Hu et al., 2019, p.539). In *Gogonasus*, the posterior overlap on the clavicle fits onto the inside edge of the cleithrum. This is different to *Eusthenopteron*, where the overlap of the cleithrum in the latter is external (Jarvik, 1980).

The 3D printout reassembly indicated that the ventral process of the anocleithrum (pr.acl, Fig. 2.2) did not fit closely against the inside of the cleithrum. Jarvik (1948, fig.25) showed this process projecting slightly in *Osteolepis* (Fig. 2.2D), and not projecting at all in *Eusthenopteron* (Fig. 2.2C). However, Hu et al. (2019, p.540) noted that the anocleithral process was not clearly preserved in *Osteolepis* and could have been much bigger. Because the process in *Gogonasus* does not fit against the cleithrum, a different function was suggested, perhaps a ligamentous attachment, comparable to the cucullaris and epaxial muscle attachments in various actinopterygians (Hu et al., 2019, p. 540).

3D printouts of the opercular and shoulder girdle series were fitted together such that the mesial edges of the cleithrum and clavicle form an even curve in ventral view (Fig. 2.3A). This indicates that the ascending process of the clavicle similarly does not fit closely to cleithrum and perhaps also functioned for ligamentous attachment.

In summary, previous studies including Holland (2013), largely followed reconstructions of *Eusthenopteron* (as the best-known Devonian fish), but all were done graphically (i.e. 2D reconstructions). Hu et al. (2019) showed that manipulation of 3D printouts permits testing of the morphological fit of extremely fragile acid-etched bones, and the new methods indicate a new way to investigate the constructional morphology of one or more mechanical units of the vertebrate skeleton.

2.4 Background

Because the ANU held one of the most complete specimens of *Gogonasus andrewsae* Long 1985, this specimen (ANU 49259, Fig.2.1A) was selected in 2012 to trial the new 3D printer ZPrinter 650. There are four described *Gogonasus* specimens- ANU 21885 (the holotype); ANU 49259 and WAM 86.9.661 described by Long et al. (1997); NMV P221807 described by

Long et al. (2006), Holland & Long (2009), and Holland (2013; 2014). The component bones of ANU 49259 were reassembled by Baz Cook (professional model maker) based on the graphical reconstruction in Long et al. (1997, fig.60A). This reassembly (Fig. 2.1A) showed discrepancies in the way the bones fitted together (e.g. the opercular series forming the gill cover). It indicated that 3D printing could be used to test previous graphical reconstructions, and also the functional morphology of fossils more generally.

The example chosen for this study was fish respiration. Fish acquire dissolved oxygen through pumping water over their gills, involving continuous opening and closing of the operculum (gill cover). The operculum protects the gills, and serves a functional role of respiration by sealing the gill chamber against the shoulder girdle. ANU 49259 had a well preserved opercular series (Fig. 2.1A), but shoulder girdle bones were missing. However, a new specimen NMV P221807 is the first to include a complete body. The head and shoulder girdle bones were etched out by Prof. John Long and described by Long et al. (2006). This specimen was borrowed, and CT scanned at ANU in 2012, and 3D printing was done in 2013.

My research aimed to test the functional fitness of the opercular series against the shoulder girdle of *Gogonasus*, using NMV P221807. The shoulder girdle of this specimen had recently been reconstructed by Holland (2013). Again, this was mainly a graphical reconstruction, because the actual bones are extremely fragile (and unique), limiting how much they can be manipulated. This problem is overcome using 3D printouts, as was demonstrated in our paper (Hu et al., 2019).

The above results depended on three main methodologies:

- X-ray microtomography as a non-destructive investigation method for examining unique and irreplaceable extremely fragile acid-etched fossil bones. The different bones could be segmented out from the CT data as separate elements.

- Scientific visualization was used to create graphical and visual representations of the results from segmented elements.

- 3D printing produces identical and enlarged duplicates of bone components of vertebrate skeleton (in this case, the shoulder girdle and opercular series of *Gogonasus*) for performing physical functional morphology tests.

I then applied methodologies to another unique acid-etched Devonian fish to investigate a more complex functional problem, namely morphology of jaws, gnathal elements, hyoid arch

and operculum (i.e. submarginal plate) of a buchanosteid placoderm from Burrinjuck, New South Wales (Hu et al., 2017, Paper 2).

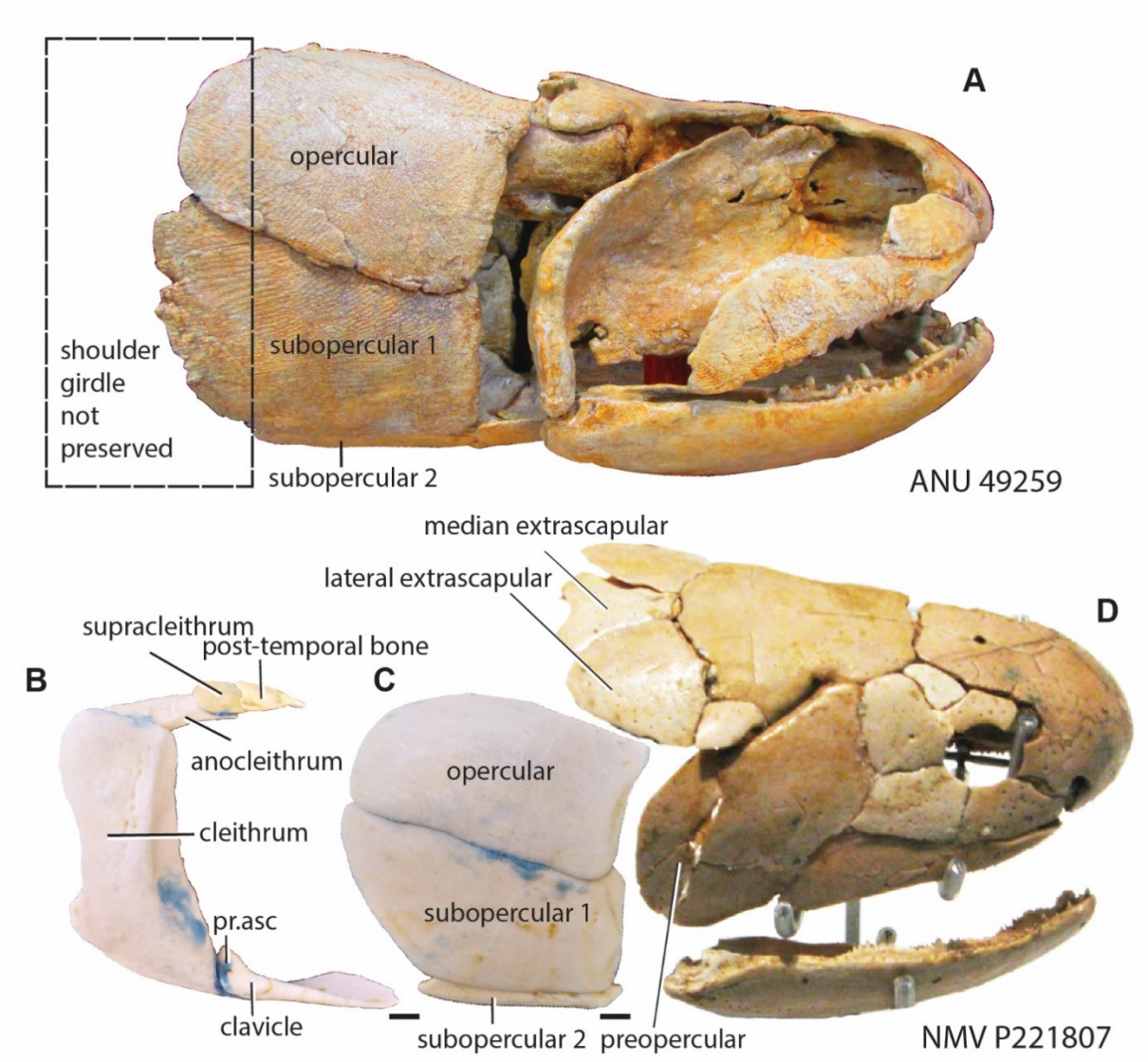

Figure 2.1 3D reconstructions of the tetrapodomorph fish, *Gogonasus andrewsae* Long 1985 in right lateral view. **A** First 3D printouts of *Gogonasus*, ANU 49259. Compared to Hu et al. (2019, fig. 6E), this is mirror imaged to match the right lateral view of NMV P221807 below. **B-C** 3D printouts of the left opercular and shoulder girdle series, reversed to fit against the right-side image of NMV P221807 (on display in Museum Victoria and therefore could not be scanned). Abbreviation: pr.asc, ascending process of the left clavicle. Scale bar: 1cm (**B-C**); not to scale (**A, D**).

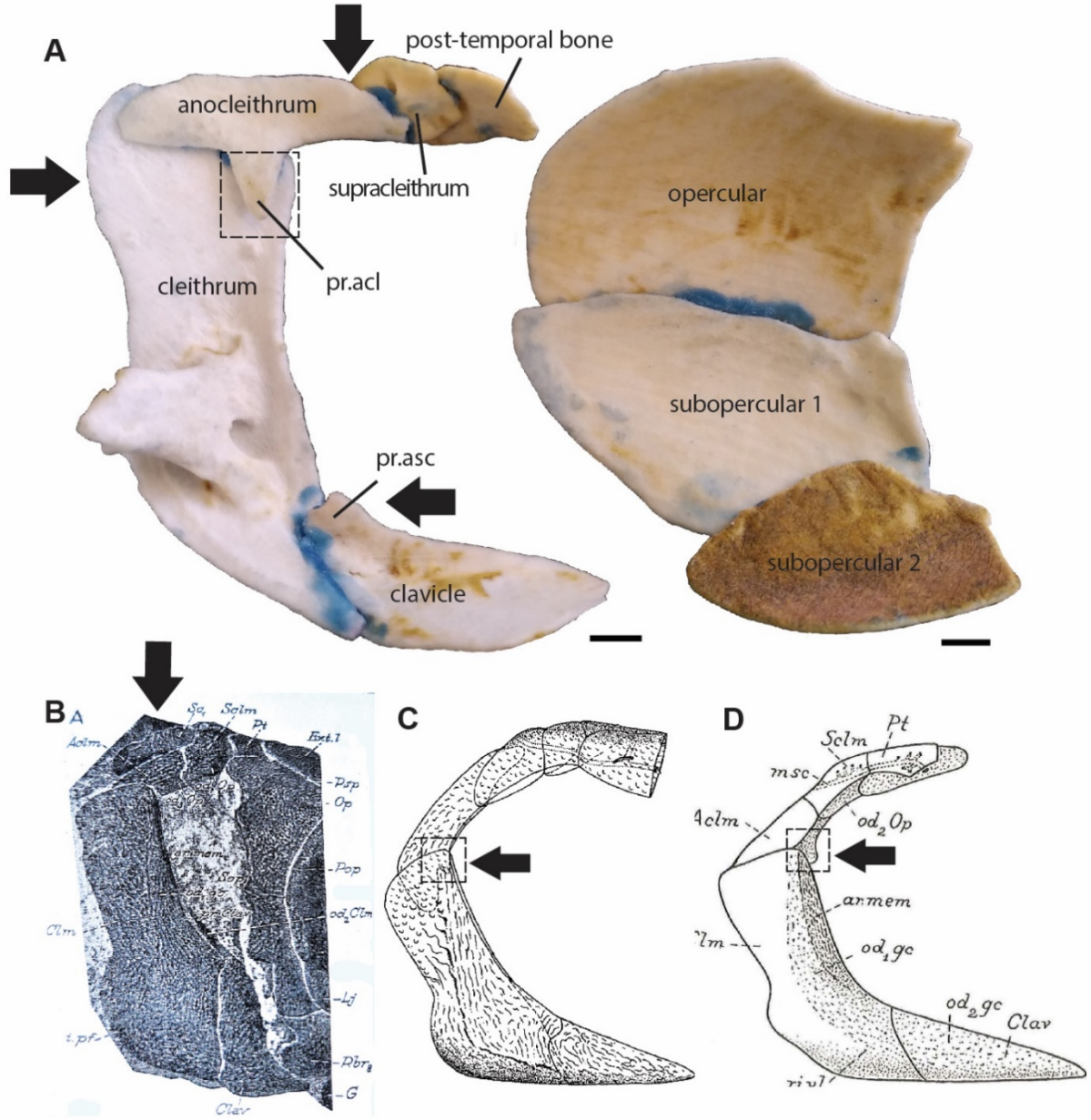

Figure 2.2 A 3D printouts reconstruction of the shoulder girdle and opercular series of *Gogonasus* (NMV P221807) in internal view. Green arrows show the more horizontally aligned anocleithrum, supracleithrum and post-temporal bones; the anocleithral process (pr.acl), and the ascending process on clavicle (pr.asc). **B** Photo of *Eusthenopteron*, from Jarvik (1944, fig.5A), demonstrating a similar more horizontal alignment, than in the graphical reconstructions of *Eusthenopteron* by Jarvik (1980, fig. 126) (**C**) and *Osteolepis* (**D**), similarly reconstructed by Jarvik (1948, fig.25) (**D**). Green arrows point out the similar process on the anocleithrum as in *Gogonasus* (**A**). Scale bar: 1cm (**A**); not to scale (**B-D**).

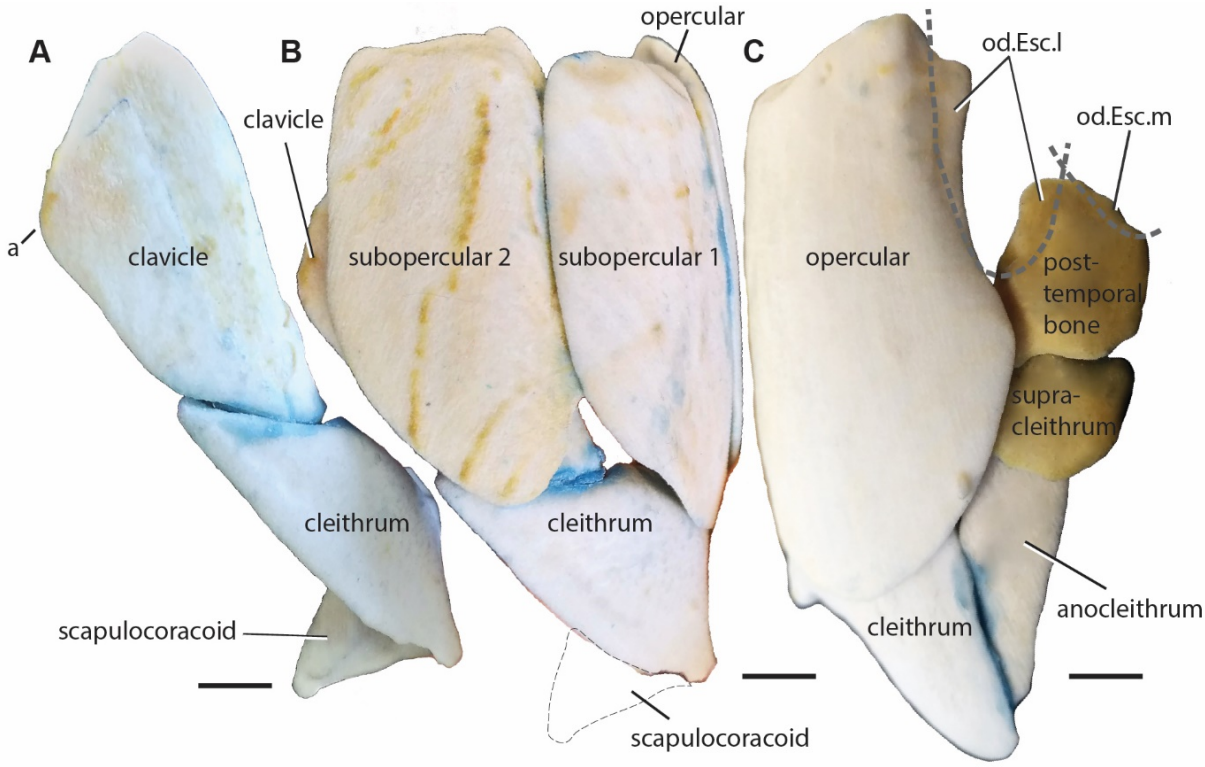

Figure 2.3 3D printout of *Gogonasus* (NMV P221807). **A** 3D printout of the left cleithrum and clavicle in ventral (**A**) view. **B-C** 3D printouts reconstruction of the shoulder girdle and opercular series in ventral (**B**) and dorsal (**C**) views. The scapulocoracoid is shown as the dashed line in (**B**) as it was covered by the finger when photo shooting. a, mesial angle; od.Esc.l, overlap for lateral extrascapular; od.Esc.m, overlap for median extrascapular. Scale bar: 1cm.

Chapter 3 Paper 2: Hu, Y.-Z., Lu, J., Young, G.C. 2017 New findings in a 400 million-year-old Devonian placoderm shed light on jaw structure and function in basal gnathostomes. *Scientific Reports* 7, 7813

[for pdf see Appendix B]

[for Supplementary pdf see Appendix C]

3.1 Statement of contribution

G.C.Y. designed the study. Y.H., G.C.Y. and J.L. performed the research. Y.H. performed C.T. restorations, digital dissections, and 3D printouts. Figures were produced by J.L., Y.H. and G.C.Y. Y.H. drafted the manuscript, all authors discussed the results and revised the manuscript.

3.2 Summary Statement

Following the groundwork of Paper 1, CT, scientific visualization and 3D printing were applied to a more complex problem of functional morphology: the structure and function of the jaws and operculum in a basal gnathostome, by study of a unique articulated example of a buchanosteid arthrodire (ANU V244, from 400 myr old limestones of Burrinjuck, NSW). This was the first complete description of the palatoquadrate and Meckel's cartilage for any arthrodire. It was also the first use of high-resolution 3D printing to investigate morphology and function in a fossil vertebrate. This involved experimentation of the morphological fit between all dermal and perichondrally-ossified endoskeletal elements of the skull, braincase, jaws and cheek. Many components were segmented out from the whole specimen CT data using *Drishti*, eight of which are displayed in Fig. 3.1. Segmented components were 3D printed at six times their original size to work out the functional morphology of jaws.

3.3 Key Results

1. Revised palatoquadrate attachments to the dermal cheek unit

2. Revised structure of the mandibular joint

3. Possible homologue to the interhyal of osteichthyans

4. Evidence for an unossified epihyal element that was separate from the opercular cartilage

5. Double ethmoid connection demonstrated between the autopalatine and the braincase

6. A more complete system of grooves for cranial blood vessels than previously known for arthrodires

7. Revised gnathal element homologies between ‘placoderms’ and osteichthyans

3.4 Background

Regarding palatoquadrate attachments to the dermal cheek unit (Key Result 1), typical arthrodires like *Eastmanosteus* from Gogo (Fig. 3.2A&C) have the autopalatine and metapterygoid parts of the palatoquadrate attached inside the dermal suborbital plate, whilst the quadrate portion is fused to the inside of the postsuborbital plate. For many decades, this was assumed to apply to all arthrodires and perhaps all placoderms; i.e. the postsuborbital plate carried the quadrate part, representing the mandibular joint, and therefore a fundamental evolutionary innovation defining the Gnathostomata.

Early work on many arthrodires (e.g. Miles & Westoll 1968; Miles 1969) was confirmed when the exceptional preserved Gogo arthrodires were first described (e.g. Gardiner & Miles, 1990), as represented by *Eastmanosteus* (Fig. 3.2A&C). This pattern was assumed primitive for arthrodires (e.g. *Dicksonosteus*, Goujet 1984) and possibly for other placoderm groups with dermal cheek plates (e.g. *Romundina*, Ørvig 1975; antiarchs, Young & Zhang, 1996). However, Hu et al. (2017) showed the mandibular joint in ANU V244 (signifying the quadrate part of the palatoquadrate) was also located inside the suborbital plate (Fig. 3.2B). The palatoquadrate of *Romundina* preserved attached to the dermal suborbital plate was reinterpreted, based on the evidence of ANU V244 (Fig. 3.2D). Hu et al. (2017) suggested that the only described and figured specimen (by Ørvig 1975) also showed the mandibular joint inside the suborbital plate. This evidence raises questions about the homology of a small posterior bone in the cheek complex in *Entelognathus*, suggested to be equivalent both to the placoderm postsuborbital, and the quadratojugal of osteichthyans, on the assumption that these bones sat outside the mandibular joint (Zhu et al., 2013). A very similar morphology, with the entire quadrate inside a large dermal element, is recently shown for *Radotina* by Vaškaninová et al. (2020, fig 2A).

Regarding the structure of the mandibular joint (Key Results 2), two articulations (dorsal and mandibular articulations) were identified on Meckel's cartilage of ANU V244 (Hu et al., 2017, fig. 4b). The mandibular articulation was wrongly interpreted to be the dorsal articulation by Young et al. (2001) and Young (2010), but re-assembly of 3D printouts showed the larger ventral articulation formed the mandibular joint. By comparison, in Gogo arthrodires there may be several articular areas on the quadrate and articular, but our specimen suggests that the mandibular joint may not always have been correctly identified, without the aid of reassembly using 3D printouts. A convex articular surface on the quadrate articulated with the corresponding concavity on Meckel's cartilage. In contrast, the mandibular joint in *Entelognathus* is described as a prearticular process and quadrate concavity, like acanthodians and chondrichthyans, and unlike the bipartite convex articulation of osteichthyans (Zhu et al., 2013). Our new evidence indicates that the early arthrodire condition resembled that of osteichthyans.

A possible homologue to the interhyal of osteichthyans (Key Result 3), results from identification of a completely separate perichondral ossification, attached inside the postsuborbital plate (Fig. 3.2B). This is positioned behind the quadrate and does not contact the quadrate. It has a slight rounded dorsal process, and a mesial protuberance that may be connected with another hyoid arch element.

Posterodorsally, this element is continuous with a pointed dermal process projecting above the edge of the postsuborbital plate (Fig. 3.2B). Reassembling the cheek unit using 3D printouts shows that this process fitted under the edge of the submarginal plate (Fig. 3.4A-B). The holotype of *Dicksonosteus* (Goujet, 1975; 1984) may have had a similar arrangement. The right postsuborbital plate on this specimen is slightly displaced behind the palatoquadrate, but suggesting a similar pointed dermal process projecting up inside the submarginal plate (Fig. 3.4C). This was interpreted as an incomplete postsuborbital plate with part of the 'quadrate' attached, suggesting that the quadrate was separately ossified, as previously assumed for *Romundina* (Goujet, 1984, p.119). As preserved, the specimen shows no distinguishing features of the quadrate ossification. Hu et al. (2017) suggested this could possibly be another separately ossified cartilage behind the palatoquadrate, with the mandibular joint confined to the suborbital plate as in ANU V244. The position of this separate cartilage (Fig. 3.2B) suggests comparison with the interhyal of osteichthyans. This is a separate element of the hyoid arch immediately behind the palatoquadrate, invariably linking it with the hyomandibula and ceratohyal. The interhyal was proposed as an osteichthyan synapomorphy (Gardiner, 1984). Recent analyses (Davis et al., 2012; Zhu et al., 2013; 2016) have assumed the interhyal was absent in placoderms, based on the hyoid arch of

ptyctodontids, where a possible interhyal (Long, 1997) was re-interpreted as a ceratohyal (Forey & Gardiner, 1986; Trinajstic et al., 2012). The new evidence suggests that the interhyal could define a larger group than proposed by Gardiner (1984). This situation in maxillate placoderms would need clarification to resolve this question.

Regarding evidence for an unossified epihyal element that was separate from the opercular cartilage (Key Result 4), ANU V244 demonstrates two separate articular areas on the anterior postorbital process (Fig. 3.1J, 3.3B, 3.4B). The position of the opercular cartilage connection is very similar to that restored for *Dicksonosteus* (Goujet,1975;1984).

The extra articulation identified by Young (1979) was previously interpreted for '*Buchanosteus*' as either for the opercular cartilage (Hu et al., 2017, supp.fig. 6a), or called the hyomandibular articulation (Giles et al., 2015). It must be for an additional element, because an otic connection with the palatoquadrate, as interpreted for *Dicksonosteus* (Goujet, 1975) and *Romundina* (Dupret et al., 2014), is not possible when 3D printouts are reassembled (Fig. 3.4A). A clear gap between the palatoquadrate and this articulation could have accommodated an additional unossified epihyal element (Fig. 3.4B), contrary to the previous claim that 'there is no room to insert a further element' in that position (Gardiner & Miles, 1990). The 3D printouts also show that the extra dorsal articulation on Meckel's cartilage could have contacted this unossified element (Fig. 3.4A-B).

The left submarginal of ANU V244 is in articulated position (Fig. 3.1J), for the first time in a placoderm demonstrating the groove for the hyomandibular branch of the facial nerve passing directly from its foramen onto the opercular cartilage. The opercular cartilage is forked proximally (Fig. 3.1H) to enclose the base of the anterior postorbital process, the dermal bone wrapping around it anteriorly, and the cartilage posteriorly (Fig. 3.1J). Neither is in contact with the extra (terminal) articular facet on the end of the anterior postorbital process just discussed. The opercular cartilage is clearly a closed structure, in contrast to the description of the Gogo arthrodire *Torosteus*, where this element was interpreted as open-ended, with an unossified continuation to the distal end of the submarginal plate. On that basis it was interpreted as an epihyal rather than an opercular cartilage (Gardiner & Miles, 1990). However, Hu et al. (2017) noted the structure in *Torosteus* is incomplete distally, with a broken end, and it was suggested that the opercular cartilage in *Torosteus* was also completely closed by perichondral bone, as demonstrated in ANU V244, and other Early Devonian arthrodires (e.g. *Arctolepis*, *Dicksonosteus*), precluding any distal cartilaginous extension.

A double ethmoid connection between the autopalatine and the braincase is demonstrated in ANU V244 (Key Result 5), comprising mesial and lateral articulations (Fig. 3.3A). The mesial ethmoid articulation fits into a large rectangular depression on the ventral surface of the subnasal shelf (Fig. 3.1J), a structure not shown in previous reconstructions (Young,1979; Long et al., 2014). This is in essentially the same position with the main anterior connection of the palatoquadrate in *Kujdanowiaspis* (Stensiö, 1963), and *Dicksonosteus* (Goujet, 1975; 1984), previously called by then an 'orbital connection'. This mesial articulation is just behind the attachment area for the anterior supragnathal (Fig. 3.1J). It is also comparable in position to the ethmoid articulation in some basal osteichthyans (e.g. *Youngolepis*, Chang, 1982), located posterolateral to the attachment area of the vomer (see Fig. 3.5B).

The system of grooves and foramina on the ventral surface of the braincase for cranial blood vessels on ANU V244 is more complete than previously known for arthrodires (Key Result 6). This shows much more detail than the previous restoration of '*Buchanosteus*' (Young, 1979), and a more complex pattern of arteries than represented for '*Buchanosteus*' as a primitive gnathostome by Giles et al. (2015). A curved lateral groove adjacent to the first spino-occipital nerve may represent the occipital artery emanating from the lateral dorsal aorta, based on comparison with *Brindabellaspis* (Young, 1980). This artery is not previously identified in arthrodires. A strong groove for the internal carotid artery, not previously documented, branches off the efferent hyoid groove with a shape showing clearly that blood flow direction was inward, from the efferent hyoid artery (Fig. 3.5A). Not previously identified in any arthrodire is an additional arterial groove with a corresponding position to a groove in *Brindabellaspis* for the palatine artery (Young, 1980). The same groove was identified in *Romundina* (Young, 1980) but is wrongly termed the internal carotid by Dupret et al. (2017). In ANU V244, it branches anteriorly, and the main mesial branch gives off numerous smaller branches forming a reticulating network through the attachment area for the anterior supragnathal (i.e. evidently the main arterial supply to this gnathal element). Similar reticulating structure is seen in acanthothoracids (Smith et al., 2017) and in some basal osteichthyans (e.g. *Youngolepis*, Fig. 3.5B). A third arterial branch originated from the efferent pseudobranchial artery immediately lateral to its junction with the internal carotid (Fig. 3.5A) and passes anterolaterally to the mesial ethmoid articulation between the palatobasal and lateral ethmoid articulations. 3D printouts, with the palatoquadrate in position against the braincase, show this notch forming a clear foramen on both sides (Fig. 3.3B). Given its connection with the arterial groove system, it can be assumed that the blood supply to the floor of the orbital cavity passed up through this foramen. The same system is connected to the 'transverse groove' on the palatoquadrate attachment surface for the posterior supragnathal, so presumably also carried arterial blood to

this region. No corresponding arterial branch is recorded in the living shark *Chlamydoselachus* (Allis, 1923), nor in the Devonian placoderms *Kujdanowiaspis* (Stensiö, 1963), *Dicksonosteus* (Goujet, 1984), or *Romundina* (Dupret et al., 2014).

New evidence presented by Hu et al. (2017) queries some similarities that formed the basis for proposed homologies between 'placoderms' and osteichthyans (Key Result 7). The anterior supragnathal of arthrodires was initially homologised with osteichthyan vomer (e.g. Stensiö, 1963). The evidence of the 'maxillate' placoderm *Qilinyu* suggested an alternative homology, to the osteichthyan premaxilla (Zhu et al., 2016). In the 'maxillate' placoderms, additional bones equivalent to the maxilla and premaxilla of osteichthyans were identified (Zhu et al., 2013; 2016). The main cheek bone (suborbital plate) was homologised with the osteichthyan jugal, and the postsuborbital with the osteichthyan quadratojugal. However, cartilage attachments inside the dermal cheek unit described above suggest that the quadratojugal could be an osteichthyan synapomorphy, if the quadrate inside the large suborbital plate was the primitive "placoderm" condition.

The same condition is recently demonstrated in 'acanthothoracids' by Vaškaninová et al. (2020). They compare the large cheek plate ('suborbital plate') in *Kosorapis* with the osteichthyan preopercular (Vaškaninová et al., 2020, figS10B), placing further uncertainty on these homologies. They interpreted a posterior denticulate element in *Kosoraspis* as a possible 'maxilla' restored to fit under the autopalatine in an equivalent position to the posterior supragnathal of arthrodires. However, for *Radotina* a region of specialised tubercles align the ventral border of the SO were labelled as 'teeth' (Vaškaninová et al., 2020, fig 2A,C). Similar infolded tubercles may form the biting margin on the ventral border of the *Romundina* suborbital plate (see Fig. 3.2D). Hu et al. (2017) had already noted that the infolded ventral tuberculate surface in this specimen could have formed the biting margin of the mouth (a posterior supragnathal is not known in *Romundina*), and that this structure may be more prominently developed in other acanthothoracids (e.g. Burrow, 2006; *Connemarraspis*, fig. 5B; undetermined acanthothoracids, fig. 9L; *Narrominaspis*, figs 13P, 14K). It was noted that whether it formed the biting margin could depend on orientation of the suborbital against the skull (oblique in ANU V244). Such detail could only be established by using micro-CT scanning and 3D printing techniques on rare articulated specimens, as was demonstrated by Hu et al. (2017).

The position of the ethmoid articulation of the autopalatine and the vascularisation of the adjacent vomer attachment area in some basal osteichthyans (e.g. Fig. 3.5B) closely compares with the anterior supragnathal attachment area and mesial ethmoid connection in

ANU V244 (Fig. 3.1J), and various other basal ‘placoderms’, as discussed above. This evidence supports the original homology of Stensiö (1963) rather than homology with the premaxilla as proposed for maxillate placoderms (Zhu et al., 2013; 2016).

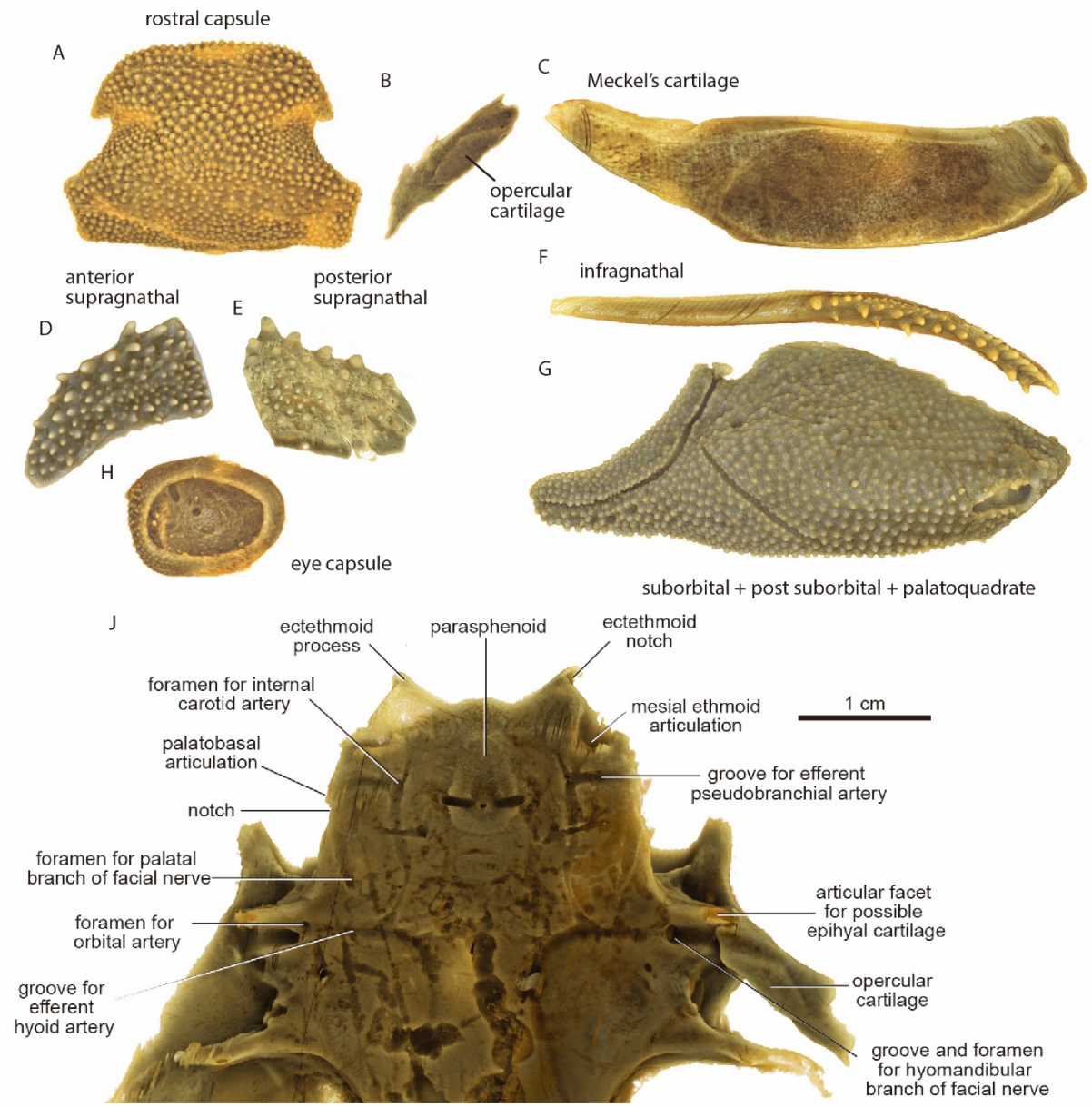

Figure 3.1 Digitally extracted components of the buchanosteid arthrodire ANU V244 used for functional analysis. **A** Rostral capsule in dorsal view. **B** Right incomplete submarginal plate with attached opercular cartilage (internal view). **C** Right Meckel's cartilage (reversed) in lateral view. **D** Right anterior supragnathal in occlusal view. **E** Right posterior supragnathal in occlusal view. **F** Left infragnathal in dorsal view. **G** Left suborbital and postsuborbital plates. **H** Left eye capsule in external view. **J** Ventral view of the braincase with dermal bones attached as preserved (anterior part only).

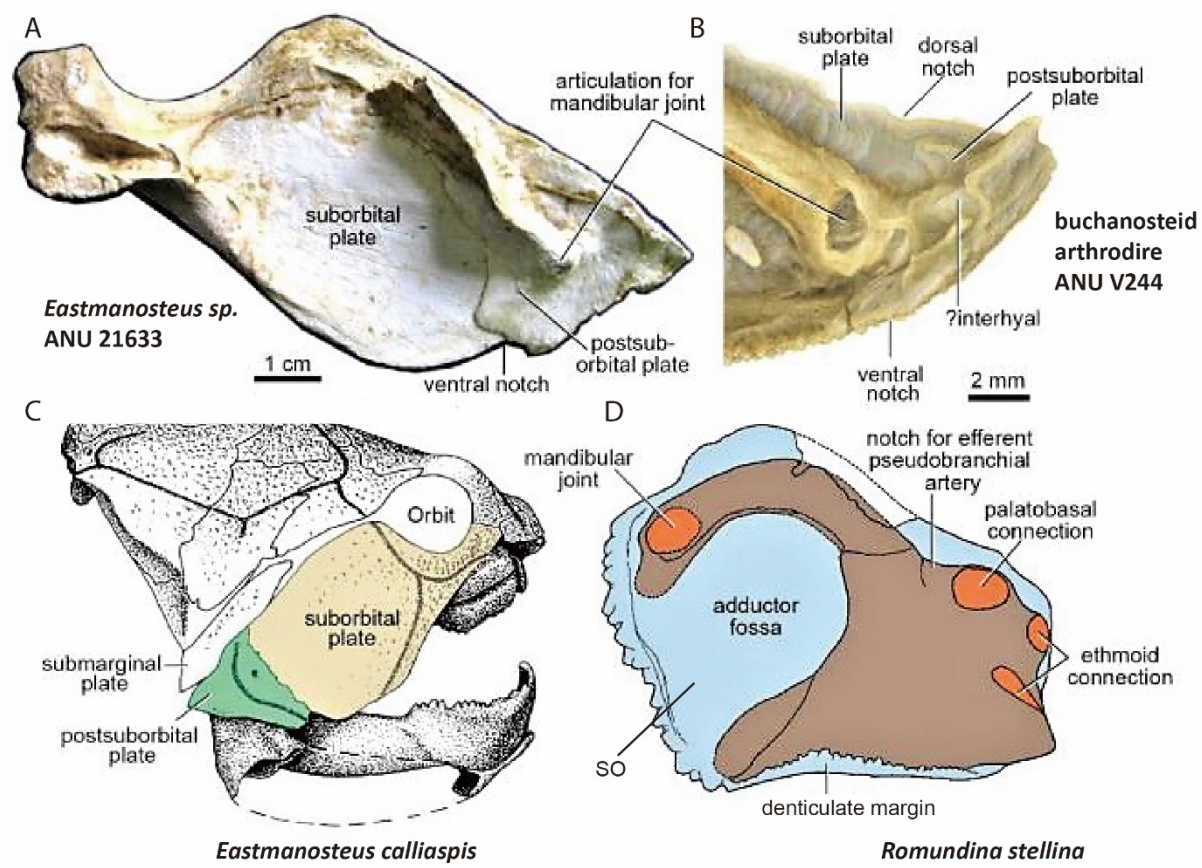

Figure 3.2 Comparisons of the dermal cheek unit, attached palatoquadrate, and mandibular joint articulation in various placoderms. **A** Internal view of the right suborbital and postsuborbital plates with attached perichondrally ossified quadrate in a Gogo *Eastmanosteus* sp. (ANU 21633, prepared and identified by G.C.Y). **B** Internal view of posterior end showing the quadrate with mandibular joint, based on high-resolution CT of ANU V244 (attached to the dermal suborbital plate), behind which is a separately ossified element compared with the osteichthyan interhyal (attached to the postsuborbital plate). **C** *Eastmanosteus calliaspis* from Gogo in lateral view (modified after Dennis-Bryan, 1987), with right cheek unit (suborbital and postsuborbital plates) highlighted. **D** Restoration in internal view of the left suborbital plate and attached palatoquadrate of *Romundina stellina* (modified after Ørvig, 1975; Young 1986), showing a new interpretation of the position of the mandibular joint, and the tuberculate surface forming the biting margin. Light blue, dermal bones; brown, visceral arch cartilages; orange, articular facets. **C** and **D** are not to scale.

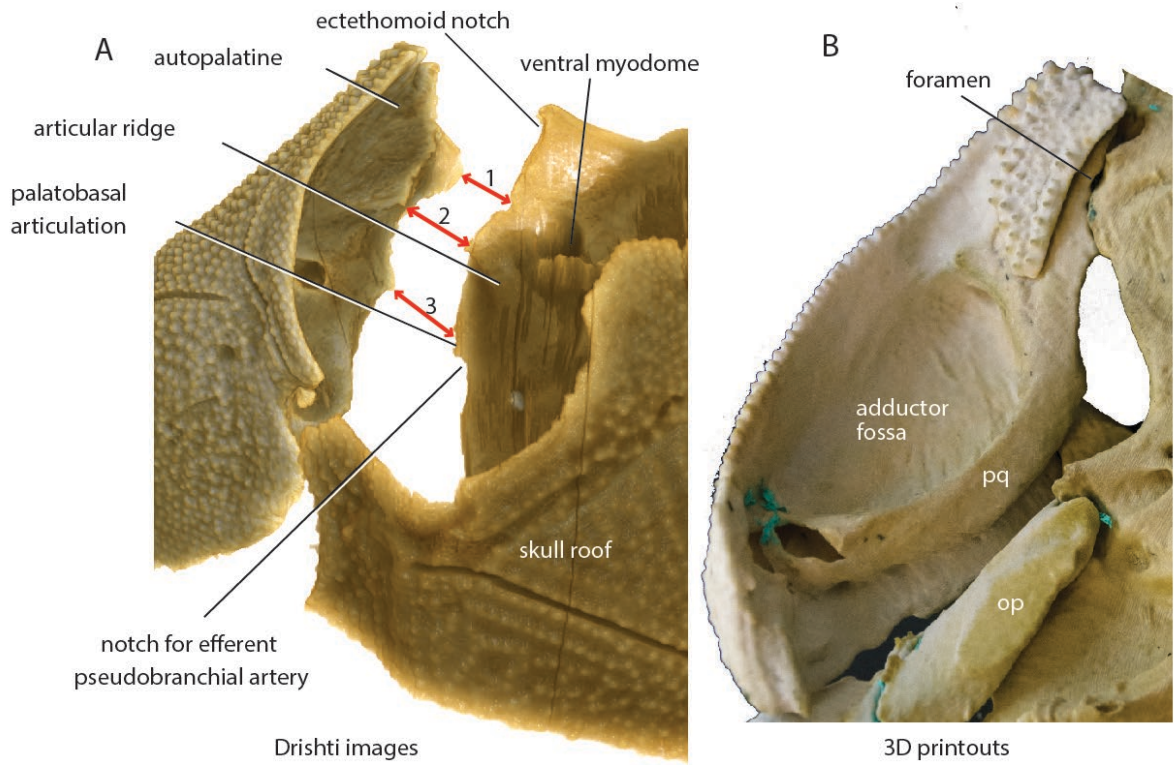

Figure 3.3 Jaw articulations of buchanosteid arthrodire (ANU V244). **A** Articulations of the left autopalatine and subnasal shelf of the braincase in dorsal view. Red arrows indicate three articulations in detail (1 and 2, mesial and lateral articulations of ethmoid connection; 3, palatobasal connection). **B** Ventromesial view showing reassembly of the right cheek complex and opercular unit in articulation against the braincase.

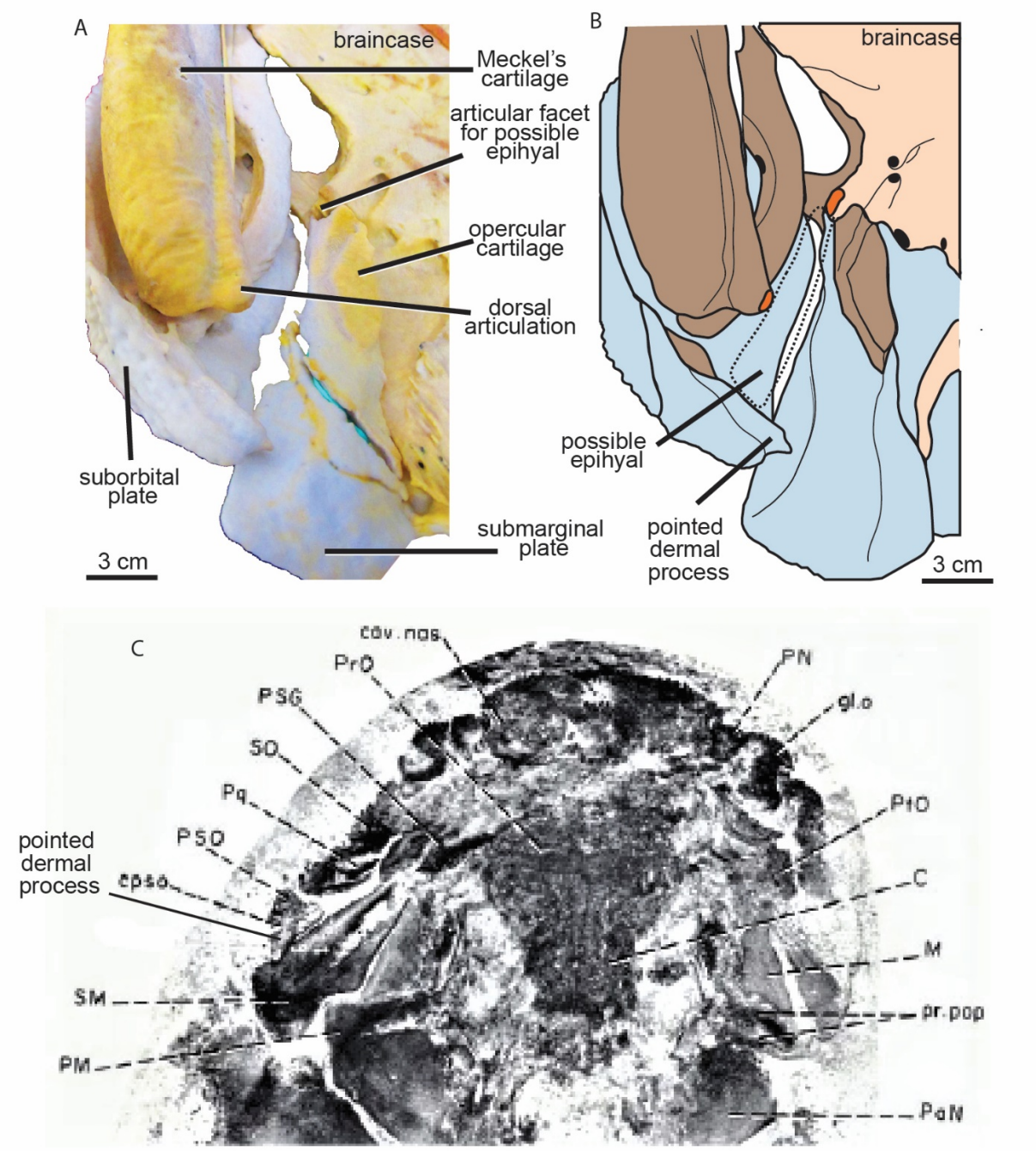

Figure 3.4 Jaw articulations of articulated buchanosteid arthrodire (ANU V244), modified from Hu et al. (2017, fig. 5b-c). **A** Assembled 3D printouts of right Meckel's cartilage, palatoquadrate, suborbital and postsuborbital plates in position against the skull and braincase (ventral view). **B** Reconstruction based on (**A**). **C** Holotype of *Dicksonosteus* Pl.1 from Goujet (1984). Light blue, dermal bones; brown, visceral arch cartilages; pale pink, braincase; orange, articular facets. 3D printouts are 6 times natural size.

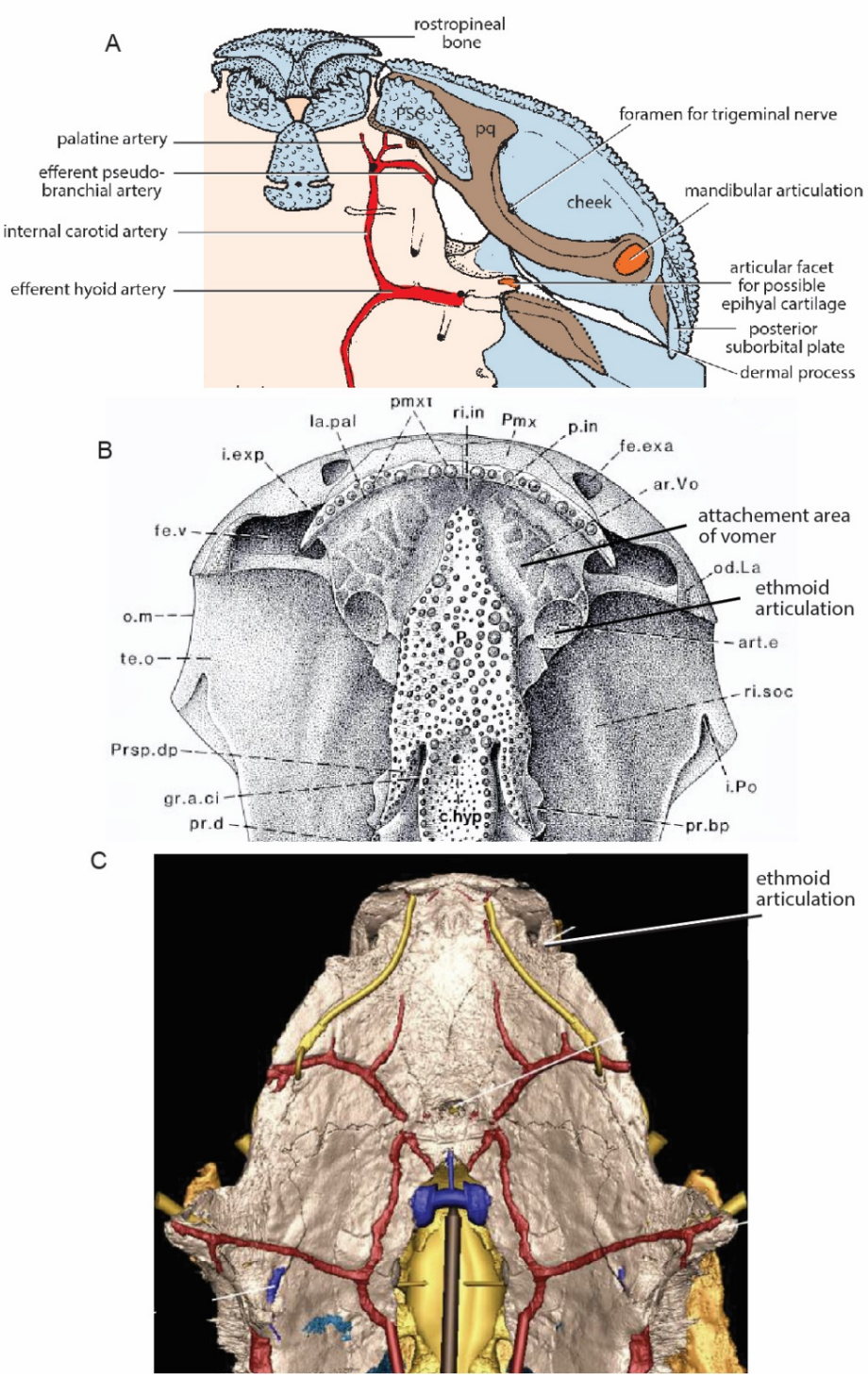

Figure 3.5 Reconstructions for **A** restoration of buchanosteid arthrodire, ANU V244 with all segmented elements against the braincase, based on physical assembly of 3D printouts, showing the left side of the braincase with skull, cheek, submarginal plate and upper gnathal plates in position. **B** ventral view of anterior part of skull of *Youngolepis* (Sarcopterygii Romer, 1995) from Chang (1982, fig.10). **C** ventral view of anterior part of braincase with nerves and blood vessels restored from *Romundina* (from Dupret et al., 2017, fig.10G). Light blue, dermal bones; brown, visceral arch cartilages; pale pink, braincase; orange, articular facets; red, blood vessels. Not to scale.

Chapter 4 Paper 3: Hu, Y.-Z., Young, G.C., Burrow, C., Zhu, Y.-A., Lu, J. 2019 High resolution XCT scanning reveals complex morphology of gnathal elements in an Early Devonian arthrodire. *Palaeoworld.* 28:4, 525-534.

[for pdf see Appendix D]

4.1 Statement of contribution

The project was conceived by G. C. Y., Y. H., and Y.-A. Z. Reconstruction of datasets, three-dimensional renderings and segmentations were accomplished by Y.H. who interpreted the results. Figures were contributed by Y.H. and J.L. Y.H. drafted the manuscript and all authors discussed the results and revised the manuscript.

4.2 Summary Statement

The anterior supragnathals (ASG), posterior supragnathals (PSG), and infragnathals (IG) of ANU V244 were elements in the functional morphology of jaws (Fig. 4.1A) as analysed by Hu et al. 2017 (Paper 2). Paper 3 focuses on analysing the dentition organization of the upper and lower gnathal elements in this buchanosteid arthrodire. The same methods of the previous papers were applied here: i.e. CT scanning, scientific visualization (including 3D segmentation using *Drishti*), and 3D printing.

4.3 Key results

1. The three gnathal elements of basal brachythoracids are characterised by numerous radiating denticle rows.

2. Ossification centres are anterolateral on the ASG (attached to the braincase), and anteromesial on the PSG (attached to the palatoquadrate), in approximately the same position as for these elements in advanced brachythoracids.

3. The ossification centre is in the central part of the biting portion of the IG, whereas it is at the anterior end in advanced brachythoracids.

4. There is no evidence of two ossification centres in the IG, as had been interpreted for more advanced arthrodires.

5. Denticle rows on the IG grew mainly forward and backward from the ossification centre, contrasting with the much stronger vertical growth in more advanced arthrodires.

6. In all three elements the denticle rows radiating from ossification centres form dental fields and resemble more the gnathal elements of phlyctaeniid and actinolepid arthrodires, and phyllolepid placoderms, rather than advanced brachythoracids.

7. Arthrodires, as a possible sister group to maxillate placoderms plus crown gnathostomes, have gnathal elements characterised by extensive palatal laminae but without a facial lamina, non-shedding dentition, and new teeth added in each of many dental fields radially from the ossification centre.

4.4 Background

The 3D printout reconstruction of the ASG (Fig. 4.1C) indicates that when in position, the lateral and mesial margins of ASG and PSG are aligned. Eleven radiating fields (Fig. 4.1C) were identified. By comparison, the ASG of advanced brachythoracids (e.g. *Plourdosteus*) have only 'anterior and medial' dental fields (Ørvig, 1980). The anterior dental field of *Plourdosteus* is represented by an 'adsymphysial tooth-row' and the medial dental field by a non-denticulate ridge, indicating the position of a 'semi-dentine column'. Similar organization (i.e. only one or two denticle rows) occur on the ASG of other advanced arthrodires, for example *Eastmanosteus* (Dennis-Bryan, 1987, figs. 18, 19). The denticulate surface of the ASG is anteroposteriorly concave, with the largest denticles along the anteromesial edge (Fig. 4.1C-D). They have blunt tips, assumed to show wear and presumably represent the functional part of the youngest generation in occlusion (occlusal part, Fig. 4.1D). The middle zone (Fig. 4.1D) contains smaller denticles possibly exposed to the oral cavity, as both sharp (non-occlusal) and blunt (significant wear) denticles are present. Relatively large denticles on the posterior edge are more pointed compared to occlusal part, and presumably projected through the soft tissue to function on the palate in gripping and holding prey (gripping part, Fig. 4.1D).

On the occlusal surface of the PSG, the most depressed part with the smallest denticles is centrally situated, approx. 20% of the total length of the long axis from the mesial side. This is interpreted as the ossification centre (oss, Fig. 4.1E). At least 13 rows of denticles can be identified, whereas in Gogo arthrodires there are only a few rows, for instance two in *Compagopiscis* (Smith & Johanson, 2003, fig. 2D) or one denticle in *Mcnamaraspis* (Long, 1995, pl. 1, figs. 4, 5). In this buchanosteid arthrodire, the IG is a slender bone compared to

the massive size of the Meckel's cartilage, and relative to the slender palatoquadrate. Added strength to the upper jaw was provided by the large dermal cheek bones (see Fig. 4.2A).

The right IG (Fig. 4.2B) was segmented out from the 2011 scan of the whole specimen. The left IG was broken into two parts. Its anterior part was scanned in 2015 and used here with the complete right IG to work out the denticle organization. The right IG contains approximately 6 radiating rows (Fig. 4.2C). In contrast to the ASG and PSG, all denticles on the IG shows significant wear, due to biting against ASG and PSG (Fig. 4.1A & 4.2A). Denticles are labelled from 1 to 12 according to different generations (1 represents the oldest generation and 12 the youngest). Larger denticles are at the ends and smaller crowded denticles occur in about the middle third, interrupted by a semicircular pit-like depression surrounded by a rim, suggested (Prof. John Long, 2017) as a possible ossification centre. The fact that the denticles progressively increase in size forwards both ends is consistent with regulation by growth of the infragnathal from this ossification centre (Hu et al., 2019). A similar pattern was found on the main longitudinal denticle row of the infragnathal in more advanced arthrodires like *Plourdosteus* (Ørvig, 1980) and *Compagopiscis* (Rücklin et al., 2012, fig. 3).

In summary, general growth of IG is interpreted in terms of bone and denticle rows growing mainly forwards and backwards from the ossification centre, with no obvious downwards growth. On the other hand, advanced brachythoracids, such as Gogo arthrodires, had much stronger vertical growth to form the deep blade of the IG (e.g. *Kimberleyichthys*, Fig. 4.3C).

Generally speaking, morphology of the gnathal elements of this basal arthrodire is very different from the much-reduced denticulation of higher brachythoracids. Using the latter to interpret the origin and early evolution of teeth (e.g. Rücklin et al., 2012; 2015), therefore may give misleading results.

The evidence provided by Silurian "maxillate" placoderms in China, suggested the three toothplates in arthrodires could be homologous to the three osteichthyan marginal jaw bones (Zhu et al., 2013; 2016). To investigate this further, additional morphological and histological data in arthrodires, and in the earliest crown jawed vertebrates, are required to bridge this large evolutionary gap. In order to segment such detailed structures (e.g. the vasculature inside IG), *Drishti* has been further improved, and new tools were developed to provide a more efficient and user-friendly segmentation workflow (see Paper 4, below).

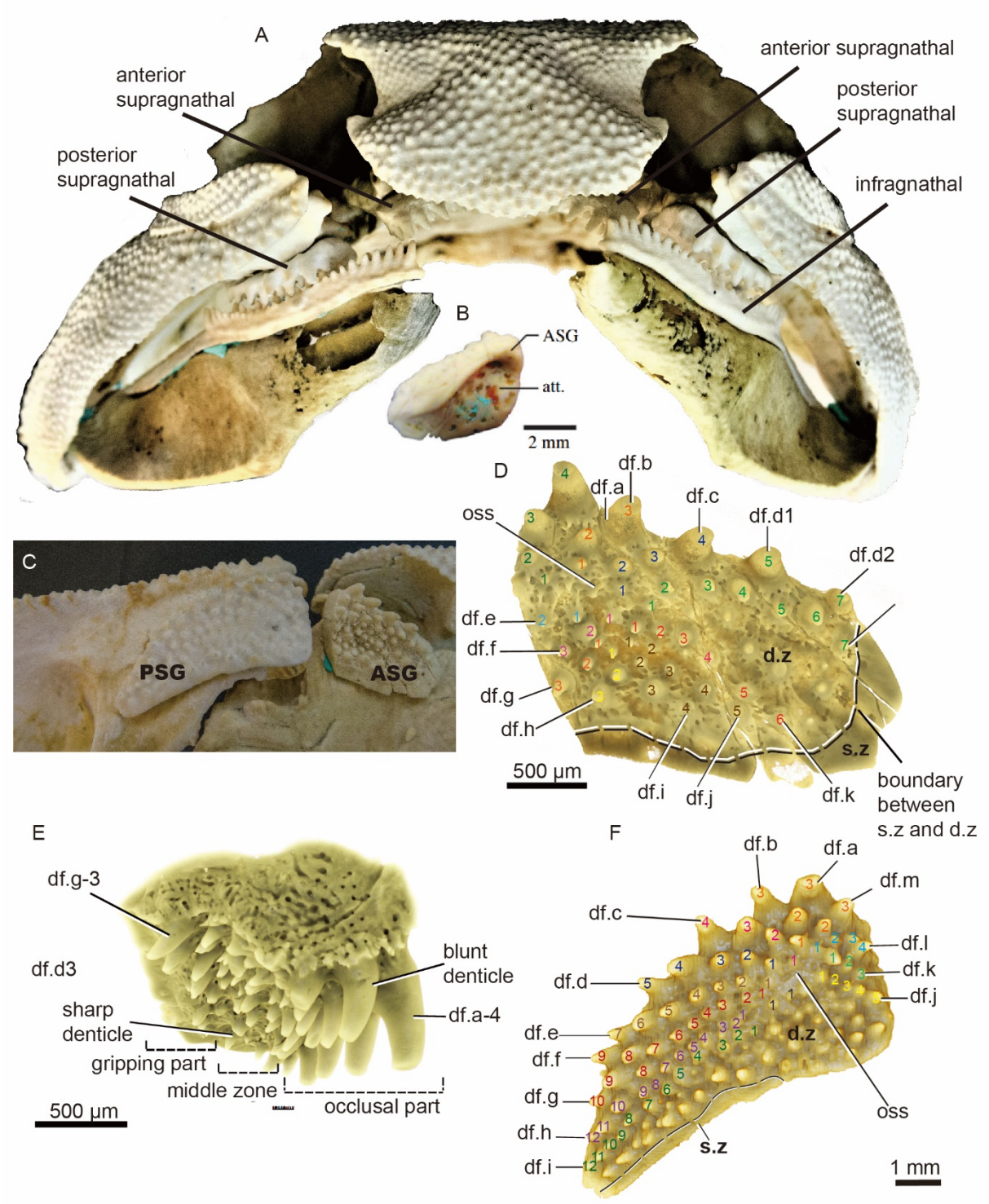

Figure 4.1 Buchanosteid arthrodire (ANU V244). **A** 3D physical reconstruction of jaw elements (anterior view). **B** First published 3D printout of right ASG (from Burrow et al., 2016, fig. 1b). **C** Ventral view of right ASG and PSG in position. **D-E** Right ASG denticulate surface (**D**) and oblique lateral view (**E**). **F** Right PSG in occlusal view. d.z, undifferentiated denticle zone; df.a-m, radiating dental field; oss, ossification centre; s.z, smooth zone.

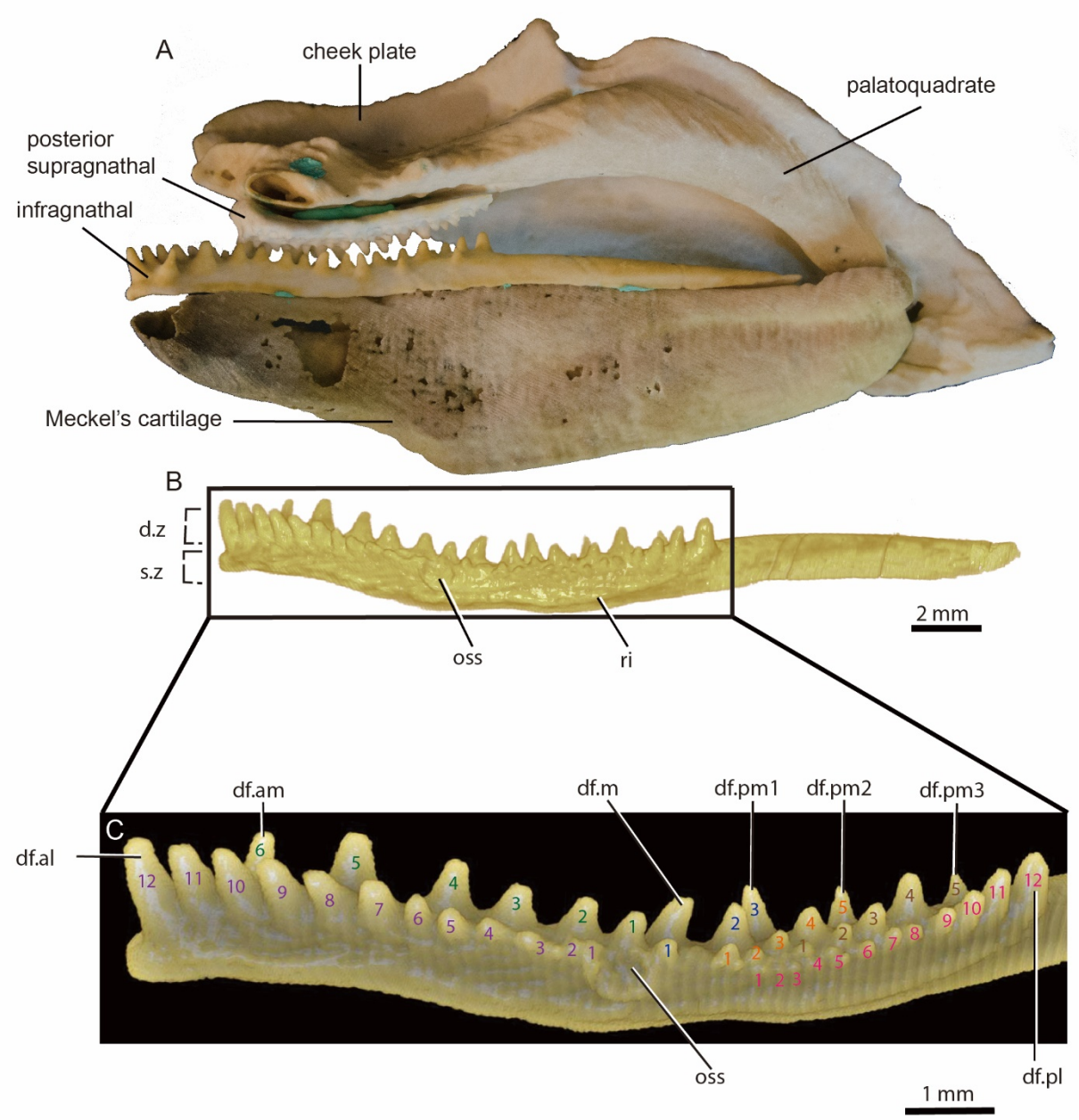

Figure 4.2 Buchanosteid arthrodire (ANU V244). **A** 3D physical reconstruction of the right cheek, posterior supragnathal, infragnathal and palatoquadrate in position (inner view). **B** Infragnathal in lateral view (mirrored image of the right infragnathal). **C** Enlargement of boxed area in (**B**). Boxed area of (**C**) shows the corresponding part of the right infragnathal. d.z, denticle zone; df.al, anterolateral dental field; df.am, anteromesial dental field; df.m, mesial row (single denticle in a new dental field); df.pl, posterolateral dental field; df.pm1-3, posteromesial dental field 1-3; oss, ossification centre; ri, ridge.

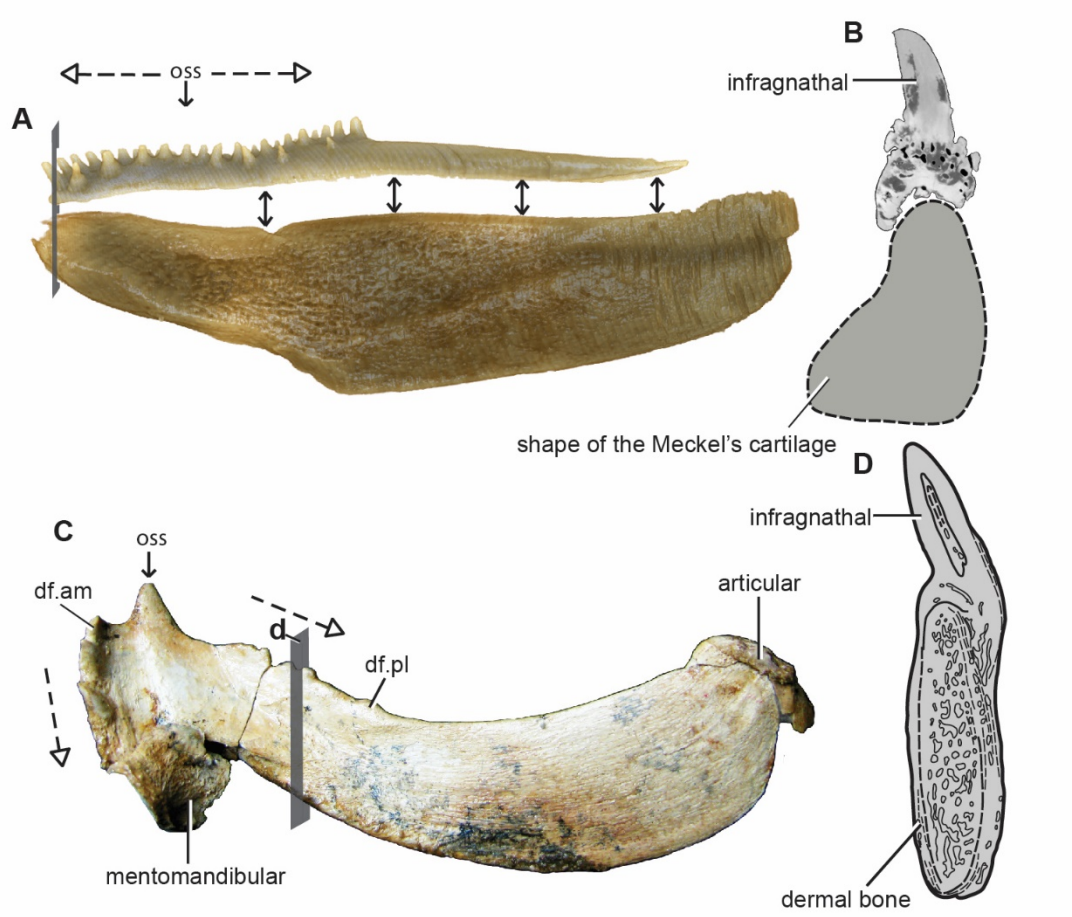

Figure 4.3 Transformation in the arthrodire lower jaw from mainly endoskeletal (e.g., buchanosteid arthrodire) to mainly dermal structural components in eubrachythoracids. **A** Inner view of the right infragnathal with its interpreted position on Meckel's cartilage (ANU V244), showing inferred growth direction (dashed arrows). **B** Vertical cross section of anterior-most denticle against the shape of Meckel's cartilage at the level indicated in (**A**). **C** Right infragnathal of *Kimberleyichthys* (ANU35687) in mesial view (ossifications of Meckel's cartilage, mentomandibular and articular attached). **D** Drawing of the vertical cross section of the infragnathal of *Compagopiscis* (adapted from Rücklin et al., 2012, fig. 2f) at the approximate level for *Kimberleyichthys* as shown in (**C**). Not to scale. Dashed arrows indicate growth direction from ossification centre. Abbreviations: df.am, anteromesial dental field; df.pl, posterolateral dental field; oss, ossification centre.

Chapter 5 Paper 4: Hu Y.-Z., Limaye A, Lu J. 2020 3D Segmentation of computed tomography data using Drishti Paint: new tools and developments. *Royal Society Open Science* 7: 201033.

[for pdf see Appendix E]

[for Supplementary pdf see Appendix F]

5.1 Statement of contribution

J.L. and Y.H. designed the study. Y.H., J.L. and A.L. performed the research and drafted the manuscript. Y.H. and J.L. prepared the figures. A.L. developed *Drishti* v.2.7. Y.H. and A.L. performed unit and functionality testing. All authors revised the manuscript. Y.H. and A.L. contributed equally.

5.2 Summary Statement

In 2004, the Department of Applied Mathematics collaborated with Dr Ajay Limaye, VizLab, National Computational Infrastructure (NCI) to develop a software program for nano-level investigations, not possible with image visualization programs then available. The first *Drishti* program was released in 2004 and has been under continuous development since then.

Limaye (2012) introduced two *Drishti* modules, *Drishti Import* and *Drishti Render*. *Drishti* was the main investigation tool for the volumetric data of *Gogonasus* (Paper 1) and the buchanosteid arthrodire (Papers 2 & 3). As an experienced user and co-contributor (documentation, functionality, unit and performance testing, user experience design, etc.) of the *Drishti* program since 2016, I collaborated with colleagues Ajay Limaye and Jing Lu to work on improving the functionality and usability of the *Drishti Paint* module. The new developments and latest tools of the *Drishti* program developed since Limaye (2012) are presented by Hu et al. (2020).

5.3 Key Results

1. The relationship between the three *Drishti* modules is summarized.

2. The *Paint* module is improved and new tools for 3D segmentation updated.

3. Two modes in *Drishti Paint* v2.7 are: Graph Cut and Curve modes

4. Mathematical morphological transformations (i.e. erosion and dilation) are implemented to speed up the 3D segmentation process.

5. The Gradient Thresholding Tool is developed to facilitate specific regions of interest, and for segmenting detailed features.

6. Added Mesh Simplification Function to help with creating smaller surface mesh files while keeping sufficient data for 3D printing.

7. Detailed 3D segmentation procedures, using the 3D Freeform Painter and multiple-thresholding methods, are provided, including mesh generation and simplification procedures.

5.4 Background

Amongst current well-known cross-platform open-source software programs, five use both surface and volume rendering (Buser et al., 2020). *Drishti* is the only program that can segment directly on a volume (Hu et al., 2020). Surface rendering reduces the amount of data to be rendered and therefore limits the calculation time effort for post-processing. Volume rendering takes the complete dataset into account, to render a 3D-image by adding the voxel values along a virtual light ray through the volume. Thus, volume rendering gives more information, but is computationally more demanding than surface rendering (Carvalho & Sobieranski, 2018).

Drishti V2.7 has three modules: *Import*, *Render* and *Paint*. *Import* works on image processing and transfer 14 different standard formats (Table 5.1) to processed volume format which the other two modules can work with. *Render* uses direct volume rendering with voxel ray casting and texture slicing algorithms and a combination of local and global illumination methods to render the volume data. *Paint* can perform both 2D, 3D segmentation and mesh generation including mesh simplification.

3D segmentation, segmenting the internal region of interest in sequences of images, is a vital tool for investigation and understanding the internal structures of target objects. 3D segmentation in *Drishti Paint* uses thresholds, edge detection, clustering, or region growing techniques to group pixels based on brightness, colour, or texture, then render them as discrete objects. 16 bits full resolution data can be read and processed using *Drishti Paint* V2.7 whereas previous versions only allow 8 bits volumetric data when performing 3D segmentation.

There are two modes developed in *Drishti Paint* v2.7: Graph Cut and Curve modes. Graph Cut mode uses the max-flow/min-cut algorithms from the maxflow-v3.01 library of the Boykov-Kolmogorov algorithms (Boykov & Kolmogorov, 2001). Curves mode uses the curve morphing by strings (Jiang et al., 2002). *Drishti Paint* is designed specifically to consider only 2D slices in a volumetric data or 3D volume directly, where the X, Y and Z axes are the width, the height and the number of slices in the 3D volume, where volume is the quantity of three-dimensional space enclosed by surfaces.

Below I briefly summarized the methods used by Dr Limaye to develop the *Drishti Paint* v2.7 module. All developments relied on testing with fossil fish data and providing feedback for improving the module. *Drishti Paint* uses a combination of discontinuity detection-based and similarity detection-based image segmentation approaches. In combination with these two image segmentation approaches, the *Paint* module is designed using the following methods:

- Multiple thresholding, based on values and gradient information (for detailed information, refer to supplementary information); In *Drishti Paint*, a region is defined by two thresholds and a combination of colour and opacity applied to selected thresholding region. Each voxel of the input volume belongs to the selected region by the lower and upper thresholds.

- Edge-based segmentation method, which is based on the rapid change of intensity value in a slice as a single intensity value does not give enough information about edges. Edge detection locates the edges that either the first derivative of density is greater than a particular threshold or the second derivative has zero crossings. In *Drishti Paint*, firstly all the edges are detected then connected to form the boundaries of the sample in order to segment the region of interest. This method uses discontinuity detection, and is already proven to be good for images having good contrast (Kaur & Kaur, 2014);

- Region-based segmentation method is based on partitioning the image into homogenous regions which are more immune to noise and useful (Kaur & Kaur, 2014) when it is easy to define similarity criteria and more computing heavy than edge-based method. *Drishti Paint* includes seeded region growing, shrink-wrapping (i.e. region-of-interest shrink wrap), region splitting and merging types of region-based methods.

In addition to segmentation methods, *Drishti Paint* v2.7 employed the following segmentation techniques, operating on 2D slices or 3D volume:

- mathematical morphology (e.g. dilation and erosion under Graph Cut mode)
- intelligent scissors (e.g. curve morphing under Curves mode)
- interactive (e.g. 3D Freeform Painter under Graph Cut mode)
- semi-automated (e.g. paint multiple 2D slices at once at both Graph Cut and Curves modes)
- fully automated (e.g. Fill and Shell under 3D Freeform Painter of the Graph Cut mode)

Different mesh simplification processes were tested, using as a case study the raw CT data of the right cheek complex (dermal suborbital, postsuborbital plates plus palatoquadrate) described by Hu et al. (2017; Paper 2) for ANU V244 (re-segmented cheek as in Fig. 3.1G). Based on the comparison between the original surface mesh (Fig. 5.1A-B) and simplified surface meshes using this case study, a mesh smoothing factor of 2 and 50% decimation (Fig. 5.1C-D) is suggested as a good combination to use for 3D printing when experiencing large surface mesh files.

Hu et al. (2020) also provided a protocol for doing 3D segmentation using new tools in *Drishti* V2.7. All procedures above were documented in the supplementary information of Paper 4. As a result of publishing this paper, Windows and Linux version of this latest version *Drishti* v2.7 were developed based on reviewers' requests during the review process of Paper 4.

Data format	Name and supporting information
*.raw	ProRay raw triangle format. a basic file format that saves the active image or stack as raw pixel data without a header
*. NIFTI	Neuroimagine Informatics Technology Initiative
TXM	Xradia X-ray transmission image data
*.jpg	Joint Photographic Experts Group
*. png	Portable Network Graphics
*.gif	Graphic Interchange Format
*.tiff/ Grayscale TIFF image	a tagged image file format
MetaImage	a particular medical image format used in the insight segmentation and registration toolkit (ITK); a text-based tagged file format
Analyse 7.6 data format	Data format from software named Analyse, which is developed by the Biomedical Imaging Resource at Mayo Clinic
*.nrrd/ NRRD	a library and file format designed to support scientific visualisation and image processing involving N-dimensional raster data
*.txm/ QMUL Tom, TXM	a file format used by ZEISS Xradia 3D X-ray Microscopes
VGL	VG Studio Project file format
DICOM	Digital Imaging and Communications in Medicine a standard medical imaging file format
.nc	Network Common Data Form (netCDF), is an interface to a library of data access functions for storing and retrieving data in the form of arrays

Table 5.1 Fourteen formats of volumetric data that can be processed by *Drishti Import* v2.7.

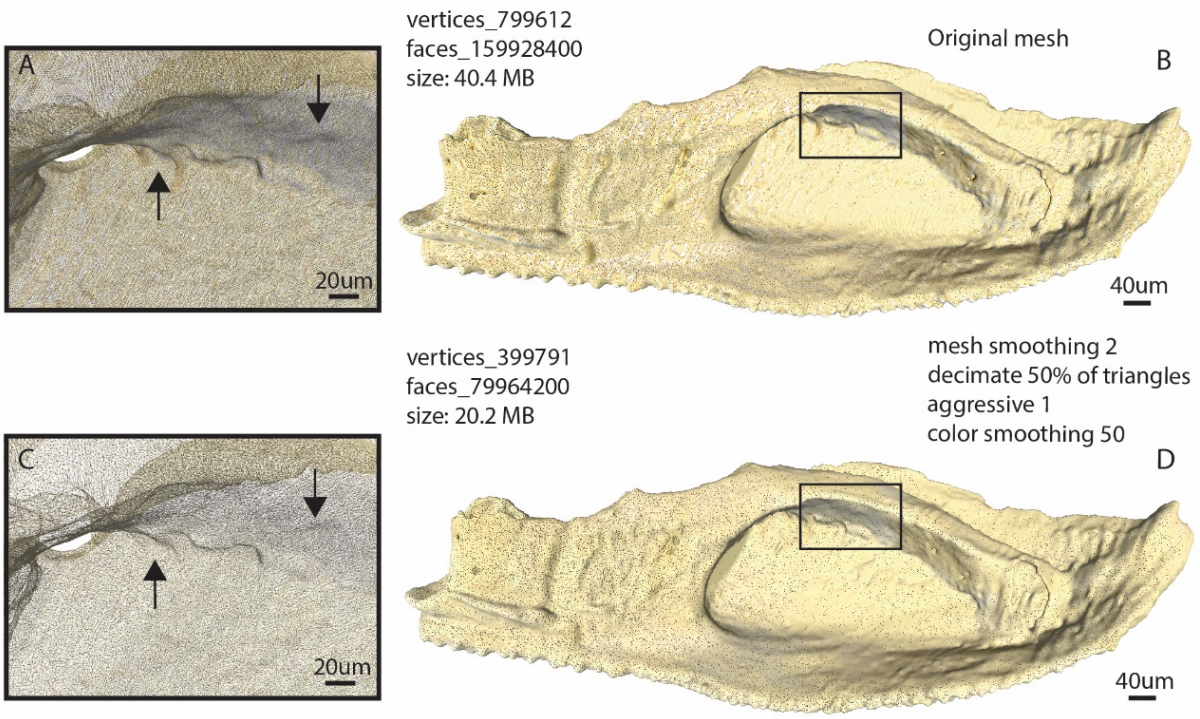

Figure 5.1 Three-dimensional surface meshes from the segmented 16 bits full resolution of the dermal cheek unit of the buchanosteid arthrodire ANU V244 previously figured in Paper 2 (Hu et al., 2017, fig.3). **A-B** Original surface mesh data without any mesh simplification. **A** Enlarged area of the black boxed area in (**B**). **C-D** Simplified surface mesh data using the suggested mesh smoothing factor of 2 and 50% decimation. **C** Enlarged area of the black boxed area in (**D**). Black arrows indicate the references points selected for comparing original and simplified surface mesh data. The vertex count for both original and simplified surface mesh data was calculated using MeshLab v. 1.3.4 (Cignoni et al. 2008).

Chapter 6 Synthesis

6.1 Outcomes

The aims of my research were to investigate whether 3D segmentation and reassembled 3D printouts could be utilised to improve skeletal reconstructions and assist functional analysis in extinct fossil vertebrates, and how they could provide insights for comparative morphology with other early vertebrate fossils, and for more general aspects of vertebrate comparative morphology.

The 3D models of *Gogonasus andrewsae* (Paper 1) have been used to compare with another Devonian lobe-finned fish *Edenopteron* from the New South Wales south coast (Young et al., 2019) to work out the possible shape of the latter's scapulocoracoid and the attachment area at the end of the anocleithral process.

Since publication, Hu et al. (2017; Paper 2) has already been cited across several scientific disciplines, as an exemplar of basal placoderm or gnathostome brain and jaw structure. Coates et al. (2018) used comparisons of the braincase described in Paper 2 to assess lateral separation of the otic capsules of the Middle Devonian considered by them to be 'stem chondrichthyan' *Gladbachus*. The ventral surface of the braincase of ANU V244 provided comparative information for analysis of the stem osteichthyan *Ligulalepis* sp. by Clement et al. (2018), who described the internal carotids, efferent pseudobranchial and ophthalmic arteries of *Ligulalepis*, but noted the absence of a parabasal canal carrying the palatine artery, a difference with osteichthyans and placoderms as evidenced by *Brindabellaspis* (Young, 1980) and ANU V244 (Hu et al., 2017). The incurrent nasal openings were compared with nasal openings of *Brindabellaspis stensioi* by King et al. (2018b). Regarding broader aspects of craniofacial development and evolvability, Fish (2019, p.17) noted the anteriorly placed nasal capsule in placoderms, including the evidence of ANU V244, and suggested "the origin of the primary palate occurred shortly after the origin of the jaw, in the placoderm lineage". This is over-simplified - there are many other gnathostomes.

Two major discussions concerning the ancestral jawed vertebrate phenotype, and the homologies of dermal jaw bones in early gnathostomes (Y.-A. Zhu et al. 2018; King & Rücklin, 2020) have relied on the morphology described by Hu et al. (2017) as the 'best known morphological data' for arthrodire placoderms (King & Rücklin, 2020, p.10, fig. 1A-B). As noted above, resulting from the discovery of the Chinese 'maxillate' placoderms (Zhu et al., 2013; 2016), new homologies were proposed for the three gnathal elements of arthrodires, the anterior and posterior supragnathals and infragnathal corresponding respectively to the three

marginal jaw bones of the osteichthyan outer dental arcade (premaxilla, maxilla, and dentary). Previously (e.g., Stensiö, 1963; 1969) the arthrodire anterior supragnathal had been equated with the osteichthyan inner dental arcade, i.e., the vomer (both sitting on the braincase adjacent to the ethmoid articulation with the palatoquadrate). The posterior supragnathal was (partly or entirely) considered the homologue of the osteichthyan dermopalatine (both sitting on the palatoquadrate just across the ethmoid articulation). However, Zhu et al. (2018) argued that the inner position of arthrodire gnathal elements was secondary; evidence against them corresponding to the inner dental arcade included the greater number of inner arcade bones in osteichthyans. However, extra placoderm gnathal elements have recently been described by Vaškaninová et al. (2020), and at least one additional denticulate element in the jaws of ANU V244 is noted below (Fig. 6.4).

Based on Paper 2, Zhu et al. (2018) suggested that there was no space for a new outer dental arcade, and also no potential facial bones that could be recruited to form the outer dental arcade in arthrodires. However, as noted above, Vaškaninová et al. (2020) have identified 'teeth' on the ventral border of the large cheek plate (suborbital) in *Radotina*, and similar modified ornament occurs in *Romundina* and other Australian placoderms (Burrow, 2006), whereas a possible 'maxilla' in *Kosoraspis* fitted inside this, on the autopalatine part of the palatoquadrate, and thus the same position as the PSG in ANU V244. A different approach by King & Rücklin (2020) identified this as a problem of 'primary homology', and they applied the concept of 'dynamic homology' analysed within a Bayesian tip-dating framework, finding support for the homology of the three arthrodire gnathal elements of arthrodires with the osteichthyan premaxilla, maxilla, and dentary. This implied there was no vomer-dermopalatine series in the gnathostome ancestor, but King & Rücklin have not taken into account some of the other detailed evidence summarised above (e.g. positional correspondence of blood supply, ethmoid articulation, parasphenoid between ANU V244 and basal osteichthyans like *Youngolepis*). These constitute additional evidence for primary homology. Although King & Rücklin found support for Zhu et al.'s (2018) outer dental arcade homology, they proposed a 'distinct scenario for the trajectory of upper jaw evolution', disputing that the plesiomorphic state for maxillae and premaxillae was in an arthrodire-like palatal position. The question of the homology of arthrodire gnathal elements thus remains uncertain, and resolution will rely on future additional morphological data for primary homology.

The sensory sulcus on the suborbital bone in ANU V244 (Paper 2) was studied in more detail by King et al. (2018a) and compared with the pit structure on the suborbital–postsuborbital complex of another isolated arthrodire specimen from Taemas-Wee Jasper (ANU V79). A full description of the sensory system of ANU V244 is part of future research.

Hu et al. (2019) analysed the complexity of arthrodire gnathal elements using ANU V244 (Paper 3). Paper 3 has contributed to the general topic of evolution of teeth, and is cited/discussed in several recent contributions on this topic; for example, Dearden & Giles (2020) on dental diversity in early chondrichthyans, and Vaškaninová et al. (2020) on the gnathal elements of Early Devonian acanthothoracids. Jobbins et al. (2021) have recently described unusual morphology in a large posterior supragnathal from the Middle Devonian of Morocco as a new genus and species of eubrachythoracid arthrodire (*Leptodontichthys ziregensis*). They used similar CT scanning techniques to Hu et al. (2019), and identify tooth rows 'which probably derived from gnathal elements with dental fields', as described in Paper 3.

Chen et al. (2020) did not have access to my unpublished work on gnathal bone histology and denticle growth (see Future Research). Their previous research was based on isolated jaw bones assigned to *Andreolepis* (Chen et al., 2016) and *Lophosteus* (Chen et al., 2017). These were identified as containing both the outer and inner dental arcade by Zhu et al. (2018). *Andreolepis* and *Lophosteus* have long been regarded as the earliest remains referred to actinopterygians (Janvier, 1978; 1996, p.183). On the assumption that they are the most basal osteichthyans, these taxa have provided detailed histological information of the tooth development in primitive gnathostomes (Botella et al., 2007; Chen et al., 2016; 2017; 2020). Chen et al. (2016) found that *Andreolepis* shed teeth by basal resorption but lacked a permanent dental lamina. This new result of resorptive tooth shedding is relevant to interpretations of the placoderm dentition. However, tooth-bearing jaw bones of *Andreolepis* and *Lophosteus* are all isolated elements and assignment to these taxa is circumstantial, mainly based on surrounding separated bones as stated by Chen et al. (2016). Nevertheless, *Andreolepis* or *Lophosteus* as primitive osteichthyans are expected to include osteichthyan-like histology. In contrast, the arthrodire gnathal elements described in Paper 3 are entirely inside the mouth of one articulated specimen (Hu et al., 2017, fig. 2a), which provides certainty regarding their taxonomic assignment compared to isolated and separated bones.

Chen et al. (2020) studied another *Lophosteus* specimen via synchrotron x-ray scanning and concluded that 'teeth and dermal odontodes are modifications of a single system, regulated and differentiated by the oral and dermal epithelia'. The histology of ANU V244 will add additional information to the general topic of evolution of teeth once the full growth sequences and generations of teeth are segmented and explained in detail (see below).

6.2 Future Research

6.2.1 Gogonasus andrewsae

Reconstruction of the opercular and shoulder girdle series of NMV P221807 based on 3D models (Paper 1) gave only provisional results for functional analysis, because adjacent bones (extrascapulars, cheek unit etc.) were unavailable for CT scanning. To fully test the functional morphology of this unique tetrapodomorph fish, a new CT scan of the whole specimen (or other specimens) is needed for achieving higher resolution, to provide 3D models of all elements for a reconstruction of the complete skeleton in a new functional analysis.

6.2.2 Buchanosteid arthrodire ANU V244

The taxon '*Buchanosteus*' has been used as an outgroup to code date sets of more than 250 characters in phylogenetic analysis of the origin of jawed vertebrates (e.g. Zhu et al., 2013; Giles et al., 2015; Brazeau & Friedman, 2015; Zhu et al., 2020; King & Rücklin, 2020). The articulated 'buchanosteid' (ANU V244) described in Papers 2 and 3 will provide the most complete and reliable information for any arthrodire, for all future analysis. Its taxonomic status is under investigation, a preliminary analysis, relying mainly on complete description of the dermal skeleton, suggesting it may be a new species. This is work in progress with other colleagues including G.C. Young, J.A. Long, J. Lu and Y.-A. Zhu. More significant is new information under study on many aspects of endocranial morphology, to be prepared for publication with colleagues, of which some preliminary results are summarised here. The 2015 CT scan was used to segment out all internal canals for nerves and vessels to provide a complete restoration of the brain cavity (see Fig. 6.1, segmentation completed by Jing Lu using Mimics 19.0). Some preliminary findings include the jugular vein canal continuous with the posterior recess of the orbital vault that may be ancestral, based on comparison with jawless stem gnathostomes (e.g. Gai et al., 2011); the large interorbital canal may correspond to the ventral cranial fissure in crown gnathostomes.

Future publications in preparation include diagnosis of the specimen, and detailed description of the neurocranium, correlation of myodomes on the braincase and the eye capsule with the various oculomotor nerve canals, also expanding and revising morphological characters for placoderms used in phylogenetic analysis.

New information on the extracted optic and rostral capsules (rhinocapsular bone) of ANU V244 are also under investigation. A rhinocapsular bone of '*Buchanosteus*' was illustrated by Miles (1971), White & Toombs (1972) and Young (1979). For ANU V244, only the external surface

was shown by Young et al. (2001). The internal structure was completely unknown before CT scanning. The dorsal view (Fig. 6.2A) is more rectangular, compared to the previous reconstruction by Young (1979, fig. 1). A smooth projection in front of the nasal notch (nn) was in contact with the anterior process of the eye capsule. A smooth flange on the posterior margin (fl) fitted under the anterior edge of the skull roof. The ventral view shows a small tuberculate ridge that could be a separate element (?IN, Fig. 6.2B). Branching grooves, probably for blood vessels (blv) cross the anterior division of the nasal cavity (n.cava). In the same position, Goujet (1984, figs. 50,74,91) labelled small foramina as for olfactory nerve fibres but this could equally be vascular. The lateral edge of perichondral bone is very clear posteriorly, with a distinct process behind the nasal notch (r.prop). The posterior division of the nasal cavity is a deep rounded structure (n.cavp). The pineal opening (pin) opens into the top of the cavity for the telencephalon of the brain (c.tel). Deep bi-lobed recesses (olf, Fig. 6.2D) contained the olfactory tracts.

This rostral capsule has been compared with ANU V2858 (unpublished incomplete buchanosteid rostral capsule, CT scanned, and 3D printed in 2011), and several other new acid-etched examples from Burrinjuck. These clearly belong to different species or genera, adding to the taxonomic diversity of 'buchanosteids' from Burrinjuck. ANU V2858 and P33612 (referred to *Parabuchanosteus murrumbidgeensis* and figured by White & Toombs (1972, pl.6, fig. 1-4)) differ in a whole range of features from ANU V244. Some features could be characters to add to definitions of the families Parabuchanosteidae and Buchanosteidae (Long et al., 2014); i.e. the superfamily Buchanosteoidea.

The extracted eye capsule (optic capsule) is shown in Fig. 6.3. Comparisons have been made with 3D printouts of the left eye capsule of the acanthothoracid *Murrindalaspis* described by Long & Young (1988) and Young (2008), and with eye capsule descriptions for the arthrodires *Dicksonosteus* (Goujet, 1984, fig. 19) and *Narrominaspis* (Burrow, 2006, fig. 12). The anterior process (a.pr) is much stronger than in *Dicksonosteus* or *Narrominaspis*, forming the ventral border of the nasal opening (see Hu et al., 2017, fig.1a). A deep recess corresponds to the large muscle insertion (m2) in *Murrindalaspis* and *Narrominaspis* (much smaller in *Dicksonosteus*). Eye capsule 3D printouts put against the braincase and rostral capsule (see Paper 2) show a prominent ring surrounding the optic nerve foramen (II, Fig. 6.3D) that includes a process (pr.x) that was in contact with the rostral capsule. This connection has never been documented before in placoderms. A foramen, presumably for the optic artery (a.opt), is beneath the optic nerve, but in *Narrominaspis*, Burrow (2006) identified the optic artery above the optic nerve, and in *Dicksonosteus* it is below and in front of the optic nerve. The internal openings for the optic nerve and artery are identified inside the right capsule (II,

a.opt, Fig. 6.3A). Other structures are labelled by comparison with *Murrindalaspis* and *Narrominaspis*. No sutures between sclerotic plates could be found using the old dataset, and a better interpretation (using *Drishti Paint* v2.7) will be possible with a higher resolution CT dataset after the whole specimen is CT scanned with the new 4K detector.

Discussed above were the extra gnathal elements recently documented in acanthothoracid placoderms by Vaškaninová et al. (2020). However, a small additional denticulate element had already been found by Hu (2015) inside the rock matrix between the PSG and IG of ANU V244, when performing 3D segmentation of the gnathal elements using the 2015 CT scan (Fig. 6.4). A possible position for this saddle-shaped element was investigated using 3D printouts of the gnathal plates in position. It could not fit on top of the Meckel's cartilage because the IG goes right back to the mandibular joint (see Hu et al., 2017, fig. 4a-b). It may be a symphysial element on the lower jaw (but is not symmetrical), or could be part of the upper jaw attached on the palatoquadrate. A higher resolution scan to make a 3D model may clarify its position. More detail on histological investigations of the gnathal elements has been carried out. The anterior end of the left IG was scanned in 2015 (1.45 microns voxel size resolution), with preliminary segmentation using *Drishti Paint.* Unpublished images (Fig. 6.5) show numerous new features. A clear line indicates the possible boundary of two separated denticle groups (Fig. 6.5A), with distinctive underneath vascular networks and supply. Some denticles (blue coloured cavity) lack connections to the deep vascular network (Fig. 6.5H-J). Others (yellow coloured cavity) connect beneath to the green coloured vascular network (Fig. 6.5E-F). Some denticles (e.g. Fig. 6.5C) have distinct pulp cavities, and others show smaller vascular spaces. According to histological studies by Chen et al. (2016; 2017), higher resolution of scans is crucial for extracting internal vascular systems and identifying any possible resorption, semi-resorption lines etc. Thus, the left IG was also synchrotron scanned (voxel size: 0.67 microns) at the European Synchrotron Radiation Facility (ESRF) in 2017. Recently, the one-micron CT scanner (ANU3) at ANU CT Lab was upgraded with a 4K detector, and the ASG and IG of ANU V244 will be re-scanned to achieve higher resolution and compare with the 2017 synchrotron data for more detailed histological investigations.

Six other infragnathals (IGs) were CT scanned for comparative study with the histology of ANU V244 (Table 6.1); all are arthrodires except V1635 (an antiarch). An IG from Burrinjuck that resembles ANU V244 in external morphology has very different histology (Fig. 6.6) that will be analysed in more detail in a future study.

Species name & Specimen number	Location	Date of scan	Voxel size (um)	Literature cited
'buchanosteid' sp. V244 (anterior part left IG)	Burrinjuck, NSW	Jun 2015	1.45	Young et al., 2001(fig. 2a-c; fig. 4a-d; 5a); Hu et al., 2017; 2019
Eastmanosteus V1045	Gogo, WA	Oct 2018	10.96	Dennis-Bryan, 1987 (fig. 18E-G)
Kimberleyichthys ANU 35687	Gogo, WA	Nov 2018	19.84	Dennis-Bryan & Miles 1983 (fig. 8)
Cavanosteus V78/ ANU 17789	Burrinjuck, NSW	Nov 2018	8.22/ 11.93	Young 2004 (fig. 2A-C; fig. 3A, B, E, F)
Nawagiaspis V1635	Broken river, QLD	Nov 2018	3.25	Young, 1990 (fig. 9c-d)
arthrodire sp. V3119	Burrinjuck, NSW	Nov 2018	5.13	NA

Table 6.1 Selected seven infragnathals for histology study.

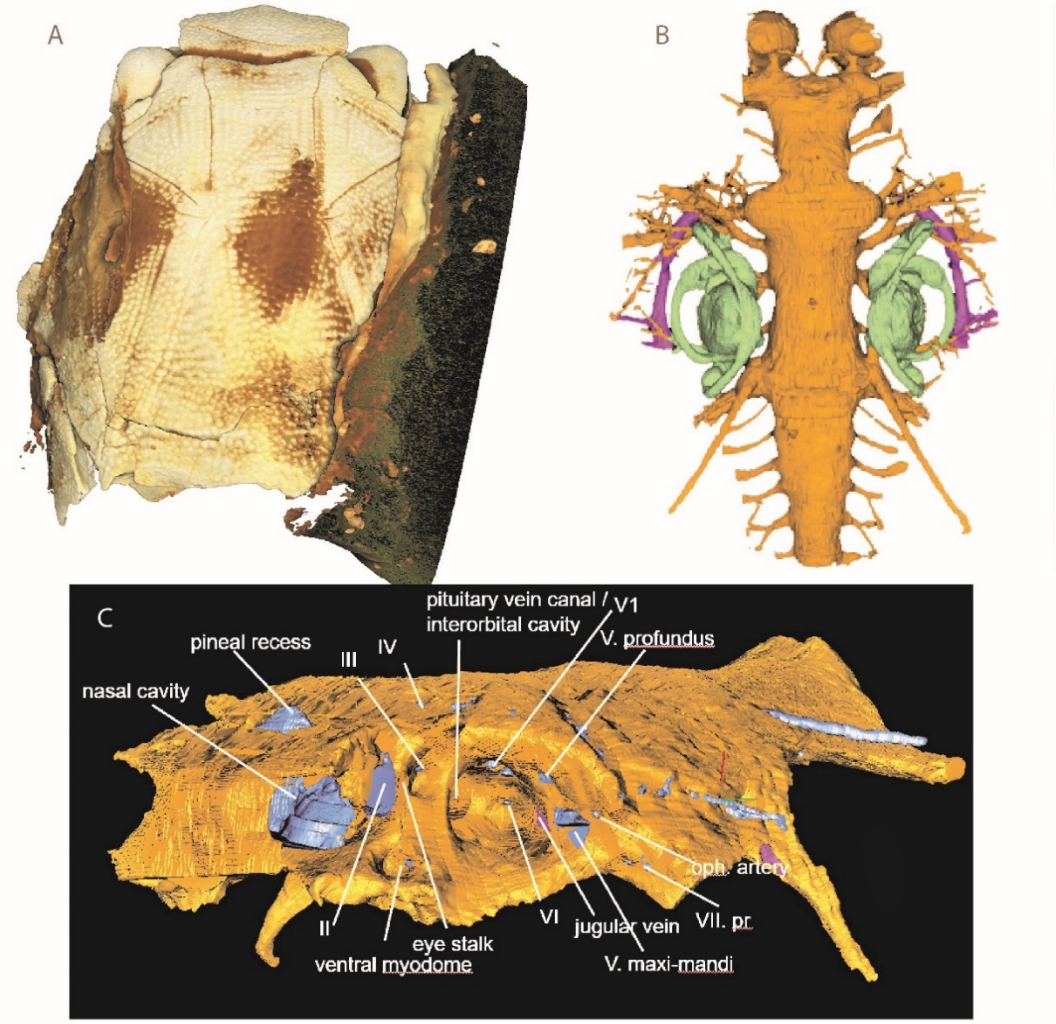

Figure 6.1 Buchanosteus arthrodire ANU V244. **A** new 3D surface mesh image of dermal skull (dorsal view). **B-C** Preliminary segmented brain cavity, nerves and vessels (**B**) and endocast (**C**) with some soft structure restored.

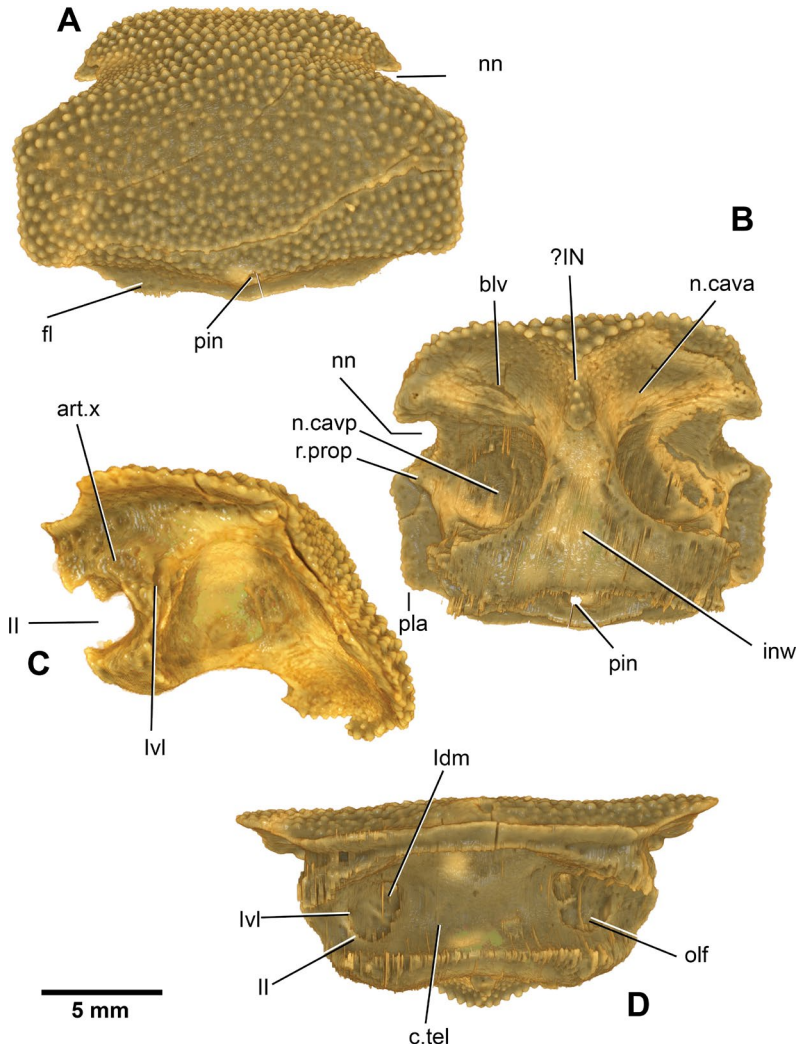

Figure 6.2 Buchanosteid arthrodire ANU V244. Extracted rostral capsule. **A** dorsal view; **B** ventral view; **C** right lateral view; **D** posterior views. art.x, depression on rostral capsule which received a process of eye capsule (pr.x, Fig. 2B-D); blv, grooves possibly for blood vessels; c.tel, cavity for telencephalon; fl, flange; IN, internasal bone; inw, internasal wall; II, foramen or canal for optic nerve; lvl, ventrolateral foramen for olfactory nerve; n.cava, anterior division of the nasal cavity; n.cavp, posterior division of the nasal cavity; olf, recess for olfactory tract; pin, pineal opening; pla, posterolateral angle of rostral capsule.

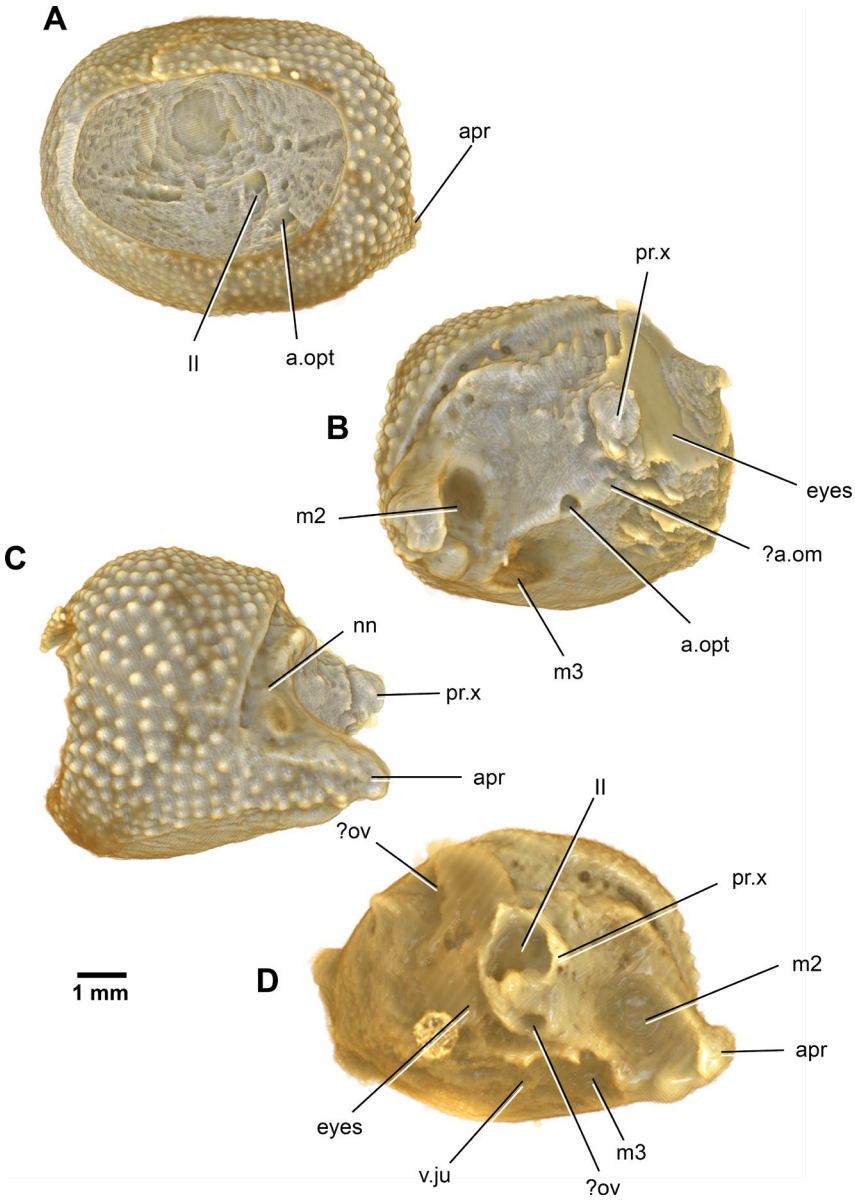

Figure 6.3 Buchanosteid arthrodire ANU V244. Extracted right eye capsule in **A** external view**; B** internal view**; C** right anterior view and **D** extracted left eye capsule in internal view, showing the foramen for optic nerve. a.om, ophthalmic artery foramen; a.opt, optic artery foramen; apr, anterior process of eye capsule; eyes, eyestalk attachment area; II, foramen or canal for olfactory nerve; m2 & m3, muscle scars for extraocular muscles on sclerotic capsule; nn, nasal notch; ov, optic vein; pr.x, process in front of optic nerve foramen on eye capsule, that contracted a depression (art.x, Fig. 1C); v.ju, ?.

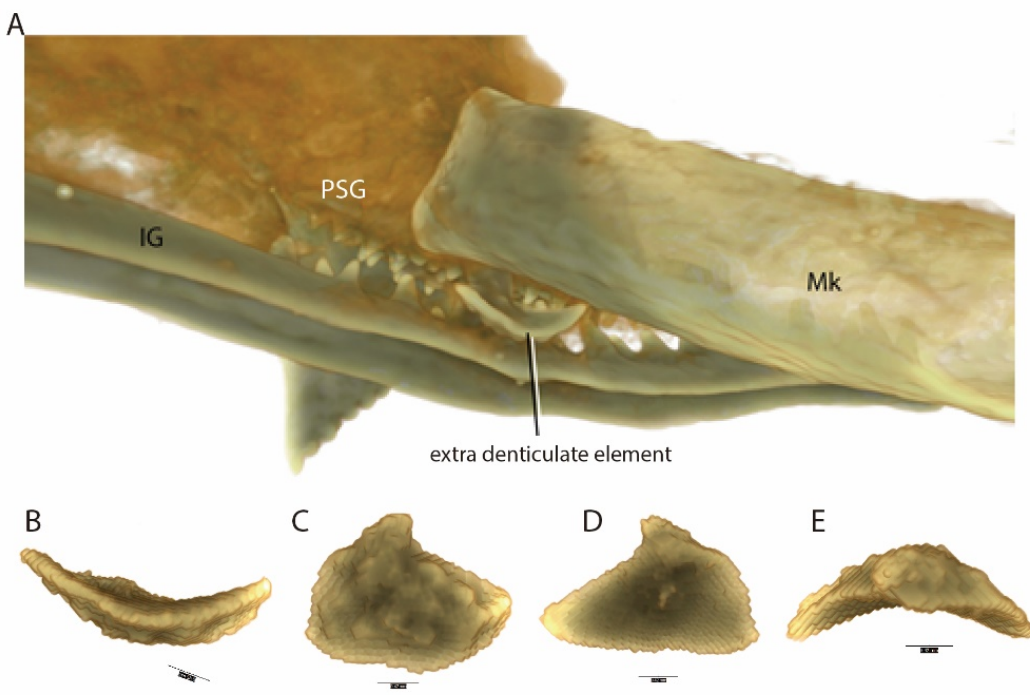

Figure 6.4 A Drishti image shows that the position of an additional denticulate element located with the posterior supragnathal, infragnathal and the Meckel's cartilage. **B-E** Segmented denticulate element when its original position as in **A**; and in external (**C**), internal (**D**) and oblique anterior (**E**) views.

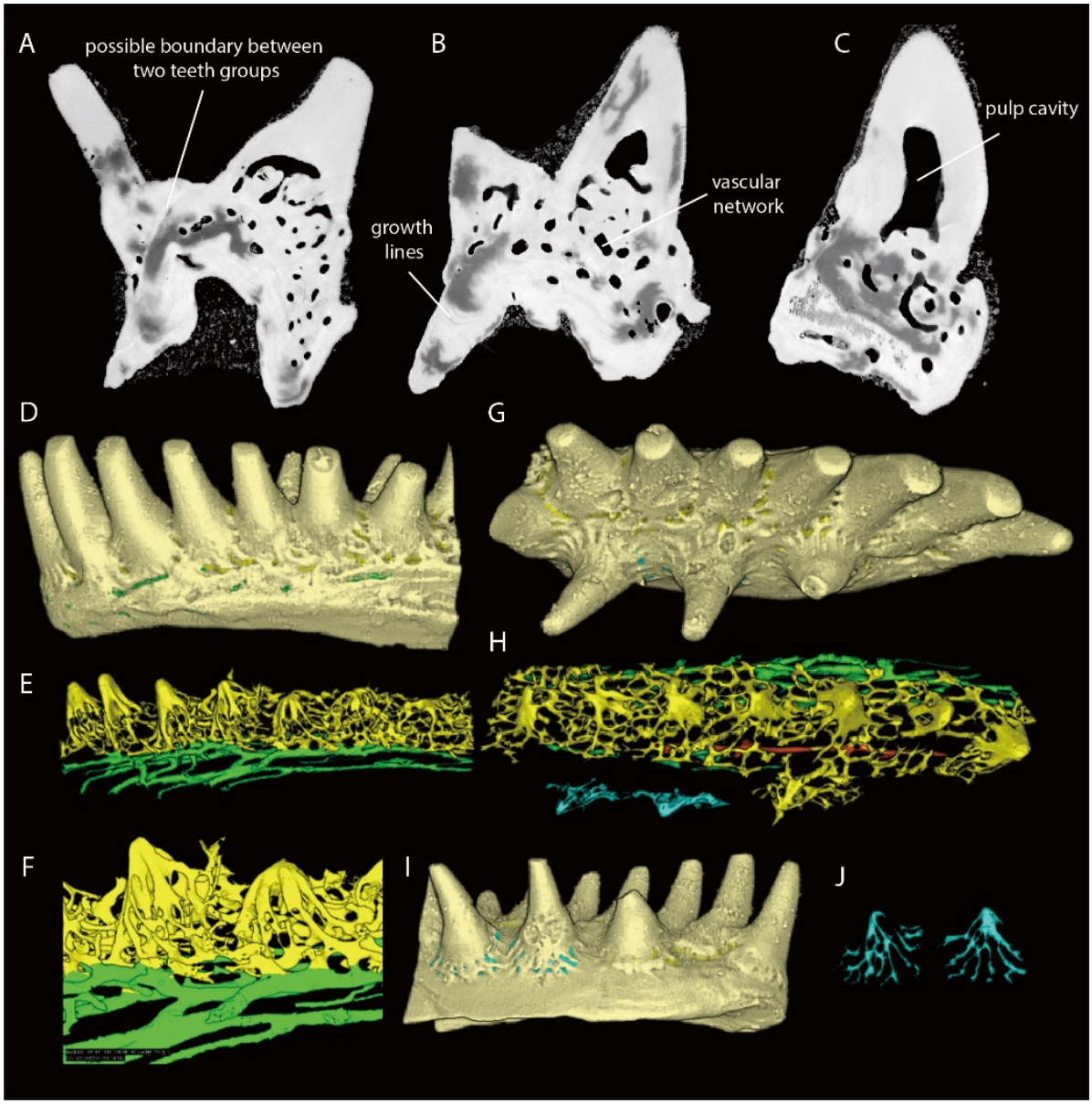

Figure 6.5 The anterior end of the left infragnathal of the Buchanosteid arthrodire ANU V244. **A-C** Vertical cross sections of the 2015 scan. **D-J** Preliminary segmented vascular network. The 'pulp cavity' is a central opening in the denticle but the surrounding tissue is not known yet, it could be semidentine in which case this would not be a pulp cavity.

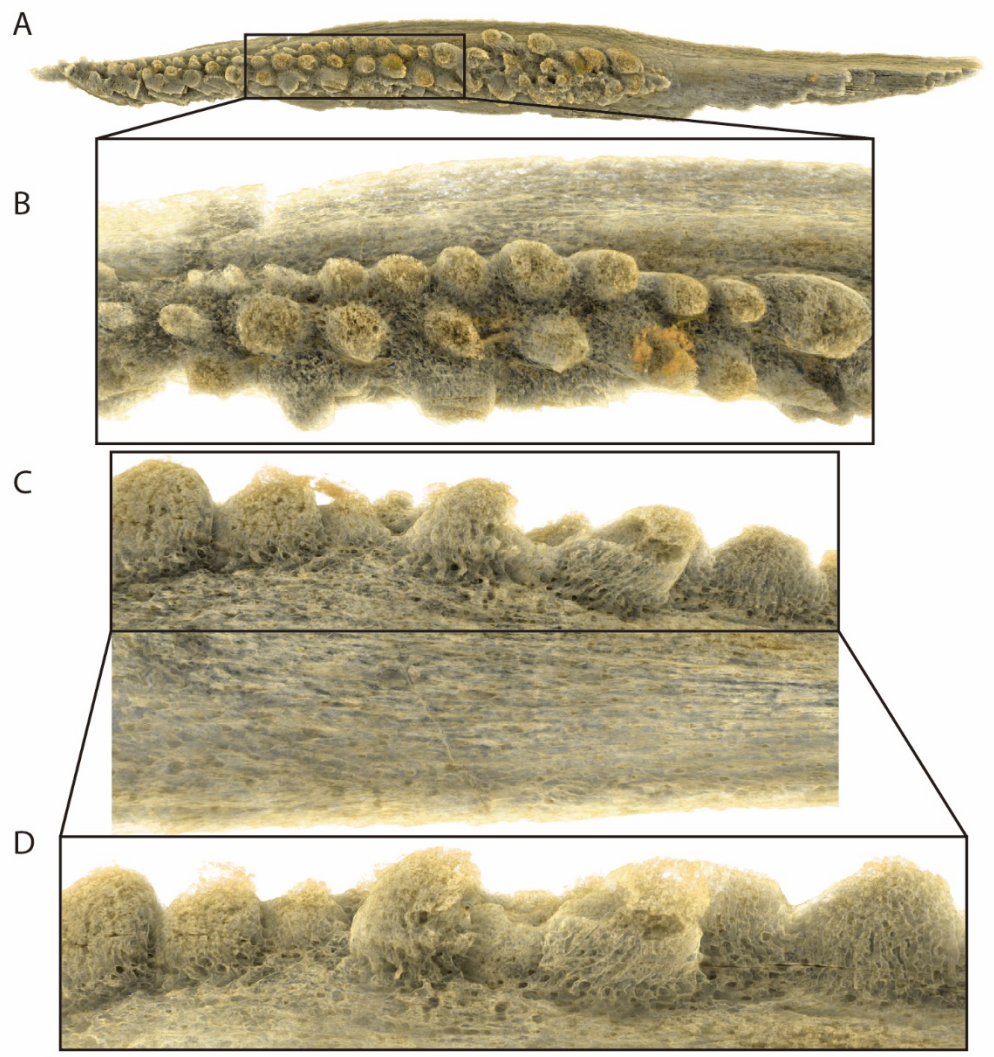

Figure 6.6 Unnamed arthrodire infragnathal with similar external morphology to the buchanosteid arthrodire ANU V244 but different histology. **A** Infragnathal in occlusal view. **B-D** Rendered *Drishti* images from CT data to demonstrate different histology.

Consolidated thesis references

Allis, E.P., 1922. The Cranial Anatomy of *Polypterus*, with Special Reference to *Polypterus bichir*. J. Anat. 56, 189-294.43.

Allis, E.P., 1923. The cranial anatomy of *Chlamydoselachus anguineus*. Acta Zool. 4, 123–221. https://doi.org/10.1111/j.1463-6395.1923.tb00161.x

Andrews, S.M., 1971. The shoulder girdle of *Eogyrinus*. Stud. Vertebr. Evol. 35–48.

Andrews, S.M., Westoll, T.S., 1970a. The postcranial skeleton of *Eusthenopteron foordi* Whiteaves. Trans. R. Soc. Edinb. Earth Sci. 68, 207–329.

Andrews, S.M., Westoll, T.S., 1970b. The Postcranial Skeleton of Rhipidistian Fishes Excluding *Eusthenopteron*. Trans. R. Soc. Edinb. Earth Sci. 68, 391–489. https://doi.org/10.1017/S0080456800014800

Botella, H., et al., 2007. Jaws and teeth of the earliest bony fishes. Nature 448, 583–586. https://doi.org/10.1038/nature05989

Boykov, Y., Kolmogorov, V., 2001. An experimental comparison of min-cut/max-flow algorithms for energy minimization in vision, in: Lecture Notes in Computer Science (Including Subseries Lecture Notes in Artificial Intelligence and Lecture Notes in Bioinformatics). pp. 359–374. https://doi.org/10.1007/3-540-44745-8_24

Brazeau, M.D., 2009. The braincase and jaws of a Devonian “acanthodian” and modern gnathostome origins. Nature 457, 305–308. https://doi.org/10.1038/nature07436

Brazeau, M.D., Friedman, M., 2015. The origin and early phylogenetic history of jawed vertebrates. Nature 520, 490–497. https://doi.org/10.1038/nature14438

Brazeau, M.D., Giles, S., Dearden, R.P., Jerve, A., Ariunchimeg, Y., Zorig, E., Sansom, R., Guillerme, T., Castiello, M., 2020. Endochondral bone in an Early Devonian ‘placoderm’ from Mongolia. Nat. Ecol. Evol. 4, 1477–1484. https://doi.org/10.1038/s41559-020-01290-2

Brodlie KW, et al., 2012. Scientific visualisation: techniques and applications. Springer Sci. Bus. Media.

Burrow, C.J., 2003. Comment on “Separate evolutionary origins of teeth from evidence in fossil jawed vertebrates”. Science 300, 1661. https://doi.org/10.1126/science.1083877

Burrow, C.J., 2006. Placoderm fauna from the Connemarra Formation (?late Lochkovian, Early Devonian), central New South Wales. Alcheringa 30, 59–88. https://doi.org/10.1080/03115510609506856

Burrow, C.J., Turner, S., Young, G.C., 2010. Middle Palaeozoic microvertebrate assemblages and biogeography of East Gondwana (Australasia, Antarctica). Palaeoworld 19, 37–54. https://doi.org/10.1016/j.palwor.2009.11.001

Burrow, C.J., Hu, Y., Young, G.C., 2016. Placoderms and the evolutionary origin of teeth: a comment on Rücklin & Donoghue (2015). Biol. Lett. 12, 20160159. https://doi.org/10.1098/rsbl.2016.0159

Buser, T.J. et al., 2020. The Natural Historian’s Guide to the CT Galaxy: Step-by-Step Instructions for Preparing and Analyzing Computed Tomographic (CT) Data Using Cross-Platform, Open Access Software. Integr. Org. Biol. 2. https://doi.org/10.1093/iob/obaa009

Cabral, B., Cam, N., Foran, J., 1994. Accelerated volume rendering and tomographic reconstruction using texture mapping hardware, in: Proceedings of the 1994 Symposium on Volume Visualization, VVS 1994. {ACM} Press. https://doi.org/10.1145/197938.197972

Carr, R.K., Johanson, Z., Ritchie, A., 2009. The phyllolepid placoderm *Cowralepis* mclachlani: Insights into the evolution of feeding mechanisms in jawed vertebrates. J. Morphol. 270, 775–804. https://doi.org/10.1002/jmor.10719

Carvalho, L.E., Sobieranski, A.C., von Wangenheim, A., 2018. 3D Segmentation Algorithms for Computerized Tomographic Imaging: a Systematic Literature Review. J. Digit. Imaging 31, 799–850. https://doi.org/10.1007/s10278-018-0101-z

Chang, M.-M., 1982. The braincase of *Youngolepis*, a Lower Devonian crossopterygian from Yunnan, South-Western China. PhD Dissertation, Stockholm University 113 pp.

Chen, D., et al., 2016. The stem osteichthyan *Andreolepis* and the origin of tooth replacement. Nature 539, 237–241. https://doi.org/10.1038/nature19812

Chen, D., et al.., 2017. Development of cyclic shedding teeth from semi-shedding teeth: The inner dental arcade of the stem osteichthyan *Lophosteus*. R. Soc. Open Sci. 4, 161084. https://doi.org/10.1098/rsos.161084

Chen, D., et al., 2020. The developmental relationship between teeth and dermal odontodes in the most primitive bony fish *Lophosteus*. Elife 9, 1–20. https://doi.org/10.7554/ELIFE.60985

Chevrinais, M., Balan, E., Cloutier, R., 2015. New insights in the ontogeny and taphonomy of the Devonian acanthodian *Triazeugacanthus affinis* from the Miguasha Fossil-Lagerstätte, eastern Canada. Minerals 6, 1. https://doi.org/10.3390/min6010001

Choudhury, Y., et al., 2017. Corrigendum: Patient-specific hepatocyte-like cells derived from induced pluripotent stem cells model pazopanib-mediated hepatotoxicity. Sci. Rep. 7, 46391. https://doi.org/10.1038/srep46391

Cignoni, P., et al., 2008. MeshLab: An open-source mesh processing tool. 6th Eurographics Ital. Chapter Conf. 2008 - Proc. https://doi.org/10.2312/ /129-136

Clement, A.M., et al., 2018. Neurocranial anatomy of an enigmatic Early Devonian fish sheds light on early osteichthyan evolution. Elife 7. https://doi.org/10.7554/eLife.34349

Cloutier, R., et al., 2020. *Elpistostege* and the origin of the vertebrate hand. Nature 579, 549–554. https://doi.org/10.1038/s41586-020-2100-8

Coates, M.I., et al., 2018. An early chondrichthyan and the evolutionary assembly of a shark body plan. Proc. R. Soc. B Biol. Sci. 285, 20172418. https://doi.org/10.1098/rspb.2017.2418

Crowther, P.R., Collins, C.J., 1987. The conservation of geological material. Geological Curator,4, 375-474.

Cunningham, J.A., et al., 2014. A virtual world of paleontology. Trends Ecol. Evol. 29, 347–357. https://doi.org/10.1016/j.tree.2014.04.004

Davies, T.G., et al., 2017. Open data and digital morphology. Proc. R. Soc. B Biol. Sci. 284, 20170194. https://doi.org/10.1098/rspb.2017.0194

Davis, S.P., Finarelli, J.A., Coates, M.I., 2012. Acanthodes and shark-like conditions in the last common ancestor of modern gnathostomes. Nature 486, 247–250. https://doi.org/10.1038/nature11080

Dearden, R.P., Giles, S., 2020. Dental diversity in early chondrichthyans and the multiple origins of shedding teeth. bioRxiv. https://doi.org/10.1101/2020.07.08.193839

Denison, R.H., 1978. Placodermi. in: Schultze, H.P. (Ed.), Handbook of Paleoichthyology, Vol. 2. Gustav Fischer Verlag, Stuttgart.

Dennis-Bryan, K., 1987. A new species of eastmanosteid arthrodire (Pisces: Placodermi) from Gogo, Western Australia. Zool. J. Linn. Soc. 90, 1–64. https://doi.org/10.1111/j.1096-3642.1987.tb01347.x

Dilpreet, K., Yadwinder, K., 2014. Various Image Segmentation Techniques: A Review, in: International Journal of Computer Science and Mobile Computing. pp. 809–814.
Donoghue, P.C.J., Rücklin, M., 2016. The ins and outs of the evolutionary origin of teeth. Evol. Dev. 18, 19–30. https://doi.org/10.1111/ede.12099
Dorador, J., Rodríguez-Tovar, F.J., 2020. CroSSED sequence, a new tool for 3D processing in geosciences using the free software 3DSlicer. Sci. Data 7. https://doi.org/10.1038/s41597-020-00614-y
Drebin, R.A., Carpenter, L., Hanrahan, P., 1988. Volume rendering. Proc. 15th Annu. Conf. Comput. Graph. Interact. Tech. SIGGRAPH 1988 22, 65–74. https://doi.org/10.1145/54852.378484
Dupret, V., et al., 2014. A primitive placoderm sheds light on the origin of the jawed vertebrate face. Nature 507, 500–503. https://doi.org/10.1038/nature12980
Dupret, V., et al., 2017. The internal cranial anatomy of *Romundina stellina* Ørvig, 1975 (Vertebrata, Placodermi, Acanthothoraci) and the origin of jawed vertebrates-Anatomical atlas of a primitive gnathostome. PLoS One 12, e0171241. https://doi.org/10.1371/journal.pone.0171241
Eaton, T.H., 1975. Schultergürtel und pectoralflosse bei actinopterygiern. Earth-Science Rev. 11, 366. https://doi.org/10.1016/0012-8252(75)90041-0
Edgeworth, F.H., 1937. the Cranial Muscles of Vertebrates. J. Nerv. Ment. Dis. 86, 221. https://doi.org/10.1097/00005053-193708000-00037
Evans, P.D., et al., 2015. Visualizing the Microdistribution of Zinc Borate in Oriented Strand Board Using X-Ray Microcomputed Tomography and SEM-EDX. J. Compos. 2015, 1–9. https://doi.org/10.1155/2015/630905
Fish, J.L., 2019. Evolvability of the vertebrate craniofacial skeleton. SeminARS Cell Dev. Biol. 91, 13–22. https://doi.org/10.1016/j.semcdb.2017.12.004
Forey, P.L., Gardiner, B.G., 1986. Observations on *Ctenurella* (Ptyctodontida) and the classification of placoderm fishes. Zool. J. Linn. Soc. 86, 43–74. https://doi.org/10.1111/j.1096-3642.1986.tb01807.x
Forey, P., Janvier, P., 1993. Agnathans and the origin of jawed vertebrates. Nature 361, 129–134. https://doi.org/10.1038/361129a0
Forey, P., Janvier, P., 1994. Evolution of the early vertebrates. Am.Sci. 82, 554–565.
Fox, R.C., et al., 1995. A new osteolepiform fish from the Lower Carboniferous Raymond Formation, Drummond Basin, Queensland. Mem. Queensl. Museum 38, 97–221.
Gai, Z., et al., 2011. Fossil jawless fish from China foreshadows early jawed vertebrate anatomy. Nature. 476, 324–327. https://doi.org/10.1038/nature10276
Gardiner, B.G., 1984. The relationships of the palaeoniscid fishes, a review based on new specimens of Mimia and Moythomasia from the Upper Devonian of Western Australia. Bull. Br. Museum (Natural Hist. Geol. 37, 173–428.
Gardiner, B.G., Miles, R.S., 1990. A new genus of eubrachythoracid arthrodire from Gogo, Western Australia. Zool. J. Linn. Soc. 99, 159–204. https://doi.org/10.1111/j.1096-3642.1990.tb00566.x
Garwood, R., Dunlop, J., 2014. The walking dead: Blender as a tool for paleontologists with a case study on extinct arachnids. J. Paleontol. 88, 735–746. https://doi.org/10.1666/13-088
Geier, B., et al., 2020. Spatial metabolomics of in situ host–microbe interactions at the micrometre scale. Nat. Microbiol. 5, 498–510. https://doi.org/10.1038/s41564-019-0664-6

Giles, S., Friedman, M., Brazeau, M.D., 2015. Osteichthyan-like cranial conditions in an Early Devonian stem gnathostome. Nature 520, 82–85. https://doi.org/10.1038/nature14065
Giles, S., Rücklin, M., Donoghue, P.C.J., 2013. Histology of “placoderm” dermal skeletons: Implications for the nature of the ancestral gnathostome. J. Morphol. 274, 627–644. https://doi.org/10.1002/jmor.20119
Goujet, D.F., 1972. Nouvelles observations sur la joue d’*Arctolepis* (Eastman) et d’autres Dolichothoraci. Ann. Paléontologie 58, 3–11.
Goujet, D.F., 1975. *Dicksonosteus*, un nouvel arthrodire du Dévonien du Spitsberg. Remarques sur le squelette viscéral des Dolichothoraci. Colloques internat. Centre nat. Rech. sci., 218, 81-99.
Goujet, D.F., 1984. Les Poissons Placodermes du Spitsberg: Arthrodires Dolichthoraci de la Formation de Wood Bay (D{é}vonien inf{é}rieur), Cah.Pal{é}ont.CNRS. Paris, Editions Centre National Recherche Scientifique, Cahiers de Paléontologie.
Goujet, D.F., Young, G.C., 2004. Placoderm anatomy and phylogeny: new insights. Recent Adv. Orig. Early Radiat. Vertebr. 109–126.
Gross, W., 1968. Beobachtung mit dem Elektronenraster Auflichtmikoskop an den Siebplatten un dem Isopedin von Dartmuthia (Osteostraci). Palaontologische Zeitschrift, 42, 74-82.
Hall, P.M., Watt, A.H., 1991. Rapid Volume Rendering Using a Boundary-Fill Guided Ray Cast Algorithm, in: Scientific Visualization of Physical Phenomena. Springer Japan, Tokyo, pp. 235–249. https://doi.org/10.1007/978-4-431-68159-5_13
Hills, E.S., 1936. On Certain Endocranial Structures in *Coccosteus*. Geol. Mag. 73, 213–226. https://doi.org/10.1017/S0016756800097399
Hoffmann, R., et al., 2018. Integrating 2D and 3D shell morphology to disentangle the palaeobiology of ammonoids: a virtual approach. Palaeontology 61, 89–104. https://doi.org/10.1111/pala.12328
Holland, T., 2013. Pectoral girdle and fin anatomy of *Gogonasus andrewsae* long, 1985: Implications for tetrapodomorph limb evolution. J. Morphol. 274, 147–164. https://doi.org/10.1002/jmor.20078
Holland, T., 2014. The endocranial anatomy of *Gogonasus andrewsae* Long, 1985 revealed through micro CT-scanning. Earth Environ. Sci. Trans. R. Soc. Edinburgh 105, 9–34. https://doi.org/10.1017/S1755691014000164
Holland, T., Long, J.A., 2009. On the phylogenetic position of *Gogonasus andrewsae* Long 1985, within the Tetrapodomorpha. Acta Zool. 90, 285–296. https://doi.org/10.1111/j.1463-6395.2008.00377.x
Hu, Y., 2015. CT investigation of the skeleton of an Early Devonian arthrodire (placoderm fish) in relation to the evolution of jaws and teeth. BSc Honours Thesis, Research School of Earth Sciences and Department of Applied Mathematics, The Australian National University (unpublished).
Hu, Y., Lu, J., Young, G.C., 2017. New findings in a 400 million-year-old Devonian placoderm shed light on jaw structure and function in basal gnathostomes. Sci. Rep. 7. https://doi.org/10.1038/s41598-017-07674-y
Hu, Y., et al., 2019. High resolution XCT scanning reveals complex morphology of gnathal elements in an Early Devonian arthrodire. Palaeoworld 28, 525–534. https://doi.org/10.1016/j.palwor.2018.12.003
Hu, Y., Young, G.C., Lu, J., 2019. The Upper Devonian tetrapodomorph *Gogonasus andrewsae* from Western Australia: Reconstruction of the shoulder girdle and opercular

series using X-ray Micro-Computed Tomography. Palaeoworld 28, 535–542. https://doi.org/10.1016/j.palwor.2019.07.008
Hu, Y., Limaye, A., Lu, J., 2020a. Three-dimensional segmentation of computed tomography data using *Drishti Paint*: new tools and developments. R. Soc. Open Sci. 7, 201033. https://doi.org/10.1098/rsos.201033
Hu, Y., Limaye, A., Lu, J., 2020b. A spark of 3D revisualization: new method for re-exploring segmented data. bioRxiv 2020.08.01.222869. https://doi.org/10.1101/2020.08.01.222869
Hunt, J.R., Young, G.C., 2011. A new placoderm fish of uncertain affinity from the Early-Middle Devonian Hatchery Creek succession at Wee Jasper, New South Wales. Alcheringa 35, 53–75. https://doi.org/10.1080/03115511003793645
Janvier, P., 1978. On the oldest known teleostome fish *Andreolepis hedei* Gross (Ludlow of Gotland), and the systematic position of the lophosteids. Eesti NSV Tead. Akad. Toim. Geoloogia 27, 88–95.
Janvier, P., 1996. Early vertebrates. Oxford, Clarendon Press. https://doi.org/10.1111/j.1502-3931.1996.tb01869.x
Janvier, P., 2007. Living Primitive Fishes and Fishes From Deep Time, in: Fish Physiology. pp. 1–51. https://doi.org/10.1016/S1546-5098(07)26001-7
Janvier, P., 2013. Palaeontology: Inside-out turned upside-down. Nature 502, 457–458. https://doi.org/10.1038/nature12695
Janvier, P., Arsenault, M., 2009. La conservation exceptionelle des fossiles du parc nationale de Miguasha. Le Nat. Can. 133, 78–83.
Janvier, P., Desbiens, S., Willett, J.A., 2007. New evidence for the controversial “lungs” of the Late Devonian antiarch *Bothriolepis canadensis* (Whiteaves, 1880) (Placodermi: Antiarcha). J. Vertebr. Paleontol. 27, 709–710. https://doi.org/10.1671/0272-4634(2007)27[709:NEFTCL]2.0.CO;2
Janvier, P., et al., 2006. Lamprey-like gills in a gnathostome-related Devonian jawless vertebrate. Nature 440, 1183–1185. https://doi.org/10.1038/nature04471
Jarvik, E., 1944. On the exoskeletal shoulder-girdle of Teleostomian fishes, with special reference to *Eusthenopteron foordi* Whiteaves. K. Sven. vetenskapsakademiens Handl. 21, 3–32.
Jarvik, E., 1948. On the morphology and taxonomy of the middle Devonian osteolepid fishes of Scotland. K. Sven. Vetenskapsakademiens Handl. 25, 1–301.
Jarvik, E., 1980. Basic Structure and Evolution of Vertebrates. Syst. Zool. 30, 575. https://doi.org/10.2307/2413058
Jiang, X., et al., 2002. Curve morphing by weighted mean of strings, in: Proceedings - International Conference on Pattern Recognition. pp. 192–195. https://doi.org/10.1109/icpr.2002.1047430
Jobbins, M., et al., 2021. A large Middle Devonian eubrachythoracid ‘placoderm’ (Arthrodira) jaw from northern Gondwana. Swiss J. Palaeontol. 140, 2. https://doi.org/10.1186/s13358-020-00212-w
Johanson, Z., Boisvert, C.A., Trinajstic, K., 2019. Early Vertebrates and the Emergence of Jaws. pp. 23–44. https://doi.org/10.1007/978-3-319-93560-7_2
Johanson, Z., Smith, M.M., 2003. Placoderm fishes, pharyngeal denticles, and the vertebrate dentition. J. Morphol. 257, 289–307. https://doi.org/10.1002/jmor.10124

Johanson, Z., Smith, M.M., 2005. Origin and evolution of gnathostome dentitions: A question of teeth and pharyngeal denticles in placoderms. Biol. Rev. Camb. Philos. Soc. 80, 303–345. https://doi.org/10.1017/S1464793104006682
Johnson, C., 2004. Top scientific visualization research problems. IEEE Comput. Graph. Appl. 24, 13–17. https://doi.org/10.1109/MCG.2004.20
Johnson, E.H., Carter, A.M., 2019. Defossilization: A Review of 3D Printing in Experimental Paleontology. Front. Ecol. Evol. 7. https://doi.org/10.3389/fevo.2019.00430
Kaur D., Kaur Y., 2014. Various image segmentation techniques: a review. Int. J. Comput. Sci. Mobile Comput. 3, 809-814.
King, B., Hu, Y., Long, J.A., 2018a. Electroreception in early vertebrates: survey, evidence and new information. Palaeontology 61, 325–358. https://doi.org/10.1111/pala.12346
King, B., Young, G.C., Long, J.A., 2018b. New information on *Brindabellaspis stensioi* Young, 1980, highlights morphological disparity in Early Devonian placoderms. R. Soc. Open Sci. 5, 180094. https://doi.org/10.1098/rsos.180094
King, B., et al., 2017. Bayesian Morphological Clock Methods Resurrect Placoderm Monophyly and Reveal Rapid Early Evolution in Jawed Vertebrates. Syst. Biol. 66, 499–516. https://doi.org/10.1093/sysbio/syw107
King, B., Rücklin, M., 2020. A Bayesian approach to dynamic homology of morphological characters and the ancestral phenotype of jawed vertebrates. Elife 9, 1–77. https://doi.org/10.7554/ELIFE.62374
Kingston, A.M., et al., 2011. Reliable automatic alignment of tomographic projection data by passive auto-focus. Med. Phys. 38, 4934–4945. https://doi.org/10.1118/1.3609096
Kingston, A.M., et al., 2018. Space-Filling X-Ray Source Trajectories for Efficient Scanning in Large-Angle Cone-Beam Computed Tomography. IEEE Trans. Comput. Imaging 4, 447–458. https://doi.org/10.1109/tci.2018.2841202
Lacroute, P., Levoy, M., 1994. Fast volume rendering using a shear-warp factorization of the viewing transformation, in: Proceedings of the 21st Annual Conference on Computer Graphics and Interactive Techniques, SIGGRAPH 1994. {ACM} Press, pp. 451–458. https://doi.org/10.1145/192161.192283
Lakare, S., Kaufman, A., 2000. 3D Segmentation Techniques for Medical Volumes. Neural Networks 65, 1–23.
Latham, S.J., et al., 2018. Reprojection Alignment for Trajectory Perturbation Estimation in Microtomography. IEEE Trans. Comput. Imaging 4, 271–283. https://doi.org/10.1109/tci.2018.2811945
Latham, S.J., Varslot, T., Sheppard, A., 2008. Automated registration for augmenting micro-CT 3D images. ANZIAM J. 50, 534. https://doi.org/10.21914/anziamj.v50i0.1389
Lautenschlager, S., 2016. Reconstructing the past: Methods and techniques for the digital restoration of fossils. R. Soc. Open Sci. 3, 160342. https://doi.org/10.1098/rsos.160342
Lebedev, O.A., 1995. Morphology of a new osteolepidid fish from Russia, in: Bulletin Museum National d'Histoire Naturelle Section C: Sciences de La Terre. pp. 287–341.
Legg, D.A., et al., 2012. A taxonomic revision of orthosternous scorpions from the english coal measures aided by x-ray micro-tomography (XMT). Palaeontol. Electron. 15. https://doi.org/10.26879/253
Lelievre, H., et al.,1994. Nouveaux Vertebres (Placodermes, Acanthodiens, Chondrichthyens et Sarcopterygiens) de la formation de Jauf (Devonien inferieur, region de Al Huj, Arabie Saoudite). Comptes Rendus - Acad. des Sci. Ser. II Sci. la Terre des Planetes 319, 1247–1254.

Lelievre, H., Janvier, P., Goujet, D., 1981. Les vertébrés dévoniens de l'Iran central. IV: Arthrodires et ptyctodontes. Geobios 14, 677–709. https://doi.org/10.1016/S0016-6995(81)80148-9

Lelièvre, H., et al., 1995. *Nefudina qalibahensis* nov. gen., nov. sp.un rhenanide (Vertebrata, Placodermi) du Dévonien inférieur de la Formation Jauf (Emsien) d'Arabie Saoudite. Geobios 28, 109–115. https://doi.org/10.1016/S0016-6995(95)80096-4

Limaye, A., 2012. Drishti: a volume exploration and presentation tool, in: Stock, S.R. (Ed.), Developments in X-Ray Tomography VIII. SPIE, p. 85060X. https://doi.org/10.1117/12.935640

Long, J.A., 1985a. A new osteolepidid fish from the Upper Devonian Gogo Formation, Western Australia. Rec. West. Aust. Museum 12, 361–377.

Long, J.A., 1985b. New information on the head and shoulder girdle of *Canowindra grossi* Thomson, from the Late Devonian Mandagery Sandstone, New South Wales. Rec. Aust. Museum 37, 91–99. https://doi.org/10.3853/j.0067-1975.37.1985.338

Long, J.A., 1995. A New Plourdosteid Arthrodire from the Upper Devonian Gogo Formation of Western-Australia. Palaeontology 38, 39–62.

Long, J.A., 1997. Ptyctodontid fishes (Vertebrata, Placodermi) from the Late Devonian Gogo Formation, Western Australia, with a revision of the European genus Ctenurella Ørvig, 1960. Geodiversitas 19, 515–555.

Long, J.A., Young, G.C., 1988. Acanthothoracid remains from the Early Devonian of New South Wales, including a complete sclerotic capsule and pelvic girdle. Mem. Assoc. Australas. Palaeontol. 7, 65–80.

Long, J.A., Mark-Kurik, E., Young, G.C., 2014. Taxonomic revision of buchanosteoid placoderms (Arthrodira) from the Early Devonian of South-eastern Australia and arctic Russia. Aust. J. Zool. 62, 26–43. https://doi.org/10.1071/ZO13081

Long, J.A., et al., 2014. Copulation in antiarch placoderms and the origin of gnathostome internal fertilization. Nature 517, 196–199. https://doi.org/10.1038/nature13825

Long, J.A., Trinajstic, K.M., 2010. The Late Devonian Gogo formation lägerstatte of Western Australia: Exceptional early vertebrate preservation and diversity. Annu. Rev. Earth Planet. Sci. 38, 255–279. https://doi.org/10.1146/annurev-earth-040809-152416

Long, J.A., Trinajstic, K.M., 2018. A review of recent discoveries of exceptionally preserved fossil fishes from the Gogo sites (Late Devonian, Western Australia). Earth Environ. Sci. Trans. R. Soc. Edinburgh 108, 111–117. https://doi.org/10.1017/S1755691018000178

Long, J.A., et al., 2006. An exceptional Devonian fish from Australia sheds light on tetrapod origins. Nature 444, 199–202. https://doi.org/10.1038/nature05243

Long, J.A., Barwick, R.E., Campbell, K.S.W., 1997. Osteology and Functional Morphology of the Osteolepiform Fish *Gogonasus andrewsae* Long, 1985, from the Upper Devonian Gogo Formation, Western Australia by. Rec. West. Aust. Museum 53, 1–89.

Lu, J., et al., 2019. The posterior cranial portion of the earliest known tetrapodomorph *Tungsenia paradoxa* and the early evolution of tetrapodomorph endocrania. Vertebr. Palasiat. 57, 93–104.

Lu, J., et al., 2012. The earliest known stem-tetrapod from the Lower Devonian of China. Nat. Commun. 3. https://doi.org/10.1038/ncomms2170

Manssour, I.H., et al., 2002. Visualizing inner structures in multimodal volume data, in: Brazilian Symposium of Computer Graphic and Image Processing. {IEEE} Comput. Soc, pp. 51–58. https://doi.org/10.1109/SIBGRA.2002.1167123

Mark-Kurik, E., 1985. *Actinolepis spinosa* n. sp. (Arthrodira) from the Early Devonian of Latvia. J. Vertebr. Paleontol. 5, 287–292. https://doi.org/10.1080/02724634.1985.10011866
Mark-Kurik, E., Young, G.C., 2003. A new buchanosteid arthrodire (placoderm fish) from the Early Devonian of the ural mountains. J. Vertebr. Paleontol. 23, 13–27. https://doi.org/10.1671/0272-4634(2003)23[13:ANBAPF]2.0.CO;2
Mays, C., Cantrill, D.J., Stilwell, J.D., Bevitt, J.J., 2018. Neutron tomography of Austrosequoia novae-zeelandia e comb. nov. (Late Cretaceous, Chatham Islands, New Zealand): implications for Sequoioideae phylogeny and biogeography. J. Syst. Palaeontol. 16, 551–570. https://doi.org/10.1080/14772019.2017.1314898
Miles, R.S., 1969. Features of placoderm diversification and the evolution of the arthrodire feeding mechanism. Trans. R. Soc. Edinburgh 68, 123–170. https://doi.org/10.1017/S0080456800014629
Miles, R.S., 1971. The Holonematidae (placoderm fishes), a review based on new specimens of Holonema from the Upper Devonian of Western Australia. Philos. Trans. R. Soc. London. B, Biol. Sci. 263, 101–234. https://doi.org/10.1098/rstb.1971.0111
Miles, R.S. & Westoll, T.S. 1968. The placoderm fish *Coccosteus cuspidatus* Miller ex Agassiz from the Middle Old Red Sandstone of Scotland. Part 1 Descriptive morphology. Trans. R. Soc. Edinburgh 67, 373–476.
Myers, G.R., et al., 2016. Rapidly converging multigrid reconstruction of cone-beam tomographic data, in: Stock, S.R., Müller, B., Wang, G. (Eds.), Developments in X-Ray Tomography X. SPIE, p. 99671M. https://doi.org/10.1117/12.2238267
Myers, G.R., et al., 2011. Extending reference scan drift correction to high-magnification high-cone-angle tomography. Opt. Lett. 36, 4809. https://doi.org/10.1364/ol.36.004809
Nelson, J.S., 2006. Fishes of the World: 4th Edition, Wiley, New York 624 pp.
Northcutt, R.G., 1989. The phylogenetic distribution and innervation of craniate mechanoreceptive lateral lines, in: The Mechanosensory Lateral Line. Springer New York, pp. 17–78. https://doi.org/10.1007/978-1-4612-3560-6_3
Olive, S., et al., 2020. Tristichopterids (Sarcopterygii, Tetrapodomorpha) from the Upper Devonian tetrapod-bearing locality of Strud (Belgium, upper Famennian), with phylogenetic and paleobiogeographic considerations. J. Vertebr. Paleontol. 40. https://doi.org/10.1080/02724634.2020.1768105
O'Rourke, J.C., et al., 2020. How Can We Show You, If You Can't See It? Trialing the Use of an Interactive Three-Dimensional Micro-CT Model in Medical Education. Anat. Sci. Educ. 13, 206–217. https://doi.org/10.1002/ase.1890
Ørvig, T., 1967. Phylogeny of tooth tissues: evolution of some calcified tissues in early vertebrates; pp. 45-110 in A. E. W. Miles (ed.), Structural and Chemical Organisation of Teeth, Volume 1. Academic Press, New York, and London.
Ørvig, T., 1975. Description, with special reference to the dermal skeleton, of a new radotinid arthrodire from the Gedinnian of Arctic Canada. Colloques Internat. Centre nat. Rech. Sci., 218, pp. 41–71.
Ørvig, T., 1980. Histologic studies of ostracoderms, placoderms and fossil elasmobranchs: 3. structure and growth of the gnathalia of certain arthrodires. Zool. Scr. 9, 141–159. https://doi.org/10.1111/j.1463-6409.1980.tb00660.x
Parker, K., Warren, A., Johanson, Z., 2005. Strepsodus (Rhizodontida, Sarcopterygii) pectoral elements from the Lower Carboniferous Ducabrook Formation, Queensland,

Australia. J. Vertebr. Paleontol. 25, 46–62. https://doi.org/10.1671/0272-4634(2005)025[0046: SRSPEF]2.0.CO;2
Playford, P.E., 1980. The Devonian “Great Barrier Reef” of the Canning Basin, Western Australia. Am. Assoc. Petrol. Geol. Bull. 64, 814–840.
Pye, F., et al., 2019. ImageJ and 3D Slicer: open source 2 / 3D morphometric software. PeerJ Prepr. 7, e27998v2. https://doi.org/10.7287/peerj.preprints.27998v2
Qiao, T., et al., 2016. Early gnathostome phylogeny revisited: Multiple method consensus. PLoS One 11, e0163157. https://doi.org/10.1371/journal.pone.0163157
Rahman, I.A., Adcock, K., Garwood, R.J., 2012. Virtual fossils: a new resource for science communication in paleontology. Evol. Educ. Outreach 5, 635–641. https://doi.org/10.1007/s12052-012-0458-2
Reif, W.-E., 1982. Evolution of dermal skeleton and dentition in Vertebrates: the odontode regulation theory. Evol.Biol. 15, 287-368.
Ritchie, A., 2005. Cowralepis, a new genus of phyllolepid fish (Pisces, Placodermi) from the late Middle Devonian of New South Wales, Australia, in: Proceedings of the Linnean Society of New South Wales. Proceedings of the Linnean Society of New South Wales, pp. 215–259.
Rixon, A.E., 1976. Fossil Animal Remains: Their Preparation and Conservation. London: The Athlone Press of the University of London. 304pp.
Romer, A., S., 1995. Herpetichthyes, Amphibioidei, Choanichthyes or Sarcopterygii? Nature 176, 126-127.
Rowe, T., Carlson, W., Bottorff, W.W., 1992. Thrinaxodon: digital atlas of the skull, a compact disc. University of Texas Press, Austin.
Rücklin, M., Donoghue, P.C.J., 2015. Romundina and the evolutionary origin of teeth. Biol. Lett. 11, 20150326. https://doi.org/10.1098/rsbl.2015.0326
Rücklin, M., et al., 2012. Development of teeth and jaws in the earliest jawed vertebrates. Nature 491, 748–751. https://doi.org/10.1038/nature11555
Rücklin, M., et al., 2011. Teeth before jaws? Comparative analysis of the structure and development of the external and internal scales in the extinct jawless vertebrate Loganellia scotica. Evol. Dev. 13, 523–532. https://doi.org/10.1111/j.1525-142X.2011.00508.x
Schultze, H.P., Cloutier, R., 1991. Computed tomography and magnetic resonance imaging studies of Latimeria chalumnae. Environ. Biol. Fishes 32, 159–181. https://doi.org/10.1007/BF00007451
Semple, T.L., Peakall, R., Tatarnic, N.J., 2019. A comprehensive and user-friendly framework for 3D-data visualisation in invertebrates and other organisms. J. Morphol. 280, 223–231. https://doi.org/10.1002/jmor.20938
Sheppard, A., et al., 2014. Techniques in helical scanning, dynamic imaging and image segmentation for improved quantitative analysis with X-ray micro-CT. Nucl. Instruments Methods Phys. Res. Sect. B Beam Interact. with Mater. Atoms 324, 49–56. https://doi.org/10.1016/j.nimb.2013.08.072
Smith, M.M., Johanson, Z., 2003a. Response to comment on “Separate evolutionary origins of teeth from evidence in fossil jawed vertebrates.” Science. 300, 1661c – 1661. https://doi.org/10.1126/science.1084686
Smith, M.M., Johanson, Z., 2003b. Separate evolutionary origins of teeth from evidence in fossil jawed vertebrates. Science. 299, 1235–1236. https://doi.org/10.1126/science.1079623

Smith, M.M., Fraser, G.J., Mitsiadis, T.A., 2009. Dental lamina as source of odontogenic stem cells: Evolutionary origins and developmental control of tooth generation in gnathostomes. J. Exp. Zool. Part B Mol. Dev. Evol. 312, 260–280. https://doi.org/10.1002/jez.b.21272

Smith, M.M., et al., 2017. Evolutionary origins of teeth in jawed vertebrates: conflicting data from acanthothoracid dental plates ('Placodermi'). Palaeontology 60, 829–836. https://doi.org/10.1111/pala.12318

Sollas, W.J., 1901. The investigation of fossil remains by serial sections. Rep. British Assoc 1901, p. 643.

Sollas, W.J., 1904. A method for the investigation of fossils by serial sections. Phil. Trans. R. Soc. London B196, 259-265.

Sollas, W.J. & Sollas I.B.J, 1904. An account of the Devonian fish *Palaeospondylus gunni* Traquair. Phil. Trans. R. Soc. London B196, 267-294.

Stensiö, E.A.,1927. The Devonian and Downtonian vertebrates of Spitsbergen. I. Family Cephalaspidae. Skrifter om Svalbard og Ishavet, 12, 1-391.

Stensiö, E.A.,1945. On the heads of certain arthrodires. 2. On the cranium and cervical joint of the Dolichothoraci. Kungliga Svenska Venenskapsakademiens Handlingar (3) 22, 1-70.

Stensiö, E.A., 1963a. Anatomical studies on the arthrodiran head. Pt 1. Preface, geological and geographical distribution, and organisation of the arthrodires, the anatomy of the head in the Dolichothoraci, Coccosteomorphi and Pachyosteomorphi. K. Sven. Vetenskapsakademiens Handl. 1, 1–419.

Stensiö, E.A., 1963b. Nansen memorial Lecture. The brain and the cranial nerves in fossil lower vertebrates. Skrifte Norske Vetenskaps-Akademi I Oslo I. Mat.-Naturv. Klass (N.S.) no. 13, 1-120.

Stensiö, E.A., 1969. Elasmobranchiomorphi Placodermata Arthrodires. In Traité de Paléontologie 4, 71–692.

Sutton, M.D., 2008. Tomographic techniques for the study of exceptionally preserved fossils. Proc. R. Soc. B Biol. Sci. 275, 1587–1593. https://doi.org/10.1098/rspb.2008.0263

Sutton, M.D., et al., 2012. SPIERS and VAXML; A software toolkit for tomographic visualisation and a format for virtual specimen interchange. Palaeontol. Electron. 15. https://doi.org/10.26879/289

Sutton, M., Rahman, I., Garwood, R., 2016. Virtual Paleontology—an Overview. Paleontol. Soc. Pap. 22, 1–20. https://doi.org/10.1017/scs.2017.5

Tafforeau, P., et al., 2006. Applications of X-ray synchrotron microtomography for non-destructive 3D studies of paleontological specimens. Appl. Phys. A Mater. Sci. Process. 83, 195–202. https://doi.org/10.1007/s00339-006-3507-2

Taylor, G.J., et al., 2020. Exploring the visual world of fossilized and modern fungus gnat eyes (Diptera: Keroplatidae) with X-ray microtomography. J. R. Soc. Interface 17, 20190750. https://doi.org/10.1098/rsif.2019.0750

Tesařová, M., et al., 2019. An interactive and intuitive visualisation method for X-ray computed tomography data of biological samples in 3D Portable Document Format. Sci. Rep. 9. https://doi.org/10.1038/s41598-019-51180-2

Thomson, K. S. & Campbell, S.W.K., 1973. The Structure and Relationships of the Primitive Devonian Lungfish-*Dipnorhynchus sussmilchi* (Etheridge). Q. Rev. Biol. 48, 24–24. https://doi.org/10.1086/407494

Toombs, H.A., 1948. The use of acetic acid in the development of vertebrate fossils. Museums Journal London 48, 54-55.
Toombs, H.A. & Rixon, A.E. 1959. The use of acids in the preparation of vertebrate fossils. Curator 2, 304-312.
Trinajstic, K., et al., 2012. New morphological information on the ptyctodontid fishes (Placodermi, Ptyctodontida) from Western Australia. J. Vertebr. Paleontol. 32, 757–780. https://doi.org/10.1080/02724634.2012.661379
Trinajstic, K., et al., 2007. Exceptional preservation of nerve and muscle tissues in Late Devonian placoderm fish and their evolutionary implications. Biol. Lett. 3, 197–200. https://doi.org/10.1098/rsbl.2006.0604
Trinajstic, K., et al., 2013. Fossil musculature of the most primitive jawed vertebrates. Science. 341, 160–164. https://doi.org/10.1126/science.1237275
Upson, C., et al., 1989. The Application Visualization System: A Computational Environment for Scientific Visualization. IEEE Comput. Graph. Appl. 9, 30–42. https://doi.org/10.1109/38.31462
Van Ooijen, P.M.A., et al., 2003. Computers in radiology. Noninvasive coronary imaging using electron beam CT: Surface rendering versus volume rendering. Am. J. Roentgenol. 180, 223–226. https://doi.org/10.2214/ajr.180.1.1800223
Varslot, T., et al., 2011. High-resolution helical cone-beam micro-CT with theoretically-exact reconstruction from experimental data. Med. Phys. 38, 5459–5476. https://doi.org/10.1118/1.3633900
Vaškaninová, V., et al., 2020. Marginal dentition and multiple dermal jawbones as the ancestral condition of jawed vertebrates. Science. 369, 211–216. https://doi.org/10.1126/science.aaz9431
Wang, J.-Q., 2005. New material of *Buchanosteus* and its biostratigrapic significance. Geol. Bull. China 24, 800-806 (In Chinese).
Weitzman, S.H., Jarvik, E., 1981. Basic Structure and Evolution of Vertebrates. Syst. Zool. 30, 506. https://doi.org/10.2307/2413058
Weitzman, S.H., Jarvik, E., 1981. Basic Structure and Evolution of Vertebrates., Systematic Zoology. Academic Press, London. https://doi.org/10.2307/2413058
Westover, L., 1990. Footprint evaluation for volume rendering, in: Proceedings of the 17th Annual Conference on Computer Graphics and Interactive Techniques - SIGGRAPH ’90. ACM Press, New York, USA, pp. 367–376. https://doi.org/10.1145/97879.97919
White, E.I., Toombs, H.A., 1972. The buchanosteid arthrodires of Australia. Bulletin of The British Museum (Natural History) Geology 22, 377–419.
White, E.I., 1952. Australian arthrodires. Bulletin of The British Museum (Natural History) Geology 1, 249-304.
White, E.I., 1978. The larger arthrodiran fishes from the area of the Burrinjuck Dam, N.S.W. Trans. Zool. Soc. London 34, 149–262. https://doi.org/10.1111/j.1096-3642.1978.tb00374.x
Witten, P.E., Sire, J.Y., Huysseune, A., 2014. Old, new and new-old concepts about the evolution of teeth. J. Appl. Ichthyol. 30, 636–642. https://doi.org/10.1111/jai.12532
Young, G.C., 1979. New information on the structure and relationships of Buchanosteus (Placodermi: Euarthrodira) from the Early Devonian of New South Wales. Zool. J. Linn. Soc. 66, 309–352. https://doi.org/10.1111/j.1096-3642.1979.tb01912.x

Young, G.C., 1980. A new Early Devonian placoderm from New South Wales, Australia, with a discussion of placoderm phylogeny. Palaeontographica 167, 10–76.
Young, G.C., 1984. Reconstruction of the jaws and braincase in the Devonian placoderm fish *Bothriolepis*. Palaeontology 27, 635–661.
Young, G.C., 1986. The relationships of placoderm fishes. Zool. J. Linn. Soc. 88, 1–57. https://doi.org/10.1111/j.1096-3642.1986.tb00876.x
Young, G.C., 2003. Did placoderm fish have teeth? J. Vertebr. Paleontol. 23, 987–990. https://doi.org/10.1671/31
Young, G.C., 2008. Early Evolution of the Vertebrate Eye—Fossil Evidence. Evol. Educ. Outreach 1, 427–438. https://doi.org/10.1007/s12052-008-0087-y
Young, G.C., 2010. Placoderms (armored fish): Dominant vertebrates of the devonian period. Annu. Rev. Earth Planet. Sci. 38, 523–550. https://doi.org/10.1146/annurev-earth-040809-152507
Young, G.C., 2011. Wee Jasper-Lake Burrinjuck fossil fish sites: Scientific background to national heritage nomination. Proc. Linn. Soc. New South Wales 132, 83–107.
Young, G.C., Lu, J., 2020. Asia–Gondwana connections indicated by Devonian fishes from Australia: palaeogeographic considerations. J. Palaeogeogr. 9, 8. https://doi.org/10.1186/s42501-020-00057-x
Young, G.C., Dunstone, R.L., Ollerenshaw, P.J., Lu, J., Crook, B., 2020. New information on the giant Devonian lobe-finned fish *Edenopteron* from the New South Wales south coast. Aust. J. Earth Sci. 67, 221–242. https://doi.org/10.1080/08120099.2019.1651769
Young, G.C., Zhang,G.R., 1996. New information on the morphology of yunnanolepid antiarchs (placoderm fishes) from the Early Devonian of South China. J. Vertebr. Paleontol. 16, 623–641. https://doi.org/10.1080/02724634.1996.10011353
Young, G.C., Lelièvre, H., Goujet, D., 2001. Primitive jaw structure in an articulated brachythoracid arthrodire (placoderm fish; early devonian) from southeastern Australia. J. Vertebr. Paleontol. 21, 670–678. https://doi.org/10.1671/0272-4634(2001)021[0670:PJSIAA]2.0.CO;2
Yin,Z.J., Lu,J., Virtual Palaeontology: when fossils illuminated by X-ray. Palaeoworld 28, 425–428. https://doi.org/10.1016/j.palwor.2019.10.001
Zhu, M., et al., 2013. A Silurian placoderm with osteichthyan-like marginal jaw bones. Nature 502, 188–193. https://doi.org/10.1038/nature12617
Zhu, M., et al., 2016. A Silurian maxillate placoderm illuminates jaw evolution. Science. 354, 334–336. https://doi.org/10.1126/science.aah3764
Zhu, Y.A., Ahlberg, P.A., Zhu, M., 2018. The Evolution of Vertebrate Dermal Jaw Bones in the Light of Maxillate Placoderms, in: Evolution and Development of Fishes. Cambridge University Press, pp. 71–86. https://doi.org/10.1017/9781316832172.005
Zhu, Y.A., et al., 2021. Endocast and Bony Labyrinth of a Devonian “Placoderm” Challenges Stem Gnathostome Phylogeny. Curr. Biol. 31, 1112-1118.e4. https://doi.org/10.1016/j.cub.2020.12.046
Zhu, Y.A., Zhu, M., 2013. A redescription of *Kiangyousteus yohii* (Arthrodira: Eubrachythoraci) from the Middle Devonian of China, with remarks on the systematics of the Eubrachythoraci. Zool. J. Linn. Soc. 169, 798–819. https://doi.org/10.1111/zoj.12089
Zhu, Y.A., Zhu, M., Wang, J.Q., 2016. Redescription of *Yinostius* major (Arthrodira: Heterostiidae) from the Lower Devonian of China, and the interrelationships of Brachythoraci. Zool. J. Linn. Soc. 176, 806–834. https://doi.org/10.1111/zoj.12356

Zuber, M., et al., 2017. Augmented laminography, a correlative 3D imaging method for revealing the inner structure of compressed fossils. Sci. Rep. 7, 41413. https://doi.org/10.1038/srep41413

Appendix A pdf of Hu et al. 2019 (Paper 1)

Hu, Y., Young, G.C., Lu, J., 2019. The Upper Devonian tetrapodomorph *Gogonasus andrewsae* from Western Australia: Reconstruction of the shoulder girdle and opercular series using X-ray Micro-Computed Tomography. Palaeoworld 28, 535–542. https://doi.org/10.1016/j.palwor.2019.07.008

Available online at www.sciencedirect.com

ScienceDirect

Palaeoworld 28 (2019) 535–542

Palaeoworld

www.elsevier.com/locate/palwor

The Upper Devonian tetrapodomorph *Gogonasus andrewsae* from Western Australia: Reconstruction of the shoulder girdle and opercular series using X-ray Micro-Computed Tomography

Yu-Zhi Hu [a,b], Gavin C. Young [a,c], Jing Lu [d,e,*]

[a] *Department of Applied Mathematics, Research School of Physics and Engineering, Australian National University, Canberra, ACT 2601, Australia*
[b] *Research School of Earth Sciences, Australian National University, Canberra, ACT 2601, Australia*
[c] *Australian Museum Research Institute, Sydney, NSW 2010, Australia*
[d] *Key Laboratory of Vertebrate Evolution and Human Origins of Chinese Academy of Sciences, Institute of Vertebrate Paleontology and Paleoanthropology, Chinese Academy of Sciences, Beijing 100044, China*
[e] *CAS Center for Excellence in Life and Paleoenvironment, Beijing 100044, China*

Received 10 April 2019; received in revised form 22 June 2019; accepted 12 July 2019
Available online 21 July 2019

Abstract

The tetrapodomorph fish, *Gogonasus andrewsae* is a three dimensionally well-preserved sarcopterygian from the Gogo Formation (Frasnian, early Upper Devonian, ~380 million years ago) in Western Australia. High-resolution X-ray Micro-Computed Tomography and 3D printouts were used to obtain a digital reconstruction of its shoulder girdle and opercular series. Our new findings show the opercular series in a close fit against the upper bones of the shoulder girdle only if the anocleithrum, supracleithrum and post-temporal are aligned more horizontally than in previous reconstructions. The lowermost subopercular bone also differs, in partly covering the clavicle of the shoulder girdle. The ascending process of the clavicle, and the ventral process of the anocleithrum, do not fit closely inside the cleithrum, and perhaps functioned for ligamentous attachment. A rugose area on the anocleithral process is in a similar relative position to the attachment of a muscle ligament on the shoulder girdle of various living actinopterygians. Our manipulation of 3D printouts permits testing of the morphological fit of extremely fragile acid-etched bones, and indicates a new way to investigate the constructional morphology of one or more mechanical units of the vertebrate skeleton. It is suggested that Micro-CT imaging, reconstruction, visualisation and 3D printing techniques will provide a rigorous new test leading to modification of previous reconstructions of extinct vertebrates that were based on graphical methods and 2D imaging.

Keywords: Sarcopterygii; Tetrapodomorph fish; Upper Devonian; High-Resolution Micro-Computed Tomography; 3D printing; mechanical morphology

1. Introduction

Osteichthyans are jawed fishes with fully ossified external and internal skeletons. Two major divisions are recognised: Sarcopterygii (lobe-finned fishes) and Actinopterygii (ray-finned fishes). The Actinopterygii (in which dermal fin rays form most of the fin surface area) are the most diverse vertebrate group living today, with up to 30,000 species (Nelson, 2006). The Sarcopterygii have fins with central fleshy lobes, which contain an internal skeletal element. There are three living sarcopterygian groups: the coelacanth, lungfishes, and the tetrapods (i.e., land vertebrates). In the Devonian, sarcopterygians were the most diverse group of osteichthyan fishes. Tetrapodomorpha is the major group of sarcopterygians, consisting of all tetrapods and fossil forms that are more closely related to living tetrapods than to living lungfish.

The famous tetrapodomorph fish *Gogonasus andrewsae* comes from the Gogo Formation (Frasnian, Late Devonian) in the Canning Basin of the Kimberley region of Western Australia (Long, 1985a; Long et al., 1997, 2006). *Gogonasus* is the only tetrapodomorph fish in the Gogo fish fauna, which

* Corresponding author at: Institute of Vertebrate Paleontology and Paleoanthropology, Chinese Academy of Sciences, Beijing 100044, China
E-mail address: lujing@ivpp.ac.cn (J. Lu).

https://doi.org/10.1016/j.palwor.2019.07.008
1871-174X/

was first described from an isolated ethmosphenoid by Long (1985a). Two more skull specimens permitted a detailed study of osteology and mechanical morphology (Long et al., 1997), making *Gogonasus* one of the best-known Devonian lobe-finned fishes. It provided crucial morphological data to compare with other less preserved fossils in understanding the early stages of fish-tetrapod transition, one of the major events in vertebrate evolution. However, the post-cranial skeleton of *Gogonasus* remained largely unknown (Long et al., 1997, 2006; Holland, 2013, 2014).

The first complete *Gogonasus* specimen (NMV P221807) was discovered in 2005, and acid-preparation confirmed preservation of the entire body and fins. The pectoral fin skeleton of NMV P221807 analysed by High-Resolution Micro-computed Tomography (μCT) suggests that *Gogonasus* is phylogenetically closer to tetrapods than *Eusthenopteron*, a tristichopterid which had been traditionally considered as tetrapods' closest fish relative (Long et al., 2006).

However, the phylogenetic position of *Gogonasus* has remained controversial. A revised phylogenetic analysis by Holland and Long (2009) placed *Gogonasus* basal to *Eusthenopteron*, essentially the same position as in the most recent phylogenies that take account of the earliest known stem-tetrapod *Tungsenia* from China (Lu et al., 2012, 2019). Thus, based on current data, *Gogonasus* is placed close to *Osteolepis*, *Gyroptychius* and megalichthyids in an unresolved polytomy (Fig. 1A).

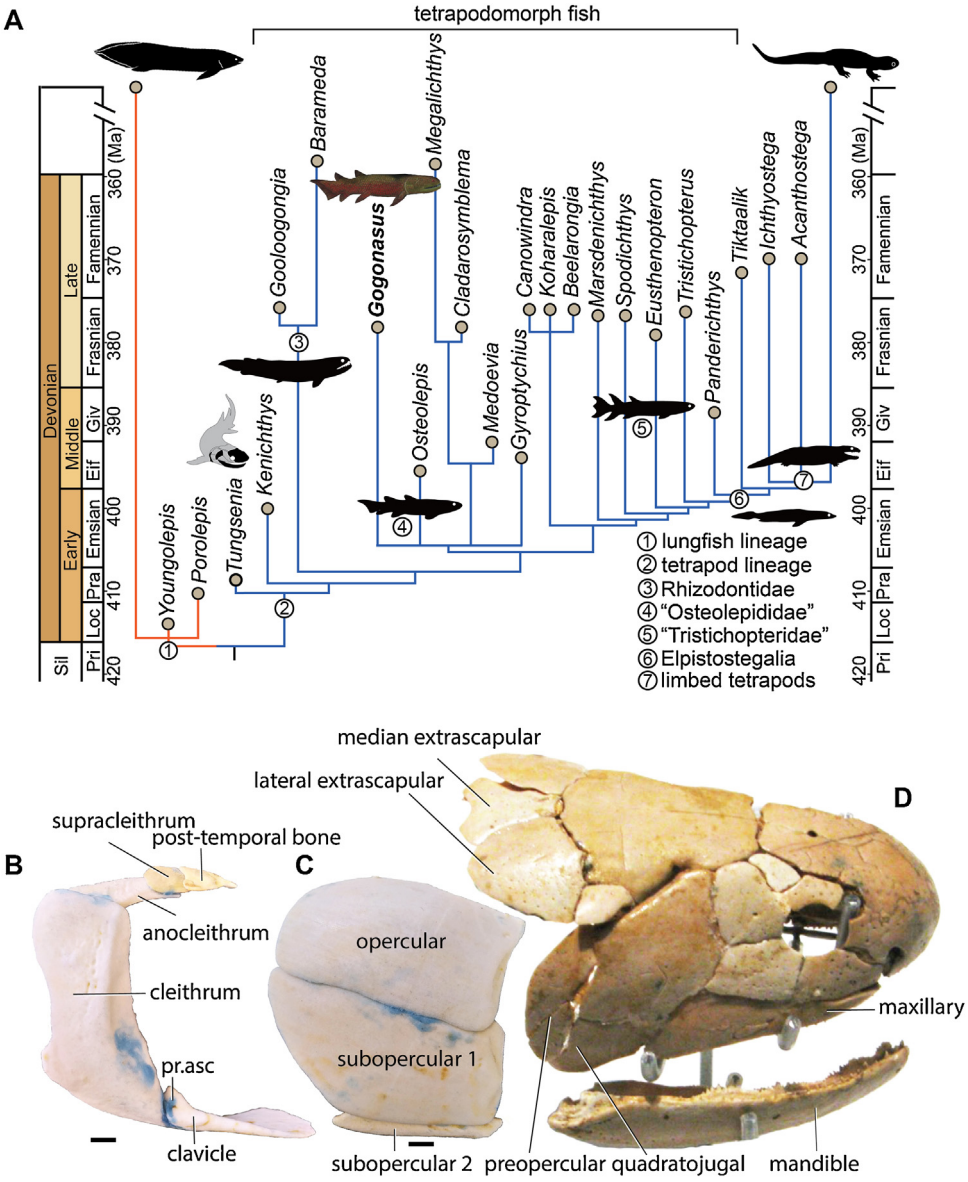

Fig. 1. The tetrapodomorph fish, *Gogonasus andrewsae* Long. (A) Calibrated cladogram of the simplified strict consensus tree, showing the phylogenetic position of *Gogonasus* (modified from Lu et al., 2012, fig. 6); live reconstruction of *Gogonasus* was illustrated by Brain Choo. (B, C) 3D printouts of left shoulder girdle elements (B) and opercular series (C) of NMV P221807 (reversed here to match the right side view of the photo (D)) in alignment. (D) Photo of NMV P221807, on display at Museum Victoria without shoulder girdle and opercular series aligned. Abbreviation: Eif, Eifelian; Giv, Givetian; Loc, Lochkovian; pr.asc, the ascending process of the left clavicle; Pra, Pragian; Pri, Pridoli; Sil, Silurian. Scale bar: (B, C), 1 cm; (D), not to scale.

Acid-prepared fossils are extremely fragile, and manipulation or skeletal reconstruction using actual bones is difficult or impossible because of the risk of breakage. We used a 3D Printer (*ZPrinter 650*) at Australian National University (ANU) to investigate whether the new technologies of HRCT scanning and 3D printing could be used to test reconstructions and mechanical interpretations of such exceptionally preserved but extremely fragile fossils. This was demonstrated by Hu et al. (2017), the first published reconstruction using 3D printouts of early vertebrates, which analysed mechanical morphology of jaw elements in an acid-prepared Devonian placoderm fish. Before this, however, the ANU *Gogonasus* specimen (ANU 49259) had already been scanned, as a trial for 3D printing. A mounted *Gogonasus* reconstruction was built, but incompleteness of the specimen limited its usefulness. To produce 3D printouts of parts missing from the ANU *Gogonasus* specimen, available cheek and shoulder girdle bones of NMV P221807 were borrowed by the ANU in 2012 for re-scanning (Fig. 1B, C). At that time, the rest of the skull, cheek and jaws of NMV P221807 were on display at Museum Victoria (Fig. 1D). Meanwhile, aspects of pectoral girdle and fin anatomy of NMV P221807 had been described by Holland and Long (2009), with a reconstruction of the full pectoral girdle by Holland (2013). The new 3D printouts provided the opportunity to test how the operculum of *Gogonasus* would fit against the recently published reconstruction of the shoulder girdle by Holland (2013).

2. Material and methods

2.1. Material

The four described specimens of *Gogonasus* are as follows: ANU 21885 (the holotype), first described by Long (1985a); ANU 49259 and WAM 86.9.661 (Long et al., 1997); and NMV P221807 (Long et al., 2006; Holland and Long, 2009; Holland, 2013, 2014). We used CT data of the left shoulder girdle and opercular series of NMV P221807 for this study, based on 3D printouts of the following five components of the shoulder girdle (Fig. 1B): clavicle, cleithrum, anocleithrum, supracleithrum, and post-temporal bones. The opercular series comprises three components (Fig. 1C): opercular bone, subopercular bone 1 and subopercular bone 2.

Museum abbreviations: NMV, Museum Victoria; WAM, Western Australian Museum.

2.2. Micro-CT scanning

All scanning for this research was done on instruments developed and built at the CT Lab, Department of Applied Mathematics, Research School of Physics and Engineering, The Australian National University. All six scans were performed with a beam voltage of 80 kV and beam current of 140 μA generated by reflection-style X-ray source. A 1-mm-thick silicon dioxide filter was used. All components were imaged through 360° rotation with 1440 radiographic projections formed on a 1024 × 1024 48-bit pixels Perkin Elmer Flat Panel camera. The left clavicle was scanned (9 July 2012) with a resolution of 63 μm (at 286 mm from the source, and the detector 457 mm from the source). The left cleithrum was scanned (6 August 2012) with a resolution of 80 μm (at 485 mm from the source, and the detector 607 mm from the source). The left anocleithrum, supracleithrum and post-temporal bone were scanned separately (12 July 2012) with a resolution of 63 μm (at 286 mm from the source, and the detector 457 mm from the source). The opercular series was scanned (with associated cheek elements) in one scan (21 June 2012) with a resolution of 84 μm (at 510 mm from the source, and the detector 607 mm from the source).

2.3. Scientific visualization and 3D printing

μ-CT scanning data was processed (without subsampling) using the program Drishti 2.6.5 (Limaye, 2012). All rendered images were from Drishti 2.6.5. Drishti is used to extract opercular series bones which were scanned together with cheek elements. The final output was sent to the *ZPrinter 650* in Stanford Triangle Format (more detail on the *ZPrinter 650*, see Hu et al., 2017, supplementary information). Separate components of the pectoral girdle and opercular series were printed at three times natural size (Figs. 1, 2, 4–6).

The 3D printouts were manipulated into assumed life positions and fixed with dental wax using various morphological criteria as summarised below. The Drishti images (Figs. 2A–C, 3) are presented here to illustrate the morphology, which is less visible on the light-coloured 3D printouts (Figs. 2D, E, 4A, D, E, 5, 6E).

3. Results

3.1. Description of opercular series

The three bones of the opercular series (left side) of *Gogonasus* are separate and very well-preserved (Fig. 2). Long et al. (1997) previously described and illustrated these bones for *Gogonasus*. They used the term 'subopercular 2' instead of 'submandibulo-branchiostegal' of Jarvik (1980), and we follow that here. The rendering images (Fig. 2A–C) generally agree with previous descriptions for *Gogonasus* (Long et al., 1997, fig. 33). The opercular series was reconstructed using 3D printouts first by fitting the upper opercular bone (Fig. 2A) onto the subopercular 1 (Fig. 2B), which has a distinct overlap along its dorsal margin (od.Op, Fig. 2B). The antero-posterior position is based on lining up the anterior overlaps on both bones, which in life would have been covered by the preopercular bone of the cheek (od.Pop, Fig. 2A, B). This gives a slight notch in the posterior border of the operculum (n1, Fig. 2D), as in previous reconstructions (Long et al., 1997, fig. 4), and also means the subopercular projects forward with its anterodorsal corner (adc, Fig. 2B, D).

The subopercular bone 2 (Sop2, Fig. 2) also has an overlap on its dorsal margin, in this case a broader triangular overlap (od.Sop, Fig. 2C). Fitting these together gives a larger notch posteriorly (n2, Fig. 2D). The anterodorsal corner of the subopercular bone 2 (adc, Fig. 2C, D) also projects slightly forward. The entire opercular unit is evenly curved in posterior view (Fig. 2E),

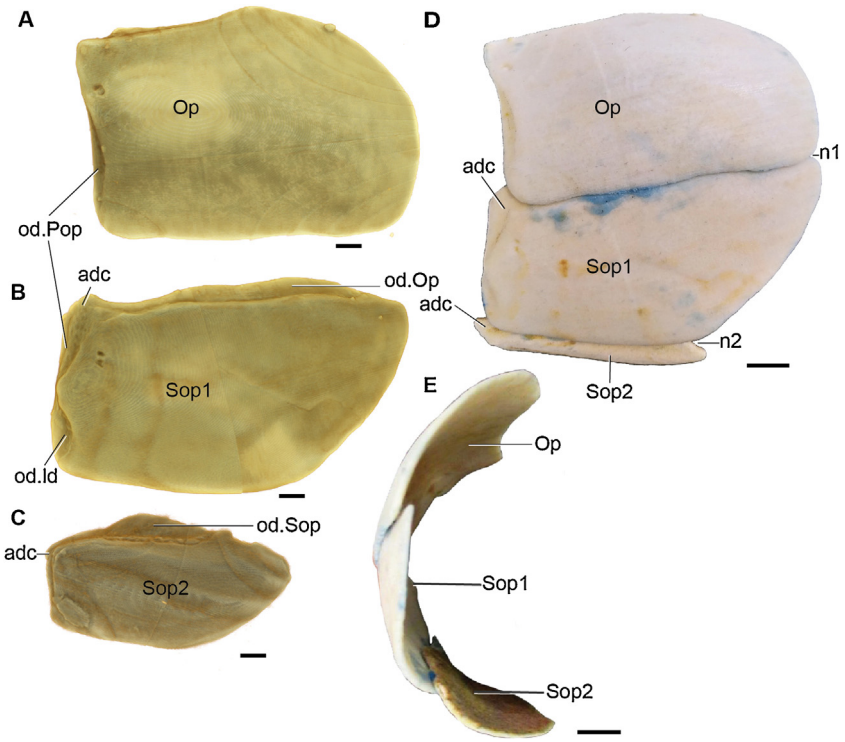

Fig. 2. Left opercular series of *Gogonasus* (NMV P221807). (A–C) Digital segmentation of opercular (A), subopercular bone 1 (B) and subopercular bone 2 (C). (D, E) 3D printouts of opercular series in alignment, lateral (D) and posterior (E) views. Abbreviations: adc, anterodorsal corner; n1, notch when opercular and subopercular 1 are aligned; n2, notch when subopercular 1 and 2 are aligned; od.ld, overlap for infradentary; od.Op, overlaps for opercular; od.Pop, overlap for preopercular; od.Sop, overlap for subopercular 1; Op, opercular; Sop1, subopercular bone 1; Sop2, subopercular bone 2. Scale bar: (A–C), 2 mm; (D, E), 1 cm.

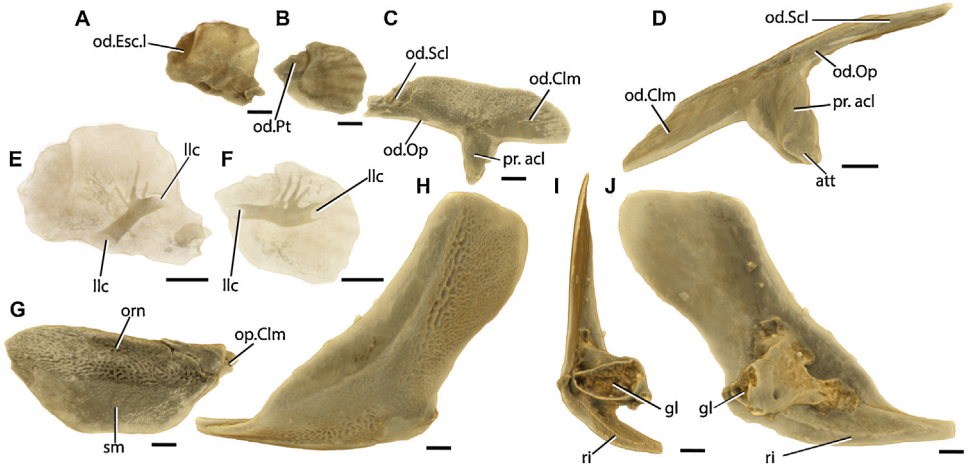

Fig. 3. Digital segmentation of left shoulder girdle components of *Gogonasus* (NMV P221807). (A, E) Post-temporal bone in external view; (E) in transparency, showing the lateral line canal. (B, F) Supracleithrum in external view; (F) in transparency, showing the lateral line canal. (C, D) Anocleithrum, in external (C) and oblique medial (D) views. (G) Clavicle in external view. (H–J) Cleithrum in external (H), anterior (I) and internal (J) views. Abbreviations: att, attachment for muscle ligament; gl, glenoid; llc, lateral line canal; od.Clm, overlap for cleithrum; od.Esc.l, overlap for lateral extrascapular; od.Op, overlap for opercular; od.Pt, overlap for post-temporal bone; od.Scl, overlap for supracleithrum; orn, ornamented area on clavicle; pr.acl, ascending process on the anocleithrum; ri, ridge; sm, smooth area on clavicle. Scale bar: 2 mm.

with the second subopercular curving under the fish, such that much of it is not visible in lateral view (Fig. 2D).

3.2. Description of shoulder girdle

The anocleithrum of *Gogonasus* was described by Holland (2013), but some aspects are unclear. Drishti images (Fig. 3C, D) and 3D printouts (Figs. 1B, 4D) show a slightly curved elongate bone with a strong unornamented anocleithral process (pr.acl, Figs. 3C, D, 4D), and distinct overlap areas for the cleithrum posteriorly, and supracleithrum anteriorly (od.Clm, od.Scl, Fig. 3C, D). A smooth bevelled edge (od.Op, Fig. 2) would have been covered by the operculum. The anocleithrum is oriented with the process pointing downwards (Figs. 3C, 4D), because this

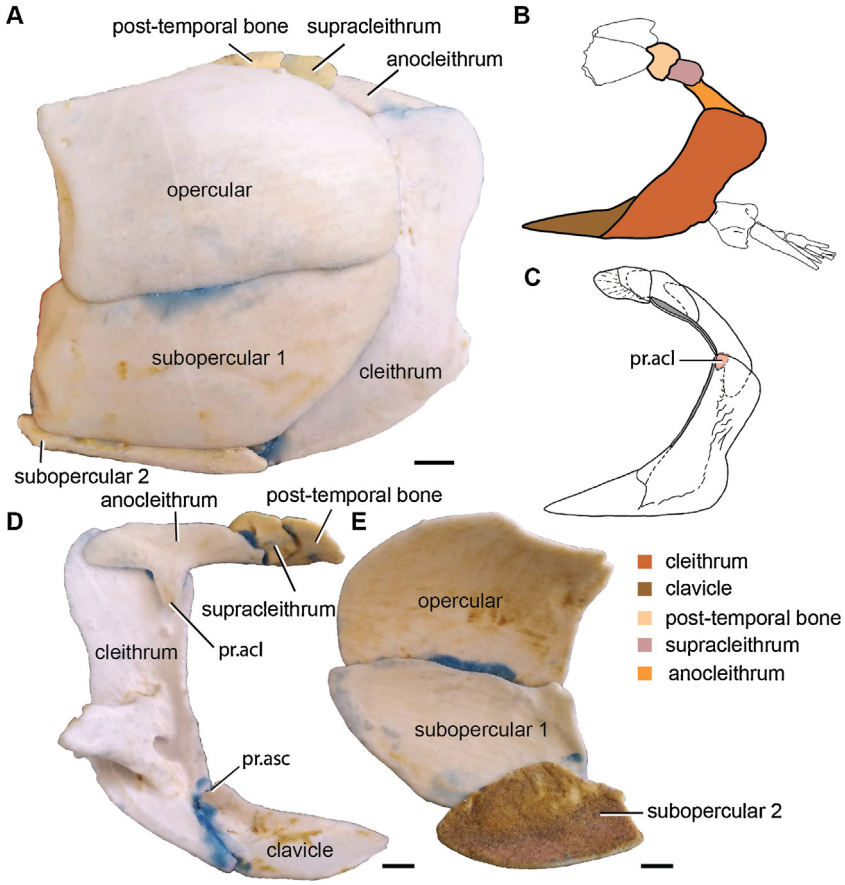

Fig. 4. 3D printout of *Gogonasus* (NMV P221807). (A) Reconstruction of shoulder girdle and opercular series based on 3D printouts. (B) Graphic reconstruction of left shoulder girdle series of *Gogonasus* (modified from Holland, 2013, fig. 9). (C) Graphic reconstruction of left shoulder girdle series of *Eusthenopteron* (exclude extrascapular bones) (modified from Jarvik, 1980, fig. 126 and Jarvik, 1944, fig. 5); light red area shows the ascending process on the anocleithrum of *Eusthenopteron*. (D, E) 3D printouts reconstruction of shoulder girdle (D) and opercular series (E) in internal view. Abbreviations: pr.acl, ascending process on the anocleithrum; pr.asc, ascending process on the clavicle. Scale bar: (A, D, E), 1 cm; (B, C), not to scale.

gives a shape for the opercular opening that corresponds to the shape of the reassembled opercular series using 3D printouts. The smaller supracleithrum and post-temporal were fully described by Holland (2013). They were restored against the skull by Holland and Long (2009, fig. 2B), presumably by aligning overlap areas and foramina for the lateral line sensory canal passing through these bones. We have used the same criteria, as shown in the Drishti images (llc, Fig. 3E, F).

The ventral edge of cleithrum was oriented in horizontal (Fig. 3H–J), with the posterior margin of the cleithrum inclined about 35° from the vertical. This is essentially as reconstructed by Holland (2013, fig. 2G). In this position the long axis of the glenoid fossa (gl, Fig. 3I) on the scapulocoracoid is also approximately horizontal (compared to the more inclined position in Holland, 2013, fig. 3A). A clear bevelled edge and ridge (ri, Fig. 3I, J) inside the ventral margin of the cleithrum presumably abutted against ventral scales of the body.

The left clavicle is preserved as a separate element (Fig. 3G). Holland (2013, fig. 3A–C) figured the right clavicle, preserved attached to the cleithrum, but we are unsure that clavicle is complete, as our separated left clavicle is a larger element. It has a rounded mesial angle (a, Fig. 5A), giving maximum breadth of its ventral lamina about one-third the length from the anterior margin. Its outer surface (Fig. 3G) has two regions: laterally ornamented area (orn, Fig. 3G), and mesially smooth area (sm, Fig. 3G). A posterior overlap (op.Clm, Fig. 3G) fits onto the inside edge of the cleithrum, which is different from that of *Eusthenopteron*, as the overlap of cleithrum of the latter is external (Jarvik, 1980, fig. 126). The two 3D printouts were fitted together such that the mesial edges of the cleithrum and clavicle form an even curve (Fig. 5A). However, this makes the ascending process of the clavicle project upwards, and away from the inner surface of the cleithrum (pr.asc, Figs. 1B, 4D).

4. Discussion

Our alignment of the overlaps (od.Esc.l, od.Pt, Fig. 3A, B) and sensory canal foramina (llc, Fig. 3F, G) for the upper bones of the shoulder girdle gives the 3D printouts a different arrangement from the graphic restoration of Holland (2013, fig. 2G). We adjusted overall alignment to fit with our 3D printouts of the opercular series. This gives the anocleithrum, supracleithrum and post-temporal a much more horizontal alignment (Figs. 1B, 4A, D) compared to Holland's (2013) graphic reconstruction, where these bones slope more strongly upward (Fig. 4B). A similar orientation has been restored for *Eusthenopteron* (Fig. 4C).

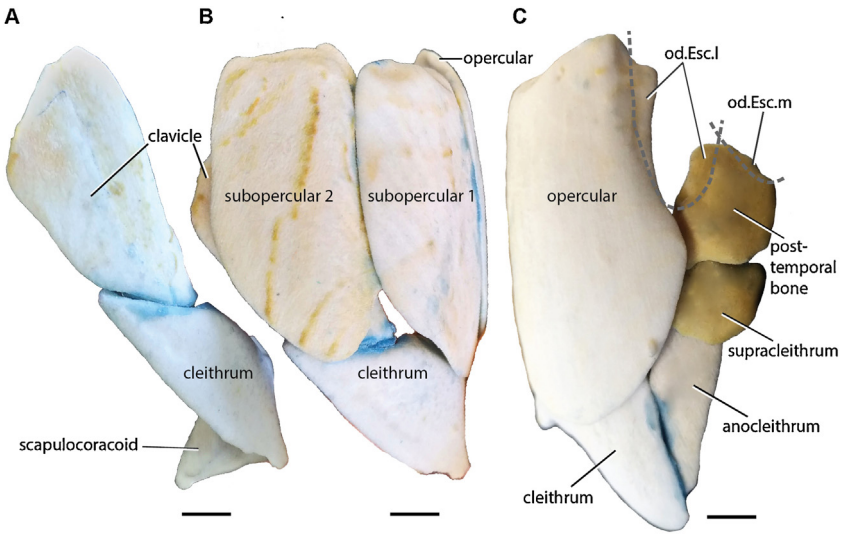

Fig. 5. 3D printout of *Gogonasus* (NMV P221807). (A) Reconstruction of left post-temporal bone, supracleithrum, anocleithrum, cleithrum and clavicle in ventral view. (B, C) Reconstruction of shoulder girdle and opercular series in ventral (B) and dorsal (C) views. The scapulocoracoid is cut out on (B) because of the appearance of fingers when holding these two series for photo shooting. Abbreviations: od.Esc.l, overlap for lateral extrascapular; od.Esc.m, overlap for median extrascapular. Scale bar: 1 cm.

However, an articulated *Eusthenopteron* specimen in which the operculum was prepared away to reveal the shoulder girdle beneath (Jarvik, 1944, fig. 5A, B), shows an anocleithrum that is markedly inclined against the cleithrum, to form a more acute posterodorsal angle to the opercular opening. This approaches the position indicated by our 3D printouts of *Gogonasus*, so it seems possible that the previous restoration of the *Eusthenopteron* shoulder girdle may need further investigation.

In *Gogonasus*, the large anocleithral process (pr.acl, Figs. 3C, D, 4D) clearly fits entirely inside the cleithrum, as in Holland's (2013) reconstruction (and as restored for *Eusthenopteron*). However, in *Osteolepis*, Jarvik (1948, fig. 25) showed the process projecting slightly anteriorly (pr.acl, Fig. 4C), and it projects more prominently in rhizodontids as restored by Andrews (1972, fig. 7) and Parker et al. (2005, fig. 5). In *Gogonasus*, the process in the 3D printouts is separated from the inner surface of the cleithrum, which shows no groove to receive it. As noted by Fox et al. (1995), the anocleithral process in *Cladarosymblema* is twice the size of *Osteolepis* as restored by Jarvik (1948, fig. 25), and it is a similar large size in *Gogonasus*. However, in the specimens of *Osteolepis* figured by Jarvik (1944, fig. 8A, B), the anocleithral process is obscured by surrounding bones, so it could have been considerably larger than restored. Another acid-prepared form, *Medoevia*, also demonstrates a very prominent anocleithral process (Lebedev, 1995, fig. 20), also seen in *Canowindra* (Long, 1985b, fig. 4). Since this is evidently also the condition in rhizodontids (e.g., Parker et al., 2005), a large process could be the primitive condition for the anocleithrum within tetrapodomorphs.

In *Gogonasus* the anocleithral process has a roughened attachment at its end (att, Fig. 3D). Perhaps this was a ligament attachment, as suggested by Fox et al. (1995) for a rugose area at the same position in *Cladarosymblema*. In dipnoans, the anocleithrum is subdermal, but in *Scaumenacia* there is an anterior ridge in a corresponding position to the anocleithral process (Jarvik, 1980, fig. 335). In various actinopterygians (e.g., *Amia*, *Lepisosteus* and *Polypterus*), there is a muscle ligament attaching in much the same relative position on the shoulder girdle (Jessen, 1972). The cucullaris and epaxial musculature attaches on the medial side of this region. The structures in actinopterygians could represent homologues of the anocleithral process in *Gogonasus* and other osteolepiforms as just discussed.

As noted above, 3D printouts of *Gogonasus* show the ascending process of the clavicle projecting upwards, and slightly separated from the inner surface of the cleithrum (pr.asc, Fig. 1B); perhaps this also served as a muscle attachment for sternohyoideus and/or hypaxial which inserts inside the clavicle in some other fishes (e.g., *Latimeria*, *Polypterus*, etc.). In contrast, the ascending process of the clavicle in *Eusthenopteron* is more elongate (Jarvik, 1944, Fig. 5A, B), and the previous reconstructions of *Eusthenopteron* show it is in a close fit against the inner surface of the cleithrum (Jarvik, 1980, fig. 100). This was followed for other detailed graphical reconstructions of the shoulder girdle in 'rhipidistian' fishes (Andrews and Westoll, 1970a, 1970b), but perhaps that assumption also needs reassessment. Andrews and Westoll (1970a, fig. 2b, c) restored the shoulder girdle of *Eusthenopteron* with a flattened ventral surface, such that the ventral lamina of the cleithrum is bent in quite sharply which agrees with probable conditions in *Osteolepis* (Andrews and Westoll, 1970a, p. 217). However, they concede that for *Eusthenopteron* the body may have been deeper and more oval in cross-section. In *Gogonasus*, the shoulder girdle bones are uncrushed, and the cleithrum in posterior view (Fig. 3I) indicates a rounded ventral surface and probably oval cross section, suggesting a fusiform mid-water predatory life-style for this fish, as is also indicated in the fusiform shape of uncrushed examples of *Eusthenopteron* (Jarvik, 1996, fig. 2b).

An unexpected result from manipulating the 3D printouts of *Gogonasus* is that the opercular series in ventral view largely covers and obscures the clavicle (Fig. 5). This is not shown in

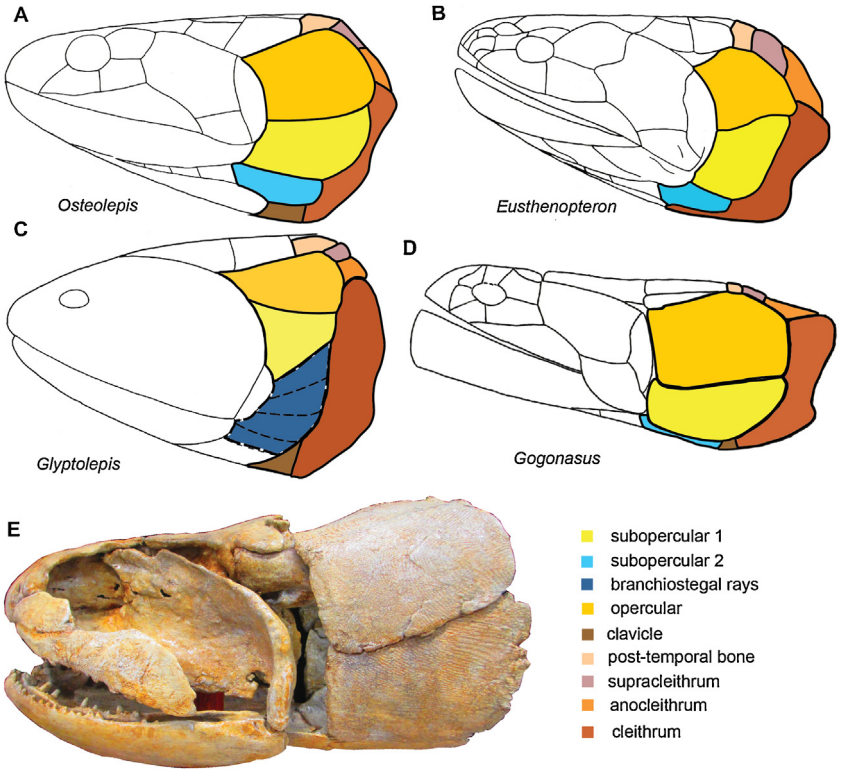

Fig. 6. The reconstructions of skull and shoulder girdle in selected rhipidistians. (A) *Osteolepis* (modified from Jarvik, 1980, fig. 144). (B) *Euthenopteron* (modified from Jarvik, 1980, fig. 122). (C) *Glyptolepis* (modified from Andrews and Westoll, 1970b, text-fig. 23). (D) *Gogonasus* (shoulder girdle and opercular series are drawn based on this study, drawing of the skull is modified from Holland and Long, 2009, fig. 2c). (E) First 3D reconstruction of *Gogonasus*, this reconstruction is not final and may be revised in future works. Not to scale.

any other ventral reconstruction of osteolepiform fishes (e.g., Jarvik, 1980, fig. 144B; Lebedev, 1995, fig. 1C). Further experimentation for other acid-prepared Devonian sarcopterygians, using 3D printing techniques described here for *Gogonasus*, are necessary to check this result, and test the accuracy of other graphic reconstructions for the shoulder girdle and operculum. We note that an interclavicle was not found in NMV P221807 (Holland, 2013), so the shape and size of this bone in *Gogonasus* is unknown. This means the angle of the midline in ventral view (Fig. 5) is uncertain.

The reconstruction using 3D printouts of the shoulder girdle and opercular series of *Gogonasus* has produced a hypothesised mechanical unit that can be manipulated. Comparisons with reconstructions of the same mechanical unit in other related sarcopterygians (*Osteolepis*, *Eusthenopteron*, and the porolepiform *Glyptolepis*) are given in Fig. 6. However, these are all graphical reconstructions, and the first 3D model of the ANU *Gogonasus* specimen (Fig. 6E) was also built on the assumption that previous graphical reconstructions were correct.

5. Conclusion

Reconstruction of the pectoral girdle and opercular series of *Gogonasus* based on μ-CT and 3D printing suggests a different configuration to the previously published graphical reconstruction (Holland, 2013). These results are provisional, because adjacent bones (e.g., extrascapulars, cheek unit etc.) were not available for inclusion in this analysis of the two mechanical units. In addition, the interclavicle, which would have held the two halves of the shoulder girdle together ventrally, is as yet unknown for *Gogonasus*, placing uncertainty on any reconstruction of the shoulder girdle. We suggest that all components of the skull, cheek, jaws, and shoulder girdle of NMV P221807 be scanned in the future. When all the bones are 3D printed at the correct size, a complete reliable reconstruction of the head and pectoral girdle skeleton of *Gogonasus* will produce the first full mechanical model. This can then be used to test previous reconstructions based on earlier tools, such as 2D graphical methods (using photos or drawings as tools of reconstruction), that we predict will soon be completely superseded in the quest to conduct functional analysis of ancient animals now extinct. It is suggested that CT imaging, reconstruction, visualisation and 3D printing technologies will be a good guide for future researches on this topic, testing the highly complex mechanical systems of fossil vertebrates and providing a much more robust evidential basis for understanding the evolutionary process.

Acknowledgements

This research was funded by the Strategic Priority Research Program of Chinese Academy of Sciences (Grant No. XDB26000000), Australian Research Council Discovery grants

DP0772138 and DP1092870, the National Natural Science Foundation of China (41872023), and 2018 Marcelja Fellowship in the Department of Applied Mathematics, Research School of Physics & Engineering, The Australian National University. We thank Tim Senden and John Long for guidance and assisting in various ways for the initial student project, Mike Turner for CT Scanning, Barry Crook for building the model of the ANU *Gogonasus* specimen. We thank Hugo Dutel and Plamen Andreev for providing valuable suggestions during the review process of the paper.

References

Andrews, S.M., 1972. The shoulder girdle of *Eogyrinus*. In: Joysey, K.A., Kemp, T.S. (Eds.), Studies in Vertebrate Evolution. Winchester Press, New York, pp. 35–48.

Andrews, S.M., Westoll, T.S., 1970a. The postcranial skeleton of *Eusthenopteron foordi* Whiteaves. Transactions of the Royal Society of Edinburgh: Earth Sciences 68, 207–329.

Andrews, S.M., Westoll, T.S., 1970b. The postcranial skeleton of rhipidistian fishes excluding *Eusthenopteron*. Transactions of the Royal Society of Edinburgh: Earth Sciences 68, 391–489.

Fox, R.C., Campbell, K.S.W., Barwick, R.E., Long, J.A., 1995. A new osteolepiform fish from the Lower Carboniferous Raymond Formation, Drummond Basin, Queensland. Memoirs of the Queensland Museum 38, 97–221.

Holland, T., 2013. Pectoral girdle and fin anatomy of *Gogonasus andrewsae* long, 1985: implications for tetrapodomorph limb evolution. Journal of Morphology 274, 147–164.

Holland, T., 2014. The endocranial anatomy of *Gogonasus andrewsae* Long, 1985 revealed through micro CT-scanning. Earth and Environmental Science Transactions of the Royal Society of Edinburgh 105, 9–34.

Holland, T., Long, J.A., 2009. On the phylogenetic position of *Gogonasus andrewsae* Long 1985, within the tetrapodomorpha. Acta Zoologica 90, 285–296.

Hu, Y.Z., Lu, J., Young, G.C., 2017. New findings in a 400 million-year-old Devonian placoderm shed light on jaw structure and function in basal gnathostomes. Scientific Reports 7, Article number 7813, https://doi.org/10.1038/s41598-017-07674-y.

Jarvik, E., 1944. On the exoskeletal shoulder-girdle of teleostomian fishes, with special reference to *Eusthenopteron foordi* Whiteaves. Kungliga Svenska Vetenskapsakademiens Handlingar 21, 1–32.

Jarvik, E., 1948. On the morphology and taxonomy of the middle Devonian osteolepid fishes of Scotland. Kungliga Svenska Vetenskapsakademiens Handlingar 25, 1–301.

Jarvik, E., 1980. Basic Structure and Evolution of Vertebrates. Academic Press, London, 575 pp.

Jarvik, E., 1996. The evolutionary importance of *Eusthenopteron foordi* (osteolepiformes). In: Schultze, H.-P., Cloutier, R. (Eds.), Devonian Fishes and Plants. Verlad Dr. Friedrich Pfeil, München, pp. 285–315.

Jessen, H., 1972. Schultergürtel und Pectoralflosse bei Actinopterygien. Fossils & Strata 1, 1–101.

Lebedev, O.A., 1995. Morphology of a new osteolepidid fish from Russia. Bulletin Museum National d'Histoire Naturelle, Paris, 4è Séries, Section C 17, 287–341.

Limaye, A., 2012. Drishti: a volume exploration and presentation tool. Proceedings Volume 8506 of SPIE Optical Engineering and Applications, Developments in X-Ray Tomography VIII, 85060X (12 October 2012), Bellingham, WA, pp. 1–9.

Long, J.A., 1985a. A new osteolepidid fish from the Upper Devonian Gogo Formation, Western Australia. Records of the Western Australian Museum 12, 361–377.

Long, J.A., 1985b. New information on the head and shoulder girdle of *Canowindra grossi* Thomson, from the Late Devonian Mandagery Sandstone, New South Wales. Records of the Australian Museum 37, 91–99.

Long, J.A., Barwick, R.E., Campbell, K.S.W., 1997. Osteology and functional morphology of the osteolepiform fish *Gogonasus andrewsae* Long, 1985, from the Upper Devonian Gogo Formation, Western Australia. Records of the Western Australian Museum Supplement 57, 1–89.

Long, J.A., Young, G.C., Holland, T., Senden, T.J., Fitzgerald, E.M.G., 2006. An exceptional Devonian fish from Australia sheds light on tetrapod origins. Nature 444, 199–202.

Lu, J., Zhu, M., Long, J.A., Zhao, W.J., Senden, T.J., Jia, L.T., Qiao, T., 2012. The earliest known stem-tetrapod from the Lower Devonian of China. Nature Communications 3, Article number 1160, https://doi.org/10.1038/ncomms2170.

Lu, J., Young, G.C., Hu, Y.Z., Qiao, T., Zhu, M., 2019. The posterior cranial portion of the earliest known Tetrapodomorph *Tungsenia paradoxa* and the early evolution of tetrapodomorph endocrania. Vertebrata PalAsiatica 57, 93–104.

Nelson, J.S., 2006. Fishes of the World (4th Edition). Wiley, New York, 624 pp.

Parker, K., Warren, A., Johanson, Z., 2005. *Strepsodus* (Rhizodontida, Sarcopterygii) pectoral elements from the Lower Carboniferous Ducabrook formation, Queensland, Australia. Journal of Vertebrate Paleontology 25, 46–62.

Appendix B pdf of Hu et al. 2017 (Paper 2)

Hu, Y., Lu, J., Young, G.C., 2017. New findings in a 400 million-year-old Devonian placoderm shed light on jaw structure and function in basal gnathostomes. Sci. Rep. 7. https://doi.org/10.1038/s41598-017-07674-y

SCIENTIFIC REPORTS

OPEN

New findings in a 400 million-year-old Devonian placoderm shed light on jaw structure and function in basal gnathostomes

Received: 18 May 2017
Accepted: 30 June 2017
Published online: 10 August 2017

Yuzhi Hu[1,2], Jing Lu[1,3] & Gavin C. Young[1]

Arthodire placoderms have been proposed as the sister group of Chinese 'maxillate' placoderms plus all the more crownward gnathostomes. These basal groups provide key information for understanding the early evolution of jaws. Here, we test previous assumptions about placoderm jaw structure and function by using high-resolution computed tomography, digital dissection, and enlarged 3D printouts on a unique articulated 400 million-year-old buchanosteid arthrodire. The upper jaw has a double ethmoid and a palatobasal connection, but no otic connection; the dermal bone attachment for the quadrate is different to other placoderms. A separately ossified cartilage behind the mandibular joint is comparable to the interhyal of osteichthyans. Two articular facets on the braincase associated with the hyomandibular nerve foramen supported a possible epihyal element and a separate opercular cartilage. Reassembling and manipulating 3D printouts demonstrates the limits of jaw kenetics. The new evidence indicates unrecognized similarities in jaw structure between arthrodires and osteichthyans, and will help to clarify the sequence of character acquisition in the evolution of basal gnathostome groups. New details on the hyoid arch will help to reformulate characters that are key in the heated debate of placoderm monophyly or paraphyly.

The extinct placoderms ('armoured fishes'), with large dermal bones that were readily preserved as fossils, are the best-known and most diverse vertebrate group of the Devonian Period (~420–360 million years ago), and were globally distributed in all habitable aquatic environments[1]. As early gnathostomes (jawed vertebrates), placoderms were traditionally viewed as a side branch to the main trajectory of jaw evolution from early osteichthyan fishes to the first tetrapods (land vertebrates). However, the recent discoveries of the 'maxillate' placoderms *Entelognathus*[2] and *Qilinyu*[3] from the Silurian of China, combining both placoderm and osteichthyan features, have changed that scenario.

Two of the major placoderm subgroups (antiarchs and arthrodires) have been placed as basal branches of a paraphyletic stem of the gnathostome tree[2]. More recent analyses have interpolated other placoderm taxa (such as *Brindabellaspis*, petalichthyids and *Romundina*) within a paraphyletic[4–8] or monophyletic[9] assemblage of stem gnathostomes. The Arthrodira, comprising about 55% of some 330 named placoderm taxa[1], included the largest marine predators of Devonian seas (e.g. the Late Devonian *Dunkleosteus* from the Cleveland Shale of Ohio). Their highly evolved blade-like dermal jaw bones have been used as exemplars in analyses of the early evolution of jaws and teeth[10–12]. However, arthrodires underwent major evolutionary changes in jaw structure during ~70 million years of their existence[1], and jaw structure and function in basal members of the group have been poorly understood.

Our new information on jaw structure is based on an exceptionally preserved specimen of 'buchanosteid' arthrodire (ANU V244) from the Early Devonian limestones (~400 Ma) at Burrinjuck, near Canberra, south-eastern Australia (Supplementary Fig. 1)[13]. It had been partly etched with formic acid before Micro-CT

[1]Department of Applied Mathematics, Research School of Physics and Engineering, Oliphant Building 60, Australian National University, Canberra, ACT, 2601, Australia. [2]Research School of Earth Sciences, Building 142 Mills Road, Australian National University, Canberra, ACT, 2601, Australia. [3]Key Laboratory of Vertebrate Evolution and Human Origins of Chinese Academy of Sciences, Institute of Vertebrate Paleontology and Paleoanthropology, Chinese Academy of Sciences, Beijing, 100044, China. Yuzhi Hu and Jing Lu contributed equally to this work. Correspondence and requests for materials should be addressed to G.C.Y. (email: gavin.young@anu.edu.au)

(computed tomography) scanning. ANU V244 belongs within the family Buchanosteidae[14], but its precise species and relation to other buchanosteids is unclear. ANU V244 shows numerous other characters unknown in most other placoderms, and is referred to in the text as a 'buchanosteid' (For more detail see Supplementary Information). The closely related *Buchanosteus*[15,16] has been used as the basal member of brachythoracid arthrodires in recent analyses[7,17,18], but key information such as the underlying jaw cartilage morphology has not been documented. Unlike later arthrodires, in which the cartilaginous endoskeleton is generally not preserved, our specimen preserves the braincase and endoskeleton of the jaws by investment of perichondral bone, permitting the first complete description of the palatoquadrate and Meckel's cartilage for any arthrodire.

For the first time in a fossil vertebrate, we have used high-resolution 3D printing to investigate placoderm jaw morphology and function by experimentation of the morphological fit between all dermal and perichondrally-ossified endoskeletal elements of the skull, braincase, jaws and cheek.

Results

The whole specimen (Fig. 1) displays a condition shown by certain basal placoderms, with the olfactory part of the braincase, and surrounding dermal bones including the pineal opening, separately ossified by an 'optic fissure' to form a discrete 'rostral capsule'. The cheek unit (best preserved on the right side) comprises dermal suborbital and postsuborbital plates attached to the outside of the upper jaw cartilage (palatoquadrate). Behind this is the dermal opercular cover (submarginal plate), that was movable against the anterior edge of the dermal shoulder girdle (trunk-armour). The various jaw components are slightly displaced and preserved partly inside the ventral dermal trunk-armour (Fig. 1b–f). The jaw cartilages show complete perichondral ossification. In the original specimen these extremely fragile structures are largely obscured by external dermal bones[13], and their detailed morphology, and experiments with gnathal plate occlusion, jaw cartilage articulation, and other functional aspects as described below, could not be investigated without the new techniques of micro-CT scanning and 3D printing (Fig. 2).

Description

Gnathal plates and Jaw cartilages. Only one anterior supragnathal was preserved. It is the right element, not the left as previously interpreted[13], when it was assumed the anterior supragnathals were in midline contact. There is a short contact face for the anterior edge of the parasphenoid (Fig. 1d). There are clearly defined attachment surfaces for both supragnathals on the palatoquadrate (posterior; Fig. 3a) and the braincase. Both have a highly-vascularized surface, and the attachment on the palatoquadrate shows distinct grooves, named anterior, transverse, and longitudinal (Fig. 3c), the last with at least six small mesial branches.

The perichondrally-ossified palatoquadrate is fused to the inside of the dermal suborbital plate (Fig. 3a). Palatoquadrate morphology generally conforms to that described from the only previously known buchanosteid palatoquadrate, which lacked the quadrate portion[15,16]. On the autopalatine, two clear articulations formed an ethmoid connection with the braincase (Fig. 3b). The lateral articulation on its upper surface is supported by a buttress-like ridge, and filled with hard tissue. The mesial articulation is an opening as previously described (i.e. cartilage-filled in life). An anteromesial notch at the front end (Fig. 3) does not connect with the braincase when the palatoquadrate is in position (Fig. 2a,b). Farther back, a distinct process on the mesial edge of the autopalatine represents the palatobasal connection with the braincase. Previous descriptions noted a double articulation here[15,16], but in V244 there is only one articular facet, behind which is a notch for the efferent pseudobranchial artery (Fig. 3c), identified from the position of the groove for this artery on the ventral braincase floor.

Behind the orbit the metapterygoid section is highly arched, with only a narrow contact area with the dermal bone (Fig. 3c). A roughened area on the inner dermal surface indicates the extent of attachment of the adductor mandibulae muscle to the dermal bone (Fig. 3a). The lateral part of the muscle would have inserted here, and the mesial adductor fibres would have attached on the palatoquadrate, but still on the lateral face of the metapterygoid, thus conforming with the fundamental relationship of the adductor mandibulae muscle lateral to the upper jaw cartilage in all fishes[15]. In the arthrodire *Dicksonosteus*, the restored adductor muscle passes from the lateral side of Meckel's cartilage to the mesial side of the palatoquadrate, which could suggest a major difference in adductor mandibulae musculature between placoderms and other gnathostomes[19]. However, closure of the adductor fossa by a lateral lamina of the palatoquadrate in *Dicksonosteus* is considered a derived state relative to the condition in other placoderms[16,20]. The ventral adductor embayment in various other placoderms such as *Holonema*[21], *Romundina*[22], *Bothriolepis*[23], and *Nefudina*[24], with adductor insertion mainly on the outer face of the palatoquadrate (between it and the dermal bone), corresponds to the situation in our buchanosteid specimen. For '*Buchanosteus*' this feature was previously incorrectly coded[25], but has been subsequently updated (character 47)[2].

The dorsal view of the palatoquadrate (Fig. 3b) shows the openings of three large canals passing between the cartilage and the dermal bone. As previously interpreted[15], the anterior two evidently carried maxillary and mandibular branches of the trigeminal nerve (V), and probably also branches of the ramus buccalis lateralis of the facial nerve (VII). The posterior opening would have transmitted lateralis fibres (ramus mandibularis externus VII) supplying most of the sensory line grooves on the exterior of the dermal cheek plates (Supplementary Fig. 4). Apart from the infraorbital groove, all other sensory grooves and pits of the cheek in fishes are supplied by this lateralis branch from the hyomandibular nerve[26]. The canals that transmitted these nerves all lie between the dermal bone and the body of the palatoquadrate, and at no point enter the latter. This is evidently a simpler relationship than restored for *Dicksonosteus*[27], in which the maxillary branch of V and the buccalis lateralis of VII are shown passing mesial to the palatoquadrate before emerging on the lateral side of the autopalatine. In our specimen, these nerves again show the fundamental position for all jawed fishes[15], as demonstrated in modern dissections (e.g. *Polypterus*[28]; *Chlamydoselachus*[29]), by being entirely external to the palatoquadrate, and presumably also to the adductor mandibulae muscle.

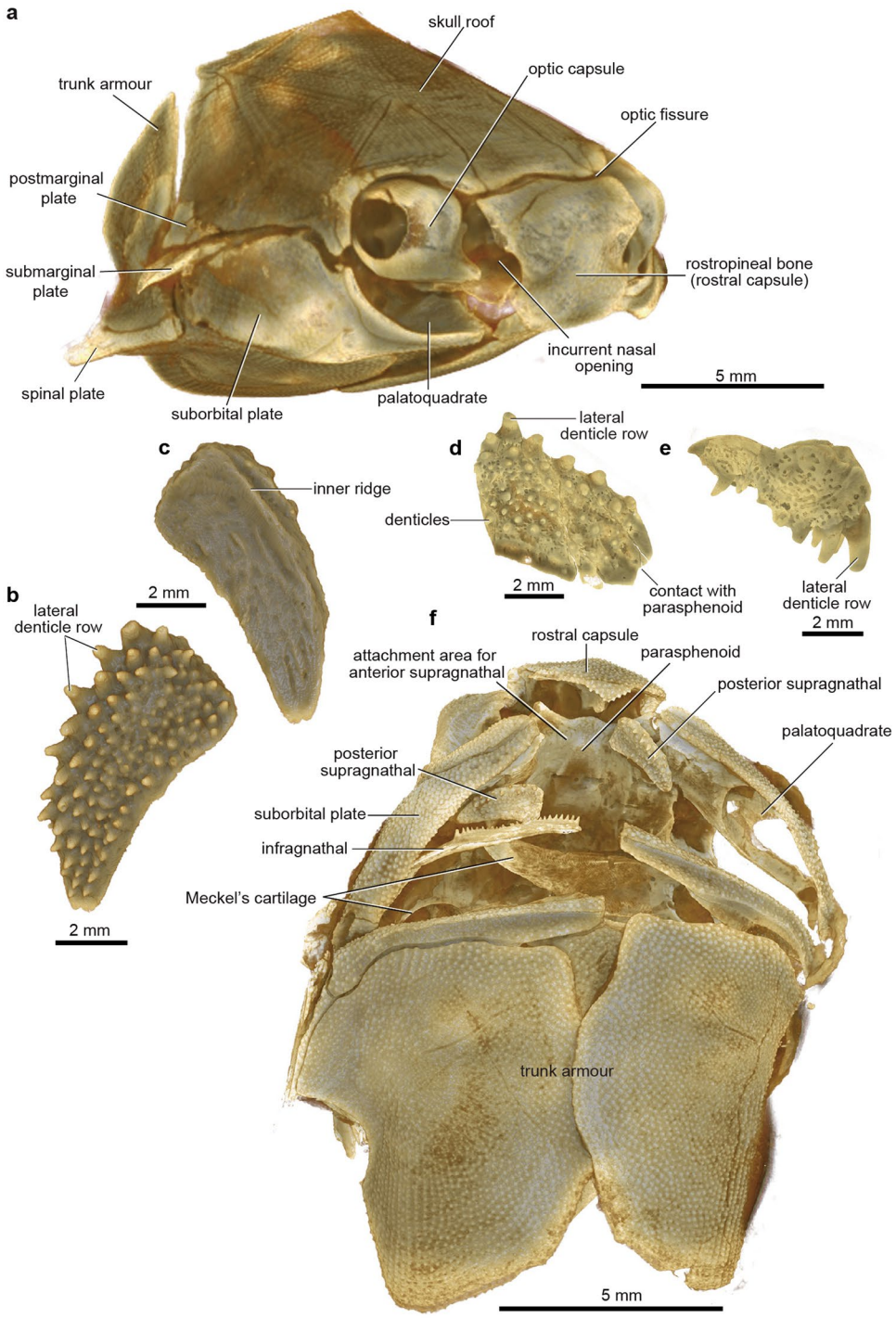

Figure 1. Articulated buchanosteid arthrodire (ANU V244) based on high-resolution CT. (**a**) Whole specimen in right anterolateral view. (**b**–**c**) Right posterior supragnathal bone in occlusal (**b**) and dorsal (**c**) views. (**d**–**e**) Right anterior supragnathal bone in occlusal (**d**) and lateral (**e**) views. (**f**) Whole specimen in ventral view.

One previous specimen of the buchanosteid palatoquadrate was described, but the quadrate portion was broken off[15]. In ANU V244 this region is well preserved, the articular surface for the mandibular joint being a distinct oval-shaped opening, partially broken on the right side, but with its margins complete on the left (Fig. 3c). The quadrate is entirely attached to the inside of the suborbital plate, contrary to previous assumptions[15,16], and the situation in other arthrodires[21,30], where the quadrate is fused inside the postsuborbital plate (Supplementary Fig. 4). In ANU V244 the position of the dermal suture is indicated by dorsal and ventral notches, and a completely separate perichondral ossification, attached inside the postsuborbital plate (Fig. 3a), is positioned just behind the quadrate, inviting comparison with the interhyal of osteichthyans. This separate ossification does not contact the quadrate. It has a slight rounded dorsal process, and a mesial protuberance that possibly connected

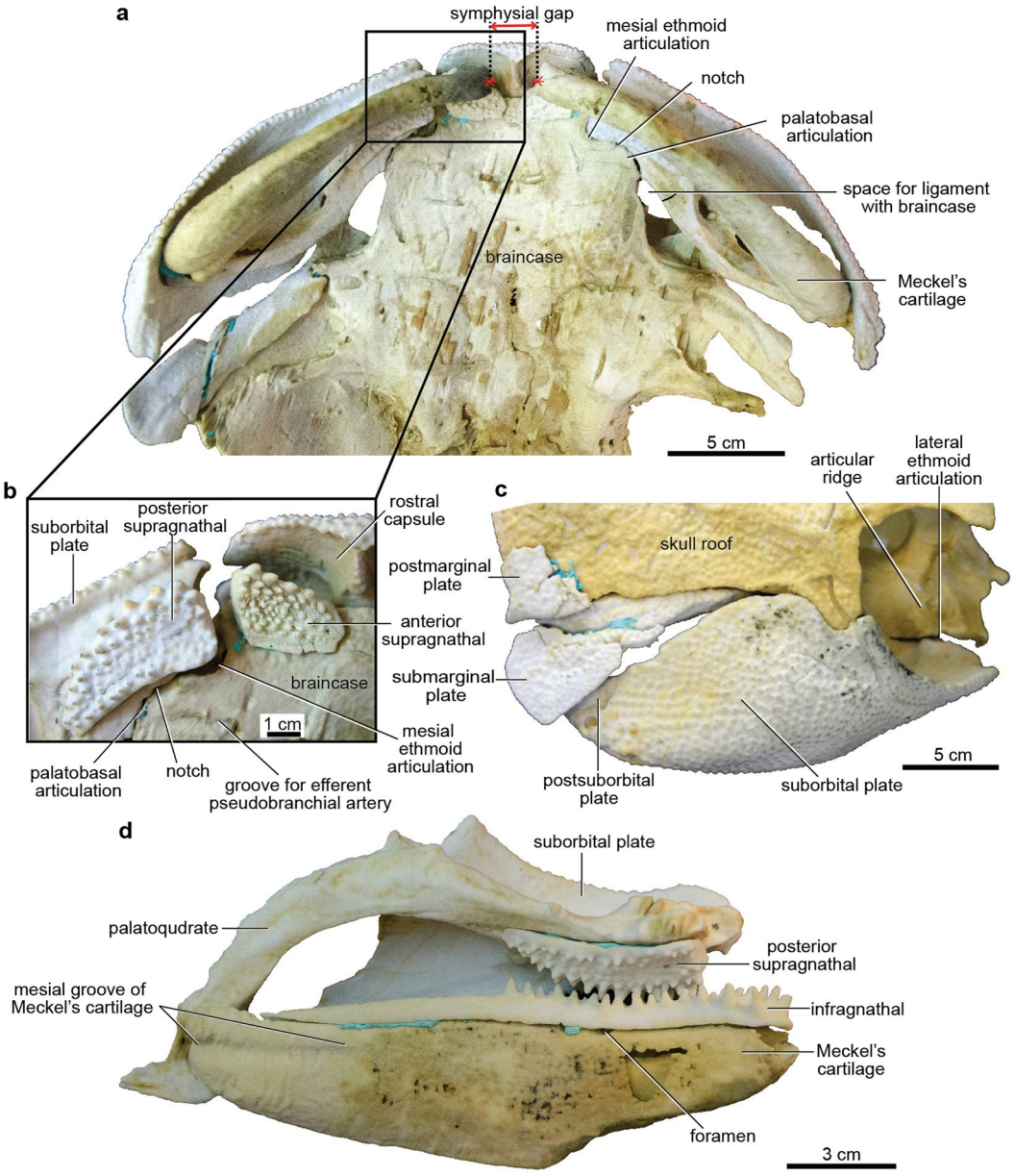

Figure 2. Articulated buchanosteid arthrodire (ANU V244) based on 3D printouts. (**a**) Ventral view of all jaw components in position against the braincase, showing a symphysial gap between left and right Meckel's cartilages. (**b**) Boxed area of (**a**), with Meckel's cartilage removed. (**c**) Dermal elements of cheek and operculum in position against the skull roof and braincase; right lateral view. (**d**) Jaw elements of left side in occlusion. 3D printouts are 6 times natural size.

with another hyoid arch element. Posterodorsally, it is continuous with a pointed dermal process projecting above the edge of the postsuborbital plate (Fig. 3a). Reassembling the cheek unit using 3D printouts shows that this process fitted under the edge of the submarginal plate (Figs 5b,c and 6b). This would have interlocked the cheek and operculum, and limited the opercular opening. We note that the holotype of *Dicksonosteus* may have had a similar arrangement, with the right postsuborbital plate clearly behind the palatoquadrate (slightly displaced), but suggesting a similar pointed dermal process projecting up inside the submarginal plate[31].

For the lower jaw, the infragnathal bone and Meckel's cartilage of both sides are preserved. The right infragnathal bone (the left previously removed and restored[13]), and both Meckel's cartilages are slightly displaced posteriorly in the specimen (Fig. 1f; Supplementary Fig. 2c). The infragnathal is a slender dermal bone with an anterior denticulate biting portion carrying two main longitudinal rows of denticles, and a slightly shorter posterior non-biting portion (Fig. 4a). A deep ventral groove (Fig. 4g) fitted over the dorsal edge of Meckel's cartilage in life. Meckel's cartilage is completely ossified perichondrally as a single element (Fig. 4b–f), a condition unrecorded for any other arthrodire. The digitally extracted left element is deepest in its anterior half, whereas the corresponding element in sharks (e.g. *Gogoselachus*[32]) is generally deepest posteriorly. A distinct lateral groove along the dorsal

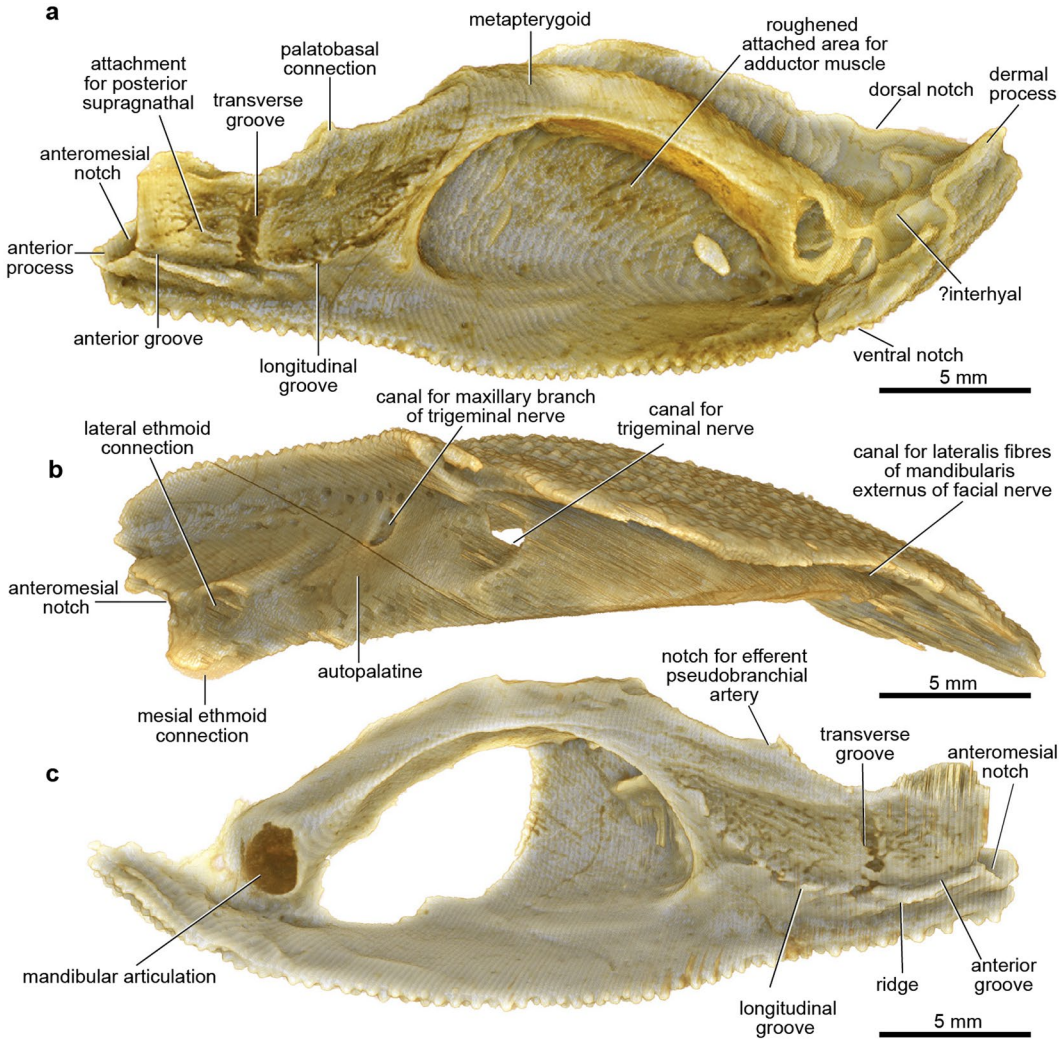

Figure 3. Dermal cheek unit with attached perichondrally ossified cartilage elements of articulated buchanosteid arthrodire (ANU V244) based on high-resolution CT. (**a**,**b**) Right suborbital and postsuborbital plates, with attached palatoquadrate and? interhyal, in internal (**a**) and dorsal (**b**) views. (**c**) Left suborbital plate (incomplete) and attached palatoquadrate in internal view.

edge (Fig. 4b), not previously recognized[13], indicates that the infragnathal extended farther back than previously restored, right to the mandibular joint, as demonstrated by 3D printouts (Fig. 2d). This also shows the massive size of Meckel's cartilage relative to the slender palatoquadrate. In contrast, most Palaeozoic elasmobranchs have the palatoquadrate of similar size or relatively larger[33]. This difference is likely due to the added strength to the upper jaw provided by the large dermal bones in placoderms.

The dorsal surface of Meckel's cartilage is notched by a diagonal groove (Fig. 4c), with a ventral thickening and notch in the corresponding position on the infragnathal (Fig. 4g). The restored lower jaw using 3D printouts (Fig. 2) shows a foramen opening into a canal that transmitted a nerve or vessel passing forwards from the mesial to the lateral side, between the dermal bone and the cartilage. Other new features of Meckel's cartilage include a ridge defining the posteroventral edge of the adductor muscle fossa on the lateral surface (Fig. 4b), also recently identified in *Gogoselachus*[32], and a mesial groove running forward from the notch between the two posterior articular surfaces (Fig. 4c). This groove extends much farther forward than previously reconstructed, with its anterior end deflected ventrally to the ventral edge of the cartilage. It may have carried the internal mandibular branch of the trigeminal nerve[13].

Mandibular joint. Assembling 3D printouts of the jaw components (Fig. 2; Supplementary Fig. 3a,b) demonstrates that the larger ventral articular surface on Meckel's cartilage formed the mandibular joint (Fig. 4e), not the dorsal articulation as previously interpreted[1,13]. The unossified mandibular articulation on the palatoquadrate (Fig. 3c) presumably contained a convex cartilaginous articular surface, given the concave shape of the corresponding articulation on Meckel's cartilage. Placing 3D printouts of the palatoquadrate and Meckel's cartilage together, with dermal gnathal elements (posterior supragnathal, infragnathal) in occlusion (Fig. 2d), shows the space beneath the arched metapterygoid part of the palatoquadrate sitting directly opposite the adductor fossa on the lateral face of Meckel's cartilage (Supplementary Fig. 2e). The 'dorsal' articular area on Meckel's cartilage

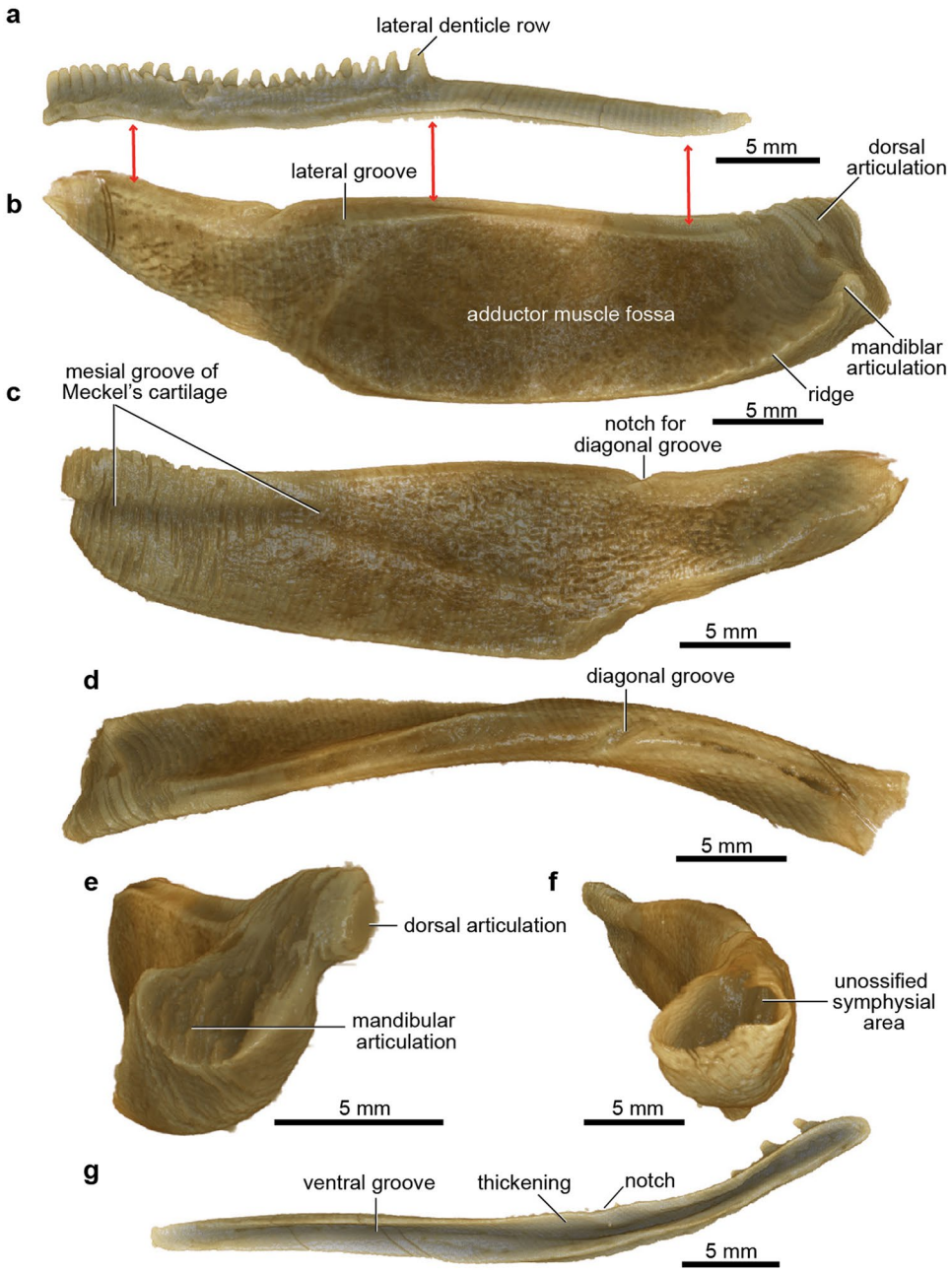

Figure 4. Lower jaw elements of articulated buchanosteid arthrodire (ANU V244) based on high-resolution CT. (**a**) Infragnathal in left lateral view. (**b**-**f**) Meckel's cartilage in left lateral (**b**), mesial (**c**), dorsal (**d**), posterior (**e**), and anterior (**f**) views. (**g**) Left infragnathal in ventral view (reversed image of extracted right element).

(Fig. 4e) projects mesially towards the skull and braincase (Fig. 5b,c). By comparison, in Gogo arthrodires there may be several articular areas on the quadrate and articular, but our specimen suggests that the mandibular joint may not always have been correctly identified, without the aid of reassembly using 3D printouts.

Jaw restoration and gnathal plate occlusion. Reassembling 3D printouts of all jaw elements against the skull and braincase (Fig. 2a) clearly demonstrates several articulations between the autopalatine and the subnasal shelf of the endocranium. The ethmoid connection of the palatoquadrate comprises two (mesial and lateral) articulations, and the anteromesial notch (Fig. 3a,c) does not contact the braincase, but sits opposite an ectethmoid notch of the subnasal shelf (Fig. 5a). The mesial ethmoid articulation on the palatoquadrate fits into a large rectangular depression on the ventral surface of the subnasal shelf (Fig. 2b; Supplementary Fig. 5), a structure not shown in previous reconstructions[14,15]. However this is in essentially the same position, and is surely homologous with the main anterior connection of the palatoquadrate in *Kujdanowiaspis*[34], and *Dicksonosteus*[27,31] (previously this has been called an 'orbital connection'[16]). The lateral ethmoid articulation (Fig. 3b) connects with the dorsal

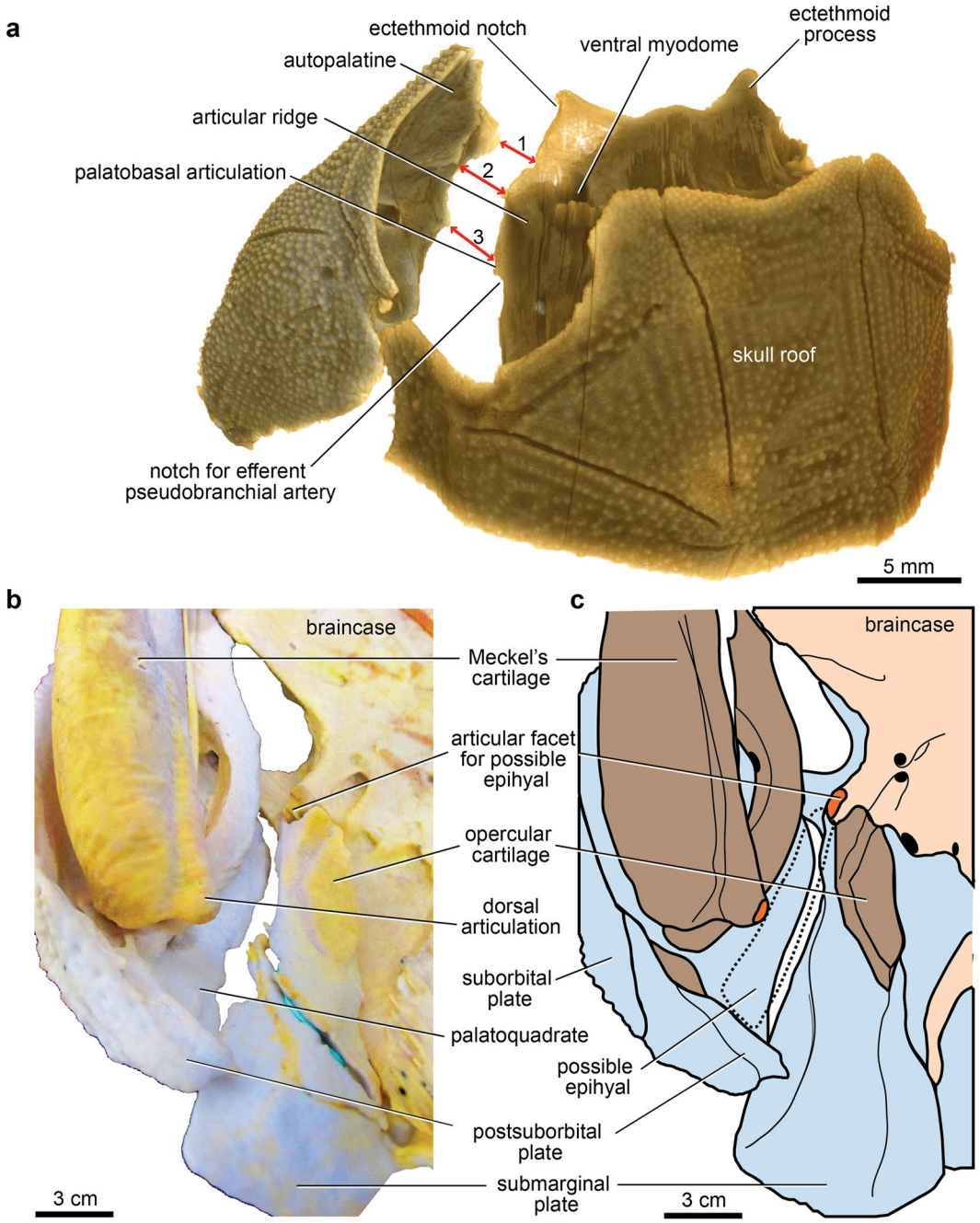

Figure 5. Jaw articulations of articulated buchanosteid arthrodire (ANU V244) based on high-resolution CT. (**a**) Dorsal view summarising articulations between the left autopalatine and subnasal shelf of the braincase (red arrows: 1, mesial articulation of ethmoid connection; 2, lateral articulation of ethmoid connection; 3, palatobasal connection). (**b**) Ventral view of assembled 3D printouts of right Meckel's cartilage, palatoquadrate, suborbital and postsuborbital plates in position against the skull and braincase. (**c**) Reconstruction based on (**b**). Light blue, dermal bones; brown, visceral arch cartilages; pale pink, braincase; orange, articular facets. 3D printouts are 6 times natural size.

surface of the subnasal shelf, where it is buttressed by an 'articular ridge' running posterolaterally from behind the ventral myodome (Figs 2c and 5a). Again this structure was not previously identified[15,16].

The single palatobasal articulation on the palatoquadrate (Fig. 3a) connects with a corresponding facet on the edge of the subnasal shelf, in front of a distinct notch at the lateral end of the ventral groove for the efferent pseudobranchial artery (Figs 5a and 6). This notch forms the anterior corner of a large space between the palatoquadrate and braincase when the two are articulated together (Figs 2a and 6b; Supplementary Fig. 2d). Possibly this space contained a ligamentous attachment to the braincase. Another notch farther forward, clearly seen on both sides to form a foramen between the palatoquadrate and braincase (Figs 2b and 6b; Supplementary Fig. 2d), separates the palatobasal from the ethmoid connection, and also transmitted an arterial branch, based on grooves

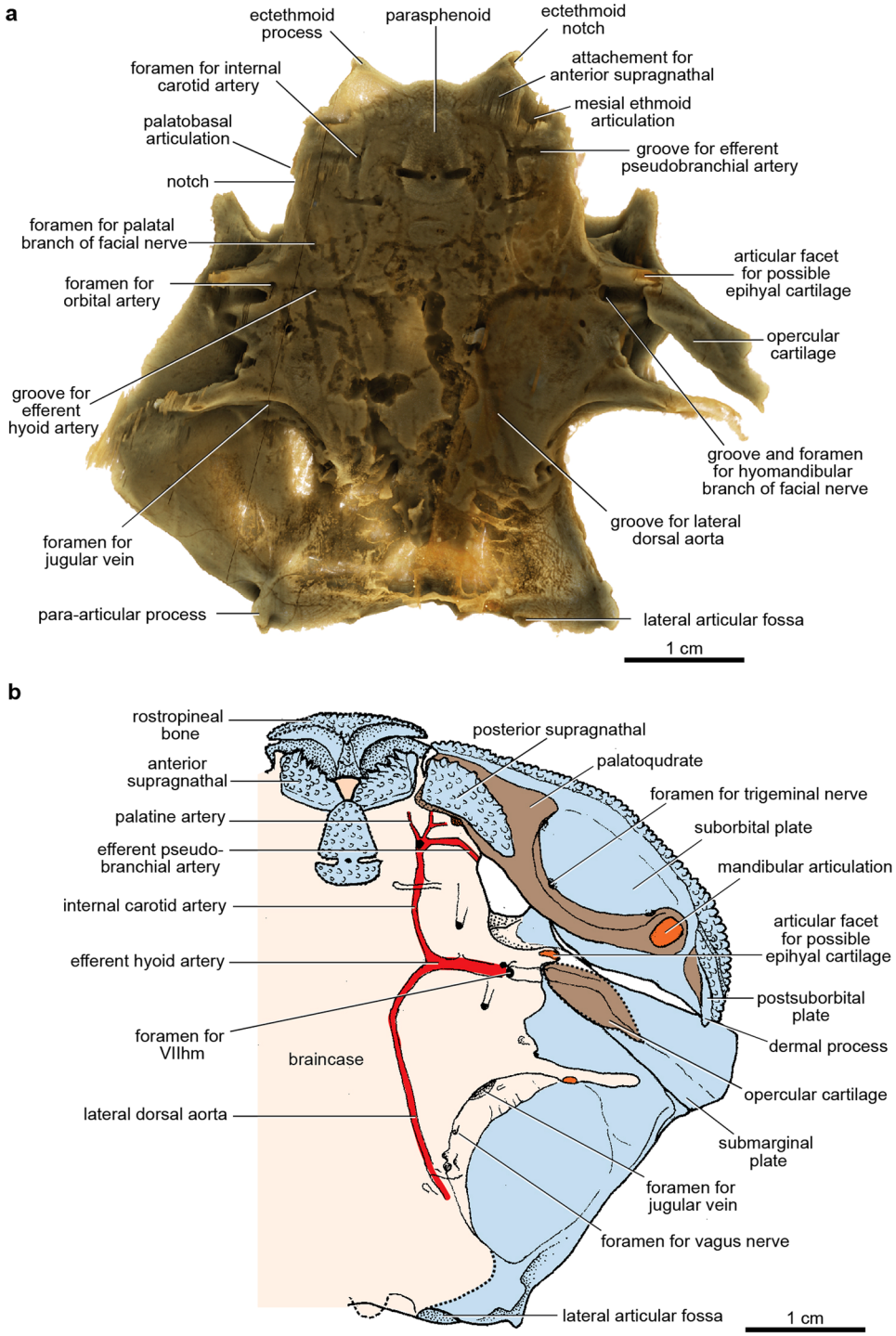

Figure 6. Braincase of articulated buchanosteid arthrodire (ANU V244) based on high-resolution CT. (**a**) Ventral view of braincase with dermal bones attached as preserved. (**b**) Reconstruction, based on 3D printouts, showing left side of skull and braincase in ventral view, with left cheek and operculum and upper gnathal elements in position. Light blue, dermal bones; brown, visceral arch cartilages; pale pink, braincase; orange, articular facets; red, blood vessels.

on the ventral braincase surface (more detail is provided in Supplementary Information). The arterial system in ANU V244 is much more complex than the pattern recently represented for '*Buchanosteus*' as a primitive gnathostome[7].

With the upper gnathal bones positioned on their clearly defined attachment surfaces, a gap remains between them (Fig. 2b); presumably this permitted some flexibility of the upper jaw against the braincase. A notch between the posterior supragnathal and the palatoquadrate (Supplementary Fig. 3c) shows that the anterior groove on the palatoquadrate (Fig. 3c) probably carried a blood vessel to the ethmoid articulation. A distinct groove behind

the ectethmoid process inside the anterior braincase margin (Fig. 6a) forms a corresponding lateral notch when the anterior supragnathal is placed on its attachment surface (Supplementary Fig. 3d). From its position, this notch probably carried a continuation of the same vessel. No equivalent notch or groove was identified in *Dicksonosteus*[27].

On all three dermal gnathal elements the lateral denticle rows are the largest. The gnathal bones are displaced in the original specimen (Supplementary Fig. 2c), but jaw reassembly using 3D printouts (Fig. 2d) shows the two main longitudinal denticle rows on the infragnathal occluded only with the larger lateral denticles of the posterior supragnathal, and along the anterior margin of the anterior supragnathal. By manipulating all jaw elements in their correct positions, a symphysial gap remains between the left and right Meckel's cartilage (Fig. 2a). Thus, the unfinished anterior end of the cartilage must have been extended as a cartilaginous (or ligamentous) connection to form the mandibular symphysis.

Dermal operculum and hyoid arch structures. The right postmarginal and submarginal plates make a good fit against the skull 3D printout (Fig. 2c). The submarginal plate broadens posteriorly, and differs in shape to that restored for *Parabuchanosteus*, which is more slender, with a posterior notch for the postmarginal corner of the skull roof[35,36]. In ANU V244 the dorsal edge of the submarginal plate shows how it connected to the skull, its broader anterior part abutting inside the ventral edge of the skull roof, and the narrow posterior edge sliding against the postmarginal plate, and projecting back behind the postmarginal corner of the skull (Figs 1a and 2c; Supplementary Fig. 2d).

A perichondrally-ossified opercular cartilage is attached inside the proximal part of the submarginal plate (Figs 5b,c and 6). It has the same structure as in the arthrodires *Arctolepis* and *Dicksonosteus*[27,31,37], and some other placoderm groups, being confined to the anterodorsal corner of the dermal operculum, with no connection to any other visceral arch element[16]. In all well-preserved examples of the placoderm opercular cartilage, including our specimen, the distal end is completely enclosed by perichondral bone. Nevertheless, that it represents a much reduced epihyal element remains a prevalent interpretation, and its articulation with the braincase has been homologised with the hyomandibular articulation in other forms[7,9].

In ANU V244, the left submarginal is in articulated position (Fig. 6a; Supplementary Fig. 2b), and for the first time in a placoderm demonstrates the groove for the hyomandibular branch of the facial nerve passing directly from its foramen onto the opercular cartilage. It crosses to its anterior edge, where lateralis fibres of the hyomandibular nerve probably branched off to enter the adjacent mandibularis externis canal on the palatoquadrate (Figs 3b and 5b,c). The proximal end of the operculum in ANU V244 does not contact the terminal articulat facet on the anterior postorbital process, which must have been for another element (see Supplementary Information).

Discussion

The palatoquadrate of *Entelognathus*[2] is interpreted to have a mesial osteichthyan-like commissural lamina enclosing the adductor fossa, but which extends forward as a 'tunnel-like anterior extension that traverses the palatoquadrate and emerges on its mesial face'[2]. This condition is unknown in osteichthyans, but was said to be similar to many arthrodires, including *Buchanosteus*. However, our new evidence indicates that this is not the condition in basal arthrodires. As described above, all canals that communicate with the adductor fossa are situated lateral to the cartilage, between it and the dermal bone, and thus do not traverse the palatoquadrate. We suggest this was the primitive condition in placoderms, and indicates the condition for basal gnathostomes.

An assumed convex articular surface for the mandibular joint on the quadrate for ANU V244 would have articulated with the corresponding concavity on Meckel's cartilage. In contrast, the mandibular joint in *Entelognathus* is described as a prearticular process and quadrate concavity, like acanthodians and chondrichthyans, and unlike the bipartite convex articulation of osteichthyans[2]. Our new evidence indicates that the early arthrodire condition resembled that of osteichthyans.

The dermal cheek unit comprises a large suborbital plate anteriorly and a smaller postsuborbital plate posteriorly in most arthrodires (Supplementary Fig. 4). However, in the 'maxillate' placoderms, additional bones equivalent to the maxilla and premaxilla of osteichthyans have been identified[2,3]. The main cheek bone (suborbital plate) has been homologised with the jugal of osteichthyans, and the postsuborbital has been compared with the osteichthyan quadratojugal. Some insights on these homologies are provided by a consideration of the cartilage attachments inside the dermal bones of the cheek.

Typical arthrodires like *Eastmanosteus* (Supplementary Fig. 4a,d) have the autopalatine and metapterygoid parts of the palatoquadrate attached inside the dermal suborbital plate, whilst the quadrate portion is fused to the inside of the postsuborbital plate[21,38,39]. However, our new evidence of the buchanosteid palatoquadrate shows the mandibular joint (signifying the quadrate part of the palatoquadrate) located inside the suborbital plate, with another separately ossified cartilage, compared above with the osteichthyan interhyal, situated inside the postsuborbital plate (Supplementary Fig. 4b). This evidence raises questions about the homology of a small posterior bone in the cheek complex in *Entelognathus*, suggested to be equivalent both to the placoderm postsuborbital, and the quadratojugal of osteichthyans, on the assumption that these bones sat outside the mandibular joint[2].

Further investigation is needed, as this small posterior dermal bone is not identified in the dermal cheek of the second maxillate placoderm *Qilinyu*[3]. Also, the restoration of *Dicksonosteus*[31] suggests an intermediate condition, with the quadrate articulation straddling the suborbital-postsuborbital dermal bone boundary (Supplementary Fig. 6b). An anterior shift in the position of the *Dicksonosteus* quadrate was argued as necessary to achieve the condition in phyllolepid placoderms[40], but they used the hypophysial foramen as a landmark, and assumed that a palatobasal connection was unknown in placoderms. However, this connection, described above, is present in several groups[16], even if more anteriorly placed than in osteichthyans.

An incomplete postsuborbital plate with part of the 'quadrate' attached was identified for *Dicksonosteus*, suggesting that the quadrate was separately ossified, as previously assumed for *Romundina*[27]. As preserved, that

specimen shows no distinguishing features of the quadrate ossification, and we suggest this could possibly be a separately ossified cartilage behind the palatoquadrate with the mandibular joint confined to the suborbital plate, as in ANU V244. We consider that the cheek unit in *Dicksonosteus* and other basal arthrodires, even if carefully described previously, could be reinvestigated in the light of the new evidence provided here.

The position of this separate cartilage (Supplementary Fig. 4b) suggests comparison with the interhyal of osteichthyans, a separate element of the hyoid arch immediately behind the palatoquadrate, invariably linking it with the hyomandibula and ceratohyal. The interhyal was proposed as an osteichthyan synapomorphy[41]. Recent analyses[2,3,25] have assumed the interhyal was absent in placoderms, based on the hyoid arch of ptyctodontids, where a possible interhyal[42] has been re-interpreted as a ceratohyal[43,44]. This character needs re-investigation for other placoderms, and the new evidence of ANU V244 demonstrates that there was an accessory element of the hyoid arch in basal arthrodires, which we propose as equivalent to the interhyal of osteichthyans.

Some ideas on recently suggested homologies between the gnathal elements of placoderms and the marginal tooth-bearing bones of osteichthyans arise from a consideration of the ethmoid connection between the palatoquadrate and the braincase. ANU V244 demonstrates there are two ethmoid articulations. The mesial articulation, located on the braincase floor just behind the attachment area for the anterior supragnathal (Fig. 6b), is comparable to the position of the ethmoid articulation in various osteichthyans, located posterolateral to the vomer (e.g. *Youngolepis*[45]). Such similarities formed the basis for proposing homology between the anterior supragnathal and the osteichthyan vomer[34]. However, the evidence of the 'maxillate' placoderm *Qilinyu* has suggested an alternative homology, to the osteichthyan premaxilla[3].

The dermal submarginal plate of placoderms is clearly the functional equivalent of the opercular dermal bones of osteichthyans, because various Early Devonian forms (e.g. *Bryantolepis*, *Dicksonosteus*, *Romundina*, *Wuttagoonaspis*) show that it was only loosely attached to the skull, as a movable operculum over the branchial region[16,27,46]. Within arthrodires the operculum undergoes major transformation, from a more ovate bone positioned behind the cheek in most Early Devonian forms, in Late Devonian eubrachythoracid arthrodires becoming an elongate element attached above and suspending the suborbital complex to take over the opercular function[1].

In *Holonema*, a perichondrally ossified structure attached inside the ovate submarginal plate was interpreted as an 'opercular cartilage', whilst that inside the elongate submarginal in *Torosteus* was interpreted as an elongate cartilaginous epihyal or hyomandibula[21,30] (but we consider the opercular cartilage of *Torosteus* is incomplete; see Supplementary Information). A similar interpretation was proposed to restore an elongate epihyal in ptyctodontid placoderms from Gogo[42], but the Gogo ptyctodontid *Materpiscis* now shows that interpretation also to be unreliable. *Materpiscis* has two separate perichondrally-ossified cartilages in this region: a small opercular cartilage inside the proximal end of the submarginal plate, and a vertically oriented epihyal, with which the opercular cartilage was evidently in articulation[42]. This supports the view that the opercular cartilage of placoderms is not homologous to the epihyal[16].

The alternative interpretation[30,40], that the placoderm opercular cartilage is a reduced epihyal, forms the basis for homology with the hyomandibular articulation of osteichthyans[7,9]. *Entelognathus*, which combines various osteichthyan and placoderm features, has a partially exposed elongate crescentic dermal 'opercular' bone homologised with the placoderm submarginal plate, also with a small internal opercular cartilage[2], essentially as described above. Our new evidence demonstrates two separate articular areas on the anterior postorbital process in buchanosteids. The position of the opercular cartilage connection is very similar to that restored for *Dicksonosteus*[27,31]. The extra articulation (Supplementary Fig. 2b), previously identified as for the opercular cartilage (Supplementary Fig. 6a), must be for an additional element, because an otic connection with the palatoquadrate, as interpreted for *Dicksonosteus*[31] and *Romundina*[4], is not possible when 3D printouts are reassembled (Fig. 5b,c). A clear gap between the palatoquadrate and this articulation could have accommodated an additional unossified epihyal element (Fig. 5c), contrary to the previous claim that 'there is no room to insert a further element' in that position[30]. The 3D printouts also show that the extra dorsal articulation on Meckel's cartilage could have contacted this unossified element (Fig. 5b,c).

The new evidence from this articulated placoderm (ANU V244) reveals much more complexity regarding composition and articulation of the hyoid arch, shown to be key characters in resolving placoderms as either monophyletic or paraphyletic[9]. For the first time, we establish jaw morphology and functional connections of the jaw cartilages to the braincase, using the evidence of the position of major cranial nerves and vessels to confirm homologies with other groups. Such information can only be ascertained from this unique articulated arthodire, making it a key taxon for resolving basal gnathostome relationships.

Material and Methods

Scanning was done on two machines developed and built in the Department of Applied Mathematics, ANU[47,48]. The scanning data was 3D rendered and segmented using the programs *Drishti 2.5* and *DrishtiPaint* (http://nci.org.au/nci-systems/scientific-visualisation/visualisation-services/) and separate components of the head skeleton were printed at 6 times natural size on a ZPrinter 650. More detail is given in Supplementary Information.

The 3D format files of the infragathal, Meckel's cartilage and suborbital, and a movie showing the posterior supragnathal, infragathal and suborbital plate in position are available on NCI (National Computational Infrastructure, Australia) Catalogue: http://dx.doi.org/10.4225/41/5978116a9e671.

References

1. Young, G. C. Placoderms (armored fish): dominant vertebrates of the Devonian Period. *Annu. Rev. Earth Planet. Sci.* **38**, 523–550, doi:10.1146/annurev-earth-040809-152507 (2010).
2. Zhu, M. *et al.* A Silurian placoderm with osteichthyan-like marginal jaw bones. *Nature* **502**, 188–193, doi:10.1038/nature12617 (2013).
3. Zhu, M. *et al.* A Silurian maxillate placoderm illuminates jaw evolution. *Science* **354**, 334–336, doi:10.1126/science.aah3764 (2016).

4. Dupret, V., Sanchez, S., Goujet, D., Tafforeau, P. & Ahlberg, P. E. A primitive placoderm sheds light on the origin of the jawed vertebrate face. *Nature* **507**, 500–503, doi:10.1038/nature12980 (2014).
5. Long, J. A. *et al*. Copulation in antiarch placoderms and the origin of gnathostome internal fertilization. *Nature* **517**, 196–199, doi:10.1038/nature13825 (2015).
6. Brazeau, M. D. & Friedman, M. The origin and early phylogenetic history of jawed vertebrates. *Nature* **520**, 490–497, doi:10.1038/nature14438 (2015).
7. Giles, S., Friedman, M. & Brazeau, M. D. Osteichthyan-like cranial conditions in an Early Devonian stem gnathostome. *Nature* **520**, 82–85, doi:10.1038/nature14065 (2015).
8. Qiao, T., King, B., Long, J. A., Ahlberg, P. E. & Zhu, M. Early gnathostome phylogeny revisited: multiple method consensus. *PLoS One* **11**, e0163157, doi:10.1371/journal.pone.0163157 (2016).
9. King, B., Qiao, T., Lee, M. S. Y., Zhu, M. & Long, J. A. Bayesian morphological clock methods resurrect placoderm monophyly and reveal rapid early evolution in jawed vertebrates. *Syst. Biol.* **2016**, syw107, doi:10.1093/sysbio/syw107 (2016).
10. Rücklin, M. *et al*. Development of teeth and jaws in the earliest jawed vertebrates. *Nature* **491**, 748–751, doi:10.1038/nature11555 (2012).
11. Rucklin, M. & Donoghue, P. C. *Romundina* and the evolutionary origin of teeth. *Biol. Lett.* **11**, 20150326, doi:10.1098/rsbl.2015.0326 (2015).
12. Burrow, C., Hu, Y.-Z. & Young, G. C. Placoderms and the evolutionary origin of teeth: a comment on Rücklin & Donoghue (2015). *Biol. Lett.* **12**, 20160159, doi:10.1098/rsbl.2016.0159 (2016).
13. Young, G. C., Lelièvre, H. & Goujet, D. Primitive jaw structure in an articulated brachythoracid arthrodire (placoderm fish; Early Devonian) from southeastern Australia. *J. Vertebr. Paleontol.* **21**, 670–678 (2001).
14. Long, J. A., Mark-Kurik, E. & Young, G. C. Taxonomic revision of buchanosteoid placoderms (Arthrodira) from the Early Devonian of south-eastern Australia and Arctic Russia. *Aust. J. Zool.* **62**, 26–43, doi:10.1071/ZO13081 (2014).
15. Young, G. C. New information on the structure and relationships of *Buchanosteus* (Placodermi: Euarthrodira) from the Early Devonian of New South Wales. *Zool. J. Linn. Soc.* **66**, 309–352 (1979).
16. Young, G. C. The relationships of placoderm fishes. *Zool. J. Linn. Soc.* **88**, 1–57 (1986).
17. Zhu, Y.-A. & Zhu, M. A redescription of *Kiangyousteus yohii* (Arthrodira: Eubrachythoraci) from the Middle Devonian of China, with remarks on the systematics of the Eubrachythoraci. *Zool. J. Linn. Soc.* **169**, 798–819, doi:10.1111/zoj.12089 (2013).
18. Zhu, Y.-A., Zhu, M. & Wang, J.-Q. Redescription of *Yinostius major* (Arthrodira: Heterostiidae) from the Lower Devonian of China, and the interrelationships of Brachythoraci. *Zool. J. Linn. Soc.* **176**, 806–834, doi:10.1111/zoj.12356 (2016).
19. Janvier, P. *Early Vertebrates*. (Clarendon, 1996).
20. Lelièvre, H., Janvier, P. & Goujet, D. Les vertébrés Dévoniens de l'Iran central. IV. Arthrodires et ptyctodontes. *Geobios* **14**, 677–709 (1981).
21. Miles, R. S. The Holonematidae (placoderm fishes), a review based on new specimens of *Holonema* from the Upper Devonian of western Australia. *Philos.Trans.R.Soc.London, Ser.B* **263**, 101–234 (1971).
22. Ørvig, T. in *Problèmes actuels de Paléontologie-Evolution des Vertébrés* Vol. 218 (ed. Lehman, J. P.) 41–71 (Colloques Internationaux du Centre National de la Recherche Scientifique, 1975).
23. Young, G. C. Reconstruction of the jaws and braincase in the Devonian placoderm fish *Bothriolepis*. *Palaeontology* **27**, 635–661 (1984).
24. Lelièvre, H., Janvier, P., Janjou, D. & Halawani, M. *Nefudina qalibahensis* nov. gen., nov. sp. un rhenanide (Vertebrata, Placodermi) du Dévonien inférieur de la formation Jauf (Emsien) d'Arabie Saoudite. *Geobios M. S.* **18**, 109–115 (1995).
25. Davis, S. P., Finarelli, J. A. & Coates, M. I. *Acanthodes* and shark-like conditions in the last common ancestor of modern gnathostomes. *Nature* **486**, 247–250, doi:10.1038/nature11080 (2012).
26. Northcutt, R. G. in *The Mechanosensory Lateral Line: Neurobiology and* Innervartion. (eds Coombs, S., Görner, P. & Münz, H.) 17–78 (SpringerVerlag, 1989).
27. Goujet, D. F. Les poissons placodermes du Spitsberg. Arthrodires Dolichothoraci de la Formation de Wood Bay (Dévonien inférieur) (CNRS, 1984).
28. Allis, E. P. The cranial anatomy of *Polypterus*, with special reference to *Polypterus bichir*. *J. Anat.* **56**, 190–294 (1922).
29. Allis, E. P. The cranial anatomy of *Chlamydoselachus anguineus*. *Acta Zool.* **4**, 123–221 (1923).
30. Gardiner, B. G. & Miles, R. S. A new genus of eubrachythoracid arthrodire from Gogo, Western Australia. *Zool. J. Linn. Soc.* **99**, 159–204 (1990).
31. Goujet, D. F. in *Problèmes actuels de Paléontologie-Evolution des Vertébrés* Vol. 218 (ed. Lehman, J. P.) 81–99 (CNRS, 1975).
32. Long, J. A. *et al*. First Shark from the Late Devonian (Frasnian) Gogo Formation, Western Australia Sheds New Light on the Development of Tessellated Calcified Cartilage. *PLoS One* **11**, e0126066, doi:10.1371/journal.pone.0126066 (2015).
33. Zangerl, R. in *Handbook of Paleoichthyology*. Volume 3A: Chondrichthyes I. Paleozoic Elasmobranchii. (ed. Schultze, H-P) 1–115 (Gustav Fischer, 1981).
34. Stensiö, E. A. Anatomical studies on the arthrodiran head. Part 1. Preface, geological and geographical distribution, the organization of the head in the Dolichothoraci, Coccosteomorphi and Pachyosteomorphi. Taxonomic appendix. *Kungl. Svenska Vetenskap. Hand.* **9**, 1–419 (1963).
35. White, E. I. & Toombs, H. A. The buchanosteid arthrodires of Australia. *Bull. Brit. Mus. (Nat. Hist.), (Geol.)* **22**, 379–419 (1972).
36. White, E. I. The larger arthrodiran fishes from the area of Burrinjuck Dam, N.S.W. *Trans. R. Soc. Lond. B Biol. Sci.* **34**, 149–262 (1978).
37. Goujet, D. Nouvelles observations sur la joue d'*Arctolepis* (Eastman) et d'autres Dolichothoraci. *Annls. Paléont.* **58**, 3–11 (1972).
38. Edgeworth, F. H. *The cranial muscles of vertebrates*. (Cambridge University, 1935).
39. Miles, R. S. Features of placoderm diversification and the evolution of the arthrodire feeding mechanism. *Trans. R. Soc. Edinb. Earth Sci.* **68**, 123–170 (1969).
40. Carr, R. K., Johanson, Z. & Ritchie, A. The phyllolepid placoderm *Cowralepis mclachlani*: Insights into the evolution of feeding mechanisms in jawed vertebrates. *J. Morphol.* **270**, 775–804, doi:10.1002/jmor.10719 (2009).
41. Gardiner, B. G. The relationships of the palaeoniscid fishes, a review based on new specimens of *Mimia* and *Moythomasia* from the Upper Devonian of Western Australia. *Bull. Br. Mus. Nat. Hist. Geol.* **37**, 173–428 (1984).
42. Long, J. A. Ptyctodontid fishes (Vertebrata, Placodermi) from the Late Devonian Gogo Formation, Western Australia, with a revision of the European genus *Ctenurella* Ørvig, 1960. *Geodiversitas* **19**, 515–555 (1997).
43. Forey, P. L. & Gardiner, B. G. Observations on *Ctenurella* (Ptyctodontida) and the classification of placoderm fishes. *Zool. J. Linn. Soc.* **86**, 43–74 (1986).
44. Trinajstic, K., Long, J. A., Johanson, Z., Young, G. & Senden, T. New morphological information on the ptyctodontid fishes (Placodermi, Ptyctodontida) from Western Australia. *J. Vertebr. Paleontol.* **32**, 757–780, doi:10.1080/02724634.2012.661379 (2012).
45. Chang, M.-M. The braincase of *Youngolepis*, a Lower Devonian Crossopterygian from Yunnan, South-western China Thesis, Stockholm Univ. (1982).
46. Denison, R. H. in *Handbook of Paleoichthyology* Volume 2: Placodermi (ed. Schultze, H-P) 1–128 (Gustav Fischer, 1978).
47. Evans, P. D. *et al*. Visualizing the micro-distribution of zinc borate in oriented strand board using X-ray micro-computed tomography and SEM-EDX. *J. Compos.* **2015**, doi:10.1155/2015/630905 (2015).
48. Sheppard, A. *et al*. Techniques in helical scanning, dynamic imaging and image segmentation for improved quantitative analysis with X-ray micro-CT. *Nucl. Instr. Meth. Phys. Res.* **324**, 49–56 (2014).

Acknowledgements

We thank T. Senden for provision of facilities, CT scanning, and general support for palaeobiological research at ANU; M. Turner for other CT scanning and laboratory support; A. Limaye for assistance in using *Drishti*, and development of the program to improve processing of fossil data; C. Wang for assistance imaging 3D printouts; E. Jewett-Hall for advice on illustration preparation; I. Thompson for providing the specimen; and Y. Zhu and B. King for helpful discussions. This research has been funded by Australian Research Council Discovery grants DP1092870 and DP140104161. J.L. was supported by the National Natural Science Foundation of China (41472016), and by a Director's strategic postdoctoral fellowship in the ANU Research School of Physics & Engineering.

Author Contributions

G.C.Y. designed the project. Y.H., G.C.Y. and J.L. performed the research. Y.H. performed C.T. restorations, digital dissections, and 3D printouts. Figures were produced by J.L., Y.H. and G.C.Y. All authors discussed the results and prepared the manuscript.

Additional Information

Supplementary information accompanies this paper at doi:10.1038/s41598-017-07674-y

Competing Interests: The authors declare that they have no competing interests.

Publisher's note: Springer Nature remains neutral with regard to jurisdictional claims in published maps and institutional affiliations.

Appendix C Supplementary pdf for Hu et al. 2017 (Paper 2)

Hu, Y., Lu, J., Young, G.C., 2017. Supplementary material from “New findings in a 400 million-year-old Devonian placoderm shed light on jaw structure and function in basal gnathostomes.” Sci. Rep. 7. https://static-content.springer.com/esm/art%3A10.1038%2Fs41598-017-07674-y/MediaObjects/41598_2017_7674_MOESM1_ESM.pdf

Supplementary materials for

New findings in a 400 million-year-old Devonian placoderm shed light on jaw structure and function in basal gnathostomes

Yuzhi Hu[1,2,+], Jing Lu[1,3,+] and Gavin C. Young[1,*]

[1] *Department of Applied Mathematics, Research School of Physics and Engineering, Oliphant Building 60, Australian National University, Canberra, ACT, Australia 2601*

[2] *Research School of Earth Sciences, Building 142 Mills Road, Australian National University, Canberra, ACT, Australia 2601*

[3] *Key Laboratory of Vertebrate Evolution and Human Origins of Chinese Academy of Sciences, Institute of Vertebrate Paleontology and Paleoanthropology, Chinese Academy of Sciences, Beijing, China 100044*

[*] *To whom correspondence should be addressed: gavin.young@anu.edu.au*

[+] *these authors contributed equally to this work*

This supplementary Information includes:

Supplementary Notes

Supplementary Figures

Supplementary References

Supplementary Notes

Geological provenance, specimen locality data, and repository

The largest exposure of Early Devonian limestones in southern New South Wales occurs in two separate outcrops around Lake Burrinjuck, a man-made reservoir on the Murrumbidgee River about 50 km NW of Canberra (Supplementary Fig. 1a). Specimen ANU V244 was found by Mr Ian Thompson in 1977, preserved in a small limestone nodule. The fossil locality is near 'Shearsby's Wallpaper', a reserved heritage fossil site in the eastern limestone outcrop ~2.5 km downstream from Taemas Bridge (Supplementary Fig. 1b). The stratigraphic level is within the '*Spirifer' yassensis* Member of the Taemas Formation (Supplementary Fig. 1c). Conodont dating shows the Pragian-Emsian boundary occurs within the underlying Cavan Limestone, and the upper limestones of the Taemas Formation are within the Emsian *serotinus* zone[1], so the fossil horizon lies within the Emsian stage of the Early Devonian. The Shearsby's Wallpaper site has produced other significant specimens, including the second skull of the lungfish *Dipnorhynchus*[2,3], as well as the only previously described example of the buchanosteid palatoquadrate[4].

With a vertebrate faunal list of some 62 genera and 70 species, the Burrinjuck fossil fish assemblage is the most diverse fossil fish fauna known from the Devonian, and also the oldest coral reef fish assemblage from the fossil record[1].

Institutional abbreviations

Institutional abbreviations for registered specimens are: ANU, College of Science, The Australian National University, Canberra, ACT; WAM, Western Australian Museum, Perth, WA.

Taxonomy

ANU V244 was previously referred to as a 'new buchanosteid'[6], a member of a complex of small to medium-sized arthrodires from the Burrinjuck fossil fish locality[7]. The genus *Buchanosteus* was erected[8] for a skull specimen from Early Devonian limestones of Buchan, Victoria, first named as '*Coccosteus osseus*'[9]. New species and genera have been documented from the Early Devonian limestones of southeastern Australia[7,10,11], and isolated skulls and other bones are known from rocks of similar age in Russia, Saudi Arabia, and China[12-14]. The superfamily Buchanosteoidea [15] was recently redefined[7] to contain two families (Buchanosteidae, Parabuchanosteidae), with two new buchanosteid species and genera: *Richardosteus barwickorum* and *Urvaspis lithuanica*. The specimen used in this study (ANU V244) belongs to the Buchanosteoidea, but its precise species and relation to other described taxa is not yet established. It displays numerous morphological features unknown in other fossils, and is the only known specimen showing the dermal bones of the cheek associated with the skull roof and braincase (Fig. 1). However the median dorsal and anterior dorsolateral plates of the trunk-armour are missing, and the overlaps on the latter were used to define the family Parabuchanosteidae[7].

We note that the parasphenoid of ANU V244 has the same shape as in *Buchanosteus confertituberculatus*, with transverse grooves that are widely open laterally (Supplementary Fig. 5) as diagnosed for the family Buchanosteidae[7]. In addition, ANU V244 lacks a subpituitary fenestra, like *Buchanosteus confertituberculatus*[7,9], whereas this opening is well developed in *Parabuchanosteus*[4,10]. Furthermore, the dermal opercular bone (submarginal plate) has a different shape to the isolated bone that was referred to *Parabuchanosteus*[10], and the postmarginal plate forming the lateral corner of the skull is a small triangular bone, in this respect resembling *Buchanosteus* rather than *Parabuchanosteus*[7]. However, the ridges on the lateral trunk-armour plates are absent in the trunk-armour specimen referred to *Buchanosteus confertituberculatus*[7]. For these reasons we consider that ANU V244 is probably a new taxon within the family Buchanosteidae, and it is referred to in the text as a 'buchanosteid'.

The genus *Buchanosteus* has been scored as a basal arthrodire in data matrices supporting various gnathostome phylogenies, but the described morphology[4] derives from a range of incomplete specimens including some earlier described as *Parabuchanosteus*[10], on the assumption there was only one genus (*Buchanosteus*) in one family[4]. However, with at least three genera in two families now recognised from SE Australia[7], and many new specimens indicating greater diversity, the morphology used in phylogenetic analyses is considered a composite of closely related forms, so we have referred to the taxon as '*Buchanosteus*'.

Specimen preparation

ANU V244 was partly acid-etched from the limestone matrix using formic acid by G.C.Y. in Paris in 1999 (laboratory of the Muséum national d'Histoire naturelle). In this process some of the jaw elements were detached and studied in detail[6]. However, the major morphological features in the inner parts of this fragile and unique specimen were not accessible until new techniques of micro-CT scanning became available.

Micro-CT scanning

ANU V244 was scanned in 10/9/2011 and 15/4/2015 on instruments developed and built at the ANU Department of Applied Mathematics. The 2011 XCT scan used an instrument with a 80kV/110uA reflection-style X-ray source and 2 mm thick silicon dioxide filter. The specimen was placed 72 mm from the source, and the detector positioned 350 mm from the source. The specimen was imaged through 360 degrees rotation. Reconstruction was based on 2880 radiographic projections formed on a 2048 × 2048 Perkin Elmer Flat Panel camera. The 2015 rescan used a new double-helix HeliScan CT Scanner with higher resolution and a new algorithm to process and reconstruct CT data. 1.2 mm aluminium and 0.35 mm stainless steel filters were used, with specimen distance 85 mm from the source, and detector position 396 mm from the source, and probed separately with a polychromatic X-ray beam (Bremsstrahlung radiation). Accelerating voltage of the electron beam generating the Bremsstrahlung radiation was 110kV with a current of 100μA. A series of X ray transmission

radiographs, collectively called the projection data, were acquired by the detector as the specimen was rotated through 360 degrees double-helically over a period of 18 hours. Reconstruction was based on 2520 radiographic projections formed on a 2048 × 1538 Varian Flat Panel camera.

Visualization, segmentation, 3D rendering

XCT scanning data was processed using the program *Drishti 2.5* (see http://nci.org.au/nci-systems/scientific-visualisation/visualisation-services/) developed to visualize 3D tomography and electron-microscopy data. Segmentation of the separate components (rostral capsule, postethmoid skull and braincase, optic capsules, jaw and cheek elements, toothplates) was undertaken using *DrishtiPaint* on 1589 slices from the 2011 scan. The 'suborbital complex' (dermal cheek unit with attached perichondrally ossified upper jaw cartilages) was also re-segmented from the 2015 data set.

The final output was sent to a ZPrinter 650 in Stanford Triangle Format (. ply). Additive manufacturing technology creates a printout by successive layering of cross-sectional slices from the tomographic data (layer thickness 0.1 mm). The printouts are built from powdered gypsum and then strengthened with cyanoacrylate resin. Elements were printed separately, enlarged by a factor of 6 for detailed investigation of the morphological fit between the various skull and jaw components. Of the paired upper gnathal elements, only one anterior supragnathal was preserved, so an opposite element was produced by reversing the CT data. The other gnathal elements (posterior supragnathal, infragnathal), and the jaw cartilages, all showed essentially identical morphology between left and right sides.

Additional notes on morphology

Supplementary Figs 2-4 illustrate more detail on reassembly of jaw elements, their attachments to the braincase, and relationship to the opercular unit (submarginal plate plus opercular cartilage).

The incomplete left submarginal plate and opercular cartilage are preserved with the proximal end still in articulation against the anterior postorbital process of the braincase (Supplementary Fig. 2b). For the first time in a placoderm, this demonstrates the groove for the hyomandibular branch of the facial nerve passing directly from its foramen onto the opercular cartilage, the groove crossing to its anterior edge. From this point, lateralis fibres of the hyomandibular nerve probably branched off to enter the adjacent mandibularis externis canal on the palatoquadrate. Distally the groove deflects back to the posterior edge of the cartilage (see also Figs. 5b, c; 6a). The efferent hyoid artery passed laterally from the anterior postorbital process[4,16], and is also represented by a strong groove in ANU V244 (Fig. 6; Supplementary Fig. 5). This artery may have also occupied the grooves shown on the opercular cartilage. By comparison, in early osteichthyans (e.g. *Eusthenopteron*)[17] two nerves (r. mandibularis VII, r. mandibularis lateralis) and a hyoid vein are also restored to pass down the hyoid arch.

The opercular cartilage in ANU V244 is forked to enclose the base of the anterior postorbital process, the dermal bone wrapping around it anteriorly, and the cartilage posteriorly (Supplementary Fig. 2b). Neither is in contact with the extra (terminal) articular facet on the end of the anterior postorbital process, previously interpreted for '*Buchanosteus*' as either for the opercular cartilage[4] (Supplementary Fig. 6a), or called the hyomandibular articulation[18]. This new evidence demonstrates two separate articular surfaces on the anterior postorbital process, a condition previously recognized in only a few other arthrodires[19,20]. In those instances the terminal articular surface was assumed to contact the palatoquadrate in an 'otic' connection, as restored for *Dicksonosteus* (Supplementary Fig. 6b).

In ANU V244 this terminal articulation is a flat articular facet, elongated in the direction of the long axis of the opercular cartilage, but facing ventrolaterally, so contact with the opercular cartilage was impossible (Supplementary Fig. 2b). Although close together, any consideration that the two articulations could have received a single element like the 'double-headed' hyomandibula of sarcopterygians (e.g. *Eusthenopteron*[17]) can be discounted. However, this is a possible interpretation for *Romundina*, where adjacent articular areas on the posterior face of the anterior postorbital process have been attributed to hyoid arch elements[21]. Various other placoderms show two separate articulations associated with the exit of the hyomandibular nerve from the braincase, that anterior to the nerve foramen interpreted as for the hyomandibula[22], or for an otic process of the palatoquadrate[19,21]. However, reassembly of 3D printouts for our specimen also demonstrates that the extra articulation could not have contacted the palatoquadrate (Supplementary Fig. 2d). By comparison, in the arthrodire *Dicksonosteus*, and in some *Kujdanowiaspis* specimens[16], there is only a single keyhole-like articulation on the posterior side of the anterior postorbital process. This corresponds precisely to the opercular cartilage articulation as preserved on the right side of ANU V244 (Supplementary Fig. 5).

The opercular cartilage in ANU V244 is clearly a closed structure, in contrast to the description of the Gogo arthrodire *Torosteus*, where this element was interpreted as open-ended, with an unossified continuation to the distal end of the submarginal plate. On that basis it was interpreted as an epihyal rather than an opercular cartilage[23]. However we consider the structure in *Torosteus* is incomplete distally, with a broken end (G.C.Y., personal observation of WAM 88.2.7). We suggest therefore that the opercular cartilage in *Torosteus* was also completely closed by perichondral bone, as demonstrated in our specimen, and other Early Devonian arthrodires (e.g. *Arctolepis*, *Dicksonosteus*), precluding any distal cartilaginous extension.

The clarification of the mandibular joint position (Supplementary Fig. 3a, b) is based on fitting the dermal gnathal elements to the palatoquadrate and Meckel's cartilage, and then placing them in occlusion. The dermal cheek complex of the Gogo arthrodire *Eastmanosteus*[24] is used to exemplify the typical position of the quadrate ossification on the postsuborbital plate (Supplementary Fig. 4a, d). On the assumption that this was a general placoderm condition, the perichondral ossification inside the suborbital plate of *Romundina* was interpreted to comprise only the autopalatine and

metapterygoid, and the quadrate was assumed to be separately ossified, and fused to the inside of the postsuborbital plate (both elements unknown)[22,25]. We present a re-interpretation of the *Romundina* palatoquadrate (Supplementary Fig. 4e) to revise the previous interpretation[22], on the assumption of similar morphology to that revealed by ANU V244, with the palatoquadrate restricted to the dermal suborbital plate.

Romundina displays the primitive 'omega' shape for the placoderm palatoquadrate[26], which was based on the Gogo arthrodire *Holenema*, at that time the only one showing a completely ossified palatoquadrate[27]. This was contrasted with a generally 'cleaver-shaped' palatoquadrate in various other groups (acanthodians, chondrichthyans, osteichthyans). Buchanosteids have larger orbits than *Holenema*, and the orbits are more laterally placed that in *Romundina* or *Bothriolepis*, giving the cheek a distinct suborbital section (equivalent to the 'handle' of a cleaver) similar to the condition in crown gnathostomes. The major difference to crown gnathostomes is the posterior embayment for the adductor fossa, in the buchanosteid palatoquadrate. This cannot be explained only by the muscle space being confined by the dermal cheek bones, because early osteichthyans (also with a dermally enclosed cheek) have a continuous 'commissural lamina' between autopalatine and quadrate parts of the palatoquadrate. This encloses the adductor fossa mesially[17], to provide a cleaver-like shape.

Originally, four articulations were inferred from the single incompletely preserved acid-etched palatoquadrate of *Romundina*[22]. Two of these represented an ethmoid ('orbital') connection as identified on the braincase[28], but better detail now indicates three articulations for the autopalatine in *Romundina*[21]. The posterior one was provisionally interpreted as part of the palatobasal connection by comparison with '*Buchanosteus*'[22]. The anterior articulation is located ventrally and mesially, and clearly corresponds to the mesial ethmoid articulation described for ANU V244, as it would also be located posterolateral to paired anterior supragnathals – these are preserved in a closely related acanthothoracid (specimen CPW.9)[28]. It is noted that the infolded ventral tuberculate surface in this specimen could have formed the biting margin of the mouth (a posterior supragnathal is not known in *Romundina*), and this structure may be more prominently developed in other acanthothoracids[29]. However whether it could have formed the biting margin depends on the orientation of the suborbital plate against the skull. In our buchanosteid this proved to be very oblique in order to place the gnathal elements in occlusion. Again, such detail can only be established by using micro-CT scanning and 3D printing techniques on rare articulated specimens, as demonstrated above.

The Meckel's cartilage was noted above to be deepest towards the anterior end, and using 3D printouts to place it in occlusion with the palatoquadrate shows this corresponds to the anterior extent of the adductor fossa (Supplementary Fig. 2e). In contrast, in Palaeozoic elasmobranchs Meckel's cartilage tends to be deepest posteriorly[30], but the adductor fossa on the palatoquadrate is entirely postorbital, indicating that the muscle was more posteriorly placed. Regarding the mandibular joint, the dorsal articulation on the buchanosteid Meckel's cartilage has a corresponding position to the 'mandibular knob' in *Gogoselachus*[31]. The mandibular

knob in various Palaeozoic and modern elasmobranchs forms a secondary articulation with a concavity on the palatoquadrate. but this was clearly not so in the buchanosteid jaw, where the dorsal articulation does not contact the palatoquadrate (Supplementary Fig. 3b).

Supplementary Fig. 5 gives additional information on the cranial arteries and veins as indicated by grooves and foramina on the ventral surface of the braincase. These are more completely preserved, and show much more detail, than the various specimens used for the previous restoration of the ventral braincase surface of '*Buchanosteus*'[4] (Supplementary Fig. 6a). A full interpretation will depend on segmentation of internal braincase structures, not yet carried out, but we note here that the grooves indicate a more complex pattern of arteries than recently represented for '*Buchanosteus*' as a primitive gnathostome[18].

The left groove for the lateral dorsal aorta is best preserved, with a similar position to the previous description for '*Buchanosteus*'[4](Supplementary Fig. 6a). However it extends farther posteriorly to the posterolateral edge of the ventral braincase surface, close to the anterior end of the row of spino-occipital nerve foramina. A curved lateral groove adjacent to the first of these may represent the occipital artery emanating from the lateral dorsal aorta. This is based on comparison with a similar foramen at the posterior end of the aortic canal in *Brindabellaspis*, previously identified as for the occipital artery[32], which forms a similar curved groove crossing the anterior spino-occipital nerve foramen.

The aortic groove in ANU V244 curves laterally towards the large foramen for the hyomandibular nerve, and presumably received the efferent hyoid artery passing up from the hyoid arch, as previously interpreted (Supplementary Fig. 6a). A distinct foramen shows where the orbital artery branched from the efferent hyoid artery to pierce the braincase floor, and emanate in the rear wall of the orbital cavity. This is essentially as previously described[4]. Not previously documented for '*Buchanosteus'* is a strong groove for the internal carotid artery, branching off the efferent hyoid groove with a shape showing clearly that blood flow direction was inward, from the efferent hyoid artery. The internal carotid groove curves forward on both sides to a distinct foramen lateral to the parasphenoid, where this major artery entered the braincase, as previously identified in other arthrodires[4,16,19].

Behind the parasphenoid the aortic groove crosses a transverse groove passing laterally from paired foramina. From their position these presumably opened dorsally into the interorbital canal for the pituitary vein, as previously described[4]. These grooves are therefore interpreted as parts of the hypophysial vein system. The preserved detail shows that the internal carotid was morphologically ventral to the vessel within the transverse groove. Fainter grooves pass anteriorly from each hypophysial vein foramen, and curve in towards the lateral notches of the parasphenoid. This course closely matches the position of the restored hypophysial vein in *Kujdanowiaspis*[19] and *Dicksonosteus*[16]. However, for '*Buchanosteus'* it was demonstrated by the acid-etched specimens that the depression in the lateral notch of the parasphenoid had no foramen for the hypophysial vein in this position[4]. Other parts of the cranial venous system are generally not visible in ventral view, the jugular

vein being completely enclosed in a canal within the lateral cranial wall. Its posterior opening is visible behind the posterior postorbital process, and an opening at the base of that process probably transmitted a posterior postorbital vein, associated with branches of the glossopharyngeal nerve, as previously interpreted[4].

At the internal carotid foramen a strong lateral arterial branch is indicated by a groove passing to the palatobasal connection for the palatoquadrate, on the edge of the subocular shelf. This contained the efferent pseudobranchial artery, which in ANU V244 passed posterolaterally into a notch behind the palatobasal articular facet (Fig. 6c). In other specimens of '*Buchanosteus*' there was a double palatobasal articulation (Supplementary Fig. 6a), with the efferent pseudobranchial artery evidently passing between them[4,22].

Not previously identified in any arthrodire is an additional arterial groove passing forward from the internal carotid foramen. This has a corresponding position to a groove in *Brindabellaspis* interpreted to have carried the palatine artery[32], by comparison with *Glyptolepis*[33], and the same groove was identified in *Romundina*[32]. Recently this groove in *Romundina* was labelled as for the internal carotid[21], but this seems erroneous. In ANU V244 the palatine groove branches anteriorly, with a main mesial branch directed to the anterior end of the parasphenoid. This gives off numerous smaller branches forming a reticulating network through the attachment area for the anterior supragnathal. This was evidently the main arterial supply to this gnathal element. A third branch in this arterial system is indicated by another groove originating from the efferent pseudobranchial artery immediately lateral to its junction with the internal carotid (Fig. 6b). This passes anterolaterally to the mesial ethmoid articulation, with a smaller branch reaching another notch on the edge of the subocular shelf, between the palatobasal and lateral ethmoid articulations for the palatoquadrate. 3D printouts, with the palatoquadrate in position against the braincase (Fig. 2b), show this notch forming a clear foramen on both sides. Given its connection with the arterial groove system, it can be assumed that the blood supply to the floor of the orbital cavity passed up through this foramen.

The same system is connected to the 'transverse groove' on the palatoquadrate attachment surface for the posterior supragnathal (Fig. 3), so presumably also carried arterial blood to this region. We note that there seems no corresponding arterial branch in the living shark *Chlamydoselachus*[34], nor in the Devonian placoderms *Kujdanowiaspis*[19], *Dicksonosteus*[16], or *Romundina*[21]. The other grooves also evidently transmitted vessels or nerves between the cartilage and the gnathal plates, because reassembly of 3D printouts shows that the inner ridge along the lateral edge of the posterior supragnathal (Fig. 1c) did not fill the anterior groove of the palatoquadrate, leaving an 'anterior notch' (Supplementary Fig. 3c). In articulation, this notch sat opposite a 'lateral notch' (Supplementary Fig. 3d), formed between the anterior supragnathal and a groove inside the ectethmoid process of the braincase (Fig. 6).

Supplementary Figures

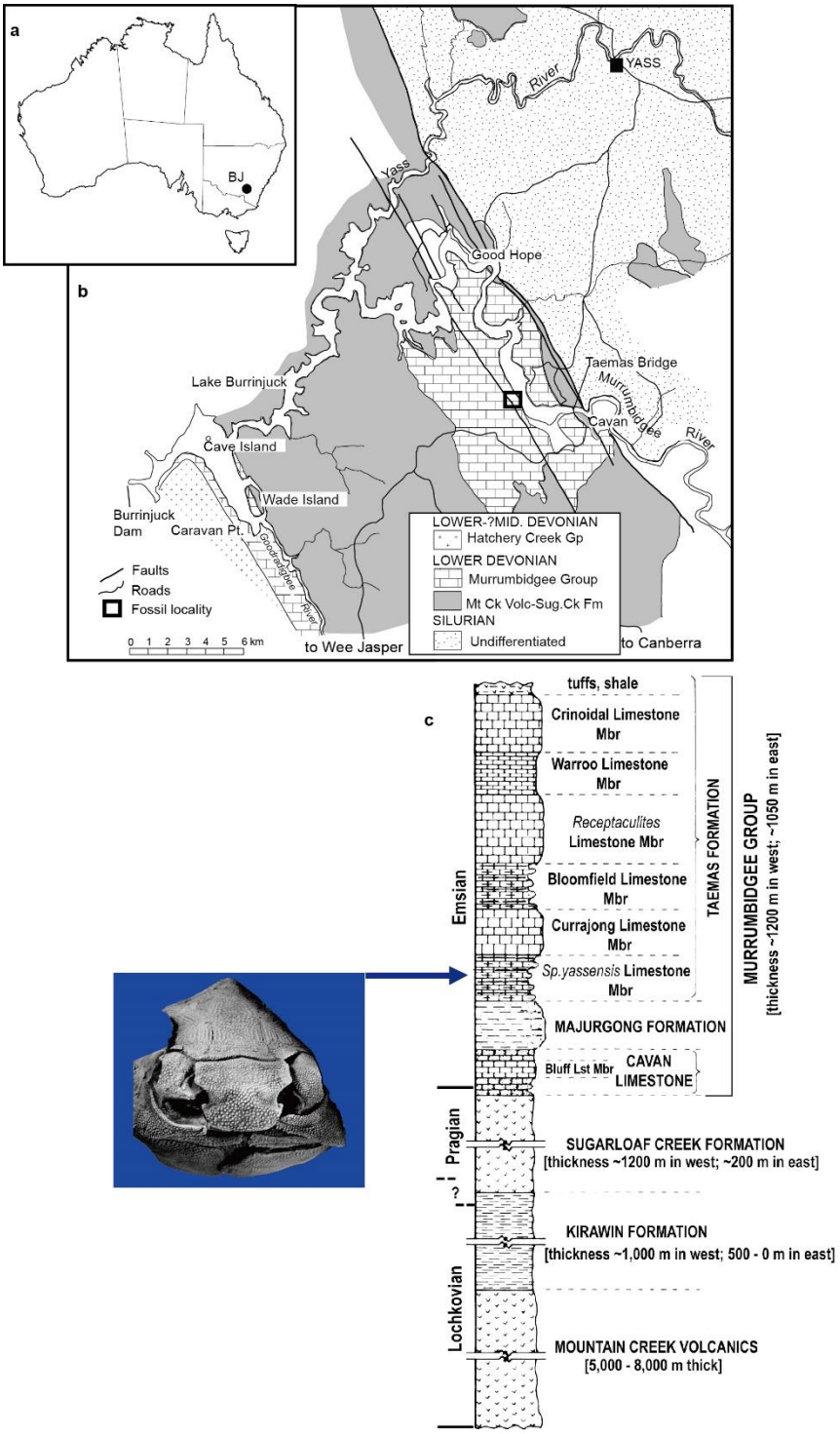

Supplementary Figure 1. Locality details for articulated buchanosteid arthrodire (ANU V244). (**a**) Location in southeastern Australia of the Early Devonian limestones at Burrinjuck (BJ), near Canberra. (**b**) Devonian geology in the vicinity of Lake Burrinjuck, showing the fossil locality for ANU V244. (**c**) Devonian stratigraphy at Burrinjuck, showing the fossil horizon for ANU V244. Maps and stratigraphic column were generated with Adobe Illustrator CS6 (http://www.adobe.com/cn/products/illustrator.html)

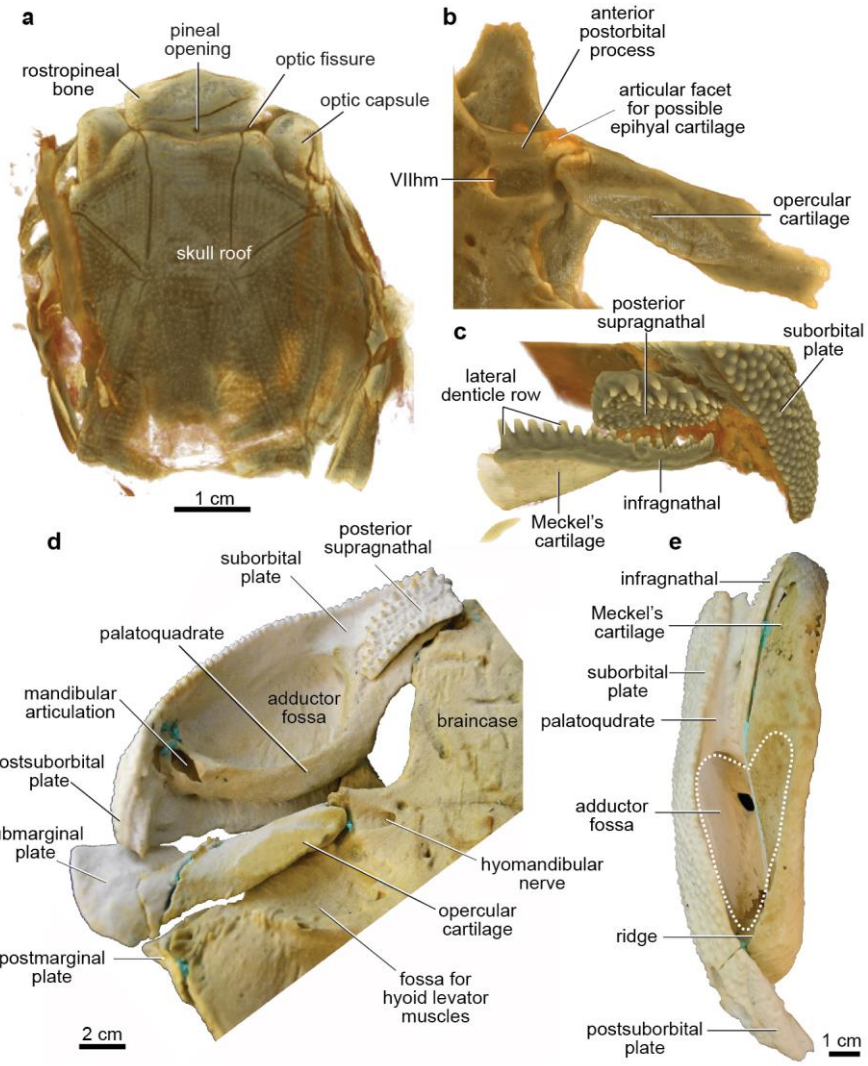

342

343 **Supplementary Figure 2. Articulated buchanosteid arthrodire (ANU V244),**
344 **based on high-resolution CT (a-c) and 3D printouts (d-e).** (**a**) Specimen in dorsal
345 view. (**b**) Ventral view showing detail of the left submarginal plate (incomplete) and
346 opercular cartilage in articulation against the anterior postorbital process of the
347 braincase, with the hyomandibular nerve foramen (VIIhm) opening in a groove
348 crossing onto the opercular cartilage. (**c**) Preserved association of the posterior
349 supragnathal, infragnathal and Meckel's cartilage inside the specimen. (**d**)
350 Ventromesial view showing reassembly of the right cheek complex (dermal suborbital
351 and postsuborbital plate, plus palatoquadrate), and right opercular unit (submarginal
352 plate plus opercular cartilage), in articulation against the braincase. (**e**) Ventral view
353 of the right jaw with posterior supragnathal and infragnathal in occlusion, and
354 Meckel's cartilage in articulation on the palatoquadrate. Dotted line outlines the limits
355 of the adductor fossa across the two cartilage elements.

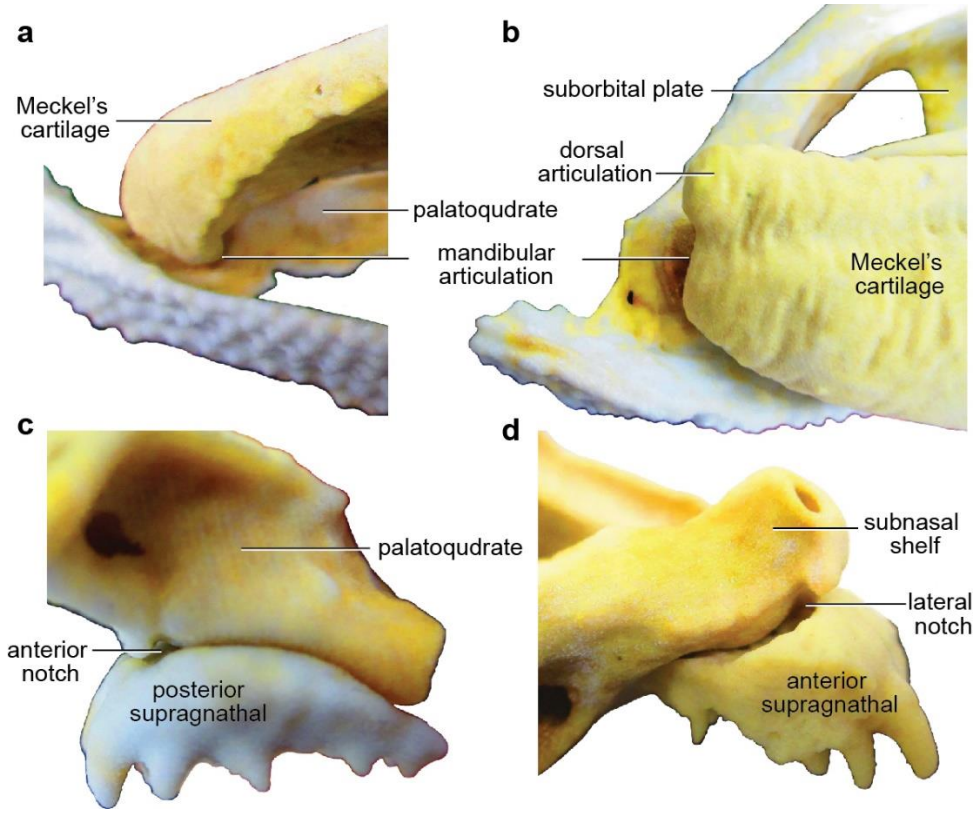

Supplementary Figure 3. Articulated buchanosteid arthrodire (ANU V244), based on 3D printouts. (a) Ventral view and (**b**) mesial view of the left mandibular joint in articulation. (**c-d**) Detail of the ethmoid connection of the palatoquadrate against the braincase, showing the articular surface at the anterior end of the right palatoquadrate, with posterior supragnathal attached (**c**), and the corresponding right lateral face of the subnasal shelf of the braincase, with anterior supragnathal attached (**d**). Not to scale.

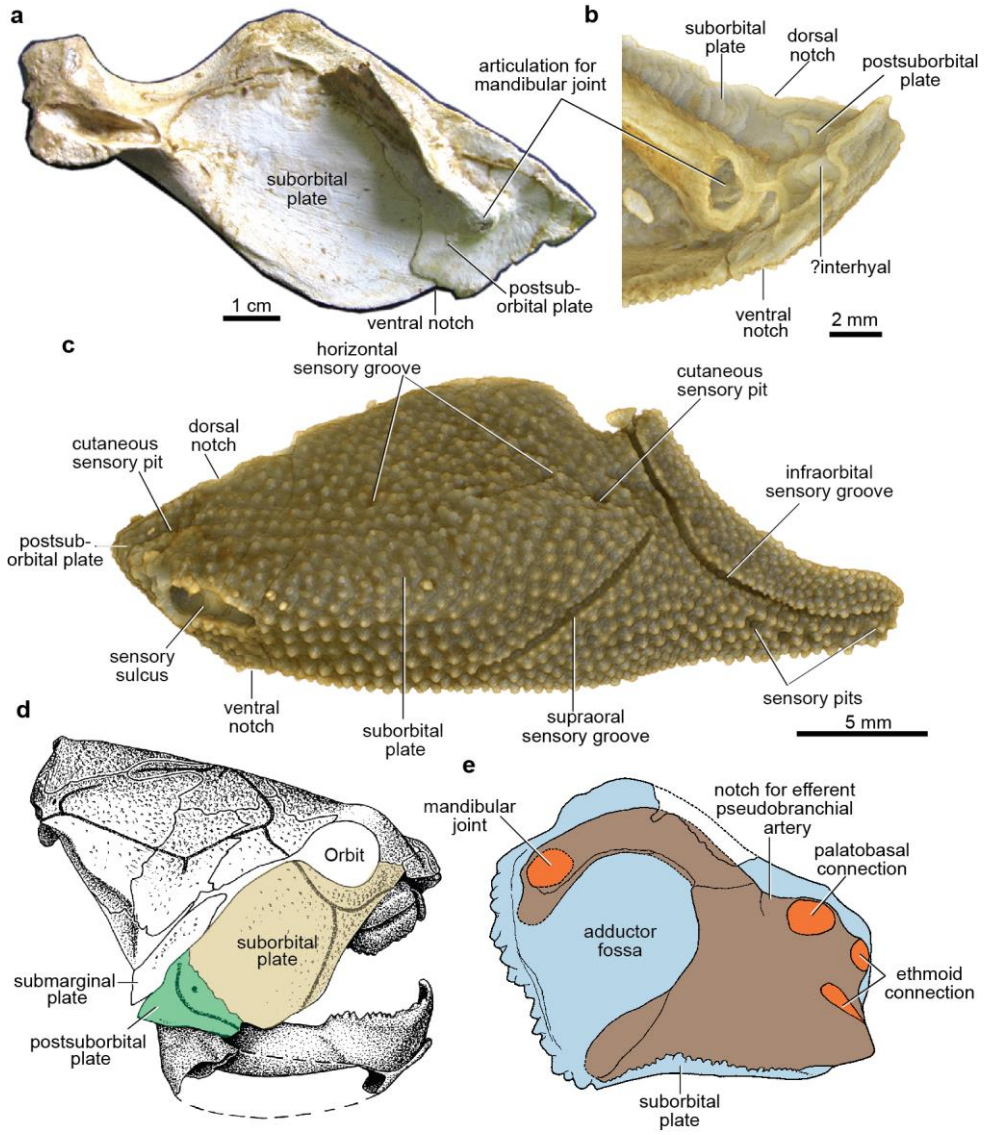

Supplementary Figure 4. Comparisons of the dermal cheek unit, attached palatoquadrate, and mandibular joint articulation in various placoderms. (**a**) Internal view of the right suborbital and postsuborbital plates with attached perichondrally ossified quadrate in *Eastmanosteus* sp. from Gogo (ANU 21633). (**b-c**) Right cheek unit of buchanosteid arthrodire ANU V244, based on high-resolution CT. (**b**) Internal view of posterior end showing the mandibular joint on the quadrate (attached to the dermal suborbital plate), behind which is a separately ossified element compared with the osteichthyan interhyal (attached to the postsuborbital plate). (**c**) External view of the right cheek unit (suborbital and postsuborbital plates). (**d**) *Eastmanosteus calliaspis* from Gogo in lateral view (modified after ref. 24), with right cheek unit (suborbital and postsuborbital plates) highlighted. **(e)** Restoration in internal view of the left suborbital plate and attached palatoquadrate of *Romundina stellina* (modified after refs. 22, 25), showing a new interpretation of the position of the mandibular joint. Light blue, dermal bones; brown, visceral arch cartilages; orange, articular facets. (**d**) and (**e**) are not to scale.

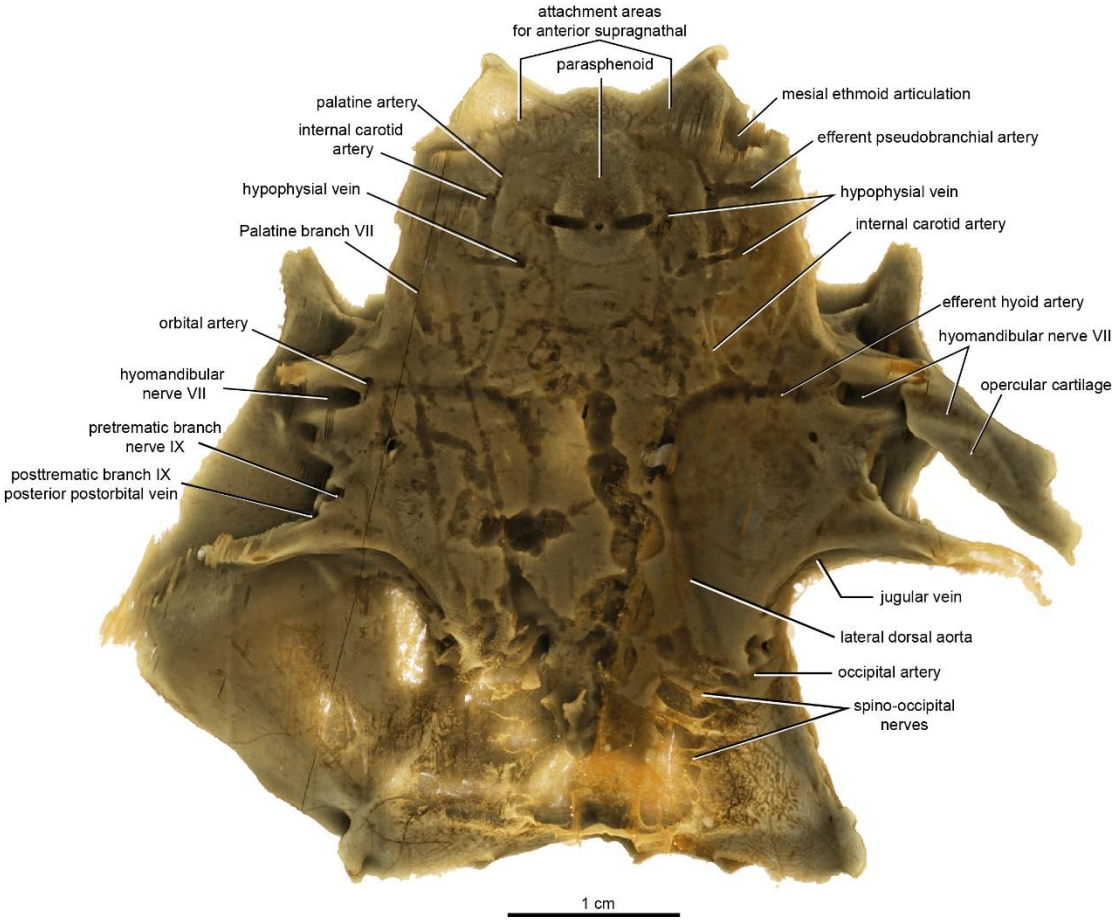

Supplementary Figure 5. Articulated buchanosteid arthrodire (ANU V244), based on high-resolution CT; interpretation of grooves on the ventral braincase surface. Interpretations are based on previous analyses, in particular for *Kujdanowiaspis*[19], '*Buchanosteus*'[4], and *Dicksonosteus*[16,20]. Grooves and foramina are labelled according to their contained structures.

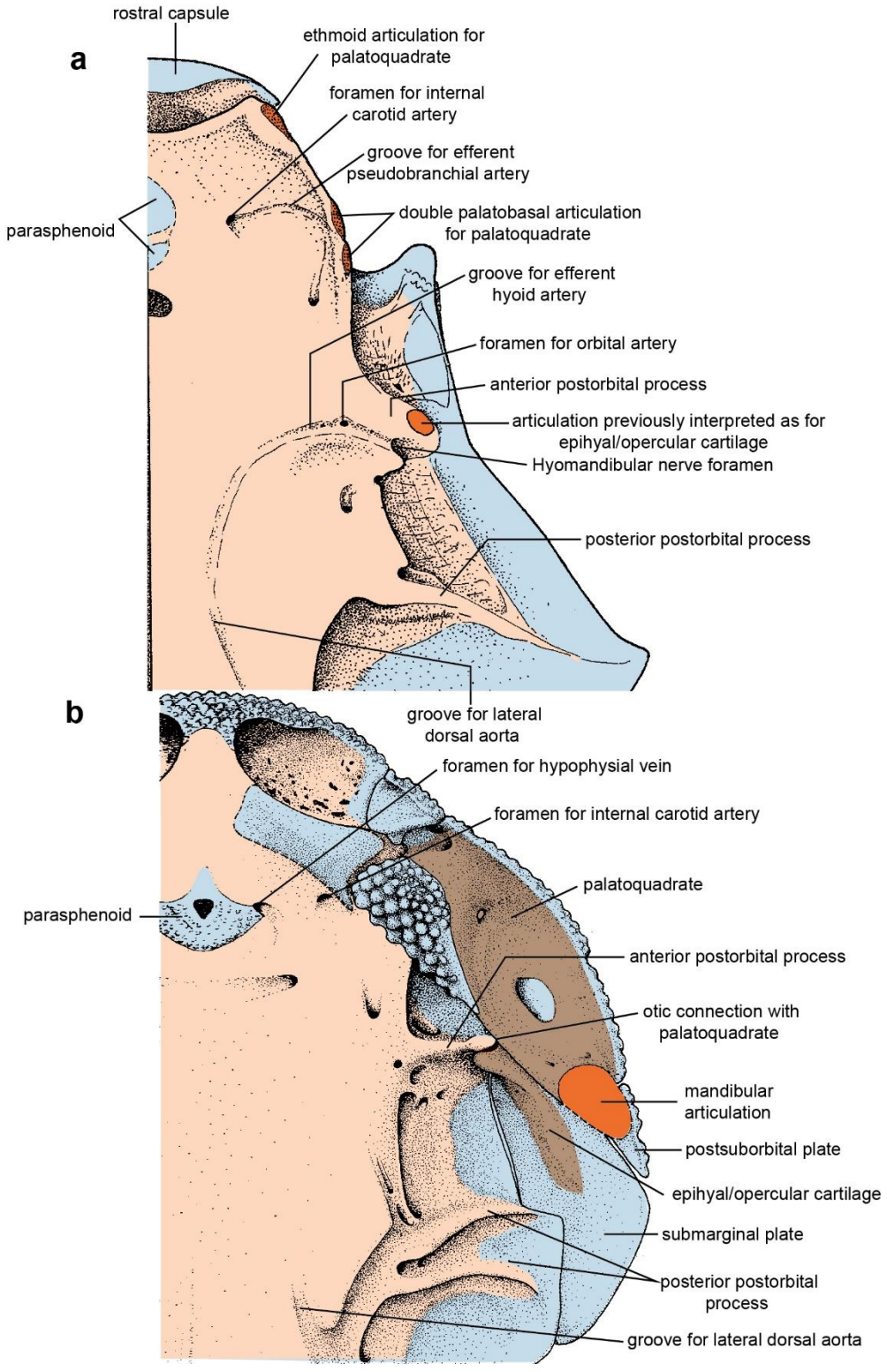

Supplementary Figure 6. Previous interpretations for '*Buchanosteus*' (a) and *Dicksonosteus* (b). (**a**) Structures on the ventral braincase surface of '*Buchanosteus*' as interpreted by ref. 4. (**b**) restoration of the ventral braincase surface, dermal cheek plates, upper jaw cartilages and gnathal elements in *Dicksonosteus*, modified after ref. 16. Light blue, dermal bones; brown, visceral arch cartilages; pale pink, braincase; orange, articular facets; red, blood vessels. Not to scale.

Supplementary References

1 Young, G. C. Wee Jasper-Lake Burrinjuck fossil fish sites: Scientific background to national heritage nomination. *Proc. Linn. Soc. N. S. W.* **132**, 83–107 (2011).

2 Thomson, K. S. & Campbell, K. S. W. The structure and relationships of the primitive Devonian lungfish - *Dipnorhynchus sussmilchi* (Etheridge). *Bull., Peabody Mus. Nat. Hist.* **38**, 1–109 (1971).

3 Campbell, K. S. W. An almost complete skull roof and palate of the Dipnoan *Dipnorhynchus sussmilchi* (Etheridge). *Palaeontology* **8**, 634–637 (1965).

4 Young, G. C. New information on the structure and relationships of *Buchanosteus* (Placodermi: Euarthrodira) from the Early Devonian of New South Wales. *Zool. J. Linn. Soc.* **66**, 309–352 (1979).

5 Hunt, J. & Young, G. C. A new placoderm fish of uncertain affinity from the Early-Middle Devonian Hatchery Creek succession at Wee Jasper, New South Wales. *Alcheringa* **35**, 1–23, doi:10.1080/03115511003793645 (2011).

6 Young, G. C., Lelièvre, H. & Goujet, D. Primitive jaw structure in an articulated brachythoracid arthrodire (placoderm fish; Early Devonian) from southeastern Australia. *J. Vertebr. Paleontol.* **21**, 670–678 (2001).

7 Long, J. A., Mark-Kurik, E. & Young, G. C. Taxonomic revision of buchanosteoid placoderms (Arthrodira) from the Early Devonian of south-eastern Australia and Arctic Russia. *Aust. J. Zool.* **62**, 26–43, doi:10.1071/ZO13081 (2014).

8 Stensiö, E. A. On the heads of certain arthrodires. 2. On the cranium and cervical joint of the Dolichothoraci. *K. Sven. Vetensk. Akad. Handl.* **22**, 1–70 (1945).

9 Hills, E. S. On certain endocranial structures in *Coccosteus*. *Geol. Mag.* **73**, 213-226, doi:https://doi.org/10.1017/S0016756800097399 (1936).

10 White, E. I. & Toombs, H. A. The buchanosteid arthrodires of Australia. *Bull. Brit. Mus. (Nat. Hist.), (Geol.)* **22**, 379–419 (1972).

11 White, E. I. Australian arthrodires. *Bull. Brit. Mus. (Nat. Hist.), (Geol.)* **1**, 249–304 (1952).

12 Mark-Kurik, E. & Young, G. C. A new buchanosteid arthrodire (placoderm fish) from the Early Devonian of the Ural Mountains. *J. Vertebr. Paleontol.* **23**, 13–27 (2003).

13 Lelièvre, H. *et al.* Nouveaux Vertébrés (Placodermes, Acanthodiens, Chondrichthyens et Sarcoptérygiens) de la formation de Jauf (Dévonien inférieur, région de Al Huj, Arabie Saoudite). *Compt. Rend. Sci., Ser. II* **319**, 1247–1254 (1994).

14 Wang, J.-Q. New material of *Buchanosteus* and its biostratigrapic significance. *Geol. Bull. Chin.* **24**, 800–806 (In Chinese) (2005).

15 Denison, R. H. in *Handbook of Paleoichthyology, Vol. 2* (ed. Schultze, H-P) 1–128 (Gustav Fischer, 1978).

16 Goujet, D. F. *Les poissons placodermes du Spitsberg. Arthrodires Dolichothoraci de la Formation de Wood Bay (Dévonien inférieur)*. Vol. 15 (CNRS, 1984).

17 Jarvik, E. *Basic Structure and Evolution of Vertebrates, Vol. 1*. (Academic Press, 1980).

18 Giles, S., Friedman, M. & Brazeau, M. D. Osteichthyan-like cranial conditions in an Early Devonian stem gnathostome. *Nature* **520**, 82–85, doi:10.1038/nature14065 (2015).
19 Stensiö, E. A. Anatomical studies on the arthrodiran head. Part 1. Preface, geological and geographical distribution, the organization of the head in the Dolichothoraci, Coccosteomorphi and Pachyosteomorphi. Taxonomic appendix. *K. Sven. Vetensk. Akad. Handl.* **9**, 1–419 (1963).
20 Goujet, D. F. in *Problèmes actuels de Paléontologie-Evolution des Vertébrés* Vol. 218 (ed. Lehman, J. P.) 81–99 (CNRS, 1975).
21 Dupret, V., Sanchez, S., Goujet, D., Tafforeau, P. & Ahlberg, P. E. A primitive placoderm sheds light on the origin of the jawed vertebrate face. *Nature* **507**, 500–503, doi:10.1038/nature12980 (2014).
22 Young, G. C. The relationships of placoderm fishes. *Zool. J. Linn. Soc.* **88**, 1–57 (1986).
23 Gardiner, B. G. & Miles, R. S. A new genus of eubrachythoracid arthrodire from Gogo, Western Australia. *Zool. J. Linn. Soc.* **99**, 159–204 (1990).
24 Dennis-Bryan, K. A new species of eastmanosteid arthrodire (Pisces: Placodermi) from Gogo, Western Australia. *Zool. J. Linn. Soc.* **90**, 1–64 (1987).
25 Ørvig, T. in *Problèmes actuels de Paléontologie-Evolution des Vertébrés* Vol. 218 (ed. Lehman, J. P.) 41–71 (Colloques Internationaux du Centre National de la Recherche Scientifique, 1975).
26 Schaeffer, B. in *Problèmes actuels de Paléontologie-Evolution des Vertébrés* Vol. 218 (ed. Lehman, J. P.) 101–109 (Colloques Internationaux du Centre National de la Recherche Scientifique, 1975).
27 Miles, R. S. The Holonematidae (placoderm fishes), a review based on new specimens of *Holonema* from the Upper Devonian of western Australia. *Philos.Trans.R.Soc.London, Ser.B* **263**, 101–234 (1971).
28 Goujet, D. F. & Young, G. C. in *Recent Advances in the Origin and Early Radiation of Vertebrates* (eds. Arratia, G. Wilson, M. V. H. & Cloutier, R.) 109–126 (Verlag Dr. Friedrich Pfeil, 2004).
29 Burrow, C. J. Placoderm fauna from the Connemarra Formation (?late Lochkovian, Early Devonian), central New South Wales, Australia. *Alcheringa* (*Special Issue 1), Suppl to vol.* **30**, 59–88 (2006).
30 Zangerl, R. in *Handbook of Paleoichthyology. Volume 3A: Chondrichthyes I. Paleozoic Elasmobranchii.* (ed. Schultze, H-P) 1–115 (Gustav Fischer, 1981)
31 Long, J. A. *et al*. First Shark from the Late Devonian (Frasnian) Gogo Formation, Western Australia Sheds New Light on the Development of Tessellated Calcified Cartilage. *PLoS One* **11**: e0126066. https://doi.org/10.1371/journal.pone.0126066 (2015).
32 Young, G. C. A new Early Devonian placoderm from New South Wales, Australia, with a discussion of placoderm phylogeny. *Palaeontogr. Abt. A* **167**, 10–76 (1980).
33 Jarvik, E. Middle and Upper Devonian Porolepiformes from East Greenland with special reference to *Glyptolepis groenlandica* n. sp., and a discussion on the structure of the head in the Porolepiformes. *Meddr. Grønland.* **187**, 1–307 (1972).

34 Allis, E. P. The cranial anatomy of *Chlamydoselachus anguineus*. *Acta Zool*. **4**, 123–221 (1923).

Appendix D pdf of Hu et al. 2019 (Paper 3)

Hu, Y., et al., 2019. High resolution XCT scanning reveals complex morphology of gnathal elements in an Early Devonian arthrodire. Palaeoworld 28, 525–534. https://doi.org/10.1016/j.palwor.2018.12.003

Available online at www.sciencedirect.com

ScienceDirect

Palaeoworld 28 (2019) 525–534

Palaeoworld

www.elsevier.com/locate/palwor

High resolution XCT scanning reveals complex morphology of gnathal elements in an Early Devonian arthrodire

Yu-Zhi Hu [a,b], G.C. Young [b], Carole Burrow [c], You-an Zhu [d,e,*], Jing Lu [b,e,f]

[a] *Research School of Earth Sciences, Australian National University, Building 142 Mills Road, Canberra, ACT 2601, Australia*
[b] *Research School of Physics and Engineering, Australian National University, Building 60, Canberra, ACT 2601, Australia*
[c] *Geosciences, Queensland Museum, 122 Gerler Road, Hendra, Queensland 4011, Australia*
[d] *Subdepartment of Evolution and Development, Uppsala University, Norbyvägen 18A, 752 36 Uppsala, Sweden*
[e] *Key Laboratory of Vertebrate Evolution and Human Origins of Chinese Academy of Sciences, Institute of Vertebrate Paleontology and Paleoanthropology, Chinese Academy of Sciences, Beijing 100044, China*
[f] *CAS Center for Excellence in Life and Paleoenvironment, Beijing 100044, China*

Received 7 October 2018; received in revised form 7 November 2018; accepted 10 December 2018
Available online 19 December 2018

Abstract

Arthodire placoderms, as a possible sister group of Chinese 'maxillate' placoderms plus crown gnathostomes, provide important information regarding early evolution of jaws and teeth. High-resolution computed tomography and digital dissection on a unique articulated 400 million-year-old buchanosteid arthrodire permitsa detailed description of the three types of gnathal elements in basal arthrodires for the first time, giving insights into their morphology and the organization of the associated dentition. In displaying numerous denticle rows (dental fields), the gnathal element morphology is very different from the much-reduced denticulation of higher brachythoracid arthrodires, even though the latter have been used recently to interpret origin and early evolution of teeth. Ossification centres are anterolateral on the anterior supragnathal (attached to the braincase), anteromesial on the posterior supragnathal (attached to the palatoquadrate), and in the central part of the biting portion of the infragnathal (attached to the meckelian cartilage). The latter bone shows no evidence of two ossification centres as has been interpreted for more advanced arthrodires. Denticle rows radiating from the ossification centre form dental fields in all three elements, and are more similar to the gnathal elements of phlyctaeniid and actinolepid arthrodires than to advanced brachythoracids. The new evidence gives insights into the primitive arthrodire condition for comparison with the dermal jaw bones of Chinese 'maxillate' placoderms that have been homologised with the premaxilla, maxilla, and dentary of osteichthyans. The new details will help clarify the sequence of character acquisition in the evolution of marginal jaw bones in basal gnathostome groups.

Keywords: Placodermi; Arthrodire; Early Devonian; Gnathal elements; Evolution; Morphology

1. Introduction

Placoderms ('armoured fishes') are an assembly of earliest gnathostomes or jawed vertebrates that share a number of characters (Janvier, 1996; Young, 2010). Whether this assembly is a monophyletic group or not is still debated (Brazeau, 2009; Young, 2010; Zhu et al., 2013; Dupret et al., 2014; Brazeau and Friedman, 2015; Long et al., 2015; Qiao et al., 2016; Zhu et al., 2016; King et al., 2017). Among placoderm subgroups, the Arthrodira is the most diverse group and often the stereotypical representative of all placoderms. Traditionally, placoderms were viewed as an extinct side branch from the main trajectory of the evolution of jawed vertebrates (Denison, 1978; Janvier, 1996; Goujet and Young, 2004; Young, 2010). Especially, various characters of the placoderm jaws and dental structures were regarded as peculiarities. This viewpoint dramatically changed in recent years, with documentation of the remarkable new Xiaoxiang Fauna from the Silurian of China, which has revealed an early radiation of the jawed fishes unrepresented elsewhere in the world (Zhu et al., 2013, 2016). This fauna has produced the 'maxillate' placoderms *Entelognathus* and *Qilinyu* (Zhu et al.,

* Corresponding author at: Subdepartment of Evolution and Development, Uppsala University, Norbyvägen 18A, 752 36 Uppsala, Sweden.
E-mail address: youan.zhu@ebc.uu.se (Y. Zhu).

https://doi.org/10.1016/j.palwor.2018.12.003
1871-174X/

2013, 2016), with typical features of the placoderm dermal skeleton in combination with marginal jaw bones previously considered unique to the bony fishes (Osteichthyes). As such, there is renewed interest in the evolution of jaws and teeth in placoderms, to investigate the attribution of characters either as the primitive gnathostome condition, or as autapomorphies of placoderms (e.g., Rücklin and Donoghue, 2015; Burrow et al., 2016; Donoghue and Rücklin, 2016; Smith et al., 2017).

Placoderms were traditionally interpreted to have a special tissue in their tubercles called 'semidentine', with cell bodies enclosed in the hard tissue, and a different mode of growth in the gnathal elements, by which their 'teeth' were said to be clearly distinguished from those of other fishes, fossil as well as recent (Ørvig, 1980). They were considered either to have lacked the capacity to grow 'true' teeth (Reif, 1982; Dennis-Bryan, 1987; Janvier, 1996; Young et al., 2001; Burrow, 2003; Young, 2003), or to have possessed convergently evolved tooth-like structures (Johanson and Smith, 2003, 2005; Smith and Johanson, 2003a, 2003b). Synchrotron radiation X-ray tomographic microscopy of a developmental series of the Gogo arthrodire *Compagopiscis* (Rücklin et al., 2012; Rücklin and Donoghue, 2015) showed a pulp cavity as in true teeth, those authors concluded that teeth did not evolve convergently amongst extant and extinct classes of early gnathostomes; i.e., the teeth of the stem gnathostomes are homologous with the teeth of the crown gnathostomes.

Apart from the 'maxillate' placoderms of China, almost all recent studies regarding tooth origins using early vertebrate fossils have relied only on fragmentary remains that have been assumed to belong to various taxa. Rücklin and Donoghue (2015) interpreted histology and growth pattern of an assumed gnathal element of the basal placoderm *Romundina*, but this element was likely mis-identified, and was interpreted as an external dermal element by Burrow et al. (2016) and Smith et al. (2017). Chen et al. (2016, 2017) have investigated growth structure of teeth in fragmentary jaw elements that are presumed to belong to the putative Silurian stem osteichthyans *Andreolepis* and *Lophosteus*. Even research on the Gogo arthrodires (e.g., Rücklin et al., 2012) has examined gnathal elements in isolation, although their assignment to specific taxa is beyond question because these are from articulated dermal skeletons.

The phylogeny of Zhu et al. (2013, 2016) showed arthrodires grouped with ptyctodontids as the sister group of 'maxillate' placoderms plus crown gnathostomes. Alternatively, arthrodires have been placed as the sister group to crown gnathostomes (Davis et al., 2012; Giles et al., 2013) or in a polytomy with rhenanids in the same position (Giles et al., 2015). Given this placement, any investigation of early arthrodires has the potential to provide key information regarding the origin and early evolution of jaws and teeth. However, the above investigations mostly sample eubrachythoracids, a group of relatively derived arthrodires that adapted towards an active predatory lifestyle (Zhu and Zhu, 2013), with corresponding specialization in their jaws and dental structures (Young, 2010). As a result, the recognition of primitive characters of the gnathal elements is more difficult. Jaw structure in basal members of the Arthrodira has remained poorly understood until recently (Hu et al., 2017).

This study uses the only described acid-etched Early Devonian arthrodire (ANU V244) from Burrinjuck, New South Wales, Australia. The specimen can be assigned unequivocally to the buchanosteid arthrodires, basal members of the brachythoracid arthrodires that display many primitive arthrodire conditions prior to the radiation of eubrachythoracid arthrodires (Zhu and Zhu, 2013). The gnathal elements are in association and only very slightly dislocated from the complete skull, braincase and jaw cartilages (Fig. 1A, B), that was preserved by complete perichondral ossification. Thus, these gnathal elements can be positioned with confidence (Fig. 1B), providing unique insights into jaw structure and function (Hu et al., 2017).

Here we present detailed morphology of the gnathal elements of ANU V244 based on high-resolution computed tomography (HRCT), focusing on the organization of the dentitions on these gnathal elements. The result provides new evidence for the investigation of gnathal and dental conditions in a primitive arthrodire, giving insights into the early evolution of jaws and teeth in the earliest jawed vertebrates.

2. Material and methods

2.1. Specimen information

Specimen locality, geological provenance, and taxonomic notes are given as supplementary data in Hu et al. (2017). ANU V244 is held in the Department of Applied Mathematics, Research School of Physics & Engineering, Australian National University (ANU), Canberra.

2.2. Micro-CT scanning

All scanning for this research was done on instruments developed and built at the ANU Department of Applied Mathematics. The three dermal gnathal elements (anterior and posterior supragnathals of the upper jaw, infragnathal of the lower jaw) were illustrated by Hu et al. (2017), based on a 2011 CT scan of the whole specimen, and images of the posterior supragnathal and whole infragnathal presented below (see Section 3) are based on this scan. The whole specimen scan used an 80 kV/110 μA reflection-style X-ray source and 2 mm thick silicon dioxide filter. The specimen was placed 72 mm from the source, and the detector positioned 350 mm from the source. The specimen was imaged through 360° rotation. Reconstruction was based on 2880 radiographic projections formed on a 2048 × 2048 Perkin Elmer Flat Panel camera.

A 2015 rescan used the new double-helix HeliScan CT Scanner with higher resolution and a new algorithm to process and reconstruct CT data. Both 1.2 mm aluminium and 0.35 mm stainless steel filters were used, with specimen distance 85 mm from the source, and detector position 396 mm from the source, and probed separately with a polychromatic X-ray beam (Bremsstrahlung radiation). Accelerating voltage of the electron beam generating the Bremsstrahlung radiation was 110 kV with a current of 100 μA. A series of X ray transmission radiographs, collectively called the projection data, were acquired by

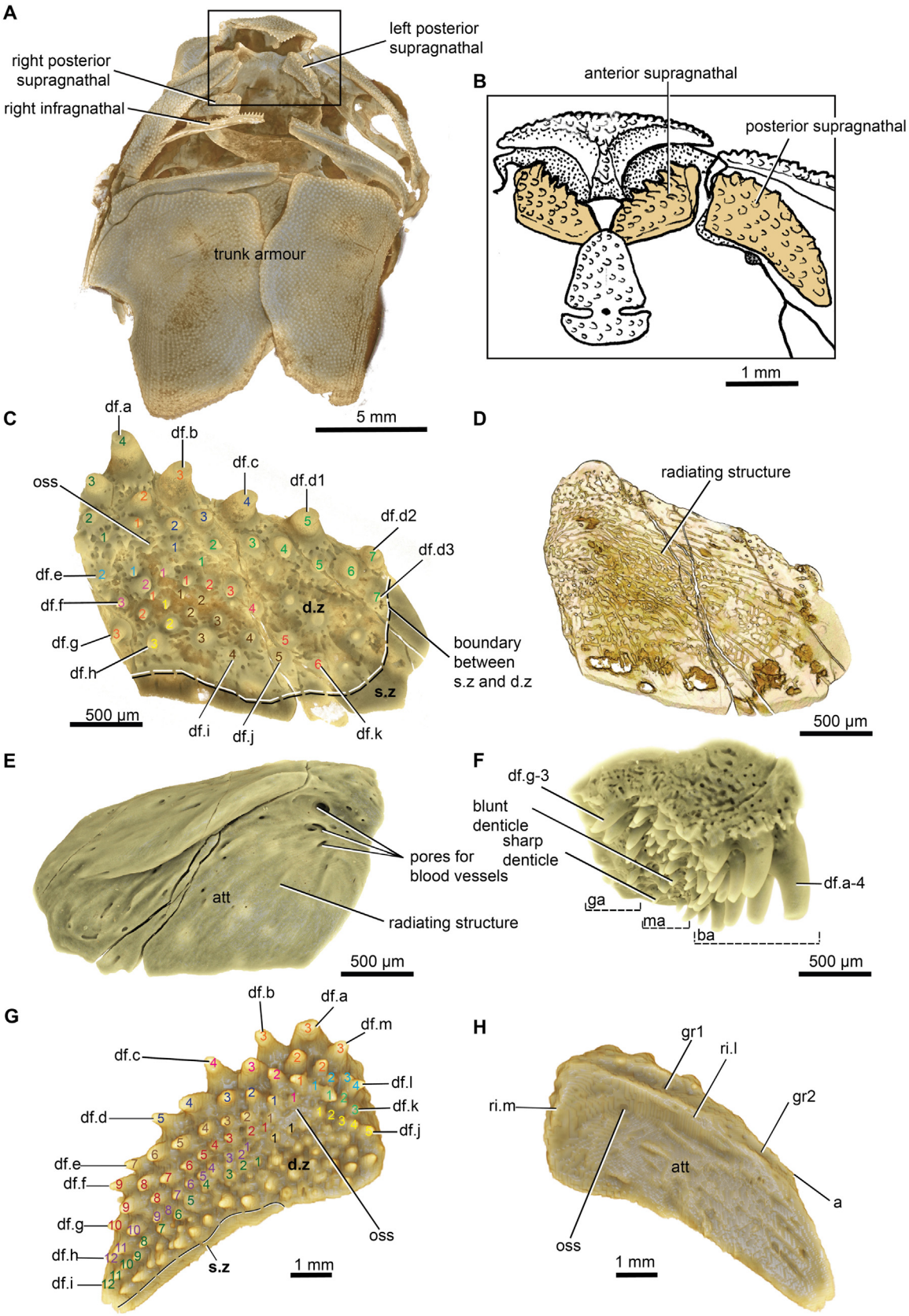

Fig. 1. Articulated buchanosteid arthrodire (ANU V244). (A) Ventral view based on high-resolution CT, showing the right and left posterior supragnathal and right infragnathal in preserved position; adapted from Hu et al. (2017). (B) Line drawing of the box area of (A), based on 3D printouts, showing the spatial relationship of anterior and posterior supragnathals (in yellow); adapted from Hu et al. (2017). (C, D) Right anterior supragnathal denticulate surface (C) and vascularisation beneath the level of denticles (D) in occlusal view. (E, F) Same element in dorsal (E) and oblique lateral (F) views. (G, H) Right posterior supragnathal bone in

the detector as the specimen was rotated through 360° double-helically over a period of 18 h. Reconstruction was based on 2520 radiographic projections formed on a 2048 × 1538 Varian Flat Panel camera.

The left infragnathal and right anterior supragnathal (removed from the articulated specimen for description in the original study; Young et al., 2001) were rescanned in 2015 as separate elements, with a higher resolution (1.45 and 1.79 microns respectively). Both were scanned with the double helix HeliScan CT Scanner at ANU CT Laboratory, scanning details as follows: **right anterior supragnathal** – 2 mm aluminium filter, specimen distance 3.95 mm from the source, detector position 309.5 mm from the source; probed separately with a polychromatic X-ray beam (Bremsstrahlung radiation), accelerating voltage of the electron beam 100 kV with a current of 76 μA. The specimen was rotated through 360° double-helically over a period of 22 h. Reconstruction was based on 3600 radiographic projections formed on a 3040 × 3040 Varian Flat Panel camera. The final resolution reached 1.79 μm. **Anterior end of left infragnathal –** 1.5 mm aluminium filter, specimen distance 3.2 mm from the source, detector position 309.5 mm from the source, and probed separately with a polychromatic X-ray beam. Accelerating voltage of the electron beam generating Bremsstrahlung radiation 100 kV with a current of 65 μA; specimen rotated through 360° double-helically over a period of 19 h; reconstruction based on 3600 radiographic projections formed on a 3040 × 3040 Varian Flat Panel camera with a final resolution of 1.45 microns, the highest resolution that can be obtained using any micro-CT scanner.

2.3. Scientific visualization

XCT scanning data from the 2011 whole specimen scan were processed using the program Drishti 2.5 (see http://nci.org.au/nci-systems/scientific-visualisation/visualisation-services/). Separate components including gnathal elements were extracted using *DrishtiPaint* on 1589 slices. The final output was sent to a ZPrinter 650 in Stanford Triangle Format (more detail is provided in Hu et al., 2017). For the 2015 scan the new CT data of the anterior supragnathal and broken end of the infragnathal are illustrated using open source 3D rendering and segmentation software Drishti 2.6.4 (see http://nci.org.au/nci-systems/scientific-visualisation/visualisation-services/).

3. Description

3.1. Anterior supragnathal

The right anterior supragnathal of ANU V244 was previously illustrated (erroneously as a left element) by Young et al. (2001, figs. 2C, 3A–C, 5C) and Young (2003, fig. 1D) and as a 3D print out and Drishti image from the 2011 CT scan by Burrow et al. (2016, fig. 1) and Hu et al. (2017, figs. 1d, e, 2b, 6b). The denticulate surface is anteroposteriorly concave, with the largest denticles along the anteromesial edge (Fig. 1C, df.a–df.d2). These have blunt tips, which show wear, and presumably represent the functional part of the youngest generation in terms of occlusion. Only the anterior zone, about three denticles across (Fig. 1F, ba), would have been directly occlusal to the corresponding zone on the infragnathal, as shown by 3D printouts placed in articulation against the respective jaw cartilages (Hu et al., 2017, fig. 2a). There is a middle zone of smaller denticles (Fig. 1F, ma), which possibly were exposed to the oral cavity as they contain both sharp (i.e., non-occlusal) and blunt (i.e., significant wear) denticles. Compared to the middle zone, the posterior edge has relatively large denticles. These denticles are more pointed compared to the blunt tips of the large anterior denticles; presumably they also projected through the soft tissue to function on the palate in gripping and holding prey items (Fig. 1F, ga). The ossification centre is identified inside the anterolateral corner (Fig. 1C, oss), where the denticles are the smallest, and large vascular pores are developed on the aboral surface (Fig. 1E). Radiating structure is evident on the adjacent attachment surface (Fig. 1E, att), and is also clearly shown by the internal vascular system (Fig. 1D). Given its position in articulation against the braincase (Fig. 1B) the anterior supragnathal must have grown faster towards the mid-line than laterally.

A radiating arrangement from the ossification centre is also discerned in the denticles on the oral surface (Fig. 1C), although this is less obvious than on the posterior supragnathal (Fig. 1G). We interpret approximately 3–6 denticles in each radiating row on the anterior supragnathal, with increasing size from the ossification centre outwards. Extra denticles fill gaps between the outer parts of the rows. Ørvig (1980) used a 'dental field' terminology to identify denticle rows on arthrodire gnathal elements, and we follow that here. Posteromesially, rows are unclear (Fig. 1C, d.z). Anteromesially, perhaps there was one big dental field radiating into three branches, or there may have been extra denticles filling gaps in the more distal parts as the anterior supragnathal grew bigger (Fig. 1C, df.d1–d3). We identify about eleven radiating fields (Fig. 1C df.a–k), and clearly these were much more numerous than on the anterior supragnathal of advanced brachythoracids like *Plourdosteus*. In that taxon Ørvig (1980) identified only 'anterior and medial' dental fields, the former represented by an 'adsymphysial tooth-row' and the latter by a non-denticulate ridge indicating the position of a 'semi-dentine column'. Only one or two denticle rows occur on the anterior supragnathal of other advanced arthrodires, for example *Eastmanosteus* (Dennis-Bryan, 1987, figs. 18, 19).

A smooth zone around the posterior and mesial edge (Fig. 1C, s.z) is thinner and less dense (represented by the dark colour in Fig. 1C). This is interpreted as the potential growth area for a

occlusal (G) and dorsal (H) views. Oral denticles numbered (1–12) based on their distance from the ossification centre in the same dental field. Abbreviations: a, angle on a margin; att, attachment area; ba, biting area; d.z, undifferentiated denticle zone; df.a-m, radiating dental field; ga, grabbing area; gr1, gr2, grooves on posterior supragnathal; ma, mixed area; oss, ossification centre; ri.l, lateral ridge; ri.m, mesial ridge; s.z, smooth zone.

new generation of denticles. The anterior and lateral edges of the anterior supragnathal are thicker and more distinct, but evidently larger denticles were also being added here.

3.2. Posterior supragnathal

Morphology of the visible denticulated surface of the posterior supragnathal in ANU V244 was briefly described by Young et al. (2001). Hu et al. (2017, figs. 1b, c, 2b, d, 6b) illustrated the dorsal surface, and the element in its restored position on the palatoquadrate. On the occlusal surface the most depressed part with the smallest denticles is centrally situated about one fifth of the long axis from the mesial side. This is interpreted as the ossification centre (Fig. 1G, oss), from which radiating rows of denticles can be interpreted and are more obvious than their counterparts on the anterior supragnathal. Ørvig (1980) named the two denticle rows on the posterior supragnathal of *Plourdosteus* as anterior and posterior dental fields. In contrast, at least 13 rows of denticles can be identified in the posterior supragnathal of the current specimen. The row including the largest denticle (with a blunt tip) is located on the anteromesial corner (Fig. 1G, df.a), and the other rows (Fig. 1G, df.b-m) are more posteriorly positioned. Shorter rows towards the mesial and posterior edge are less clear (Fig. 1G, d.z), and have not been distinguished. By comparison, in Gogo arthrodires there are only a few rows, for instance only two in *Compagopiscis* (Smith and Johanson, 2003b, fig. 2DSmith and Johanson, 2003bSmith and Johanson, 2003b, fig. 2D) or one denticle in *Mcnamaraspis* (Long, 1995, pl. 1, figs. 4, 5). The inner surface (Fig. 1H) also shows evidence of denticle addition on the lateral margin. Grooves (gr1, gr2) and a ridge (ri.l) run back to a slight angle (Fig. 1H, a), and define the two younger generations seen on the denticulate surface. The ossification centre (Fig. 1G, oss) is in the deepest depression of the attachment area (Fig. 1H, att) on the dorsal surface, inside where two ridges meet at the anteromesial corner. There are possible openings for the blood vessels openings here as in the anterior supragnathal, but the scan lacks resolution for an absolute interpretation. The mesial ridge (Fig. 1H, ri.m) in ANU V244 may correspond in position to the posterior process of the posterior supragnathal in advanced arthrodires (Young et al., 2001, fig. 3H–L).

3.3. Infragnathal

The left infragnathal was removed and described by Young et al. (2001, fig. 4), with only the right element included in the 2011 whole specimen scan (Fig. 1A). Detailed information on the right infragnathal was extracted from the 2011 CT scanning dataset using *Drishtipaint* (Hu et al., 2017, fig. 4a, g). Study of 3D printouts shows the infragnathal to be a ~23 mm long slender bone with a mesial curvature, comprising an anterior denticulate biting portion (~56% total length), and a slightly shorter posterior non-biting portion (Fig. 2A). There is no evidence from external morphology that the infragnathal formed from two independent components, although this was suggested by Ørvig (1980), and supported by Rücklin et al. (2012). We have identified only a single ossification centre for this element.

The anterior biting portion was stated to contain two main longitudinal denticle rows (Hu et al., 2017), in detail with ~44 prominent denticles (Fig. 2B) that we now interpret to comprise up to six radiating rows. In contrast to the anterior and posterior supragnathals, in which an area of denticles remains mostly unworn, all denticles on the infragnathal shows significant wear as they bite to the supragnathals. In lateral view (Fig. 2A, right element with image mirrored), a distinct ridge (Fig. 2A, ri) forms a boundary between the denticle zone (Fig. 2A, d.z) and a ventral smooth zone (Fig. 2A, s.z). The lateral longitudinal row comprises ~26 denticles, with larger denticles at each end and smaller crowded denticles about the middle third. In the middle, these smaller crowded denticles are interrupted by a semicircular pit-like depression surrounded by a rim, which is interpreted as the ossification centre (Fig. 2A, B, oss). The fact that the denticles progressively reduce in size from both ends is consistent with regulation by growth of the infragnathal from this ossification centre. A similar pattern has been noted on the main longitudinal denticle row of the infragnathal in more advanced arthrodires like *Plourdosteus* (Ørvig, 1980) and *Compagopiscis* (Rücklin et al., 2012, fig. 3).

These rows are also described using the 'dental field' terminology of Ørvig (1980). The lateral longitudinal row (Fig. 2B, right element with image mirrored) shows an anterior series increasing in size anteriorly, and a posterior series increasing in size posteriorly, each series consisting of 12 denticles (Fig. 2B, df.al, df.pl). These can be compared with the anterior and posterior 'dental fields' as identified in the infragnathal of advanced arthrodires (Fig. 3C; dfa, dfp of Ørvig, 1980, figs. 18, 20). The denticles in the new specimen are labelled from 1 to 12 according to different generations, with the biggest being the youngest (number 12) and the smallest the oldest (number 1). The mesial longitudinal row has less numerous and more irregularly sized denticles, but we interpret six more widely spaced denticles in front of the ossification centre as an anterior mesial row (Fig. 2B, df.am), again with the biggest denticles (numbers 5, 6) at the front. Behind the ossification centre, small and big denticles are mixed without particular order, but alternate mesial then lateral denticles can be interpreted to form three radiating rows (Fig. 2B, df.pm1–3) comprising 3, 5 and 5 denticles. One large denticle (Fig. 2B, df.m) closest to the ossification centre is anomalous, but can be interpreted to represent the last generation, i.e., a new denticle row with no previous denticles, because it attains a similar size to the last several generations in the other dental fields. The previously removed left infragnathal was broken in two pieces, and the anterior piece has been scanned at high resolution for digital extraction of internal histology (work in progress). This piece (Fig. 2C) shows essentially the same denticle arrangement as the anterior end of the right infragnathal. Internal structure of the anterior-most denticle is shown as a section in relation to the Meckel's cartilage in Fig. 3B.

4. Discussion

Based on the above descriptions, all three gnathal elements in this Early Devonian brachythoracid arthrodire ANU V244

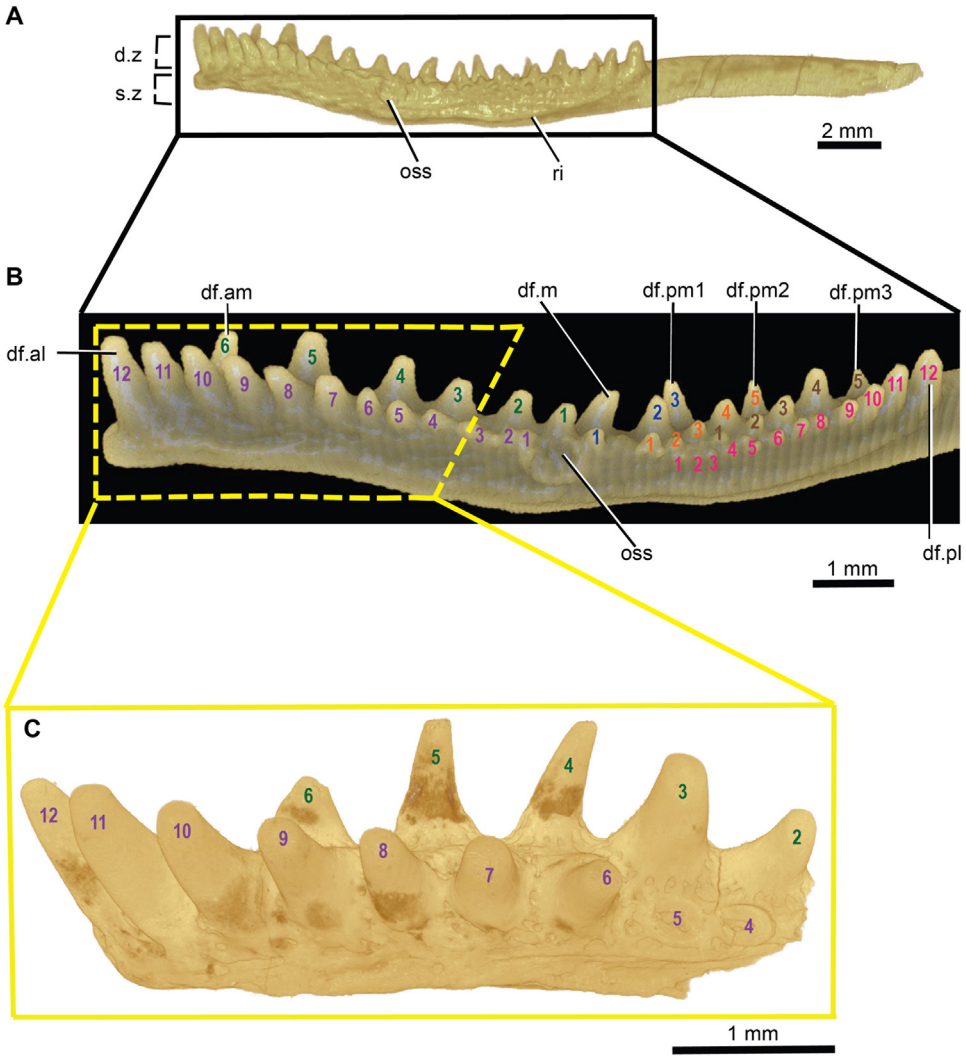

Fig. 2. Infragnathal of buchanosteid arthrodire (ANU V244). (A) In left lateral view (mirrored image of the right element). (B) Enlargement of boxed area in (A). (C) Broken end of the left infragnathal in dorsolateral view. Yellow boxed area of (B) shows the corresponding part of the right infragnathal. Abbreviations: d.z, denticle zone; df.al, anterolateral dental field; df.am, anteromesial dental field; df.m, mesial row (single denticle in a new dental field); df.pl, posterolateral dental field; df.pm1-3, posteromesial dental field 1-3; oss, ossification centre; ri, ridge.

are characterised by numerous radiating denticle rows. Ossification centres for the anterior and posterior supragnathals are respectively placed anterolaterally and anteromesially, adjacent to the ethmoid articulation between the palatoquadrate and the braincase (Hu et al., 2017), and approximating the ossification centre position for these elements in advanced brachythoracids. However, in the latter the denticle rows are much reduced to one or two dental fields (Fig. 4, node C; Ørvig, 1980; Smith et al., 2009) along the outer (labial) margins of these bones, and the posteromesial denticle rows have disappeared. As summarised by Young et al. (2001) for advanced brachythoracids, enlarged denticles along the labial margin of both supragnathals coalesced as a vertical ridge forming the main body of the bone, and the posterior part lost its denticles and is much reduced, except adjacent to the ethmoid articulation between the autopalatine and the braincase, where both elements have pronounced posterior processes. In general aspect the upper gnathal elements resemble more those of the phlyctaeniid arthrodires *Dicksonosteus* and *Arctolepis decipiens* as illustrated by Goujet (1984, figs. 74, 82). Another basal arthrodire, *Actinolepis spinosa* Mark-Kurik, 1985, shows significantly larger denticles than *Dicksonosteus* and *Arctolepis decipiens*, presumably a variation for different feeding adaptation. The occlusal aspect of gnathal elements in *Actinolepis spinosa* is not shown, but it seems the denticles were also arranged in sequentially added dental rows or fields radiated from the ossification centre (Mark-Kurik, 1985,fig. 3). The gnathal elements and the associated dentiton of *Cowralepis*, a phyllolepid placoderm (Ritchie, 2005, fig. 10), seem to resemble the condition in our specimen. Young et al. (2001) suggested that a significant difference was the position of the ossification centre on the anterior supragnathal in ANU V244, but at that time this element was erroneously interpreted to come from the opposite side; in fact the ossification centre has a similar position in *Arctolepis* and ANU V244. Compared to the above arthodires, the ossification centre was evidently more centrally located on the anterior supragnathal of *Romundina* and related acanthothoracids, based on the interpretation by Smith et al. (2017).

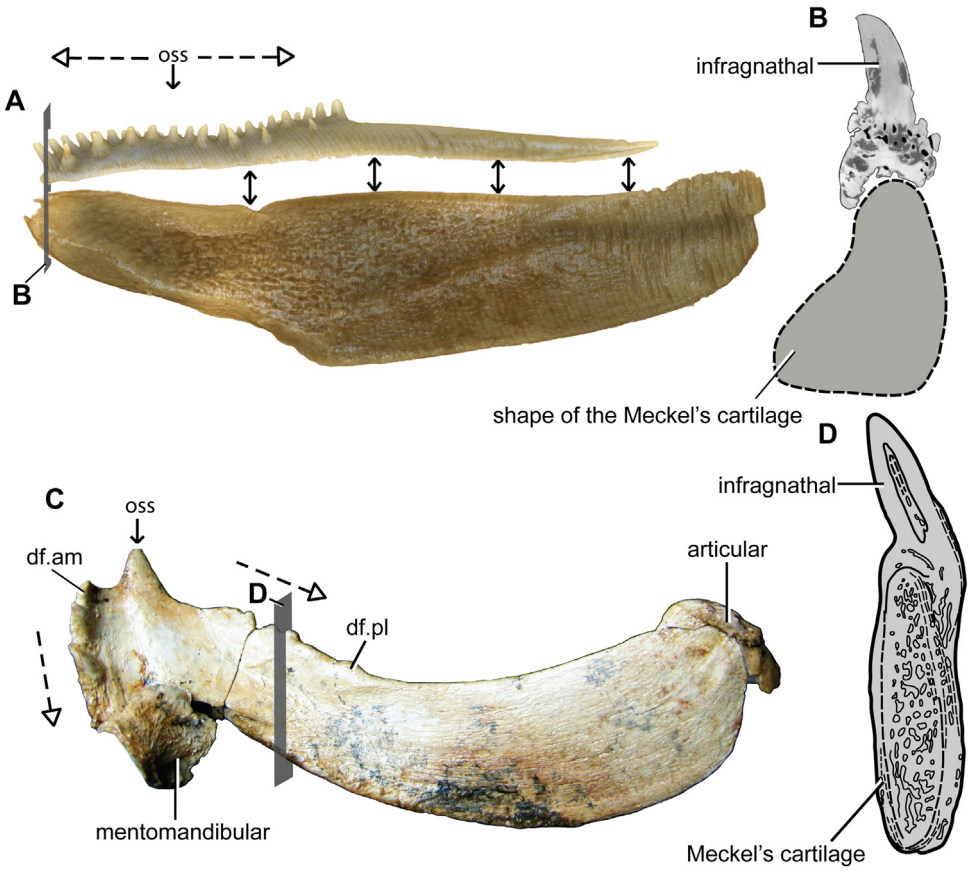

Fig. 3. Transformation in the arthrodire lower jaw from mainly endoskeletal (e.g., buchanosteid arthrodire) to mainly dermal structural components in eubrachythoracids. (A) Inner view of the right infragnathal with its interpreted position on Meckel's cartilage (ANU V244), showing inferred growth direction (dashed arrows). (B) Vertical cross section of anterior-most denticle against the shape of Meckel's cartilage at the level indicated in (A). (C) Right infragnathal of *Kimberleyichthys* (ANU 35687) in mesial view (ossifications of Meckel's cartilage, mentomandibular and articular attached). (D) Drawing of the vertical cross section of the infragnathal of *Compagopiscis* (adapted from Rücklin et al., 2012, Fig. 2f) at the approximate level for *Kimberleyichthys* as shown in (C). Not to scale. Dashed arrows indicate growth direction from ossification centre. Abbreviations: df.am, anteromesial dental field; df.pl, posterolateral dental field; oss, ossification centre.

For the infragnathal, general growth is interpreted in terms of bone and denticle rows growing mainly forwards and backwards from the ossification centre (Fig. 3A, dashed arrows), with no obvious downwards growth. In contrast, advanced brachythoracids, such as *Compagopiscis*, had much stronger vertical growth, to form the deep blade of the infragnathal (absent in this early buchanosteid arthrodire, where the lower jaw was supported instead by a massive single meckelian cartilage ossification (Hu et al., 2017)). We suggest that the strong vertical growth in advanced arthrodires caused some denticle rows also to become vertical, as illustrated by Ørvig (1980, figs. 18, 20) and Rücklin et al. (2012, fig. 2h, i). This is illustrated for the infragnathal of *Kimberleyichthys* from Gogo in Fig. 3C. The approximate level of the cross section of *Compagopiscis* (Fig. 3D) is indicated on our *Kimberleyichthys* specimen (Fig. 3C, 'D').

The Silurian 'maxillate' placoderms *Entelognathus* and *Qilinyu* from China (Fig. 4, node E; Zhu et al., 2013, 2016) indicate that osteichthyan-like marginal jaw bones may have been primitively present in placoderms. *Qilinyu* shows the same extra dermal bones in the jaw margin that were homologized in *Entelognathus* with the premaxilla and maxilla (upper jaw) and dentary (lower jaw) of osteichthyans. These bones are folded inside the jaw margins, the internal part presumably providing a biting surface. *Qilinyu* also has an infolded part on the 'dentary' equivalent of the lower jaw (this was absent in *Entelognathus*). Zhu et al. (2016) proposed a one-to-one homology with the standard three gnathal bones of various placoderms: premaxilla = anterior supragnathal (on the braincase); maxilla = posterior supragnathal (on the palatoquadrate); dentary = infragnathal (on the Meckel's cartilage). The gnathal plates of *Entelognathus* were described as having 'close-packed rounded tubercles', with 'no teeth or cusps on the oral margin' (Zhu et al., 2013, p. 190). This tuberculation was evidently similar to that on the facial dermal bones, and differs from the arthrodire condition, in which the gnathal plates bear odontode units that differ from the ornament on the rest of dermal skeleton in being more pointed (denticulate). However, new observations suggest that the oral odontode units in *Entelognathus* were likely composed of needle-sharp cusps instead of blunt tuberculation, and the organization of the dentition is not yet described in mechanically prepared specimens (M. Zhu, 2018, personal communication).

All three gnathal elements in ANU V244 are entirely inside the mouth, with no contact to external dermal bones of the cheek (see Hu et al., 2017, fig. 2a). Previously (e.g., Stensiö, 1963,

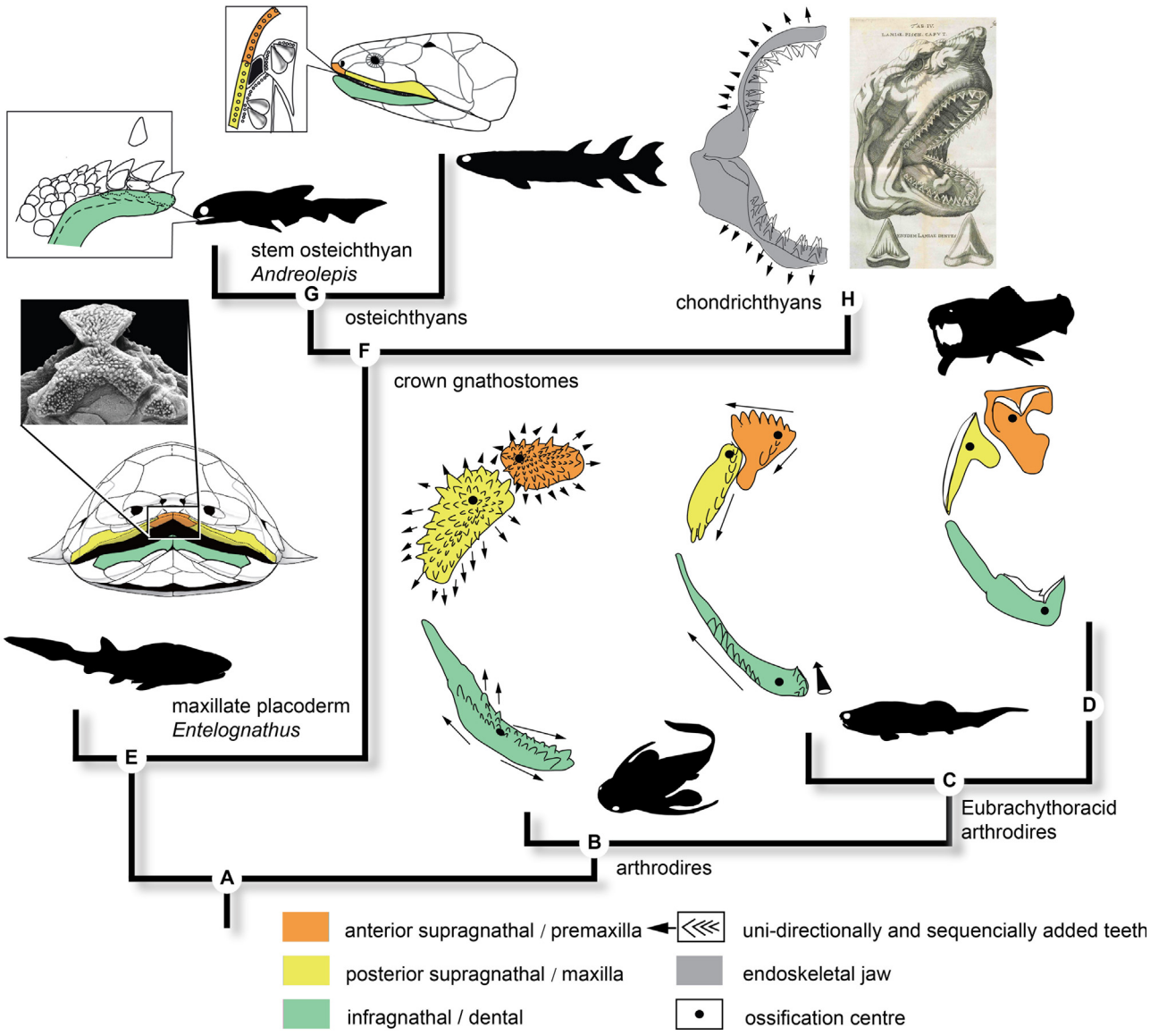

Fig. 4. Suggested evolution of dermal gnathal bones and dental organizations in early gnathostomes. The phylogeny is simplified from (Zhu et al., 2016). The gnathal plates of arthrodires (above node B, C, and D) are shown in occlusal view, the arrowhead in perspective indicates the vertical growth of the denticle row. Key character acquisition at each alphabetic node: (A) [Jawed vertebrate], origin of jaws, dermal jaw bones and the associated dentition; (B) [arthrodires], gnathal elements with extensive palatal laminae but without a facial lamina, non-shedding dentition, new teeth added in each of the many dental fields radially from the ossification centre; (C) [eubrachythoracid arthrodire], fewer dental fields, resembling the linear row of marginal teeth in osteichthyans; (D) [higher eubrachythoracids], dentition functionally replaced by reorganized shearing edges resulting from earlier wear of gnathal element; (E) ['maxillate' placoderm plus higher gnathostomes], marginal jaw bones with facial and palatal laminae; (F) [crown gnathostomes], teeth that can be shed and replaced; (G) [osteichthyans] teeth shed by basal-resorption, monolinear tooth row on marginal jaw bones (except in most primitive taxa, e.g., *Andreolepis*); (H) [chondrichthyans] loss of bone, teeth shed and replaced in a "conveyor belt" style.

1969) the arthrodire anterior supragnathal was equated with the osteichthyan inner dental arcade, i.e., vomer (both sitting on the braincase adjacent to the ethmoid articulation with the palatoquadrate). The posterior supragnathal was (partly or entirely) considered the homologue of the osteichthan dermopalatine (both sitting on the palatoquadrate just across the ethmoid articulation). Our new evidence sheds no new light on this, given that vomers and dermopalatines (and other denticulate bones inside the osteichthyan mouth; pterygoids, coronoids etc.) represent additional bones under these proposed homologies. There is always an unresolvable problem in proposing bone homologies between taxa involving an unequal number of bones, because it cannot be known without further data whether the additional bones arose *de novo*, or resulted from subdivision of existing bones. Thus, the three gnathal bones inside the mouth of *Qilinyu* could have subdivided to give the more numerous denticulate bones inside the mouth of typical osteichthyans, but this seems unlikely because in other respects *Qilinyu* is more 'placoderm-like' than *Entelognathus*. For example, it lacks the additional dermal bones on and between the lower jaws of *Entelognathus*, which makes that form very 'osteichthyan-like'. Instead, *Qilinyu* has a large ventral space under the head, between the jaws and the front of the trunk-armour, as in our arthrodire ANU V244 (Fig. 1A).

5. Conclusion

The dental structures on articulated gnathal plates of an Early Devonian arthrodire (ANU V244) have been reinterpreted, correcting previous erroneous identifications. The dentition in this specimen is composed of dental fields radiating from the ossification centre, with the largest and youngest generation of denticles lining the margin of the supragnathal elements. This condition presumably provided good grip, and is probably shared in primitive arthrodires including basal brachythoracids. In the eubrachythoracid arthrodires, however, dental fields are either very limited in number or even lost in re-organization of the dentition into specialized feeding structures such as cusps, serrations, and edges in advanced eubrachythoracids, providing much more versatile feeding adaptations that are functionally comparable to, but phylogenetically independent of the crown gnathostomes. Based on the evidence provided by Silurian 'maxillate' placoderms, the gnathal plates in arthrodires are currently hypothesized to be homologous to the osteichthyan marginal jaw bones. However, due to the poorly understood organization in the dentition of the 'maxillate' placoderms, the question remains how the organization and growth of dentition in arthrodires is linked to the very different condition in crown gnathostomes. Additional morphological and histological data in arthrodires, maxillate and other placoderms, and in the earliest crown gnathostomes are required to bridge this large evolutionary gap, and provide more insights into the earliest evolution of jaws and teeth in crown gnathostomes.

Acknowledgements

This research has been supported by the Strategic Priority Research Program of Chinese Academy of Sciences (Grant No. XDB26000000), Australian Research Council Discovery grants DP1092870 and DP140104161. J.L. was supported by the National Natural Science Foundation of China (41872023 and 41530102), and by a Director's strategic postdoctoral fellowship in the ANU Research School of Physics & Engineering. Y.Z. was supported by Swedish Research Council grant 2014-4102 and a Wallenberg Scholarship from the Knut and Alice Wallenberg Foundation, both awarded to Per E. Ahlberg. C.B. acknowledges the support of the Queensland Museum. We thank Tatsuya Hirasawa and Oskar Bremer for providing valuable suggestions during the review process of the paper. We thank Mike Turner for micro-CT Scanning and Tim Senden for his support towards palaeontology. We thank Ajay Limaye for helping with improving segmentations, updating and developing Drishti for scientific illustration and segmentation features.

References

Brazeau, M.D., 2009. The braincase and jaws of a Devonian 'acanthodian' and modern gnathostome origins. Nature 457, 305–308.

Brazeau, M.D., Friedman, M., 2015. The origin and early phylogenetic history of jawed vertebrates. Nature 520, 490–497.

Burrow, C.J., 2003. Comment on separate evolutionary origins of teeth from evidence in fossil jawed vertebrates. Science 300, 1661.

Burrow, C., Hu, Y.Z., Young, G., 2016. Placoderms and the evolutionary origin of teeth: a comment on Rücklin & Donoghue (2015). Biology Letters 12, 20160159.

Chen, D.L., Blom, H., Sanchez, S., Tafforeau, P., Ahlberg, P.E., 2016. The stem osteichthyan Andreolepis and the origin of tooth replacement. Nature 539, 237–241.

Chen, D.L., Blom, H., Sanchez, S., Tafforeau, P., Marss, T., Ahlberg, P.E., 2017. Development of cyclic shedding teeth from semi-shedding teeth: the inner dental arcade of the stem osteichthyan *Lophosteus*. Royal Society Open Science 4, 161084.

Davis, S.P., Finarelli, J.A., Coates, M.I., 2012. *Acanthodes* and shark-like conditions in the last common ancestor of modern gnathostomes. Nature 486, 247–250.

Denison, R.H., 1978. Placodermi. In: Schultze, H.-P. (Ed.), Handbook of Paleoichthyology, Vol. 2. Gustav Fischer Verlag, Stuttgart, pp. 1–128.

Dennis-Bryan, K., 1987. A new species of eastmanosteid arthrodire (Pisces: Placodermi) from Gogo, Western Australia. Zoological Journal of the Linnean Society 90, 1–64.

Donoghue, P.C.J., Rücklin, M., 2016. The ins and outs of the evolutionary origin of teeth. Evolution & Development 18, 19–30.

Dupret, V., Sanchez, S., Goujet, D., Tafforeau, P., Ahlberg, P.E., 2014. A primitive placoderm sheds light on the origin of the jawed vertebrate face. Nature 507, 500–503.

Giles, S., Rücklin, M., Donoghue, P.C.J., 2013. Histology of "placoderm" dermal skeletons: implications for the nature of the ancestral gnathostome. Journal of Morphology 274, 627–644.

Giles, S., Friedman, M., Brazeau, M.D., 2015. Osteichthyan-like cranial conditions in an Early Devonian stem gnathostome. Nature 520, 82–85.

Goujet, D.F., 1984. Les poissons placodermes du Spitsberg. Arthrodires Dolichothoraci de la Formation de Wood Bay (Dévonien inférieur). Editions Centre National Recherche Scientifique, Cahiers de Paléontologie, Paris, 284 pp.

Goujet, D.F., Young, G.C., 2004. Placoderm anatomy and phylogeny: new insights. In: Arratia, G., Wilson, M.V.H., Cloutier, R. (Eds.), Recent Advances in the Origin and Early Radiation of Vertebrates. Verlag Dr. Friedrich Pfeil, München, pp. 109–126.

Hu, Y.Z., Lu, J., Young, G.C., 2017. New findings in a 400 million-year-old Devonian placoderm shed light on jaw structure and function in basal gnathostomes. Scientific Reports 7, 1–12.

Janvier, P., 1996. Early Vertebrates. Clarendon Press, Oxford, 408 pp.

Johanson, Z., Smith, M.M., 2003. Placoderm fishes, pharyngeal denticles, and the vertebrate dentition. Journal of Morphology 257, 289–307.

Johanson, Z., Smith, M.M., 2005. Origin and evolution of gnathostome dentitions: a question of teeth and pharyngeal denticles in placoderms. Biological Reviews 80, 303–345.

King, B., Qiao, T., Lee, M.S.Y., Zhu, M., Long, J.A., 2017. Bayesian morphological clock methods resurrect placoderm monophyly and reveal rapid early evolution in jawed vertebrates. Systematic Biology 66, 499–516.

Long, J.A., 1995. A new plourdosteid arthrodire from the Upper Devonian Gogo Formation of Western Australia. Palaeontology 38, 39–62.

Long, J.A., Mark-kurik, E., Johanson, Z., Lee, M.S., Young, G.C., Zhu, M., Ahlberg, P.E., Newman, M., Jones, R., Blaauwen, J.D., Choo, B., Trinajstic, K., 2015. Copulation in antiarch placoderms and the origin of gnathostome internal fertilization. Nature 517, 196–199.

Mark-Kurik, E., 1985. *Actinolepis spinosa* n. sp. (Arthrodira) from the Early Devonian of Latvia. Journal of Vertebrate Paleontology 5, 287–292.

Ørvig, T., 1980. Histologic studies of ostracoderms, placoderms and fossil elasmobranchs 3. Structure and growth of gnathalia of certain arthrodires. Zoologica Scripta 9, 141–159.

Qiao, T., King, B., Long, J.A., Ahlberg, P.E., Zhu, M., 2016. Early gnathostome phylogeny revisited: multiple method consensus. PLoS One 11, e0163157, http://dx.doi.org/10.1371/journal.pone.0163157.

Reif, W.-E., 1982. Evolution of dermal skeleton and dentition in vertebrates: the odontode regulation theory. Evolutionary Biology 15, 287–368.

Ritchie, A., 2005. *Cowralepis*, a new genus of phyllolepid fish (Pisces, Placodermi) from the Late Middle Devonian of New South Wales, Australia. Proceedings of the Linnean Society of New South Wales 126, 215–259.

Rücklin, M., Donoghue, P.C., 2015. *Romundina* and the evolutionary origin of teeth. Biology Letters 11, 20150326.

Rücklin, M., Donoghue, P.C.J., Johanson, Z., Trinajstic, K., Marone, F., Stampanoni, M., 2012. Development of teeth and jaws in the earliest jawed vertebrates. Nature 491, 748–751.

Smith, M.M., Johanson, Z., 2003a. Response to comment on separate evolutionary origins of teeth from evidence in fossil jawed vertebrates. Science 300, 1661.

Smith, M.M., Johanson, Z., 2003b. Separate evolutionary origins of teeth from evidence in fossil jawed vertebrates. Science 299, 1235–1236.

Smith, M.M., Fraser, G.J., Mitsiadis, T.A., 2009. Dental lamina as source of odontogenic stem cells: evolutionary origins and developmental control of tooth generation in gnathostomes. Journal of Experimental Zoology Part B: Molecular and Developmental Evolution 312B, 260–280.

Smith, M.M., Clark, B., Goujet, D., Johanson, Z., Smith, A., 2017. Evolutionary origins of teeth in jawed vertebrates: conflicting data from acanthothoracid dental plates ('Placodermi'). Palaeontology 60, 829–836.

Stensiö, E.A., 1963. Anatomical studies on the arthrodiran head. Part 1. preface, geological and geographical distribution, the organization of the head in the Dolichothoraci, Coccosteomorphi and Pachyosteomorphi. Taxonomic appendix. Kungliga Svenska Vetenskapsakademiens Handlingar 9, 1–419.

Stensiö, E.A., 1969. Elasmobranchiomorphi Placodermata Arthrodires. In: Piveteau, J. (Ed.), Traité de Paléontologie. Masson, Paris, pp. 71–642.

Young, G.C., 2003. Did placoderm fish have teeth? Journal of Vertebrate Paleontology 23, 987–990.

Young, G.C., 2010. Placoderms (armored fish): dominant vertebrates of the Devonian period. Annual Review of Earth and Planetary Sciences 38, 523–550.

Young, G.C., Lelièvre, H., Goujet, D., 2001. Primitive jaw structure in an articulated brachythoracid arthrodire (placoderm fish; Early Devonian) from southeastern Australia. Journal of Vertebrate Paleontology 21, 670–678.

Zhu, M., Yu, X.B., Ahlberg, P.E., Choo, B., Lu, J., Qiao, T., Qu, Q.M., Zhao, W.J., Jia, L.T., Blom, H., Zhu, Y.A., 2013. A Silurian placoderm with osteichthyan-like marginal jaw bones. Nature 502, 188–193.

Zhu, M., Ahlberg, P.E., Pan, Z.H., Zhu, Y.A., Qiao, T., Zhao, W.J., Jia, L.T., Lu, J., 2016. A Silurian maxillate placoderm illuminates jaw evolution. Science 354, 334–336.

Zhu, Y.A., Zhu, M., 2013. A redescription of *Kiangyousteus yohii* (Arthrodira: Eubrachythoraci) from the Middle Devonian of China, with remarks on the systematics of the Eubrachythoraci. Zoological Journal of the Linnean Society 169, 798–819.

Appendix E pdf of Hu et al. 2020 (Paper 4)

Hu, Y., Limaye, A., Lu, J., 2020. Three-dimensional segmentation of computed tomography data using *Drishti Paint*: new tools and developments. R. Soc. Open Sci. 7, 201033. https://doi.org/10.1098/rsos.201033

ROYAL SOCIETY OPEN SCIENCE

royalsocietypublishing.org/journal/rsos

Research

Cite this article: Hu Y, Limaye A, Lu J. 2020 Three-dimensional segmentation of computed tomography data using *Drishti Paint*: new tools and developments. *R. Soc. Open Sci.* **7**: 201033. https://doi.org/10.1098/rsos.201033

Received: 8 June 2020
Accepted: 24 November 2020

Subject Category:
Earth and environmental science

Subject Areas:
palaeontology/image processing/software

Keywords:
three-dimensional segmentation, *Drishti Paint*, computed tomography, 3D Freeform Painter, gradient threshold

Author for correspondence:
Jing Lu
e-mail: lujing@ivpp.ac.cn

Electronic supplementary material is available online at https://doi.org/10.6084/m9.figshare.c.5230339.

THE ROYAL SOCIETY PUBLISHING

Three-dimensional segmentation of computed tomography data using *Drishti Paint*: new tools and developments

Yuzhi Hu[1,2], Ajay Limaye[3] and Jing Lu[4]

[1]Department of Applied Mathematics, Research School of Physics, Australian National University, Canberra, ACT 2601, Australia
[2]Research School of Earth Sciences, Australian National University, Canberra, ACT 2601, Australia
[3]National Computational Infrastructure, Building 143, Corner of Ward Road and Garran Road, Ward Rd, Canberra, ACT 2601, Australia
[4]Institute of Vertebrate Paleontology and Paleoanthropology, Chinese Academy of Sciences, Beijing 100044, People's Republic of China

YH, 0000-0002-4794-0935; JL, 0000-0002-5791-4749

Computed tomography (CT) has become very widely used in scientific and medical research and industry for its non-destructive and high-resolution means of detecting internal structure. Three-dimensional segmentation of computed tomography data sheds light on internal features of target objects. Three-dimensional segmentation of CT data is supported by various well-established software programs, but the powerful functionalities and capabilities of open-source software have not been fully revealed. Here, we present a new release of the open-source volume exploration, rendering and three-dimensional segmentation software, *Drishti* v. 2.7. We introduce a new tool for thresholding volume data (i.e. gradient thresholding) and a protocol for performing three-dimensional segmentation using the 3D Freeform Painter tool. These new tools and workflow enable more accurate and precise digital reconstruction, three-dimensional modelling and three-dimensional printing results. We use scan data of a fossil fish as a case study, but our procedure is widely applicable in biological, medical and industrial research.

1. Introduction

Computed tomography (CT) has become widely used in medical, scientific and industrial research [1–5]. To have a better understanding of the data generated from CT, micro-CT and

synchrotron radiation phase-contrast imaging, three-dimensional scientific visualization has become more and more crucial for researchers to obtain better insights [6–9]. For over three decades, the field of three-dimensional scientific visualization has been developed considerably with many new techniques to visualize and analyse data more accurately [10–19]. Two techniques have emerged to provide different visualizations: surface rendering, the method of interpreting datasets by generating a set of polygons that represent surfaces of the desired feature; and volume rendering [10], for the reconstruction of three-dimensional structures both internally and externally. Volume rendering represents three-dimensional objects as a collection of cube-like building blocks called voxels, or volume elements. A range of well-established commercial software, such as Mimics, VG Studio and AVIZO provide numerous functionalities and good rendering outputs. However, the potential of open-source software, which is both freely available and easy to access, has not been fully explored. Three-dimensional segmentation, segmenting the internal region of interest in sequences of images, is a vital tool for investigating and understanding the internal structures of target objects [6,20–22]. Two-dimensional segmentation uses each image or slice in a volumetric dataset to construct a three-dimensional presentation. By contrast, three-dimensional segmenting methods, the main focus of this paper, use thresholding, edge detection, clustering or region growing techniques to group pixels based on brightness, colour or texture [21], and then render them as discrete objects.

Among 10 well-known cross-platform software programs [23], five use both surface and volume rendering, but only *Drishti* [24] with 'an intuitive user interface' [23], can perform three-dimensional segmentation directly on a volume (using the new tool presented here, 3D Freeform Painter). *Drishti* uses direct volume rendering with voxel ray casting and texture slicing algorithms; combinations of local and global illuminations along with a two-dimensional transfer function which merges colour and opacity to volume to provide realism on different materials and textures through lighting, shading or shadowing via different user-generated light volumes and change of opacity. As an open-source volume exploration and rendering software [24], *Drishti* has demonstrated three-dimensional rendering of high quality [6,25–27].

Here, we present the most recent release of *Drishti* v. 2.7, and introduce new tools for three-dimensional segmentation (two- and three-dimensional painters) of volumetric data. We also introduce a new tool-gradient threshold and suggest protocols for how to perform three-dimensional segmentation using *Drishti Paint* v. 2.7 efficiently and precisely, using the CT scan data of a fossil fish as a case study. New features in *Drishti*, such as mesh generation and simplification, are also explained and discussed.

Volume rendering does require datasets to be loaded into graphics memory. The minimum requirements to run *Drishti* are graphics processing unit (GPU)—a graphics card with 1 GB memory—and random access memory (RAM)—4GB. *Drishti* does not have a specific requirement for the central processing unit (CPU). For readers who do not have much computing power, we suggest trying other open-source software such as SPIERS [28] and 3D Slicer [29,30]. Both software perform excellent surface rendering and allow meshes to be handled, which can then be modified in Meshlab [31] or Blender [32].

2. Materials and methods

2.1. Materials

The CT data used for this study is from a 400-million-year-old fossil fish from Burrinjuck, near Canberra, southeastern Australia (ANU V244, held at the Department of Applied Mathematics, Research School of Physics, Australian National University, Canberra). The whole specimen was scanned in 2011 and rescanned in 2015 at CT Lab, ANU [33]. The voxel size of the second scan is 21 µm.

2.2. Methods

CT data were reconstructed using an in-house software called *Mango* (https://physics.anu.edu.au/appmaths/capabilities/mango.php). *Mango* can perform three-dimensional tomographic reconstruction on CPU or GPU clusters. The CPU-only code is limited to analytic methods: Feldkamp–Davis–Kress (FDK) filtered back-projection (FBP) for a circular X-ray source trajectory and Katsevich FBP for helical/double-helical X-ray source trajectories [34]. The GPU code can also perform multi-grid iterative reconstruction [35] for a space-filling X-ray source trajectory [1]. The reconstruction code has software for automatic geometric alignment capabilities [36], X-ray source movement correction [37] and component or rigid-body sample movement correction [38].

The original whole specimen CT dataset was saved as 16-bit images. These data were loaded into *Drishti Import* v. 2.7. The contrast was incremented with the help of histograms, and slices were filtered by selecting the best range on the tomogram. The raw data of the whole specimen was then cropped to focus on a

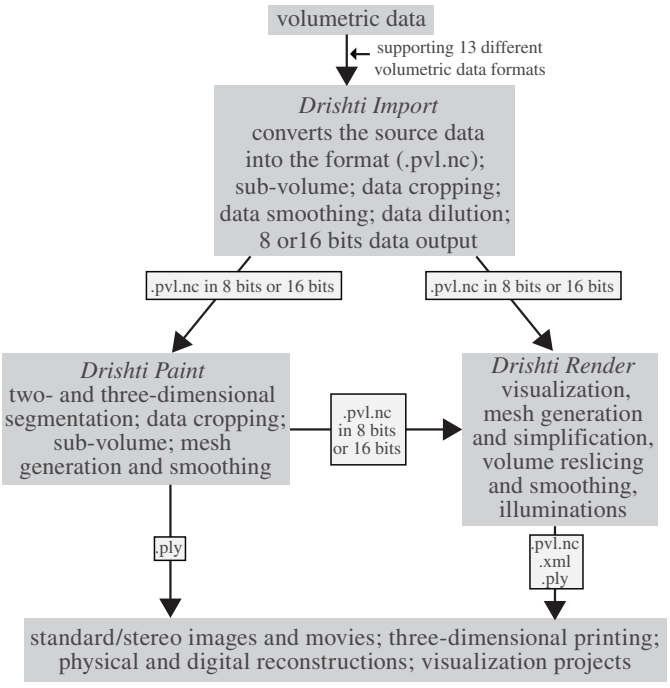

Figure 1. The general workflow for operating *Drishti* v. 2.7. Data formats in this figure are given as abbreviations, for which detailed information is presented in the electronic supplementary material, table S1.

selected region for the right cheek complex, which was segmented out and is used as a case study here. Raw data of the selected region of interest was saved in the format *.pvl.nc (i.e. processed volume format) and can be downloaded from figshare: https://doi.org/10.6084/m9.figshare.12073809. We developed a general protocol to segment the three-dimensional volumetric data using *Drishti Paint* v. 2.7 (see electronic supplementary material for the detailed segmentation procedure).

3. Results and discussion

Here, we highlight the workflow and key features of the *Paint* module for *Drishti* and the general applications of *Drishti*. We have developed a protocol and a workflow, summarized in figure 1, to facilitate a more efficient and accessible (i.e. open-source freeware) means of overcoming the time-intensive nature of preparing fossils digitally and extracting complex information from samples. Detailed information on new tools-gradient thresholding and 3D Freeform Painter are provided in the electronic supplementary material. Our protocol and workflow (figure 1) can be used as a baseline or starting point to be adapted to obtain an ideal result for any given dataset. The electronic supplementary material also provides details on other aspects of *Drishti*, including installation instructions, a summary of all *Drishti*-supported import formats, additional learning resources and other background information.

Three modules, *Drishti Import*, *Drishti Render* and *Drishti Paint*, have different capacities and features, which can be combined to ensure an accurate and precise segmentation along with volume rendering to help visualize a region-of-interest for detailed analysis. *Drishti Paint* uses a variety of discontinuity detection-based and similarity detection-based image segmentation approaches. These two approaches are both implemented in two modes in *Drishti Paint* v. 2.7, i.e. 'Graph Cut' and 'Curve' (previously known as livewire).

The right cheek complex has been segmented from the original CT dataset for our case study. Figure 2 shows an overview of our case study, where a fossil fish skull (figure 2*a*,*b*) is cropped (figure 2*c*) and segmented using the latest tools in *Drishti* v. 2.7 (figure 2*d*–*e*). Processed data is exported as a separate volume by using the tagging function to extract the region of interest. Segmentation (in this cheek complex example) was carried out in 16-bits full resolution in alignment with the raw data to include all information from the original scan (8-bits resolution could be used, if computing power is limited).

Two transformations in mathematical morphology (i.e. dilation and erosion) can be implemented in *Drishti Paint*. Dilation adds pixels to the boundaries of objects in an image, while erosion removes pixels on object boundaries. Morphological dilation makes objects more visible and fills in small holes in objects. Morphological erosion removes islands and small objects so that only substantive objects remain. These two transformations can be used in any order. We used a combination of these two

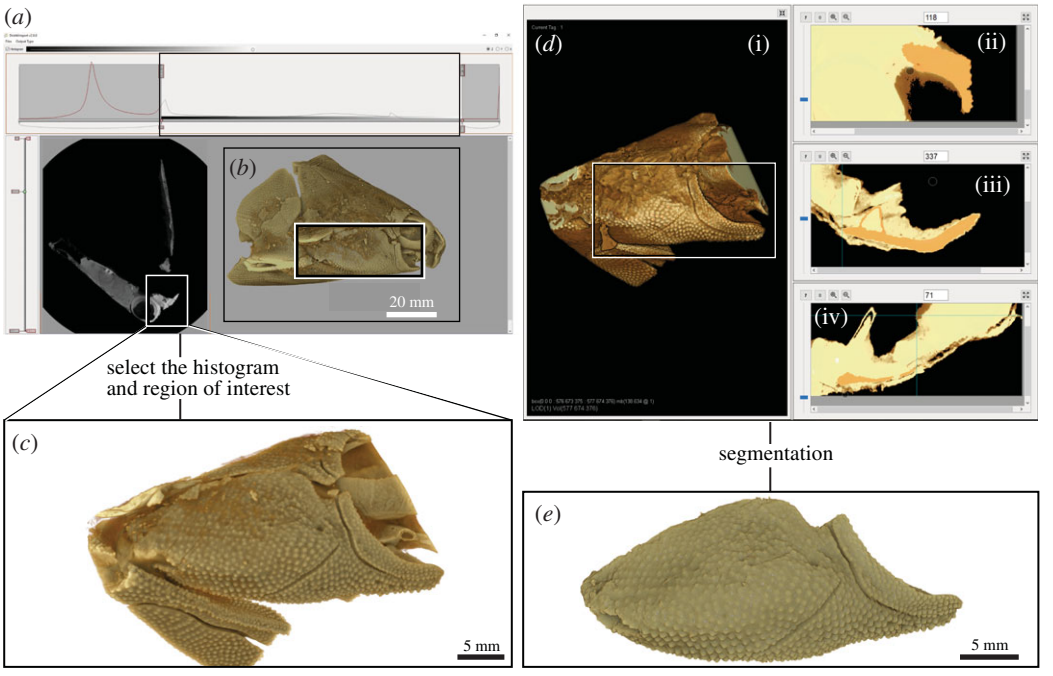

Figure 2. Extracting a three-dimensional virtual volumetric model in *Drishti* v. 2.7. (*a*) original data of the whole fossil fish specimen (V244) used for our case study. (*b*) original data in *Drishti Render* v. 2.7 (right lateral view of skull) showing the selected region of interest (*c*). (*d*) Region of interest in *Drishti Paint* v. 2.7. (*e*) Extracted right cheek complex in *Drishti Render* v. 2.7 (external view).

transformations with Graph Cut and 3D Freeform Painter. These two transformations are more useful when using clean and high-contrast data as there is a risk of changing the morphology of the input datasets by doing multiple transformations. We recommend keeping a copy of the original volume data, before doing multiple transformations, to avoid losing any information of the original dataset. Interpolation is another tool which can be used in Curve mode. However, interpolation is not recommended for palaeontological datasets (due to lack of reproducibility).

Three types of gradient thresholding are developed and implemented in *Drishti Paint* v. 2.7. Values thresholding was developed in *Drishti* v. 2.3.1, but this is the first implementation of gradient thresholding in an open-source volume rendering software program. Gradient thresholding can be combined with values thresholding to clarify and more precisely identify the boundaries between different phases, which then makes the three-dimensional segmentation process easier. Multiple-thresholding (i.e. use both values and gradient thresholding) in *Drishti Paint* v. 2.7 is beneficial for volume segmentation and usually is the first step towards segmenting a volume (figure 2*d*).

In the gradient thresholding tool, gradient type 1 uses the magnitude of central difference (i.e. surface gradient vector). Gradient type 2 takes the sum of all voxel values in one neighbourhood (i.e. $3 \times 3 \times 3$ box), then subtracts the central value from the above sum and divides it by 10. The absolute of the difference between the central value and the above result after dividing by 10 is restricted to a value between 0.0 and 1.0. Gradient type 3 takes the sum of all voxel values in two neighbourhoods (i.e. $5 \times 5 \times 5$ box), then subtracts the central value from the above sum and divides it by 70. As for type 2, the absolute of this difference is also restricted to a value between 0.0 and 1.0. In gradient types 2 and 3, the 'gradient' value is shifted according to the voxel value (i.e. gradients for lower voxel values will be smaller compared to those for higher voxel values). For our case study, type 2 gradient thresholding combined with values thresholding were used to select the range of the histogram for segmenting out the right cheek complex. Gradient thresholding is also sensitive to noise and intensity inhomogeneities. There is no best combination when it comes to which gradient type one should use. Generally speaking, most boundaries can be clarified using gradient types 2 and 3. By contrast, gradient type 1 is more applicable with a cleaner dataset with fewer phases, such as medical datasets.

The segmented right cheek unit has also been extracted as surface meshes (figure 3), which also illustrates the use of the new mesh simplification function in *Drishti* v. 2.7. In this case, the inner surface of the cheek unit is used to test different simplification procedures, because of its more complex structure (the upper jaw cartilage of the fish has surface ossification and is fused to the inside of the cheek bones). The surface mesh data went through different stages of simplification (see electronic supplementary

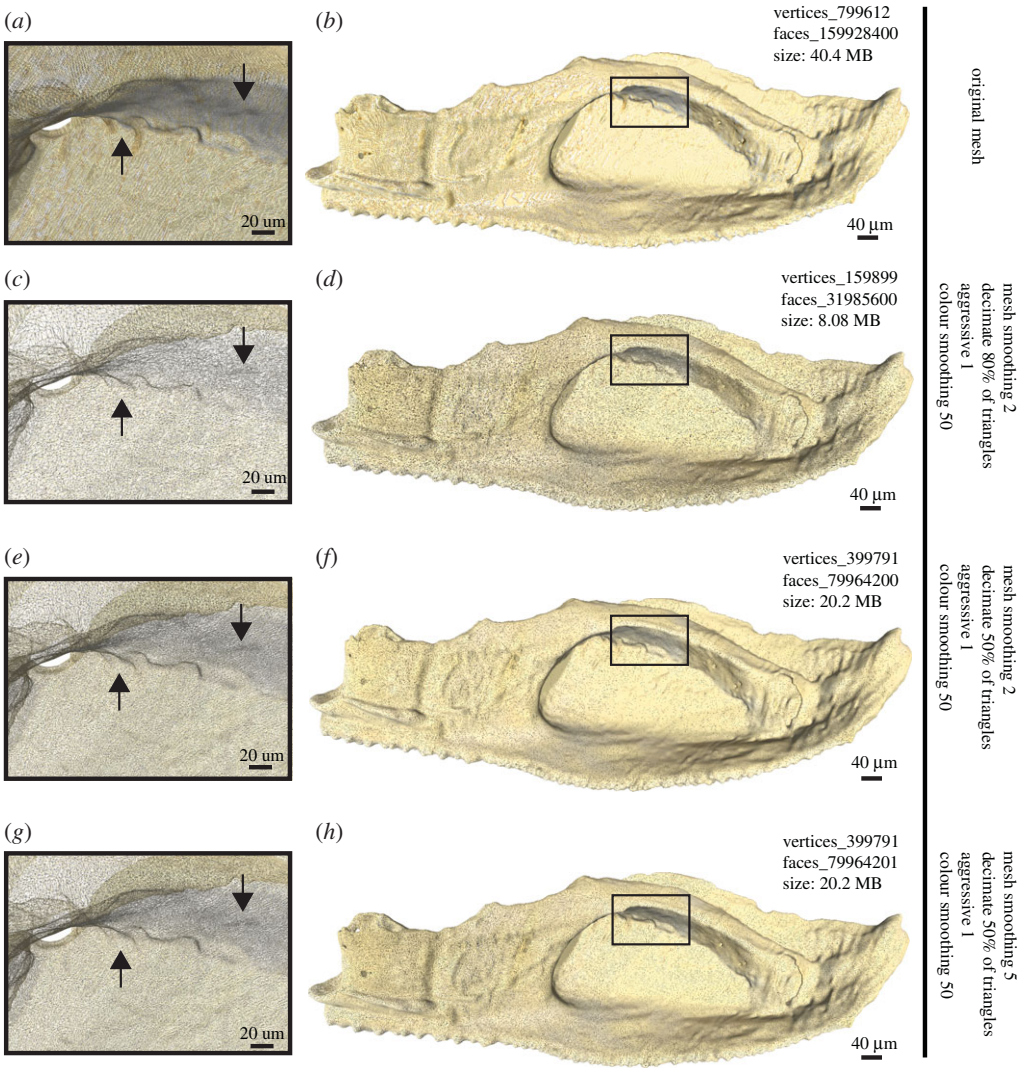

Figure 3. Three-dimensional surface meshes of the extracted right cheek unit of figure 2*e*, showing the inner surface with attached perichondrally ossified jaw cartilages. The differences of vertex count and file size after different mesh simplification applications are summarized for each. The vertex count was calculated in MeshLab v. 1.3.4 [31]. Arrows indicate the reference points for detailed structure compared under the different simplified procedures (see discussion in the text).

material) to produce good quality surface models with relatively small file size. This allows faster physical analysing (e.g. finite-element analysis) and three-dimensional printing. Different mesh simplification gives different number of vertices, which affects the presentation of the information and the detection of details (figure 3*a*,*c*,*e*,*g*). When more triangles have been decimated, the loss of information results in a reduction in file size, which allows for easier sharing of the digital three-dimensional model [20], or uploading the model to an open data repository for educating the public [21]. By comparing the number of details lost or preserved in our case study (arrows in figure 3), a mesh smoothing factor of 2 and 50% decimation is recommended (figure 3*e*,*f*). This halves the data size but still preserves most of the information. Three-dimensional models can then be used to generate three-dimensional printouts [39] or three-dimensional portable documents [40], which can test a previous hypothesis, help with functional morphology investigations, or be used for science communication and public outreach [41].

4. Conclusion

The new tools and proposed workflow to segment volumetric data in the latest *Drishti* version (*Drishti* v. 2.7) are generally accessible to the public, to provide more accurate and precise digital reconstruction, three-dimensional modelling and three-dimensional printing. The protocol and workflow we have developed

can be used as a framework to segment computed tomography data and other forms of volumetric data and is widely applicable in biological, medical and earth science research. Our work will facilitate further cross-discipline collaborations using three-dimensional segmentation of computed tomography data.

Data accessibility. Three-dimensional surface mesh data of the segmented right cheek complex with different levels of simplification and the cropped raw data of the region-of-interest including the right cheek complex are available from the figshare Repository: https://doi.org/10.6084/m9.figshare.12073809.

Drishti v. 2.7 (Windows and Linux versions) and relevant code for this research work are stored in GitHub: https://github.com/nci/drishti and have been archived within the Zenodo repository: https://doi.org/10.5281/zenodo.4092471.

Authors' contributions. J.L. and Y.H. designed the study. Y.H., J.L. and A.L. performed the research and drafted the manuscript. Y.H. and J.L. prepared the figures. A.L. developed *Drishti* v. 2.7. All authors revised the manuscript. Y.H. and A.L. contributed equally.

Competing interests. The authors declare no competing interests.

Funding. This research was funded by the Strategic Priority Research Program of the Chinese Academy of Sciences (grant no. XDB26000000) and the National Natural Science Foundation of China (grant no. 41872023). Y.H. was supported by a Postgraduate Research Scholarship at the Research School of Physics, Australian National University. The development of *Drishti* is supported by National Computational Infrastructure, Australian National University. CT scans and three-dimensional printing are supported by the Department of Applied Mathematics, Research School of Physics and ANU CT Lab, with funding support from Prof. T. Senden and Australian Research Council Discovery Grant DP160102460.

Acknowledgements. We thank Prof. T. Senden (Director, RSPhys, ANU) for provision of facilities, CT scanning and general support for palaeobiological research at ANU. We thank Dr G. Young for help with proofreading; Dr M. Turner for CT scanning; Dr L. Beeching for laboratory support and Dr A. Kingston for help with *Mango*. We thank Dr Russell Garwood for his involvement towards testing the Linux version of *Drishti* v. 2.7. We thank Dr Garwood and another anonymous reviewer for providing valuable suggestions that greatly improved this paper.

References

1. Kingston AM, Myers GR, Latham SJ, Recur B, Li H, Sheppard AP. 2018 Space-filling X-ray source trajectories for efficient scanning in large-angle cone-beam computed tomography. *IEEE Trans. Comput. Imaging* **4**, 447–458. (doi: 10.1109/TCI.2018.2841202)
2. Zhu M, Ahlberg PE, Pan Z, Zhu Y, Qiao T, Zhao W, Jia L, Lu J. 2016 A Silurian maxillate placoderm illuminates jaw evolution. *Science* **354**, 334–336. (doi:10.1126/science.aah3764)
3. Geier B, Sogin EM, Michellod D, Janda M, Kompauer M, Spengler B, Dubilier N, Liebeke M. 2020 Spatial metabolomics of *in situ* host-microbe interactions at the micrometre scale. *Nat. Microbiol.* **5**, 498–510. (doi:10.1038/s41564-019-0664-6)
4. O'Rourke JC, Smyth L, Webb AL, Valter K. 2020 How can we show you, if you can't see it? Trialing the use of an interactive three-dimensional micro-CT model in medical education. *Anat. Sci. Educ.* **13**, 206–217. (doi:10.1002/ase.1890)
5. Taylor GJ, Hall SA, Gren JA, Baird E. 2020 Exploring the visual world of fossilised and modern fungus gnat eyes (Diptera: Keroplatidae) with X-ray microtomography. *J. R. Soc. Interface* **17**, 20190750. (doi:10.1098/rsif.2019.0750)
6. Lautenschlager S. 2016 Reconstructing the past: methods and techniques for the digital restoration of fossils. *R. Soc. Open Sci.* **3**, 160342. (doi:10.1098/rsos.160342)
7. Davies TG *et al.* 2017 Open data and digital morphology. *Proc. R. Soc. B.* **284**, 20170194. (doi:10.1098/rspb.2017.0194)
8. Hoffmann R, Lemanis RE, Falkenberg J, Schneider S, Wesendonk H, Zachow S. 2018 Integrating 2D and 3D shell morphology to disentangle the palaeobiology of ammonoids: a virtual approach. *Palaeontology* **61**, 89–104. (doi:10.1111/pala.12328)
9. Semple TL, Peakall R, Tatarnic NJ. 2019 A comprehensive and user-friendly framework for 3D-data visualisation in invertebrates and other organisms. *J. Morphol.* **280**, 223–231. (doi: 10.1002/jmor.20938)
10. Drebin RA, Carpenter L, Hanrahan P. 1988 Volume rendering. *ACM Siggraph Comput. Graphics* **22**, 65–74. (doi:10.1145/378456.378484)
11. Upson C, Faulhaber T, Kamins D, Laidlaw D, Schlegel D, Vroom J, Gurwitz R, Dam A. 1989 The application visualisation system: a computational environment for scientific visualisation. *IEEE Comput. Graph. Appl.* **9**, 30–42. (doi:10.1109/38.31462)
12. Westover L. 1990 Footprint evaluation for volume rendering. In *Proc. of the 17th Annual Conf. on Computer Graphics and Interactive Techniques*. Dallas, TX: Association for Computing Machinery.
13. Hall PM, Watt AH. 1991 Rapid volume rendering using a boundary-fill guided ray cast algorithm. In *Scientific visualization of physical phenomena* (ed. NM Patrikalakis), pp. 235–249. Tokyo, Japan: Springer.
14. Cabral B, Cam N, Foran J. 1994 Accelerated volume rendering and tomographic reconstruction using texture mapping hardware. In *Proc. of the 1994 Symposium on Volume Visualisation*, pp. 91–98. New York, NY: ACM.
15. Lacroute P, Levoy M. 1994 Fast volume rendering using a shear-warp factorisation of the viewing transformation. In *Proc. of the 21st Annual Conf. on Computer Graphics and Interactive Techniques*, pp. 451–458. New York, NY: ACM.
16. Manssour IH, Furuie SS, Olabarriaga SD, Freitas CM. 2002 Visualising inner structures in multimodal volume data. In *Proc. XV Brazilian Symp. on Computer Graphics and Image Processing.* IEEE.
17. Johnson C. 2004 Top scientific visualisation research problems. *IEEE Comput. Graph. Appl.* **24**, 13–17. (doi:10.1109/MCG.2004.20)
18. Latham SJ, Varslot T, Sheppard A. 2008 Automated registration for augmenting micro-CT 3D images. *Anziam J.* **50**, 534–548. (doi:10.21914/anziamj.v50i0.1389)
19. Brodlie KW *et al.* 2012 *Scientific visualisation: techniques and applications*. Berlin, Germany: Springer Science & Business Media.
20. Lakare S, Kaufman A. 2000 *3D segmentation techniques for medical volumes*, pp. 59–68. Stony Brook, NY: Center for Visual Computing, Department of Computer Science, State University of New York.
21. Kaur D, Kaur Y. 2014 Various image segmentation techniques: a review. *Int. J. Comput. Sci. Mobile Comput.* **3**, 809–814.
22. Carvalho LE, Sobieranski AC, von Wangenheim A. 2018 3D segmentation algorithms for computerized tomographic imaging: a systematic literature review. *J. Digit. Imaging* **31**, 799–850. (doi: 10.1007/s10278-018-0101-z)

23. Buser TJ, Boyd OF, Cortés Á, Donatelli CM, Kolmann MA, Luparell JL, Pfeiffenberger JA, Sidlauskas BL, Summers AP. 2020 The natural historian's guide to the CT galaxy: step-by-step instructions for preparing and analysing computed tomographic (CT) data using cross-platform, open access software. *Integr. Org. Biol.* **2**, 1. (doi:10.1093/iob/obaa009)
24. Limaye A. 2012 Drishti: a volume exploration and presentation tool. In *Developments in X-ray tomography VIII,* vol. 8506, p. 85060X. San Diego, CA: International Society for Optics and Photonics.
25. Cunningham JA, Rahman IA, Lautenschlager S, Rayfield EJ, Donoghue PCJ. 2014 A virtual world of paleontology. *Trends Ecol. Evol.* **29**, 347–357. (doi:10.1016/j.tree.2014.04.004)
26. Johnson EH, Carter AM. 2019 Defossilization: a review of 3D printing in experimental paleontology. *Front. Ecol. Evol.* **7**, 430. (doi: 10.3389/fevo.2019.00430)
27. Sutton M, Rahman I, Garwood R. 2017 Virtual paleontology—an overview. *Paleontol. Soc. Papers* **22**, 1–20. (doi:10.1017/scs.2017.5)
28. Sutton M, Garwood R, Siveter D, Siveter D. 2012 SPIERS and VAXML; a software toolkit for tomographic visualisation and a format for virtual specimen interchange. *Palaeontol. Electron.* **15**, 1–14.
29. Dorador J, Rodríguez-Tovar F. 2020 CroSSED sequence, a new tool for 3D processing in geosciences using the free software 3DSlicer. *Sci. Data* **7**, 1–8. (doi:10.1038/s41597-020-00614-y)
30. Pye F, Raja N, Shirley B, Kocsis Á, Hohmann N, Murdock D, Jarochowska E. 2019 ImageJ and 3D Slicer: open source 2/3D morphometric software. *PeerJ Preprints* **7**, e27998v2. (doi:10.7287/peerj.preprints.27998v2)
31. Cignoni P, Callieri M, Corsini M, Dellepiane M, Ganovelli F, Ranzuglia G. 2008 Meshlab: an open-source mesh processing tool. In *Eurographics Italian Chapter Conf. 2008*, pp. 129–136.
32. Garwood R, Dunlop J. 2014 The walking dead: Blender as a tool for paleontologists with a case study on extinct arachnids. *J. Paleontol.* **88**, 735–746. (doi:10.1666/13-088)
33. Hu Y-Z, Lu J, Young GC. 2017 New findings in a 400 million-year-old Devonian placoderm shed light on jaw structure and function in basal gnathostomes. *Sci. Rep.* **7**, 1–12. (doi:10.1038/s41598-017-07674-y)
34. Varslot T, Kingston A, Myers G, Sheppard A. 2011 High-resolution helical cone-beam micro-CT with theoretically-exact reconstruction from experimental data. *Med. Phys.* **38**, 5459–5476. (doi:10.1118/1.3633900)
35. Myers G, Kingston A, Latham S, Recur B, Li T, Turner M, Beeching L, Sheppard A. 2016 Rapidly converging multigrid reconstruction of cone-beam tomographic data. In *Developments in X-Ray tomography X,* vol. 9967, p. 99671M. San Diego, CA: International Society for Optics and Photonics.
36. Kingston A, Sakellariou A, Varslot T, Myers G, Sheppard A. 2011 Reliable automatic alignment of tomographic projection data by passive auto-focus. *Med. Phys.* **38**, 4934–4945. (doi:10.1118/1.3609096)
37. Myers G, Kingston A, Varslot T, Sheppard A. 2011 Extending reference scan drift correction to high-magnification high-cone-angle tomography. *Opt. Lett.* **36**, 4809–4811. (doi: 10.1364/OL.36.004809)
38. Latham S, Kingston A, Recur B., Myers G, Delgado-Friedrichs O, Sheppard A. 2018 Reprojection alignment for trajectory perturbation estimation in microtomography. *IEEE Trans. Comput. Imaging* **4**, 271–283. (doi:10.1109/TCI.2018.2811945)
39. Hu Y-Z, Young GC, Lu J. 2019 The Upper Devonian tetrapodomorph *Gogonasus andrewsae* from Western Australia: reconstruction of the shoulder girdle and opercular series using X-ray micro-computed tomography. *Palaeoworld* **28**, 535–542. (doi:10.1016/j.palwor.2019.07.008)
40. Tesařová M *et al.* 2019 An interactive and intuitive visualisation method for X-ray computed tomography data of biological samples in 3D portable document format. *Sci. Rep.* **9**, 1–8. (doi:10.1038/s41598-019-51180-2)
41. Rahman I, Adcock K, Garwood R. 2012 Virtual fossils: a new resource for science communication in paleontology. *Evol. Educ. Outreach* **5**, 635–641. (doi:10.1007/s12052-012-0458-2)

Appendix F Supplementary pdf for Hu et al. 2020 (Paper 4)

Hu, Y., Limaye, A., Lu, J., 2020. Supplementary material from “Three-dimensional segmentation of computed tomography data using *Drishti Paint*: new tools and developments.” R. Soc. Open Sci. 7, 201033. https://doi.org/10.6084/m9.figshare.c.5230339.v1

Supplementary materials for

3D segmentation of computed tomography data using *Drishti Paint*: new tools and developments

Yuzhi Hu[1,2], A. Limaye[3], Jing Lu[4]*

[1]Department of Applied Mathematics, Research School of Physics, Australian National University, Canberra, ACT, Australia 2601

[2]Research School of Earth Sciences, Australian National University, Canberra, ACT, Australia 2601

[3]National Computational Infrastructure, Building 143, Corner of Ward Road and Garran Road, Ward Rd, Canberra, ACT, Australia 2601

[4]Institute of Vertebrate Paleontology and Paleoanthropology, Chinese Academy of Sciences, Beijing, China 100044

*Corresponding author: lujing@ivpp.ac.cn

Table of Contents

SUPPLEMENTARY TEXT

This supplementary information covers the necessary installation, user resources, essential background and supported data formats for *Drishti* (Supplementary Table 1).

Drishti has been a part of the emerging new virtual science world (Supplementary Figure 1). From 2012 to the end of 2018, some 14 scientific fields have used the *Drishti* program and benefited from the accessibility, transparency and reproducibility.

Drishti v2.7

Installation

Drishti v2.7 is available to download from https://github.com/nci/*Drishti* under "Releases".

When clicked, it will lead to a version-specific webpage where the.zip file is located at the bottom of the page; click *Drishti* v2.7.zip to download *Drishti*.

Source code and detailed information about this new release are also available on GitHub. Please note that *Drishti* v2.7 currently can run on the Windows and Linux operating systems but not MAC.

Once the download is finished, unzip the .zip file. Go to the "bins" folder, and then you should be able to run *Drishti* v2.7. *Drishti* is designed as a portable application.

MIT Licence

Other resources

Users can access helpful videos through the *Drishti* YouTube channel: https://www.youtube.com/channel/UCIomt3mEje4mGj_fwCNpxbQ

Tutorials and open datasets are available for practice: https://cloudstor.aarnet.edu.au/plus/s/ykqMmmikfXxHxKC?path=%2FTutorials

Community

Anyone can join the *Drishti* user community by subscribing to the *Drishti* user group via https://groups.google.com/forum/#!forum/*Drishti*-user-group/join. Besides *Drishti* user group, the authors, also help users through the social media communication channel WeChat. *Drishti* WeChat group now has more than 100 subscribers. Please feel free to email the authors to be added to both groups.

Drishti Import v2.7

Drishti Import v2.7 converts the source data into the format (. pvl.nc) which Render (8 or 16 bits per voxel) and Paint (8 or 16 bits per voxel) read.

Drishti Import v2.7 can read and convert 13 different file formats (see Figure 1 main text).

The main window (Supplementary Figure 2) is divided into two windows - the histogram window and the image window. The histogram window is used for the display of 1D histogram of the loaded volume (on the top). The image window displays the currently selected slice of volume.

Drishti Paint v2.7

Drishti Paint is designed for segmentation and data cropping of volumetric data. *Drishti Paint* v2.7 (Supplementary Figure 3) allows users to segment semi-automatically/manually and generate surface mesh for regions from the volume. To facilitate the segmentation process, *Drishti Paint* v2.7 provides two modes - Graph Cut and Curves. *Drishti Paint* v2.7 has been updated and now allows input of 16 bits full resolution volumetric data.

Detail procedures of how to perform 3D segmentation using new tools in *Paint* v2.7 and generate 3D surface mesh are displayed below. [see Procedures]

SUPPLEMENTARY TABLE

Supplementary Table 1. Thirteen formats of volumetric data that can be processed by *Drishti* v2.7.

Data format	**Name and supporting information**
*.raw	ProRay raw triangle format; a basic file format that saves the active image or stack as raw pixel data without a header
*. NIFTI	Neuroimagine Informatics Technology Initiative
TXM	Xradia X-ray transmission image data
*.jpg	Joint Photographic Experts Group
*. png	Portable Network Graphics
*.gif	Graphic Interchange Format
*.tiff/ Grayscale TIFF image	a tagged image file format
MetaImage	a particular medical image format used in the insight segmentation and registration toolkit (ITK); a text-based tagged file format
Analyse 7.6 data format	Data format from software named Analyse, which is developed by the Biomedical Imaging Resource at Mayo Clinic
*.nrrd/ NRRD	a library and file format designed to support scientific visualisation and image processing involving N-dimensional raster data
*.txm/ QMUL Tom, TXM	a file format used by ZEISS Xradia 3D X-ray Microscopes
VGL	VG Studio Project file format
DICOM	Digital Imaging and Communications in Medicine a standard medical imaging file format

SUPPLEMENTARY FIGURES 1-3

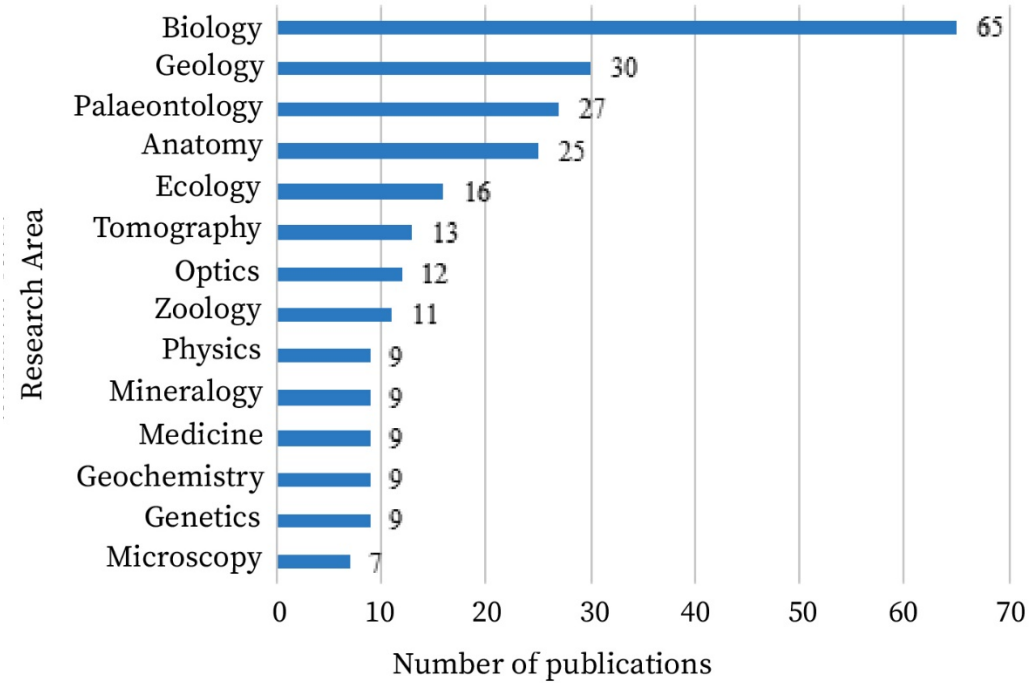

Supplementary Figure 1. Histogram of the number of publications that have used *Drishti* after Limaye (2012), [ref 24], categorised by research area. Original data from Google Scholar and Microsoft Academic. Data analysed using Microsoft Excel 2018.

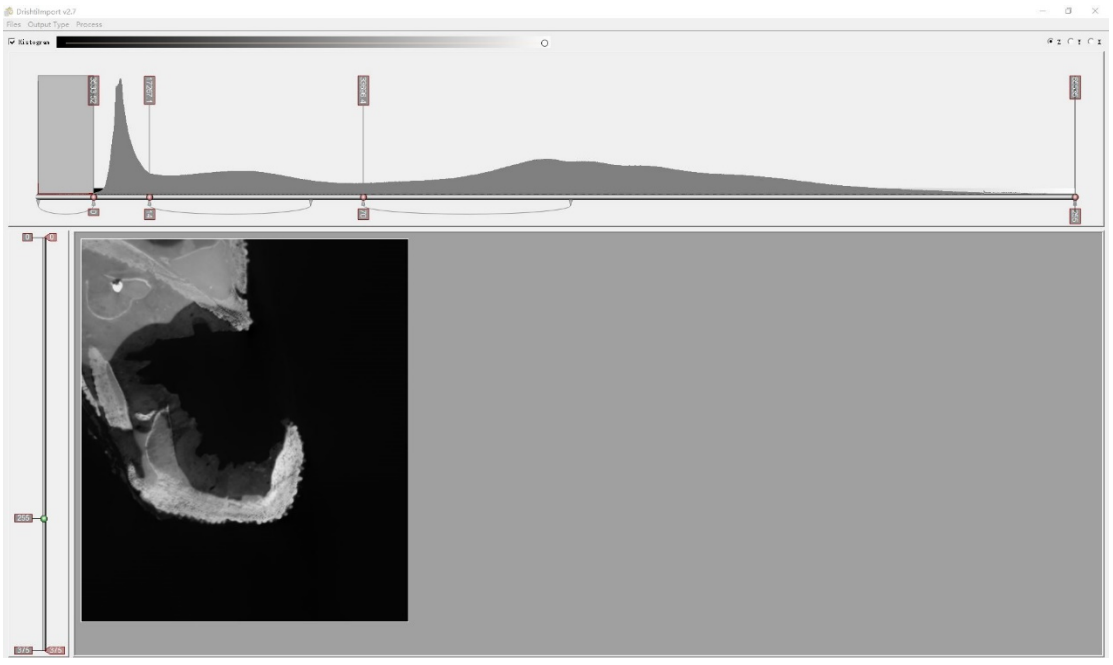

Supplementary Figure 2. A view of the main window of *Drishti Import* v2.7.

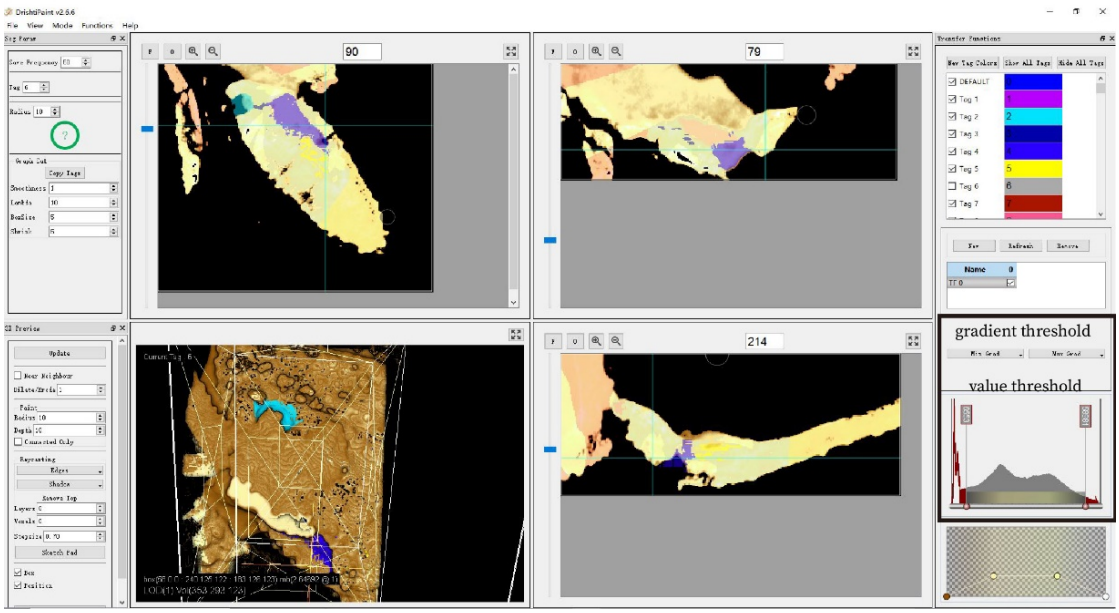

Supplementary Figure 3. A view of the user interface of *Drishti Paint* v2.7 with newly developed value and gradient multi-thresholding for both Graph Cut and Curves modes highlighted using a black box.

PROCEDURES

1. 3D segmentation using *Drishti Paint* v2.7

Download the provided volume data from Fig share:
V244_2015_selected-16bits.pvl.nc and V244_2015_selected-16bits.pvl.nc.001

Once the download is completed, open *Drishti Paint* v2.7, to show the following screen.

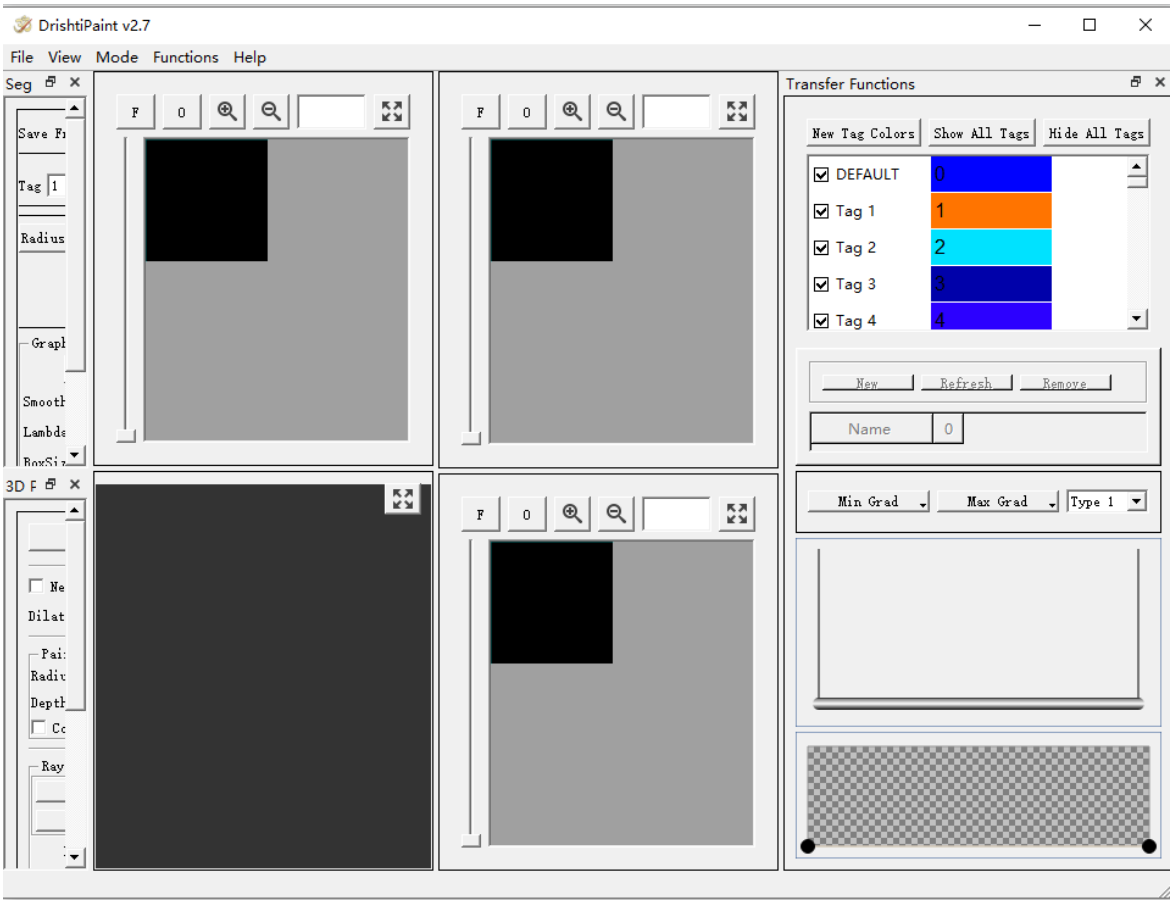

Import V244_2015_selected-16bits.pvl.nc by dragging it into *Drishti* Paint or clicking "File" →"Load"→ select V244_2015_selected-16bits.pvl.nc.

Select "1" when the Subsampling Level dialogue pops up.

[**Note** You can also subsample the volume data to ensure a quicker response while segmenting it if you do not have a good graphics card. Subsampling level 1 means keep the data as it is.]

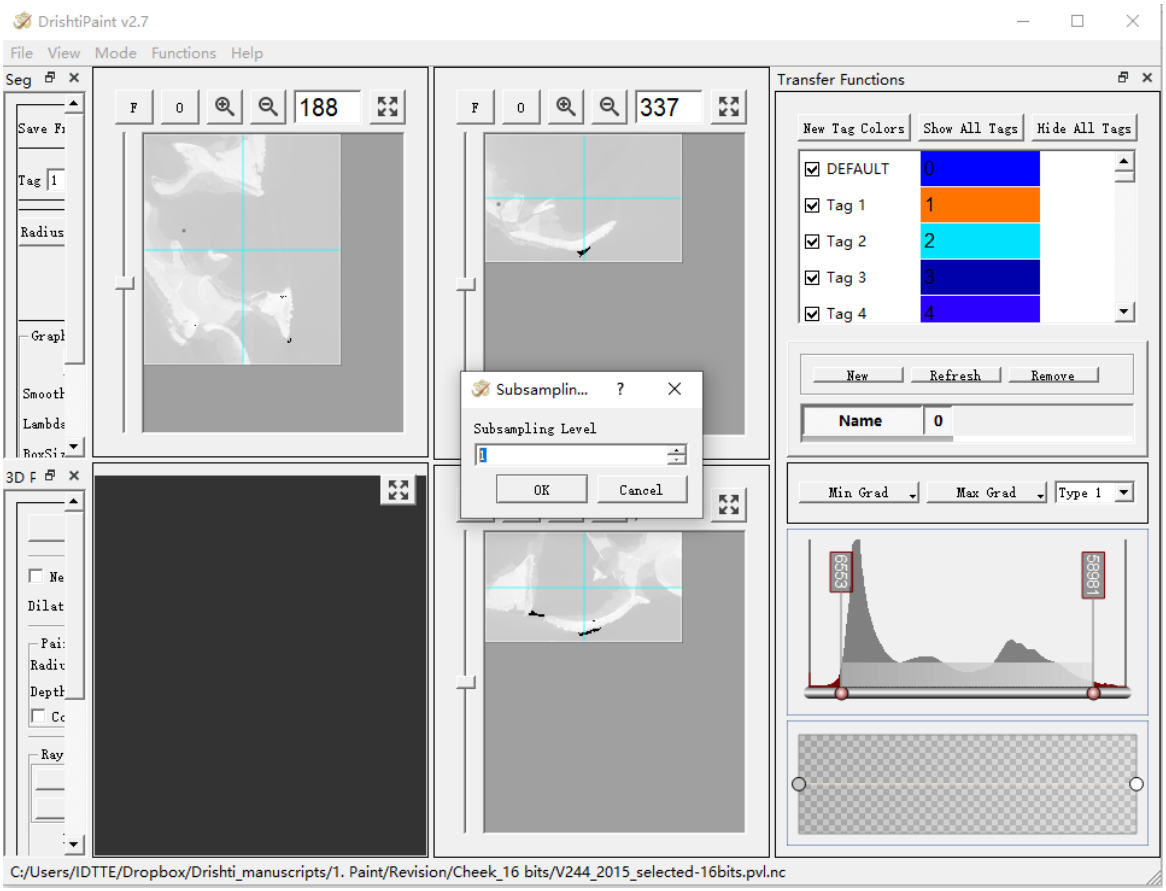

There are two modes in Paint v2.7, and the default mode is "Graph cut" which we use to segment the right cheek complex, as shown below.

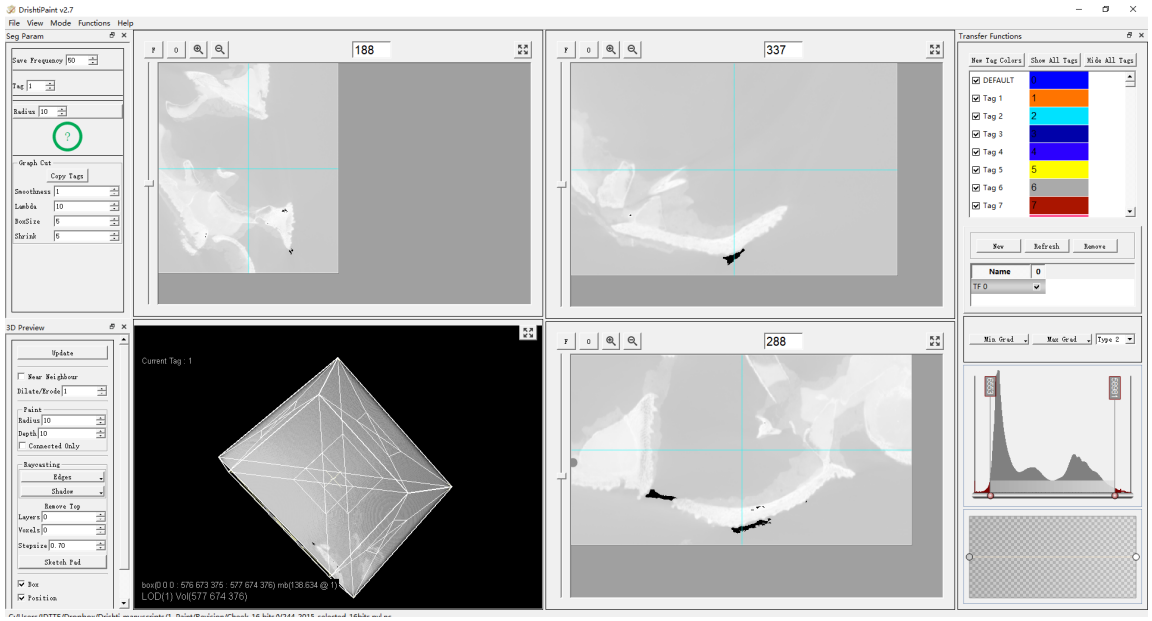

Change the colour and opacity of the data by hovering over the Colour-Opacity Gradient Interface, then press the space bar.

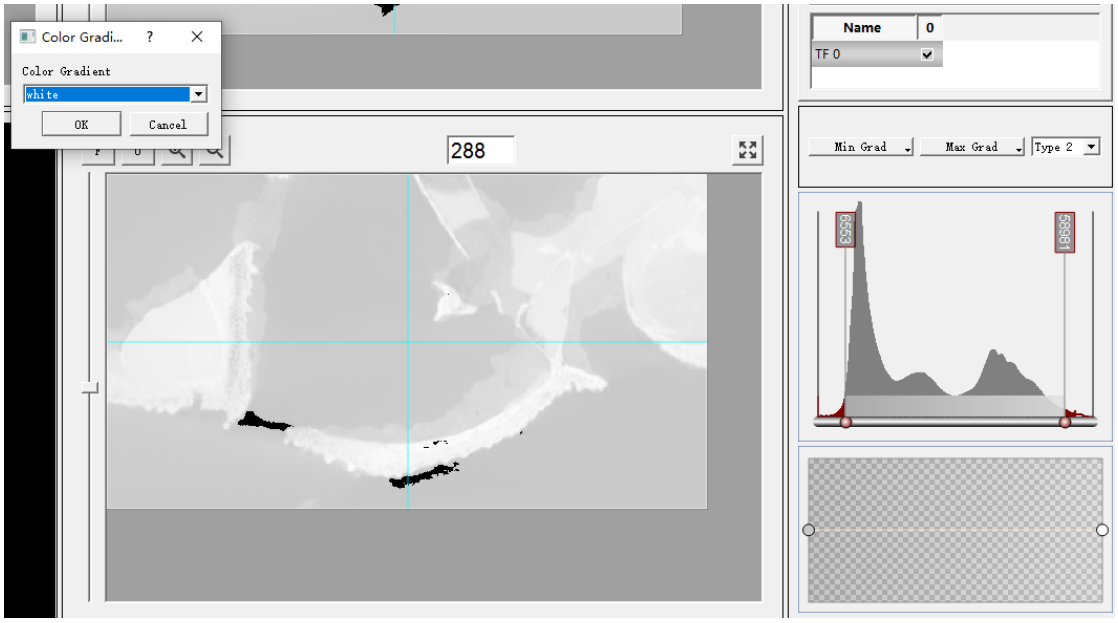

Change the Colour Gradient from white to cream-brown. [Feel free to change to any colours you prefer.] Then adjust the Transfer function Interface until the right cheek complex is shown clearly in the 3D view window at the bottom right of the four split screens, as below.

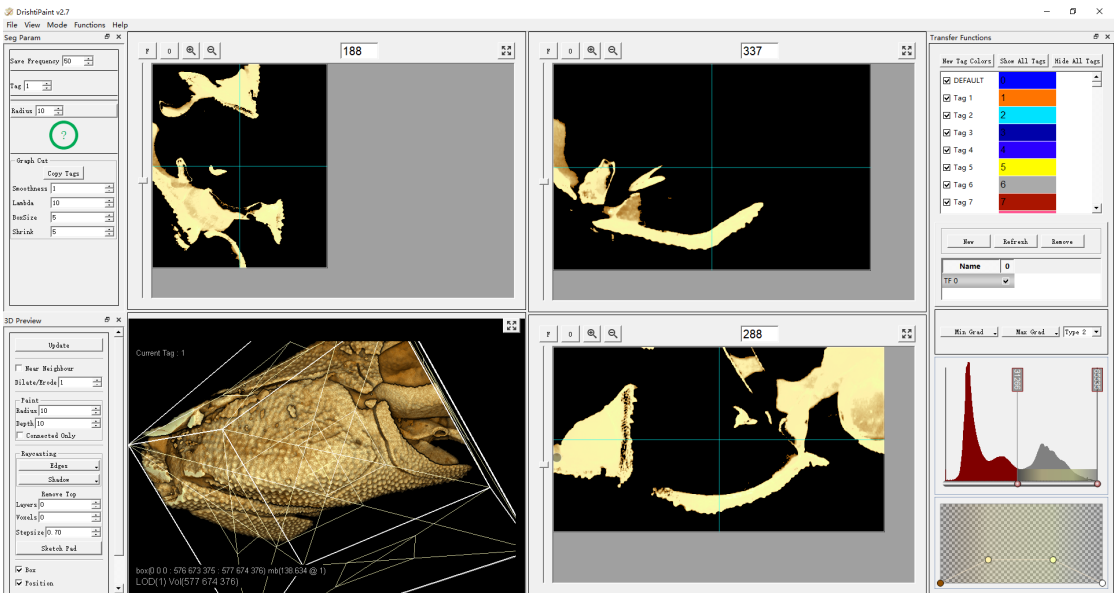

Adjust the cream-brown gradient to clear the volume, as shown.

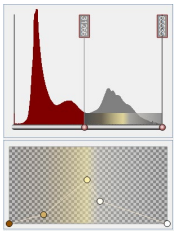

A cleared volume displays as below.

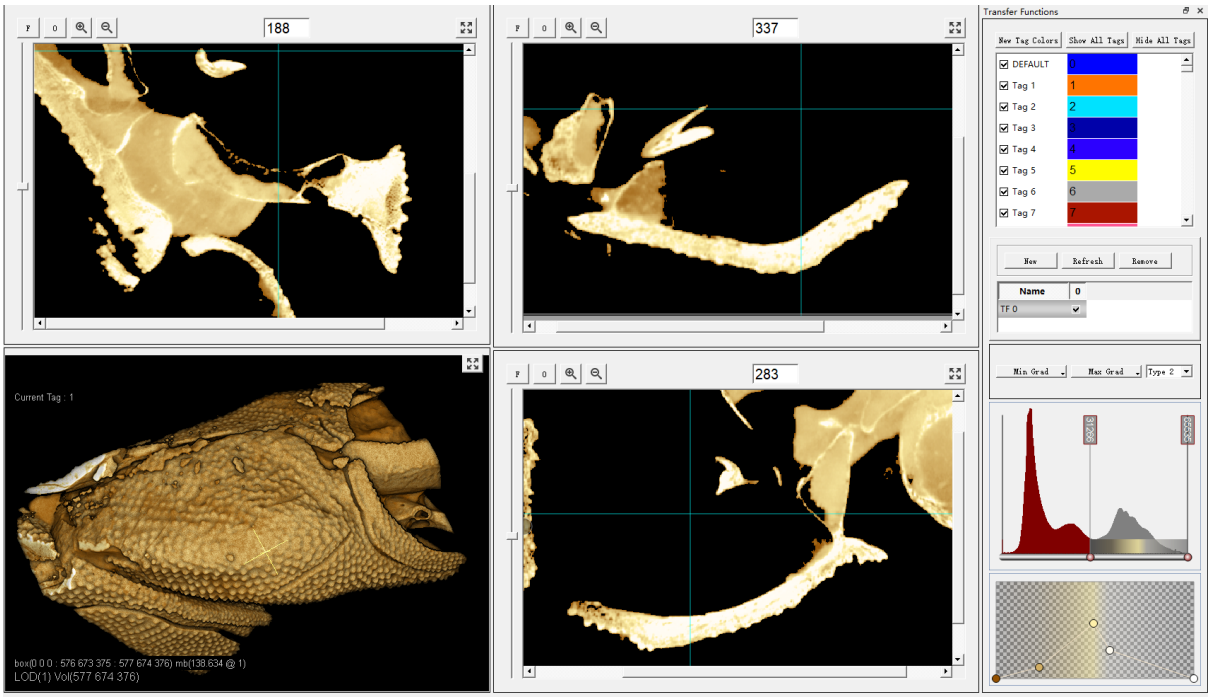

Look at this data firstly by:

1. Using arrow keys/mouse wheel or the slider bar on the left to move between slices.
2. Using Up/Down arrows to move to next/previous slice or Mouse wheel to move to next/previous slice.

Adjust the image size by using the F, O, + and - buttons for changing the image size.

- O: Original image size.
- F: Fit image size to the current window size.
- +: Increase image size.
- -: Decrease image size.

On the left panel, there are two separate panels- Seg Param and 3D Preview. Both panels are free to move anywhere on the screen. On the Seg Param panel, shown below, one can choose any tag number. Select tag number from the Tag box.

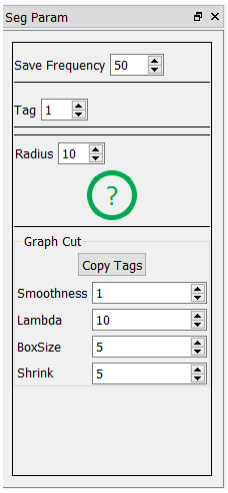

Change tag colour by clicking on tag colour patch in the "Tag Colour Editor". Double click the tag colour patch to change the tag colour.

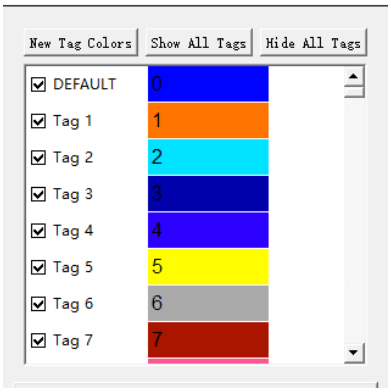

Under the "Graph Cut" mode, The Paint dot can be changed by adjusting the Radius and Depth for a better tagging result. Every dataset is different, so one will need to take time to find out the best setting. Tagging result also depends on the Smoothness, Lambda, BoxSize and Shrink features.

- Smoothness: can be used for smoothing, dilation and erosion operations.
- Lambda: controls the tightness of the curvature object region as defined by the graph cut algorithm. It is internally used to increase/decrease the average gradient magnitude
- BoxSize: indicates the average gradient magnitude which is calculated over the region of size.
- Shrink: can be used when copying tag from the previous slice to be used as seeds for tagging operation for the next slice.

The YouTube channel contains general tutorials for how to perform 2D Graph Cut, 3D Painter. We suggest using those tutorials for a detailed guide for short cuts and general introduction.

Here, we demonstrate new tools in Paint v2.7- gradient thresholding with 3D Free Form Painter.

Use gradient thresholding to clean this data further and remove unwanted noise, for example, matrices inside the fossil during preservation.

For this particular data, we used the Type 2 gradient thresholding.

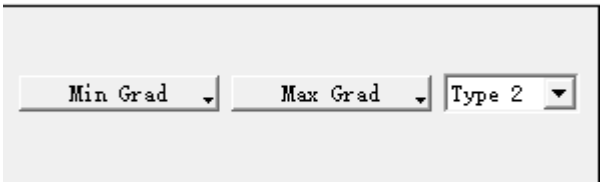

The Min Grad and Max Grad can be adjusted whenever needed while using 3D Freeform Painter to segment this data.

Use 100 Min Grad and 100 Max Grad to identify the boundaries between the right cheek complex and other unwanted elements in this data.

Then tick both Near Neighbour and Connected Only boxes to ensure your 3D segmentation only considers the connected regions.

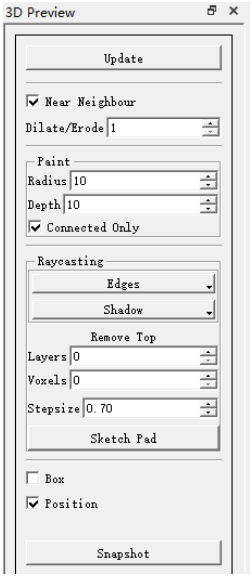

Use tag 1 to segment the cheek complex. Hold Shift then use the left mouse button to paint in the 3D view window. We used Radius 30 and Depth 12.

[Note: you can use any value as long as it gives you the correct depth and includes your region of interest.]

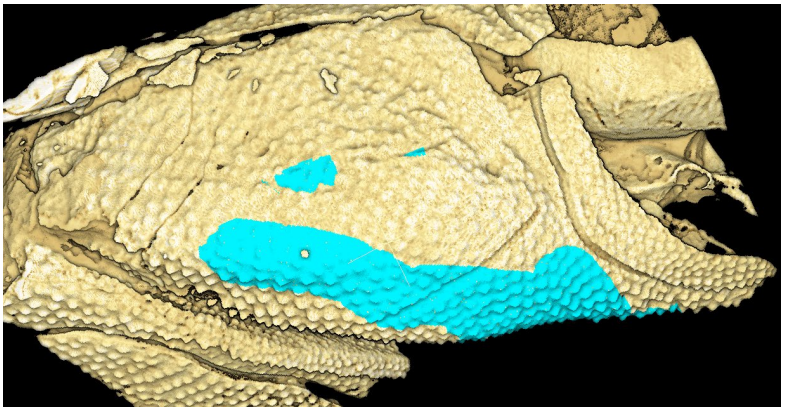

Zone into the tagged region and identify the small bits missed, for example:

Fix this by pressing "D" to perform a dilation.

[**Note** When dilating the tagged region of interest, a pop-up message may appear- “cannot dilate. You are on voxel with tag 0, was expecting tag 1”. This occurs only when the cursor is not on a voxel with the appropriate tag value. The Near Neighbour switch under 3D Preview parameter panel gives a better view of voxels (default is trilinear interpolation of voxels which gives smoother rendering but may obstruct appropriate voxel selection). This helps to select the correct voxel.]

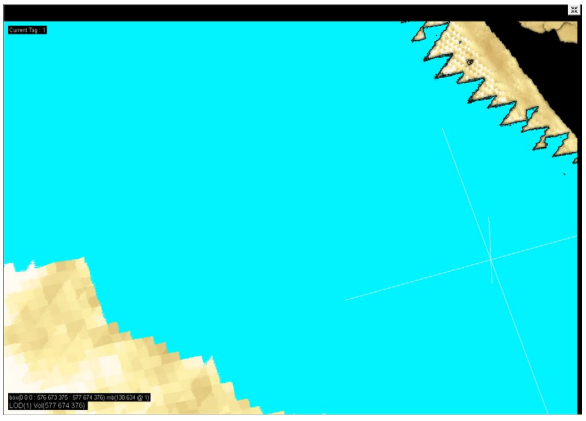

Repeat when all spaces have been filled using tag 1. Then Continue.

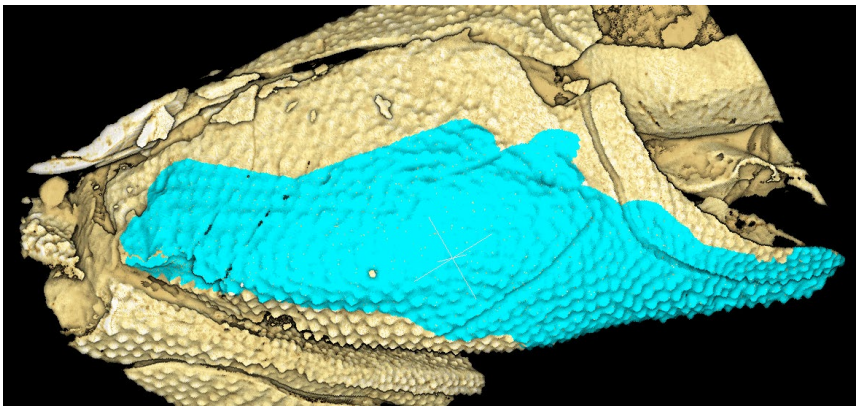

Adjust Min and Max Grad, Radius and Depth for different regions on the cheek complex, then paint the whole element. Unclick tag0 to hide all unwanted regions and only display tag 1, as below.

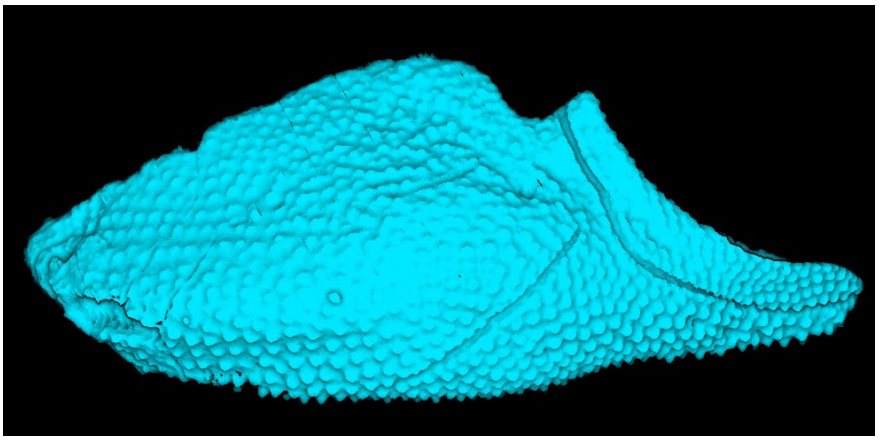

The segmented cheek complex can be extracted as either as volumetric data or surface mesh.

Extracting segmented region as volumetric data

To extract segmented volume, go to File then Extract Tagged Region. Then select 1 for tag1. Click Ok to proceed.

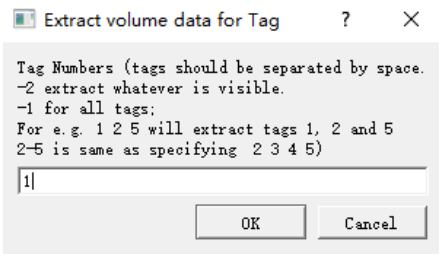

Choose Tag only.

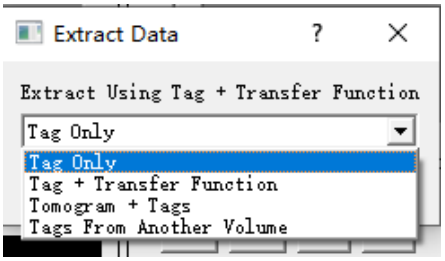

Set Outside value as 0, then click Ok to proceed.

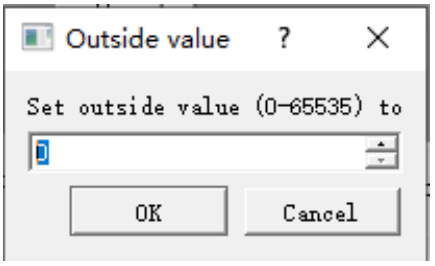

Name the file.

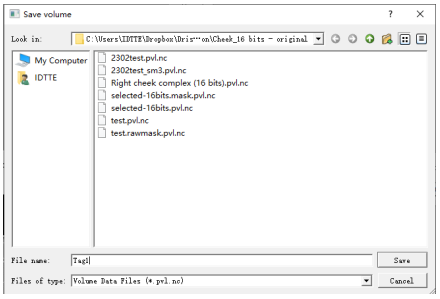

The segmented volume data of this segmented right cheek complex is now saved to the host folder- Tag1.pvl.nc & Tag1.pcl.nc.001. The saved volume can then be imported in *Drishti* or any preferred software.

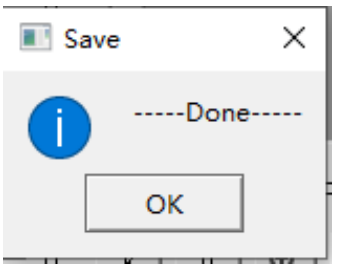

Extracting segmented region as surface mesh

To extract segmented volume as surface mesh, go to File then Mesh Tagged Region. Then select "1" for tag1.

Click Ok to proceed.

Choose the colour for this mesh using the drop-downs:

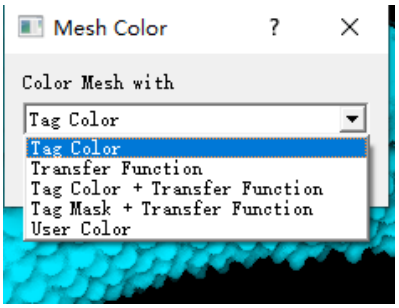

Choose No Scaling or Yes depends on what do you want to do as the next steps. Click Ok to proceed.

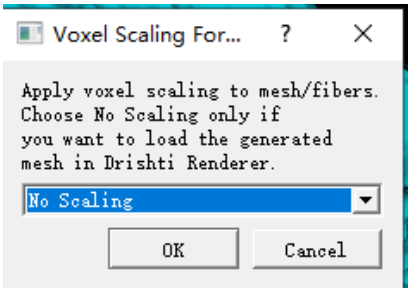

Enter "1" if you do not want any subsampling. You can also enter any number if you want to subsample your surface mesh. Click Ok to proceed.

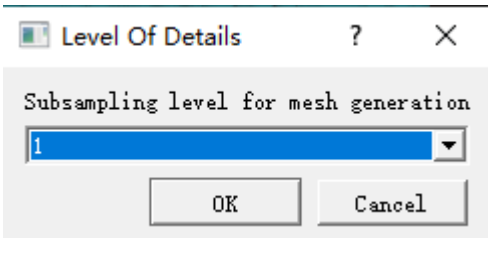

Enter the file name to save this surface mesh

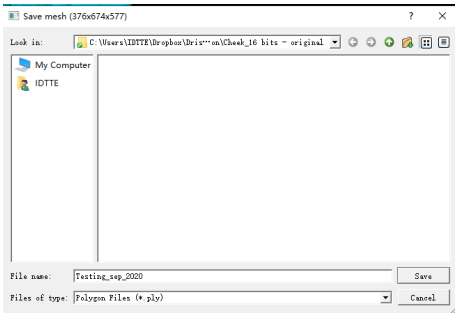

You can choose to close holes for this surface mesh data. In this case, we did not want to close any holes as we want to keep the original surfaces.

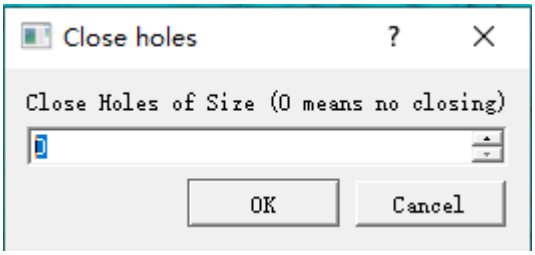

You can choose to smooth or not smooth your volume data before Paint meshing the surfaces. Here, we used the smooth factor of 3 as an example. Feel free to use any smooth factor until you get the ideal results you prefer for your data.

You can also choose to smooth your mesh. We used a factor of 3 as an example.

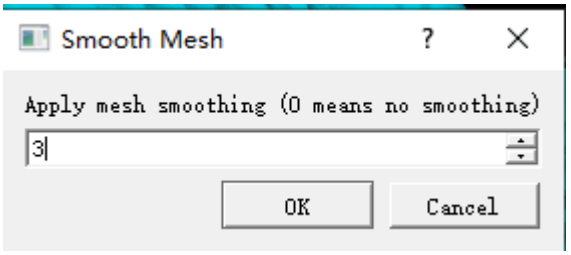

You should now have the surface mesh data of this segmented right cheek complex saved to your preferred folder. If you have followed all the steps identically, you can compare your saved output with the provided file- Testing_sep_2020.ply in Meshlab or any preferred software.

2. Mesh generation in *Drishti* v2.7

Import Tag1.pvl.nc into Drishti v2.7. By default, Drishti is in Low-resolution mode, as shown below.

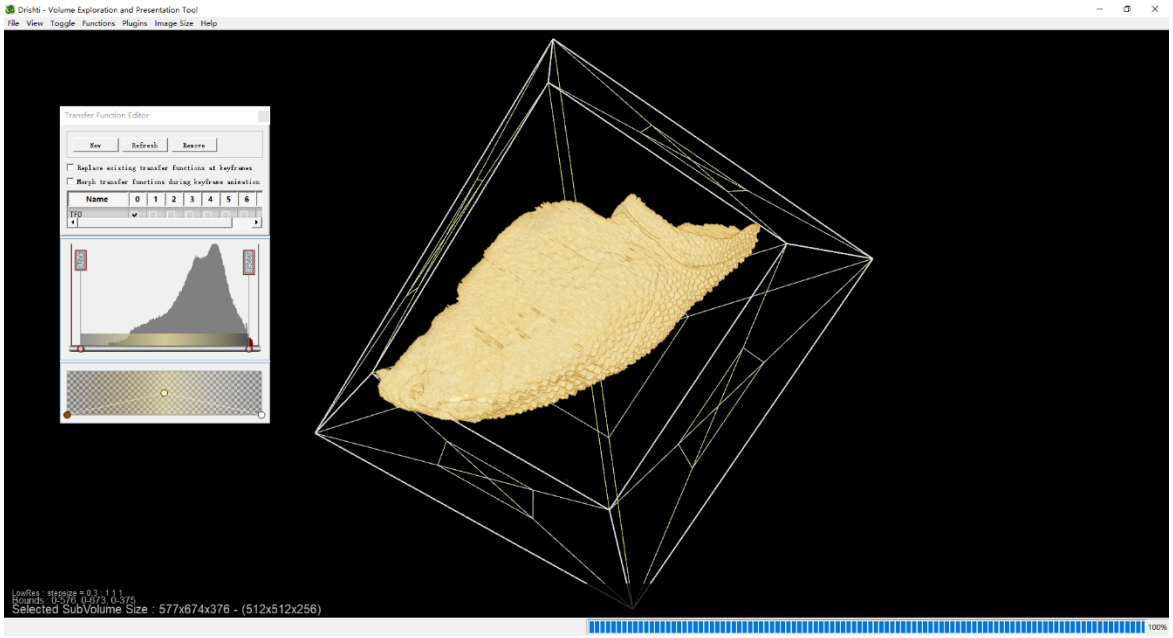

Press F2 to bring up the High-resolution mode. Select the transfer function that represents the dataset. Then adjust the Colour-Opacity Gradient Interface to "cream-brown" colours then adjust the opacity to observe this data.

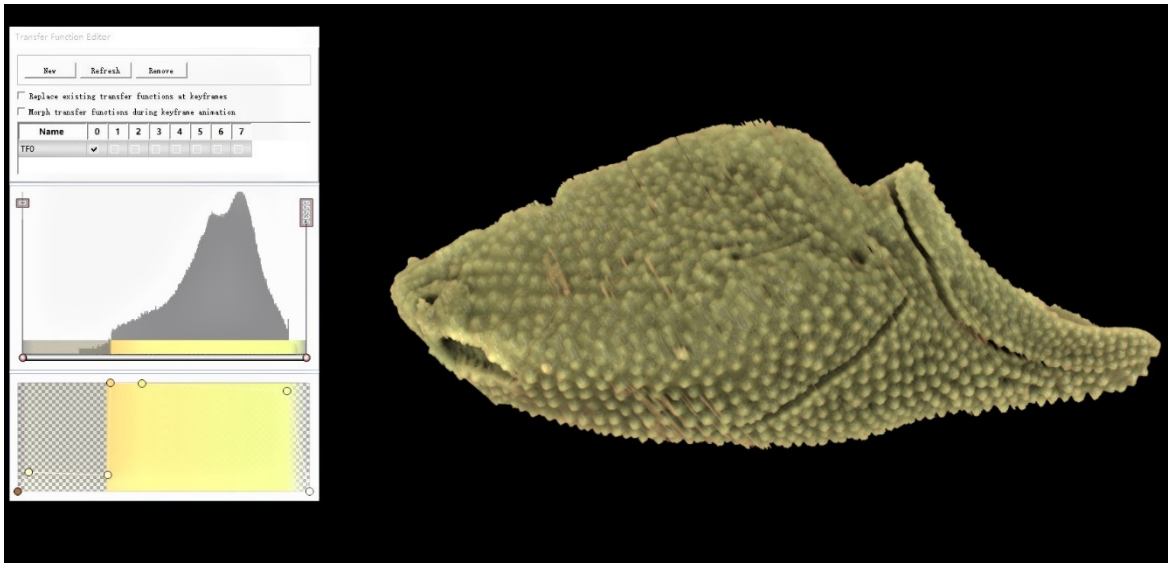

Click on Plugins on the toolbar locates at the top right corner of the screen.

Select Mesh Generator from the dropdowns. Then you should be able to see the pop-up window for Mesh Generator Parameters.

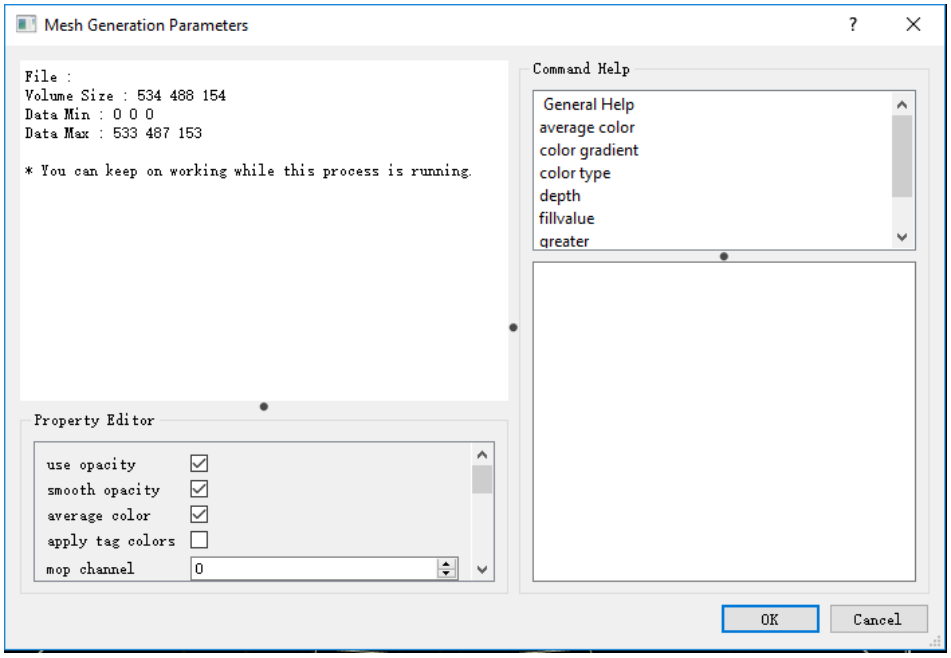

Under Property Editor, Depth is the parameter that is very useful for palaeontological data. Depth gives the user a possibility to texture the surface with the inside structure - it reveals what is “beneath the skin”. On the other hand, adjusting Depth can help to make a non-distinct feature look clearer on the surface of the object.

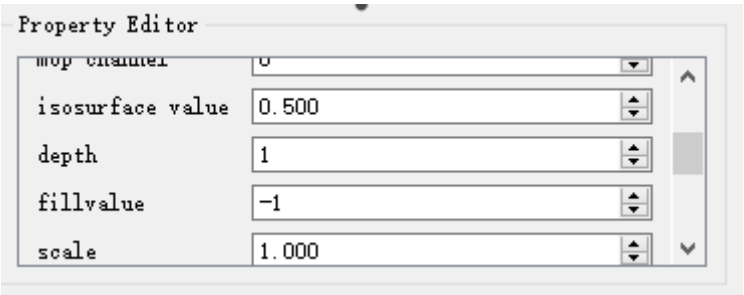

Type 3 for depth. Then press Ok to continue.

[**Note** User can specify how much memory is used for mesh generation. If not enough memory is available to accommodate all the required data, then the mesh will be generated in several slabs. These slabs are then joined together to form the complete mesh. We usually put 4 GB for a larger dataset (9GB), however how much memory you want to use is truly depending on your hardware and settings.]

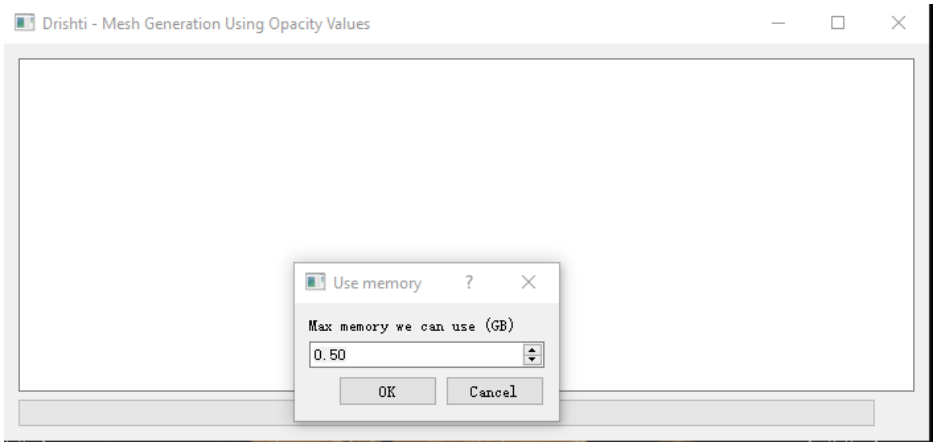

Click Ok to continue.

A pop-up window will appear to ask where you want your mesh to be saved. Select a preferred location then click Save.

If you follow all the steps above, your output should be the same as the provided data file: Cheek_Mesh.ply

Please note that both *.ply and *.stl formats are available when exporting mesh.

Your saved mesh will then be ready to import into your preferred 3D printing software.

3. Mesh simplification in *Drishti* v2.7

Import Cheek_Mesh.ply into *Drishti* v2.7
or
Click on Plugins on the toolbar locates at the top right corner of the screen.

Then select Mesh Simplify from the dropdowns. Then *Drishti* will ask you to select a mesh data to import. Select Cheek_Mesh.ply.

Drishti then asks what name and where do you want to save this simplified mesh data, enter the preferred name and pick a location to save this file. Once finished, the Mesh Simplification Parameters dialogue will pop up:

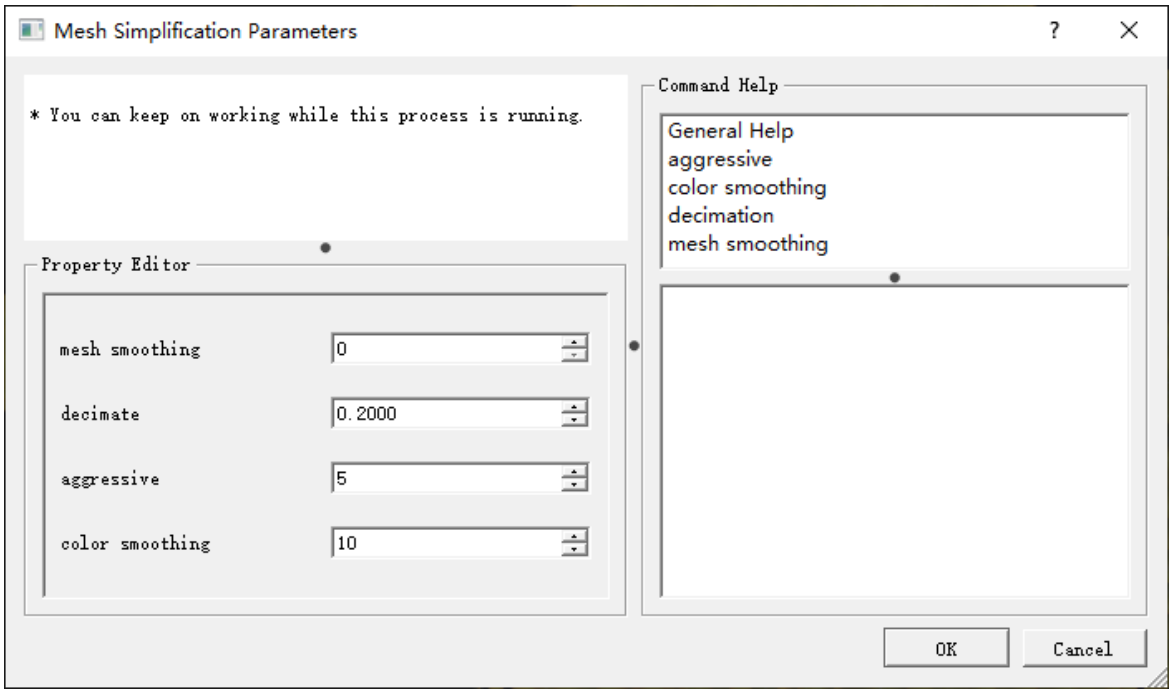

Feel free to play with the four properties. Under the Command Help, we also listed all the information/explanation of each property.

Let use: mesh smoothing 2 and decimate 0.5 (50%) as an example. Click Ok to perform this mesh simplification.

The simplified mesh is now saved: Cheek_Mesh_Simp_test.ply.

Appendix G List of my publications

Burrow, C.J., **Hu, Y.,** Young, G.C., 2016. Placoderms and the evolutionary origin of teeth: a comment on Rücklin & Donoghue (2015). Biol. Lett. 12, 20160159. https://doi.org/10.1098/rsbl.2016.0159

Hu, Y., Lu, J., Young, G.C., 2017. New findings in a 400 million-year-old Devonian placoderm shed light on jaw structure and function in basal gnathostomes. Sci. Rep. 7. https://doi.org/10.1038/s41598-017-07674-y

Hu, Y., et al., 2019. High resolution XCT scanning reveals complex morphology of gnathal elements in an Early Devonian arthrodire. Palaeoworld 28, 525–534. https://doi.org/10.1016/j.palwor.2018.12.003

Hu, Y., Young, G.C., Lu, J., 2019. The Upper Devonian tetrapodomorph *Gogonasus andrewsae* from Western Australia: Reconstruction of the shoulder girdle and opercular series using X-ray Micro-Computed Tomography. Palaeoworld 28, 535–542. https://doi.org/10.1016/j.palwor.2019.07.008

Hu, Y., Limaye, A., Lu, J., 2020. Three-dimensional segmentation of computed tomography data using *Drishti Paint*: new tools and developments. R. Soc. Open Sci. 7, 201033. https://doi.org/10.1098/rsos.201033

King, B., **Hu, Y.,** Long, J.A., 2018. Electroreception in early vertebrates: survey, evidence and new information. Palaeontology 61, 325–358. https://doi.org/10.1111/pala.12346

Lu, J., Young, G., **Hu, Y.,** Qiao, T., Zhu, M., 2019. The posterior cranial portion of the earliest known tetrapodomorph *Tungsenia paradoxa* and the early evolution of tetrapodomorph endocrania. Vertebr. Palasiat. 57, 93–104.

Zhu, Y. A., Giles, S., Young, G.C., **Hu, Y.,** Bazzi, M., Ahlberg, P.E., Zhu, M., Lu, J., 2021. Endocast and Bony Labyrinth of a Devonian “Placoderm” Challenges Stem Gnathostome Phylogeny. Curr. Biol. 31, 1112-1118.e4. https://doi.org/10.1016/j.cub.2020.12.046